

University of Virginia – Department of Chemistry

## PhD Thesis

*Author:*

Mi wha Jin

---

**ASTROCHEMICAL MODELING WITH  
NON-DIFFUSIVE MECHANISMS AND A STUDY  
OF CHEMICAL EVOLUTION IN VARIOUS  
STAR-FORMING REGIONS**

---

*Advisor :*

Prof. Dr. Robin T. Garrod

Defense: Nov 11th, 2021

*Committee Members*

Prof. Dr. Eric Herbst	Chair
Prof. Dr. Anthony J. Remijan	Member
Prof. Dr. Kateri H. DuBay	Member



# Acknowledgements

First and foremost, I would like to express my sincere gratitude to my primary advisor, Dr. Robin Garrod. When I first met Dr. Garrod in Charlottesville, I felt like a kid who was delighted to meet her favorite rock star. I finally got to meet the author of the works I had often referenced, and I knew at that moment that he would be a great mentor. He has fostered the knowledge and skills needed to be successful in my grandest academic endeavor so far. As his first international student in the cohort, I presented new challenges for Dr. Garrod. Nevertheless, he showed unwavering support through his composure and patience, which I dearly appreciate. Although he was extremely busy, I always felt welcomed whenever I had sought his advice. I could not have accomplished all my doctoral goals without Dr. Garrod's help and guidance.

I would also like to thank my secondary advisor, Dr. Anthony Remijan. He was always willing to help. Thanks to his immense knowledge and resources, I gained crucial expertise on observational studies, as well as professional experience. He encouraged me to actively participate in group discussions and confront my fear of public speaking. All these valuable experiences have helped me grow as a scientist over the past two years. Furthermore, he always kept his faith in my work throughout delays, which I truly appreciate.

In addition, I would like to thank the rest of my committee, Dr. Eric Herbst and Dr. Kateri DuBay, for their encouragement, insightful comments, and compelling questions.

I would also like to thank all my past and present colleagues in the Garrod Group, for the stimulating discussions and the fun we have had. I am especially thankful to Kamil, Aspen, and Gwen. I enjoyed jogging and exploring restaurants in Charlottesville with Kamil, who also broke down the barrier between an international and American student to always be available for a chat. Kamil's support was especially meaningful during my intense last year of the Ph.D. program. Aspen and Gwen helped me fit into the cohort when I had a hard time meeting people. They even understood my introverted tendencies, so they were not reluctant to keep approaching me. The memory of our trip to death valley always makes me smile, and the weekly game nights provided a much-needed break. I will never forget the beautiful summer night in Aspen's cabin for the celebration of my future career with wine and BBQ. It is one of my favorite memories in America.

I also like to thank my friends in Charlottesville. Seula and Mia are part of my church family in Charlottesville. Thanks to our uplifting Bible study every week, I could keep pushing through the long journey of Ph.D. despite many obstacles. I will always be grateful for that. Eunji and Yeeji were a constant source of joy in my early days in Charlottesville. I will never forget their silly jokes and beer nights, which were therapeutic. Sarah and Margaret's weekly barbecue recharged me consistently. I really enjoyed teaming up with them to clear the many stages of their game called "Overcooked?". Venting my frustration with research with Sarah and Margaret made the Ph.D studies more manageable. I can't forget Gwon and Chen for their emotional support. The aforemen-

tioned lifelong friends were some of the best parts of my time in Charlottesville. I am also thankful to the owner of Bamboo House for her authentic Korean food, which often cured my homesickness.

Last but not least, my heartfelt gratitude goes to my family for being a constant source of support and unconditional love. Thanks always for being there for me with patience, and helping me through some of the darkest times of my life. I dedicate this thesis to my mother, father, and brother.





# Contents

<b>1</b>	<b>Introduction</b>	<b>1</b>
1.1	Star Formation . . . . .	2
1.2	Astrochemical Modeling . . . . .	3
1.3	Observational Astrochemistry . . . . .	5
1.3.1	Gas-phase observations : mm/sub-mm regime . . . . .	5
1.3.2	Solid-phase observations : infrared regime . . . . .	7
1.4	Astrochemical Theory . . . . .	8
1.4.1	Gas-phase chemistry . . . . .	8
1.4.2	Grain-surface chemistry . . . . .	9
1.5	This Thesis . . . . .	11
<b>2</b>	<b>Formation of Complex Organic Molecules through nondiffusive chemistry</b>	<b>15</b>
2.1	Introduction . . . . .	16
2.2	Chemical model . . . . .	21
2.2.1	New chemical mechanisms . . . . .	22
2.2.2	Eley-Rideal reactions . . . . .	26
2.2.3	Photodissociation-induced reactions . . . . .	28
2.2.4	Three-body reactions . . . . .	29
2.2.5	Excited three-body reactions . . . . .	31
2.2.6	Physical conditions . . . . .	33
2.3	Results . . . . .	35
2.3.1	Column density analysis . . . . .	42
2.3.2	Column densities of O-bearing COMs toward the core center . . . . .	44
2.3.3	Optimization of the 3-BEF model . . . . .	49
2.3.4	CO hydrogenation and CH <sub>3</sub> OH abundances . . . . .	52
2.4	discussion . . . . .	54
2.4.1	H-abstraction/recombination as an amplifier of chemical desorption . . . . .	54
2.4.2	COM distribution and COM peaks . . . . .	56
2.4.3	The effect of diffusion barriers . . . . .	57
2.4.4	Gas-phase processes . . . . .	60
2.4.5	Other surface processes . . . . .	61
2.4.6	O <sub>2</sub> production . . . . .	65
2.5	Conclusions . . . . .	66

---

<b>3</b>	<b>Spatial distribution of acetaldehyde in Orion KL: Observations and chemical modeling</b>	<b>69</b>
3.1	Introduction . . . . .	70
3.2	Methods . . . . .	71
3.2.1	Observations and data reduction . . . . .	71
3.2.2	Chemical Model . . . . .	72
3.3	Data analysis and Results . . . . .	74
3.3.1	Emission map . . . . .	74
3.3.2	Line identification and spectra . . . . .	77
3.3.3	Derivation of physical parameters . . . . .	78
3.4	Discussions . . . . .	78
3.4.1	Spatial distribution of acetaldehyde and other HCO-bearing species	78
3.4.2	Aldehyde chemistry and chemical modeling . . . . .	81
3.4.3	Searching for other aldehyde species . . . . .	90
3.5	Summary . . . . .	90
<b>4</b>	<b>Chemo-dynamical modeling to predict new ice species for detection with JWST</b>	<b>93</b>
4.1	Introduction . . . . .	94
4.2	Chemo-dynamical Model . . . . .	96
4.2.1	Chemical model . . . . .	97
4.2.2	Radiative-hydrodynamics simulations . . . . .	101
4.3	Results & Discussions . . . . .	102
4.3.1	Physical/dynamical behavior . . . . .	102
4.3.2	Main ice constituents . . . . .	104
4.3.3	Other volatiles expected to be abundant in the ice mantles . . . . .	108
4.3.4	Calculated ice column densities . . . . .	112
4.3.5	Synthesis of model ice spectra and diagnostic detectability of new ice species with JWST . . . . .	115
4.3.6	Gas-phase abundances . . . . .	122
4.3.7	High ice column density of H <sub>2</sub> O . . . . .	124
4.3.8	The effect of nondiffusive chemical mechanisms . . . . .	124
4.3.9	Implications of this study and future perspectives . . . . .	126
4.4	Conclusions . . . . .	127
<b>5</b>	<b>Conclusions</b>	<b>131</b>

# List of Figures

1.1	The process of solar-type star formation (upper panel), and chemical processes on dust surfaces with the change of underlying physical conditions along the way (lower panel). Images are taken from Öberg (2016) . . . . .	4
1.2	Cumulative number of known interstellar molecules with the advent of observational instruments over time. The image taken from McGuire (2021)	6
2.1	Illustration of alternative mechanisms for acetaldehyde formation: (a) the regular diffusive grain-surface reaction between radicals $\text{CH}_3$ and $\text{HCO}$ , and (b) a postulated three-body excited-formation mechanism involving $\text{H}$ , $\text{CH}_2$ and $\text{CO}$ , followed by a regular diffusive reaction between the radical product, $\text{CH}_3\text{CO}$ , and another $\text{H}$ atom. In case (a), reaction is slow at low temperatures. In case (b), a rapid initiating reaction between $\text{H}$ and $\text{CH}_2$ , with exothermicity $\Delta H_f^0 = 4.80$ eV, provides enough energy to the product $\text{CH}_3$ that it may immediately overcome the barrier to reaction with a neighboring $\text{CO}$ molecule. This produces a precursor to acetaldehyde, $\text{CH}_3\text{CO}$ , that can easily be hydrogenated by a mobile $\text{H}$ atom to form $\text{CH}_3\text{CHO}$ . . . . .	32
2.2	Time evolution of the gas-phase abundances of the three O-bearing COMs, at the core center, for models using each of the new mechanisms. The abundance from the control model is denoted as a black dashed line. Diamonds indicate the abundances at the end of each model run. The black dot-dash lines and the gray shaded regions indicate the observational abundances and their uncertainties, obtained from Jiménez-Serra et al. (2016) for L1544. The gas density is indicated by the right-hand vertical axis and the similarly colored line. . . . .	36
2.3	Time evolution of the abundances in the dust-grain ice mantles of the three O-bearing COMs at the core center, for models using each of the new mechanisms. The abundance from the control model is denoted as a black dashed line. Diamonds indicate the abundances at the end of each model run. The gas density is included for reference, indicated by the right-hand vertical axis and the similarly colored line. . . . .	37

2.4	Radial distribution of the gas-phase abundances of the three O-bearing COMs depending on the mechanisms. The black dotted line and grey shaded region indicates the abundance from the observation and error, respectively. The observational data and its error is referred from the Jiménez-Serra et al. (2016). The observational error of the CH <sub>3</sub> CHO is not provided in the reference. The abundance from the control model is denoted as a black dashed line and a black dotted line, respectively. While the result from the 3-B combined with the 3-BEF is denoted as a black solid line, a green line represent the 3-B only model. The red and blue solid line indicates the abundances from the E-R model and PD-Induced model, respectively. . . . .	38
2.5	Radial distribution of the solid-phase abundances of the three O-bearing COMs depending on the mechanisms. The black dotted line and grey shaded region indicates the abundance from the observation and error, respectively. The observational data and its error is referred from the Jiménez-Serra et al. (2016). The observational error of the CH <sub>3</sub> CHO is not provided in the reference. The abundance from the control model is denoted as a black dashed line and a black dotted line, respectively. While the result from the 3-B combined with the 3-BEF is denoted as a black solid line, a green line represent the 3-B only model. The red and blue solid line indicates the abundances from the E-R model and PD-Induced model, respectively. . . . .	39
2.6	Radial distribution of the ice abundances of the main ice constituents. The abundance of CO and CO <sub>2</sub> is denoted as a black solid and a black dashed line, respectively. A blue, green, and red solid line represents the abundances of CH <sub>4</sub> , NH <sub>3</sub> , and CH <sub>3</sub> OH, respectively. . . . .	41
2.7	Column densities calculated from each model. Red, blue, and green histogram represents the molecular column densities of AA, DME, and MF, respectively. The errors of the modeled column densities are not presented here as those values are relatively small (< 3%) compared to the bar size. The observed value and its error bound are presented together with solid and dashed horizontal lines respectively. For the COM peak position (middle panel), the the observations was performed towards 4000 AU, corresponding to the observational methanol peak of L1544 (Jiménez-Serra et al., 2016), while the off-position for the model is 2000 AU, where fractional abundance peak occurs. . . . .	46
2.8	Time evolution of the fractional ice composition of the reactants on the grain-surface related to the 3-B+3-BEF mechanisms forming CH <sub>3</sub> OCH <sub>3</sub> (red lines) and CH <sub>3</sub> OCHO(black lines). Note that the abundances shown refer specifically to species on the outer grain/ice surface and not within the ice mantles. A fractional abundance of $\sim 1.3 \times 10^{-12}$ corresponds to one particle per grain. . . . .	47
2.9	Rotation diagrams for the three O-bearing COMs at the core center. The black dashed lines represent the fit. . . . .	50
2.10	Comparison of chemical distribution of the 3-BEF Best (solid lines) in the gas with those of the normal 3-B+3-BEF (dashed lines). Control model results are also shown (dotted lines). . . . .	51

2.11	(a) Radial distribution of fractional abundance of CH <sub>3</sub> OH for each model. The abundance value from the observations toward the core center is denoted a black dotted line. Gas density as a function of radius is also indicated. (b) The normalized, convolved intensity of a representative emission line for methanol and for each of the three COMs of interest, shown as a function of the offset of the beam from the on-source position.	52
2.12	The rotation diagram for CH <sub>3</sub> OH. The black dashed lines represent the fit.	53
2.13	Comparison of chemical distribution of the COMs in the 3-BEF Best models with different values of $E_{\text{dif}}:E_{\text{des}}$ for atoms.	58
2.14	Comparison of chemical distribution of the reactants in the 3-BEF Best models with different values of $E_{\text{dif}}:E_{\text{des}}$ for atoms.	58
2.15	Radial distribution of the solid-phase abundances of O <sub>2</sub> (solid lines) and H <sub>2</sub> O <sub>2</sub> (dashed lines) in the PD-Induced model.	65
3.1	Acetaldehyde integrated intensity map at 312.78377 GHz. The synthesized beam is shown in the bottom right corner. The contour levels are (3,5,7,9) × sigma ( $\sigma=0.07$ Jy/beam km/s; uncorrected for primary beam). Yellow contour is at 3 $\sigma$ while black contours are at above 5 $\sigma$ . The cross mark the AA peak positions above 3 $\sigma$ .	75
3.2	Channel map of the representative AA transition (312.78377 GHz)	76
3.3	The XCLASS model spectra of acetaldehyde (blue) overlaid with ALMA observations toward AA1 (black solid)	79
3.4	Extrapolation of $k$ from two different experimental data for MF	85
3.5	Surface reaction diagram for the formation of acetaldehyde	86
3.6	Time-dependent ice abundances of CO and OH on the grain surface	87
4.1	Snapshots of the physical conditions as functions of radius at four different evolutionary times in the RHD model ; 1 yr (blue), 192,400 yr (green), 254,800 yr (yellow), and 255,100 yr (red)	103
4.2	Physical evolution of the innermost trajectory as a function of time during the RHD model. The black solid line and the yellow dashed line indicates the evolution of density and temperature, respectively.	104
4.3	Radial distribution of the main ice constituent abundances during the evolution of Cha-MMS1; H <sub>2</sub> O (solid black), CO (solid green), CO <sub>2</sub> (dashed green), NH <sub>3</sub> (solid red), CH <sub>4</sub> (dashed red) and CH <sub>3</sub> OH (solid blue). The yellow lines indicate density profile within the source obtained from the RHD simulation.	106
4.4	Final distribution of the main ice constituent abundances within Cha-MMS1; H <sub>2</sub> O (solid black), CO (solid green), CO <sub>2</sub> (dashed green), NH <sub>3</sub> (solid red), CH <sub>4</sub> (dashed red) and CH <sub>3</sub> OH (solid blue). The magenta lines indicate the temperature profile within the source obtained from the RHD simulation.	107
4.5	Final distribution of the main ice constituent abundances w.r.t. water ice within Cha-MMS1; H <sub>2</sub> O (solid black), CO (solid green), CO <sub>2</sub> (dashed green), NH <sub>3</sub> (solid red), CH <sub>4</sub> (dashed red) and CH <sub>3</sub> OH (solid blue). The yellow lines indicate the density profile within the source determined by solving the RHD equations.	108

4.6	Radial distribution of the ice abundances with respect to water ice abundances at the end of the evolution. The yellow lines indicate the density profile within the source determined by solving the RHD equations. . . . .	109
4.7	Radial distribution of the column density produced by our model of Cha-MMS1 for large O-bearing ice species. Gray dashed lines indicate the observed radial offsets from the center of Cha-MMS1 for the lines of sight toward a selection of background stars. . . . .	111
4.8	Map field of ice mapping in the ice age project. Green contours indicates high- $A_V$ 870 $\mu\text{m}$ dust continuum emission (Belloche et al., 2011). The targets of ice age are denoted as large white crosses. From the left, Ced 110 IRS4 (Class I protostar), Cha-MMS1 (Class 0 protostar), and C2 (prestellar core). . . . .	112
4.9	Simulated IR spectrum at NIRCAM/WFSS coverage. The left panel shows the one based on the regular ice composition without scaling (setup A) while the right panel shows the one from scaled down ice composition ( $0.01 \times N_i$ ; setup B.1). . . . .	119
4.10	Simulated IR spectrum at NIRCAM/WFSS coverage when 2.5 times higher ice abundances for COMs are assumed (setup B.2). The left panel shows the spectrum including all ice species, while the right panel has the contribution by the main ice constituents subtracted. . . . .	120
4.11	Simulated IR spectrum at MIRI coverage when 2.5 times higher ice abundances for COMs are assumed (setup B.2) The left panel shows the spectrum including all ice species, while the right panel has the contribution by the main ice constituents subtracted. The grey dashed line indicates the position of $9.7\mu\text{m}$ silicate dust absorption band which is assumed to be already subtracted. . . . .	121

# List of Tables

2.1	Initial elemental and chemical abundances . . . . .	21
2.2	Gas-phase reactions newly included in chemical network . . . . .	23
2.3	Important and/or newly-included grain-surface and ice-mantle reactions . .	24
2.4	nondiffusive mechanisms included in model setups . . . . .	34
2.5	Abundances relative to the H <sub>2</sub> O ice column density. . . . .	42
2.6	List of targeted transitions with their spectroscopic properties . . . . .	43
2.7	The molecular column densities of the COMs at the core center . . . . .	44
2.8	The molecular column densities of the COMs toward the off-center COM peak . . . . .	45
2.9	The molecular column densities of the COMs toward the outer-shell (radius 9000 AU) . . . . .	45
2.10	Column densities of COMs in the 3-BEF Best model . . . . .	50
2.11	List of methanol transitions with their spectroscopic properties . . . . .	53
2.12	Local fractional abundances of COMs at the core center when the H- abstraction reaction listed is <i>switched off</i> in the 3-BEF Best. . . . .	55
3.1	Comparison of the observation specification . . . . .	72
3.2	Initial elemental and chemical abundances . . . . .	74
3.3	Source parameters characterized by 2-D Gaussian map fitting . . . . .	75
3.4	Line parameters for the detected transitions for AA1 . . . . .	77
3.5	Column densities of HCO-bearing species . . . . .	81
3.6	Ice abundances of the control model at the end of prestellar phase . . . . .	81
3.7	Gas-phase abundances of the control model at the end of warm-up ( $T_{\text{kin,max}}=120$ K) . . . . .	82
3.8	Updated / newly-included gas-phase reactions . . . . .	83
3.9	Updated / newly-included grain-surface and ice-mantle reactions . . . . .	84
3.10	Ice abundances ( $n(i)/n_{\text{H}}$ ) with the model update . . . . .	84
3.11	The update of binding energies of species . . . . .	88
3.12	Gas-phase abundances at different warm-up temperature . . . . .	88
3.13	Relative abundance ratios w.r.t. FA column densities at different warm-up temperature . . . . .	89
4.1	Initial elemental and chemical abundances . . . . .	99
4.2	Updated and/or newly-included grain-surface and ice-mantle reactions . . .	100
4.3	The relative abundances of the main ice constituents with respect to water ice column density . . . . .	105
4.4	Ice species investigated in this study . . . . .	107

4.5	Spatial distribution of ice abundance of COMs w.r.t. water ice within Cha-MMS1 . . . . .	111
4.6	The information on background stars near to Cha-MMS1 . . . . .	114
4.8	Ice compositions for the synthesis of IR spectra . . . . .	118
4.7	Ice spectral parameters assumed for the synthesis of ice spectrum . . . . .	118
4.9	Comparison of the abundances of gas-phase species between the model and the observation . . . . .	123
4.10	The effect of the nondiffusive mechanisms on the main ice constituents . .	125
4.11	The effect of the nondiffusive mechanisms on the O-bearing ice species . .	126

# 1

# Introduction

## Contents

---

<b>1.1</b>	<b>Star Formation</b> . . . . .	<b>2</b>
<b>1.2</b>	<b>Astrochemical Modeling</b> . . . . .	<b>3</b>
<b>1.3</b>	<b>Observational Astrochemistry</b> . . . . .	<b>5</b>
1.3.1	Gas-phase observations : mm/sub-mm regime . . . . .	5
1.3.2	Solid-phase observations : infrared regime . . . . .	7
<b>1.4</b>	<b>Astrochemical Theory</b> . . . . .	<b>8</b>
1.4.1	Gas-phase chemistry . . . . .	8
1.4.2	Grain-surface chemistry . . . . .	9
<b>1.5</b>	<b>This Thesis</b> . . . . .	<b>11</b>

---

Our Galaxy is replete with molecules: from simple species such as  $\text{H}_2$  and  $\text{CO}$  to more complex organic molecules (COMs)<sup>1</sup>, a rich chemical diversity has been unveiled in the interstellar medium (ISM) over the past several decades. Understanding the degree to which chemical complexity can occur during the star formation process and how much of this complexity may be inherited by emerging planetary systems is important to answer our fundamental questions about the origin of life (Jørgensen, Belloche & Garrod, 2020).

Astrochemistry is the study of chemical composition and evolution under astrophysically relevant conditions, namely, low pressures and low temperatures. Chemical processes in the ISM are generally distinguished based on where the reaction takes place – gas-phase chemistry and grain-surface chemistry. One of the heated discussions in the astrochemistry community over the last decade is over where the formation of COMs is dominantly processed between the two phases. Although the answer is not necessarily an “either/or” argument in general, the origin of some specific species may be dominantly explained by formation mechanisms within a single phase.

---

<sup>1</sup>Per common use in astrochemistry: Carbon-bearing molecules containing 6 or more atoms

The cross-disciplinary study throughout observational / chemical modeling / laboratory / quantum mechanical approaches is indispensable to precisely answer this question. There have been significant advances in our observational understanding with the advent of the state-of-the-art telescopes such as the Atacama Large Millimeter/submillimeter Array (ALMA). This urges the dedicated studies for the other research fields to carve out the underlying chemistry by interpreting the abrupt accumulation of observational data. This thesis is prepared to keep up with those challenges in a timely manner. We deal with astrochemistry with a particular focus on gas-grain chemical modeling but also taking context from the observations and laboratory works. Before beginning the details of this thesis, here we provide relevant background information as an introduction. Section 1.1 depicts the process of star formation with the perspective of astrochemistry. Section 1.2 summarizes the overview of astrochemical modeling. Section 1.3 discusses a brief history of observational astronomy in both gas- and solid-phase regime. Lastly, section 1.4 touches the key concepts of astrochemistry that are relevant to this work.

## 1.1 Star Formation

Understanding the process of star formation is indispensable to investigate the origin of chemical complexity therein. The chemical processes involving the formation and the destruction of various species are strongly dependent on the underlying physical evolution during the star formation, such as the changes in density, temperature, intensity of irradiation, and visual extinction. Over the last decades, the canonical scenario for the formation of a solar-type protostar has been established. In this section, one of the most prevailing schemes of grain-surface chemistry will be introduced in this story along the way.

The star formation begins when the equilibrium balance of molecular clouds is locally broken down. Some of the local condensations as a result of the imbalance become seeds of star, so-called, prestellar cores, forming cold ( $\sim 10$  K) and dense ( $10^5 - 10^8 \text{ cm}^{-3}$ ) cores by collecting mass via gravitational collapse. In this environment, gaseous atoms and molecules accrete onto bare grain surfaces, forming ice mantles – the accumulation of ice layers beneath the outer ice surface. The surface chemistry at this stage should be dominated by hydrogenation of the accreted materials because only atomic hydrogen is mobile in such a cold environment. This results in the formation of simple hydrides such as  $\text{H}_2\text{O}$ ,  $\text{NH}_3$ ,  $\text{CH}_4$ , and  $\text{CH}_3\text{OH}$ , which are the main constituents of ice mantles.

A noteworthy feature at this stage is the formation of  $\text{CH}_3\text{OH}$  ice via ongoing hydrogenation of CO. Methanol is believed to be a parental molecule of other larger COMs : methanol can be broken down into radicals through photodissociation, and these photo-products can become main ingredients to drive chemical complexity via radical-radical recombination when dust temperature increases. However, for a long evolutionary time, the temperature of the core hardly changes because it is optically thin to thermal emission.

Further infall leads to the development of an adiabatic core where gravitational potential energy efficiently heat the infalling envelope of dust and gas. Once the star-forming core is warmed up to temperatures of 20 K – 30 K, radicals on the surface become mobile and experience diffusion to meet another reaction partner to form larger COMs. However,

the dust temperature is not high enough to thermally release the surface species into the gas at this stage. Desorption processes then are more likely to rely on non-thermal mechanisms such as chemical (or reactive) desorption<sup>2</sup>, of which efficiency is not high enough for large COMs to be detected in the gas.

Further collapse develops a protostar - a star-like object but its core is not yet hot enough for driving nuclear fusion - at the center. The protostar interacts with the surrounding infalling envelope through an accretion disk where the infalling material spins inward to the protostar and falls upon it, and this disks typically accompany jets and outflows<sup>3</sup> as a result of conservation of angular momentum. At this stage, dust and gas is warmed up to temperatures of tens or hundreds of K. The ice mantle material is then thermally desorbed at temperature typically on the order of 100 K, forming the chemically rich regions surrounding low-mass embedded protostars, also referred to as hot corinos. Many of the first detection of COMs have been made toward this type of objects. This scenario is well presented in figure 1.1.

## 1.2 Astrochemical Modeling

In this thesis, a rate-equation based astrochemical model, *MAGICKAL* (Garrod et al., 2008), is used as an exclusive tool of study. These types of models calculate the time-evolution of chemical abundances using chemical kinetics which is characterized by reaction networks and their rates. A generic rate equation model has superior stability and computational feasibility to other types of models. This feature allows the adoption of large reaction networks involving hundreds of molecules into the model, which enables the model to serve as a virtual laboratory; the chemical outputs from the experimental studies on a microscopic scale are tested in comprehensive ways to the scale up to astrophysically relevant ones.

A generic form of astrochemical models now consist of a coupled phase - gas phase and grain surfaces (in some cases, both grain surfaces and icy mantles). Gas-phase reactions are generally described in two-body collisions, while chemical processes for a single atom/molecule such as ionization and photodissociation also exist. In the case of grain surface, chemical reactions are also treated as two-body processes, but the Langmuir-Hinshelwood mechanism is relevant to this: the surface species diffuses across the surface until it encounters another reaction partner to proceed a grain-surface reaction. The chemistry between gas and grain-surface is linked with accretion (adsorption) and desorption processes. A generic formalism of the chemical processes described above is provided in section 1.4.

Some astrochemical models "including *MAGICKAL*" consider the third phase to represent the chemistry taking place within the ice mantle. In this case, the surface layer represents the outermost layer of ice, and the mantle is allowed to grow as the surface coverage on the grains increases (Garrod & Pauly, 2011). The chemistry between icy mantles and grain surfaces is coupled with transfer of materials. The kinetics within the ice mantle is described similarly to the case of grain surface, but the diffusion within the

---

<sup>2</sup>breaking the bond between molecule and grain surface by the excess of energy released by a reaction

<sup>3</sup>warm and fast gas flows from the poles of a protostar

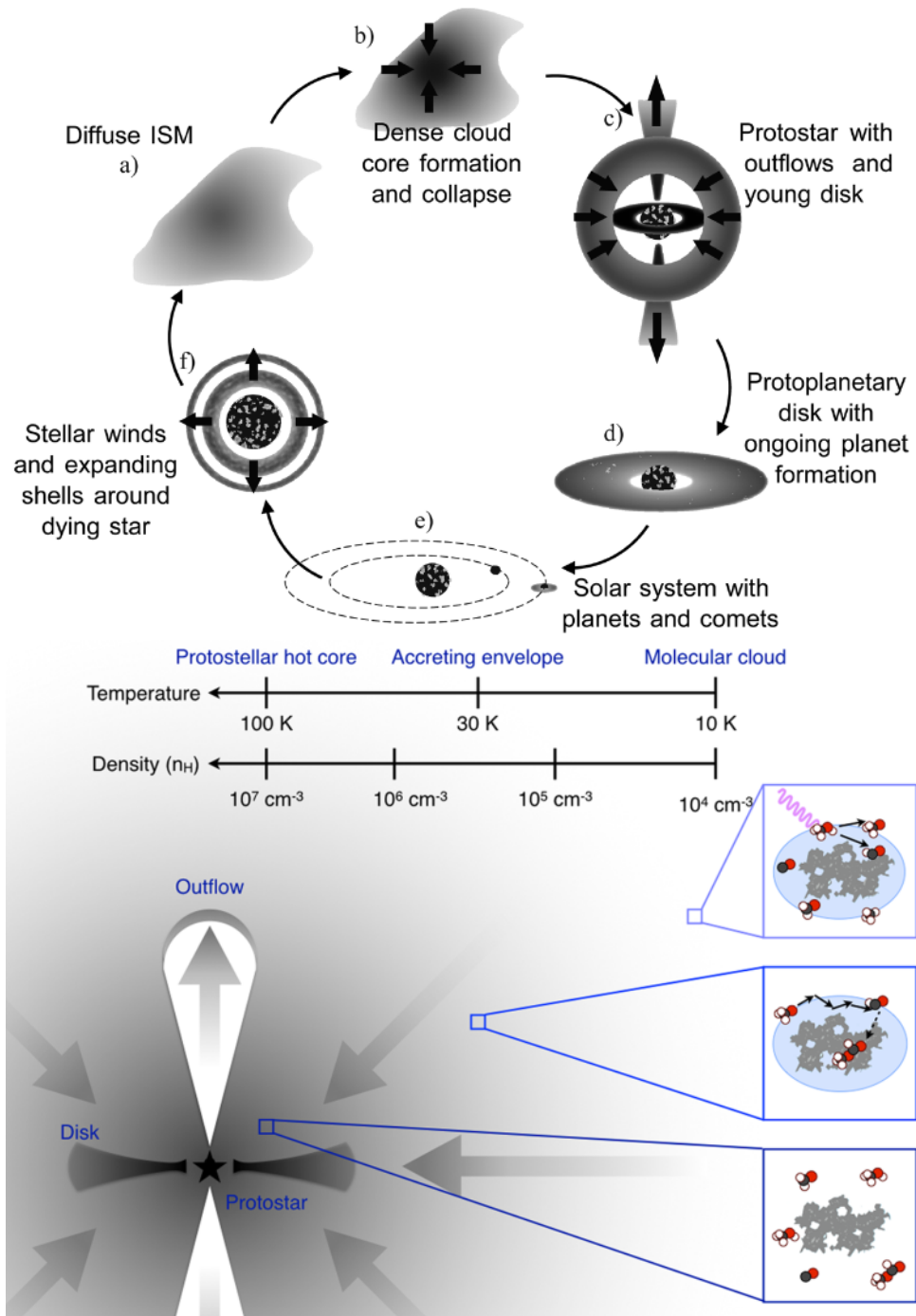


Figure 1.1: The process of solar-type star formation (upper panel), and chemical processes on dust surfaces with the change of underlying physical conditions along the way (lower panel). Images are taken from Öberg (2016)

mantle is assumed to be slower or even ignored for large species (Garrod et al., 2021). A bulk-ice molecule is bound to more binding partners than a surface counterpart.

Advances in astrochemical models have been made in various ways over the past decade. Substantial progress on our understanding of reaction systems enables the expansion of chemical networks and the detailed treatment of grain-related chemistry applicable to chemical models (Jørgensen, Belloche & Garrod, 2020). With observational improvements, astrophysical inputs such as density, temperature, and radiation fields have been better constrained with unprecedented sensitivity and resolving power. This allows physico-chemical investigation, triggering the development of chemical models tailored for a specific source (e.g. Barger et al., 2021). Furthermore, dedicated theoretical / experimental studies are now testing many of the assumptions within the models that have not been understood so far. Such sophistications of the model would become the basis for the further interdisciplinary studies in a more elaborate way in the future.

## 1.3 Observational Astrochemistry

### 1.3.1 Gas-phase observations : mm/sub-mm regime

Gas-phase observations has provided a wealth of indirect evidence for the presence of the ice chemistry through the detection of species originating from sublimating ices (e.g. Jørgensen et al., 2016) and the depletion of molecules (e.g. CO) in dense clouds (Bergin & Tafalla, 2007). Furthermore, the chemical inventory of the ISM has been largely expanded through gas-phase observations of rotational spectra over the decades. The rotational transitions can be traced at the mm/sub-mm regime, and figure 1.2 shows the cumulative number of known interstellar molecules over time with the advent of new mm/sub-mm observational facilities.

Some recent observational discoveries are particularly noteworthy as reviewed in more detail by Jørgensen, Belloche & Garrod (2020). Substantial abundances of iso-propyl in space implies the efficient formation of branched molecules (Belloche et al., 2014). Also, the detection of propylene oxide (McGuire et al., 2016) and benzonitrile (McGuire et al., 2018a) expanded the interstellar chemical inventory to the new types of molecular structures (chiral molecules and aromatic COMs, respectively). These findings revealed a wider complexity of interstellar chemistry than was previously thought possible.

Such ongoing identifications of new interstellar species has been possible thanks to the significant improvements of the observational facilities, in particular, with the advent of ALMA : the unprecedented spatial resolution and sensitivity as well as the increase of the instantaneous bandwidths covered with high spectral resolution. These key features are mutually complementary to each other, helping with the efficient detection of new species. The detection of faint signals from molecules at lower abundances becomes possible with the improvements in sensitivity. But it also raises new challenges, the so-called spectral-confusion limit<sup>4</sup>. Performing spectral line modeling is a critical step to overcome this.

---

<sup>4</sup>almost every single channel contains spectral lines from some species, implying strong blending and difficulty determining the baseline level

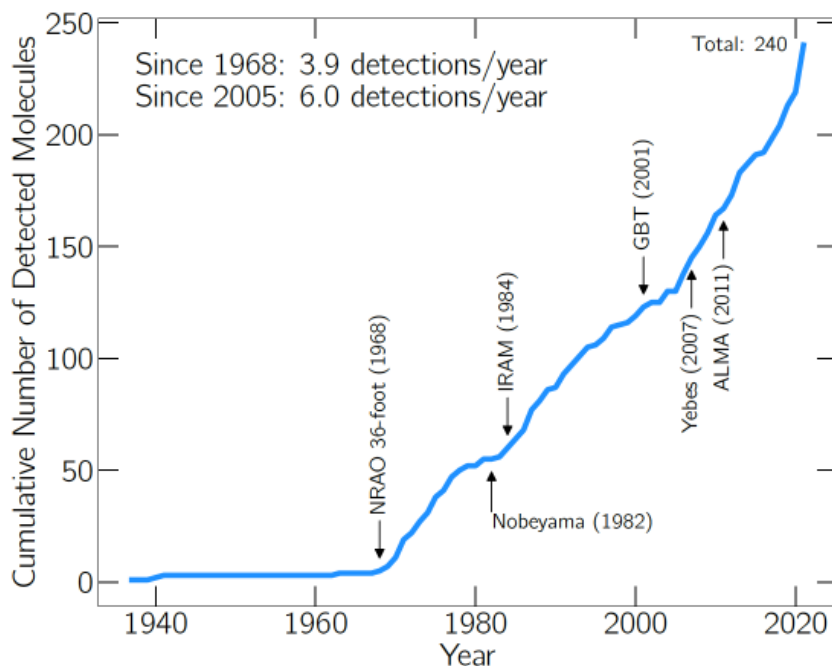


Figure 1.2: Cumulative number of known interstellar molecules with the advent of observational instruments over time. The image taken from McGuire (2021)

Given that, a range of energy levels and line strengths covered within a large bandwidth provides highly accurate constraints. High spectral resolution indeed partially alleviates this issue, while high spatial resolution observation is another strategy to deal with the line confusion. It spatially separates the contribution of the different sources. In addition to that, the spatial distribution of different species revealed with a high resolving power allows us to understand the physico-chemical behavior of interstellar species.

Thanks to the technical improvements as described above, many of the first detection of saturated COMs has been made, in particular, through the dedicated ALMA surveys toward three hot corinos / hot cores (the counterpart of hot corinos in high-mass star formation) – Sgr B2 (N), IRAS 16293B, and Orion KL. Their exceptional brightness and molecular richness allows the historical difficulties in detecting large interstellar species to be overcome.

*Exploring molecular complexity with ALMA* (EMoCA) and its follow-up survey with higher sensitivity, ReMoCA – are the cutting-edge surveys exploring molecular content of Sgr B2(N) (Belloche et al., 2016, 2019), which is one of the most active star-forming regions in our Galaxy located close to the center of the Milky Way. These surveys lead to the first interstellar detection of several complex organic molecules including the first branched alkyl molecules, isopropyl cyanide ( $C_3H_7CN$ ) and pre-nucleobase, urea ( $NH_2CONH_2$ ), making a significant impact in the field of astrochemistry.

*ALMA Protostellar Interferometric Line Survey* (PILS) performed an unbiased line survey of the infant sun-like binary stars IRAS 16293-2422 using ALMA (Jørgensen et al., 2016). The new detection of various complex species as well as deuterated and less abundant isotopologues are reported. This includes chloromethane ( $CH_3Cl$ ) which implies the direct link between protostellar chemistry and the constituents observed in icy bodies in our own Solar System (Fayolle et al., 2017).

Orion KL is the closest high-mass star-forming region, and this enables chemical distri-

butions of various species to be explored in greater detail. Tercero et al. (2018) reported a general spatial segregation between O-bearing COMs depending on their structure, which may be caused by the chemistry dominated by two different radicals ( $\text{CH}_3\text{O}$  and  $\text{CH}_2\text{OH}$ ). High resolution spectral survey with ALMA is also performed toward this region based on the early scientific verification program and its follow-up observations. These reveal several species not previously seen in Orion KL, including both the straight chain (n) and the branched (i) isomers of propyl cyanide ( $\text{C}_3\text{H}_7\text{CN}$ ) (Pagani et al., 2017). On the same lines, in chapter 4, we report the first secure identification of acetaldehyde toward Orion KL and investigate its origin together with astrochemical modeling.

While hot corinos / hot cores are the sources where most of the saturated COM detection are reported, some O-bearing COMs such as acetaldehyde ( $\text{CH}_3\text{CHO}$ ), methyl formate ( $\text{HCOOCH}_3$ ), and dimethyl ether ( $\text{CH}_3\text{OCH}_3$ ) have also been detected toward prestellar cores (e.g. Bacmann et al., 2012; Vastel et al., 2014; Jiménez-Serra et al., 2016). This detection was highlighted by the astrochemical community because the production of those highly-saturated COMs in cold ( $\sim 10$  K) and quiescent regions cannot be explained by the standard scenario of grain-surface chemistry (see section 1.1). Many chemical mechanisms have been proposed to explain the presence of COMs therein (Ruaud et al., 2015; Chang & Herbst, 2016; Bergner et al., 2017; Shingledecker et al., 2018; Balucani et al., 2015). However, it would appear that the standard rate description for those new mechanisms is inefficient to treat all temperature regimes. Motivated by this, in chapter 2, we implemented the so-called nondiffusive chemistry into the conventional chemical model to tackle this problem.

### 1.3.2 Solid-phase observations : infrared regime

Ices in interstellar environments can be traced almost exclusively by the infrared (IR) absorption of molecular vibrational transitions against a background source. The first ice detection was reported for the ice feature of  $3.0 \mu\text{m}$   $\text{H}_2\text{O}$  band toward Orion KL region (Gillett & Forrest, 1973). Since then, dedicated IR observations have been made to expand our understanding of the characteristics of interstellar ices and their role in the astrophysical context. Earlier ice features had been observed by both space- and ground-based observatories. But a significant part of our knowledge of ice chemistry is envisioned with the former such as the Infrared Space Observatory (ISO) and Spitzer due to the severe obscuring effects of Earth's atmosphere in the IR regime.

Interstellar ices can be characterized as substantially complex, and various ice profiles can be seen within the same type of star-forming regions. (Boogert et al., 2015). Despite their complexity, some general trends have been identified : water ice is the most abundant ice constituent, and interstellar ices are not perfectly mixed but rather present in at least two different phases, a water-rich phase and water-poor (or CO-rich) phase (Öberg, 2016). This two-layer feature is well explained with the standard grain-surface scenario as described in section 1.1.

Despite the progress in our understanding of interstellar ice over the decades, however, the determination of mantle compositions through direct ice observations has been limited to a small number ( $\sim 10$ ) of most abundant, simple ice species. Methanol is the only COM securely detected in the ice, while about 250 molecules have been detected in interstellar

gas (McGuire, 2021).

This discrepancy exists partly because of the intrinsic characteristics of IR spectroscopy: ice profile can significantly vary depending on the ice composition, structure (thermal history), and grain shape and size (Boogert et al., 2015). This imposes a large uncertainty in interpreting the ice spectrum. In addition, as opposed to gas-phase features, the intrinsic overlap bands between infrared ice features of related molecules hinders unique identification of specific molecules (Öberg, 2016). Larger complex organics are more likely suffering from this issue. Thus, elaborate spectral modeling is required to accurately interpret the profile, and more than one vibrational mode should be detected for secure identification. The depth and profile should be successfully fitted with models and laboratory spectra.

Some other observational obstacles also exist besides the IR spectroscopic difficulties described above. The sensitivity provided by IR instrumentation is relatively poor compared to mm/sub-mm counterparts for gas-phase observations. Also, the detection of ice features generally rely on the presence of IR continuum point sources. This limits the number of lines of sights where ice observation is eligible. Moreover, higher visual extinction is generally required for the detection of larger species. This makes the secure detection of icy COMs more challenging

However, the upcoming launch of the James Webb Space Telescope (JWST) with the unprecedented sensitivity / resolution could allow the full realm of ice chemistry to be explored. Besides its own technical improvements, it has driven laboratory and quantum mechanical studies to characterize the chemical behavior of larger species in the ice. This accumulation of spectroscopic/chemical information provides synergy between observational and modeling work to reveal new ice species larger than  $\text{CH}_3\text{OH}$ . In chapter 4, we predict the expected ice composition within a class 0 protostar, Cha-MMS1, and diagnose the detectability of icy COMs with JWST.

## 1.4 Astrochemical Theory

### 1.4.1 Gas-phase chemistry

Although gas-phase chemistry alone cannot fully explain the observed chemical complexity in the ISM, it is indisputable that many interstellar species, including some large chemical compounds, can be readily formed through purely gas-phase kinetics. It has been believed that only exothermic reactions without activation energy barriers are efficient due to low-density and cold conditions of the ISM. Astrochemical interest thus has been focused on specific types of reactions such as ion-molecule reactions. However, recent laboratory studies show that some neutral-neutral reactions with barriers can proceed at interstellar temperature much more efficiently than previous thoughts via tunneling (Shannon et al., 2013). These studies open a new insight on gas-phase chemistry and reveal its potential to exert influence on the molecular complexity in space.

Gas-phase kinetics are basically described in two-body collisions. The reaction rates

for a generalized two-body reaction,  $A + B \rightarrow C + D$ , can be represented as follows.

$$R_{\text{reaction}} = \frac{dn(C)}{dt} = \frac{dn(D)}{dt} = -\frac{dn(A)}{dt} = -\frac{dn(B)}{dt} = k(T) n(A) n(B) \text{ cm}^{-3}\text{s}^{-1} \quad (1.1)$$

where  $n(i)$  is an absolute number density for species  $i$ .  $k(T)$  is a rate coefficient and generally described in the form of a modified Arrhenius equation as follows.

$$k(T) = \alpha \left( \frac{T}{298 \text{ K}} \right)^\beta \exp\left(-\frac{\gamma}{T}\right) \quad (1.2)$$

where  $\gamma$  is the activation energy barrier. The parameters  $\alpha$ ,  $\beta$ , and  $\gamma$  are determined empirically.

Chemical processes for a single atom/molecule such as ionization and dissociation are also critical to drive chemistry by feeding reactive charged species and neutral radicals into the ISM. Energetic photons (mainly far-UV) and/or cosmic rays (CR)<sup>5</sup> are generally in charge of these processes. While cosmic rays are ubiquitously found in space, far-UV (FUV) photons are locally dominant due to their vulnerability to extinction<sup>6</sup>. Thus efficient ionization / dissociation processes driven by a direct interaction with interstellar UV photons are limited to specific interstellar conditions such as diffuse/translucent clouds, outer edges of protostellar envelopes, and the vicinities of main sources of FUV photons – OB type stars.

In a dense molecular cloud where seeds of stars form, photo-chemical processes are unlikely to be driven by the direct interstellar radiation field (ISRF). However, the cloud has an internal source of radiation – secondary FUV photons driven by cosmic rays. Cosmic rays in dense regions can ionize molecular hydrogen to form energetic electrons. Both the liberated electrons and cosmic rays themselves in turn excite hydrogen molecules within the cloud, which then decays to its ground state by emitting FUV photons. This is an important source to increase chemical complexity at this early phase of star-forming regions. The cosmic ray induced ionization rate for  $\text{H}_2$  molecules is typically assumed on the order of  $10^{17} \text{ s}^{-1}$ .

The rate for photo-ionization via the ISRF depends on the frequency-dependent flux of ionizing photons  $J(\nu)$  and photo-ionizing cross section  $\sigma_{\text{P-I}}(\nu)$ . The so-called Draine radiation field is typically assumed to describe the standard ISRF. The photo-ionization rate of species  $i$ , in turn, can be described as follows.

$$k_{\text{P-I}}(i) = \int J_{\text{ISRF}}(\nu) \sigma_{\text{P-I}}(\nu) d\nu \quad (1.3)$$

Photo-dissociation process for chemical species can be described similarly to this case, that is, the flux of ISRF, times photo-dissociating cross section. Typical photoionization / photodissociation rate are in range of  $10^{-12} - 10^{-10} \text{ s}^{-1}$  and  $10^{-10} - 10^{-9} \text{ s}^{-1}$ , respectively.

## 1.4.2 Grain-surface chemistry

Solid-phase chemistry taking place on the surfaces of interstellar dust grains is another critical part to explain the production of many interstellar species in star-forming regions:

<sup>5</sup>A highly energetic particle such as protons that are found throughout the interstellar medium

<sup>6</sup>The absorption and scattering of electromagnetic radiation by dust and gas

chemical compounds in the gas could accrete and diffuse across grain surfaces until a reaction takes place, promoting the reactions that hardly proceed in the gas. In addition, grain surfaces can absorb the excess of energy from the exothermic chemical reactions, stabilizing the products. Species on a grain surface generally experience four types of processes : (i) accretion onto the surface, (ii) desorption from the surface, (iii) diffusion across the surface or on/within the ice mantle, and (iv) reaction. In this section, the general formalism for each process is summarized based on Garrod & Herbst (2006); Garrod et al. (2007); Garrod & Pauly (2011) and a recent review by Cuppen et al. (2017).

Accretion process is described by the collisional frequency of a gas-phase species,  $i$ , with a grain, times a sticking efficiency,  $S(i)$ .

$$R_{\text{acc}}(i) = S(i)n_i n_g \sigma_g \langle v \rangle \quad (1.4)$$

where  $n_i$  and  $n_g$  is the number density of species and grains in the gas phase, respectively.  $\sigma_g$  is the cross section of dust grains, and  $\langle v \rangle$  is the average gas-phase thermal velocity. For most species at low gas and grain temperatures, sticking coefficient value near unity is appropriate for anything other than atomic hydrogen.

The desorption is an inverse process of accretion and is generally categorized into two types depending on the involvement of thermal kinetic energy during this process. The thermal desorption is mainly characterized by a binding energy (or desorption energy)  $E_{\text{des}}$  which holds the chemical compounds to the surface :

$$k_{\text{des}} = \nu \exp\left(-\frac{E_{\text{des}}}{kT_{\text{gr}}}\right). \quad (1.5)$$

$\nu$  is a characteristic attempt frequency for which the characteristic frequency of a harmonic oscillator is usually assumed.

The non-thermal desorption can proceed via various mechanisms such as chemical (or reactive) desorption, photodesorption, and sputtering by cosmic rays. In particular, chemical desorption may play an important role in quiescent regions such as dense molecular clouds. This process is statistically characterized by a probability where the excess of energy released by an exothermic reaction breaks the bond between molecule and grain surface rather than lost to the surface (Garrod & Herbst, 2006). Following Garrod et al. (2007), the probability where a total energy released from the reaction,  $E_{\text{reac}}$ , exceeds  $E_{\text{des}}$  to be present in the bond is :

$$P = \left[1 - \frac{E_{\text{des}}}{E_{\text{reac}}}\right]^{-1}. \quad (1.6)$$

The fraction of reactions resulting in desorption is in turn

$$f = \frac{aP}{1 + aP} \quad (1.7)$$

where  $a$  is defined as the ratio of the surface-molecule bond frequency to the frequency at which energy is lost to the grain surface. This efficiency parameter  $a$  has not been constrained well and is generally assumed to be around 1%.

Under astrophysical conditions, diffusive reactions following L-H mechanisms are dominant on grain surfaces. The formalism for this surface is almost identical to the the case

of thermal desorption, but the diffusion (or hopping) is now relevant to a diffusion energy  $E_{\text{dif}}$  rather than  $E_{\text{des}}$ :

$$k_{\text{dif}} = \nu \exp\left(-\frac{E_{\text{dif}}}{kT_{\text{gr}}}\right). \quad (1.8)$$

$E_{\text{dif}}$  is the energy required to hop from one surface binding site to another, while  $E_{\text{des}}$  is the energy required for a particle to leave the surface entirely. Thus the diffusion energy is typically assumed to be as some fraction (0.3 – 0.8) of the desorption energy. The total rate at which two species,  $i$  and  $j$ , meet each other and react without activation energy barrier can be analytically described as follows.

$$R_{\text{reac}}(i + j) = [k_{\text{scan}}(i) + k_{\text{scan}}(j)] n_s(i) n_s(j) \quad (1.9)$$

where  $n_s(i)$  is the number of species  $i$  present on the surface and  $k_{\text{scan}}(i)$  the rate by which species  $i$  scans the grain surface. The scanning rate is given by

$$k_{\text{scan}} = \frac{k_{\text{dif}}}{N_{\text{sites}}} \quad (1.10)$$

where  $N_{\text{sites}}$  is the number of binding sites per grain, which is generally assumed  $\sim 10^6$  binding sites per grain for a standard grain of  $0.1 \mu\text{m}$ .

As for the reactions on grain surfaces involving activation energy barriers, the total rate can be parameterized by employing additional efficiency  $\kappa(i+j)$ .

$$R_{\text{reac}}(i+j) = \kappa(i+j)[k_{\text{scan}}(i) + k_{\text{scan}}(j)] n_s(i) n_s(j) \quad (1.11)$$

The efficiency of the reaction is defined based on the competition between reaction and diffusion as follows:

$$\kappa(i+j) = \frac{k_{\text{reac}}}{k_{\text{reac}} + k_{\text{dif}}(i) + k_{\text{dif}}(j)} \quad (1.12)$$

with

$$k_{\text{reac}} = v_{ij} P_{\text{reac}}. \quad (1.13)$$

For reactions with an activation energy barrier  $E_A$ , the probability  $P_{\text{reac}}$  that the reactants will overcome a barrier thermally on any one collision is given by the Boltzmann factor:

$$P_{\text{reac}} = \exp\left(-\frac{E_A}{T_{\text{gr}}}\right). \quad (1.14)$$

## 1.5 This Thesis

The interdisciplinary investigation of astrochemistry has highlighted the important role of chemistry taking place on interstellar grain surfaces and within ice mantles. However the standard scheme of grain surface chemistry to explain the formation of COMs in space relies on thermal / energetic processes, which cannot fully explain the presence of saturated COMs in cold and quiescent environments. To tackle this problem, we developed an elaborate astrochemical model to treat all temperature regimes in a consistent way.

Throughout this thesis, the underlying chemistry in various phases of star formation are investigated based on this advanced model.

In Chapter 2 we provide the details of the implementation of the new chemical treatment into the rate-equation gas-grain chemical model. This new model is then applied to a cold and quiescent prestellar condition in which the presence of saturated COMs is previously unexplained. The next application is an extension to another end, an active and energetic star-forming region. In Chapter 3, we investigate an extensive ALMA archive dataset to search for acetaldehyde and other chemically related species toward an active star-forming region Orion KL. Key physical parameters and underlying aldehyde chemistry to explain the observations are explored with this new model. Besides the interpretations of the readily available observational data, Chapter 4 provides the prediction of the ice composition for a young and deeply embedded protostar. The detectability of new ice species with JWST is then assessed as a part of the Early Release Science program of JWST. Chapter 5 contains the conclusion of this thesis and an outlook into future studies. The topics covered in this thesis will touch a number of key scientific questions as follows:

1. What chemical mechanisms are in charge of the formation of COMs in prestellar environments? Is nondiffusive mechanism efficient enough to explain the chemistry therein?
2. Can one generalized scenario explain the chemistry in all temperature regimes for both in the gas and on within ice?
3. How does chemistry change with the underlying physical condition? Can we define a best tracer for a specific physical condition through chemical modeling?
4. What are the dominant formation and destruction pathways of the COMs of interest – on dust grain surfaces or in the gas phase?
5. What is the chemical composition of the ice within the young star-forming core?
6. Can COMs within the icy mantle be detected with JWST ? To what degree the ice abundance is required for the secure identification?

List of publications:

1. R.T. Garrod, **M. Jin**, K.A. Matis, D. Jones E.R. Willis, and E. Herbst *Formation of complex organic molecules in hot molecular cores through nondiffusive grain-surface and ice-mantle chemistry*, 2021, ApJS, in press
2. S. Ioppolo, G. Fedoseev, K.-J. Chuang, H.M. Cuppen, A.R. Clements, **M. Jin**, R.T. Garrod, D. Qasim, V. Kofman, E.F. van Dishoeck, and H. Linnartz *A non-energetic mechanism for glycine formation in the interstellar medium*, 2021, Nature Astronomy, 5, 197.

3. **M. Jin**, and R.T. Garrod *Formation of complex organic molecules in cold interstellar environments through nondiffusive grain-surface and ice-mantle chemistry*, 2020, ApJS, 249, 26J
4. **M. Jin**, J.-E. Lee, K.-T. Kim, and N.J. Evans *The infall signature toward different evolutionary phases of massive star formation*, 2016, ApJS, 225, 21
5. **M. Jin**, J.-E. Lee, and K.-T. Kim *The HCN/HNC abundance ratio toward different evolutionary phases of massive star formation*, 2015, ApJS, 291, 2

In preparation:

6. **M. Jin**, K. Lam, M.K. McClure, J. Terwisscha van Scheltinga, Z.-Y. Li, A. Boogert, E. Herbst, S.W. Davis, and R.T. Garrod *Ice Age : Chemo-dynamical modeling of Cha-MMS1 to predict new solid-phase species for detection with JWST*
7. **M. Jin**, A.J. Remijan, R.T. Garrod, and E. Herbst *Spatial distribution of acetaldehyde in Orion KL: Observations and chemical modeling*



# 2

# Formation of Complex Organic Molecules through nondiffusive chemistry

## Contents

---

<b>2.1</b>	<b>Introduction</b>	<b>16</b>
<b>2.2</b>	<b>Chemical model</b>	<b>21</b>
2.2.1	New chemical mechanisms	22
2.2.2	Eley-Rideal reactions	26
2.2.3	Photodissociation-induced reactions	28
2.2.4	Three-body reactions	29
2.2.5	Excited three-body reactions	31
2.2.6	Physical conditions	33
<b>2.3</b>	<b>Results</b>	<b>35</b>
2.3.1	Column density analysis	42
2.3.2	Column densities of O-bearing COMs toward the core center	44
2.3.3	Optimization of the 3-BEF model	49
2.3.4	CO hydrogenation and CH <sub>3</sub> OH abundances	52
<b>2.4</b>	<b>discussion</b>	<b>54</b>
2.4.1	H-abstraction/recombination as an amplifier of chemical desorption	54

2.4.2	COM distribution and COM peaks . . . . .	56
2.4.3	The effect of diffusion barriers . . . . .	57
2.4.4	Gas-phase processes . . . . .	60
2.4.5	Other surface processes . . . . .	61
2.4.6	O <sub>2</sub> production . . . . .	65
<b>2.5</b>	<b>Conclusions . . . . .</b>	<b>66</b>

---

## 2.1 Introduction

Complex organic molecules (COMs), usually defined as carbon-bearing molecules with six or more atoms, have been detected within the interstellar medium and in various protoplanetary environments (Blake et al., 1987; Fayolle et al., 2015; Bottinelli et al., 2010; Arce et al., 2008; Öberg et al., 2010; Bacmann et al., 2012). COMs synthesized at the early stages of star formation are suggested to have been a starting point for the organic materials that went on to seed the nascent solar system (Herbst & van Dishoeck, 2009). While the degree to which the interstellar synthesis of COMs may contribute to pre-biotic/biotic chemistry on Earth is still a matter of debate, many recent studies have shed light on the possible interstellar/protostellar origins of chemical complexity. For instance, the sugar-like molecule glycolaldehyde ( $\text{CH}_2(\text{OH})\text{CHO}$ ) has been detected toward the class 0 protostellar binary source IRAS16293-2422 (Jørgensen et al., 2012), as well as the Galactic Centre source Sgr B2(N) and other hot cores (Hollis et al., 2000; Beltrán et al., 2009). A related molecule, ethylene glycol ( $\text{HOCH}_2\text{CH}_2\text{OH}$ ), has also been found toward low-mass protostars (Maury et al., 2014; Jørgensen et al., 2016), having first been detected in SgrB2(N) (Hollis et al., 2002). The simplest amino acid, glycine ( $\text{NH}_2\text{CH}_2\text{COOH}$ ), has not been detected in the interstellar medium, but numerous amino acids have been found in meteorites (Kvenvolden et al., 1970), and glycine has been detected in two comets: Wild 2 (Elsila et al., 2009) and Churyumov-Gerasimenko (Altwegg et al., 2016). In the laboratory, (Meinert et al., 2016) observed the generation of numerous sugar molecules, including the aldopentose ribose, through photochemical and thermal processing of interstellar ice analogs initially composed of  $\text{H}_2\text{O}$ ,  $\text{CH}_3\text{OH}$ , and  $\text{NH}_3$ .

One of the prevailing theories explaining the formation of interstellar COMs is based on radical chemistry occurring on dust-grain particles, following the formation of ice mantles on their surfaces. In dark clouds and prestellar cores, where temperatures may be as low as around 10 K, hydrogen atoms are the most mobile species on the grain. Their high mobility allows them to find reaction partners on the surface easily. Thus, the accretion of other atoms and simple molecules, such as O, C, N and CO, onto the grain surfaces often leads to reactions with atonondiffusivemic H, producing an ice mantle composed of commonly-observed stable hydrides like water, methane, and ammonia, through repetitive hydrogenation. In dense regions, almost all of the CO produced in the gas phase may ultimately freeze out onto the dust grains (e.g. Caselli et al., 1999), producing an outer

ice surface that is rich in CO. Atomic H may also react with CO to produce methanol ( $\text{CH}_3\text{OH}$ ); although there are activation energy barriers that prevent all of this CO being hydrogenated, a substantial fraction of the ice – up to as much as around 30% with respect to water toward some protostars, but generally of the order of 5% (Boogert et al., 2015) – is found observationally to be composed of  $\text{CH}_3\text{OH}$ .

Grain-surface methanol, and indeed other molecules, may be broken down into radicals through UV-induced photolysis, caused either by external photons or by the secondary UV field induced by cosmic-ray collisions with gas-phase  $\text{H}_2$ ; however, in the standard picture used in most astrochemical models, these radicals are still immobile on the grain surfaces at low temperatures, hindering their ability to react with anything other than mobile H atoms. As a star-forming core evolves to be heated to temperatures greater than  $\sim 20$  K, radicals such as  $\text{CH}_3$  and  $\text{HCO}$  become more mobile, allowing them to meet via diffusion and quickly react to form larger COMs (Garrod & Herbst, 2006; Garrod et al., 2008). At this stage, most of the COMs produced in this way are unable to desorb effectively into the gas phase where they may be directly detected; only non-thermal mechanisms such as chemical desorption (Garrod et al., 2007) and photo-desorption (Öberg et al., 2009a,b) are active, with the former expected to yield only around 1% of reaction products to the gas phase, while the latter would be weaker still in such regions where visual extinction is high. Only when the dust-grains in the core reach a high enough temperature (typically on the order of  $\sim 100$  K), through protostellar heating, can large COMs sublime efficiently from the grains. This process is reviewed in more detail by Öberg et al. (2010).

According to this scenario, it would be unlikely that COMs other than methanol would be effectively synthesized under the low-temperature conditions of dark clouds and prestellar cores, due to the immobility of heavy species on the grains, while methanol would still be formed as the result of the diffusion and reaction of H alone. The detection of COMs in these cold environments therefore presents a significant challenge to current astrochemical models based on diffusive grain-surface chemistry. In particular, three O-bearing COMs, acetaldehyde (AA;  $\text{CH}_3\text{CHO}$ ), methyl formate (MF;  $\text{CH}_3\text{OCHO}$ ), and dimethyl ether (DME;  $\text{CH}_3\text{OCH}_3$ ), have been detected in prestellar cores such as L1689B, L1544 and B1-b (Bacmann et al., 2012; Vastel et al., 2014; Cernicharo et al., 2012) as well as in the cold outer envelopes of protostars (Öberg et al., 2010; Bergner et al., 2017).

Many chemical mechanisms have been proposed to explain the presence of COMs in cold cores: The Eley-Rideal process combined with complex-induced reactions on the grains (Ruaud et al., 2015); nondiffusive reactions (Chang & Herbst, 2016); oxygen insertion reactions (Bergner et al., 2017); cosmic-ray induced chemistry (Shingledecker et al., 2018); and gas-phase formation through radical reactions (Balucani et al., 2015). In particular, the latter gas-phase formation scheme is noteworthy in that it suggests a chemical link between gas-phase methyl formate and dimethyl ether via the radical  $\text{CH}_3\text{OCH}_2$ , which would be formed through the abstraction of a hydrogen atom from DME by atoms such as F and Cl. The dimethyl ether itself would form through the efficient radiative association of the radicals  $\text{CH}_3$  and  $\text{CH}_3\text{O}$  in the gas phase.

Although many of the above-mentioned studies provide plausible routes to one or more complex molecules, some suffer from poorly constrained parameters due to the lack of experimental data or detailed computational chemistry studies (e.g. the radiative association reaction to produce DME), or require somewhat extreme chemical conditions. For example, the fractional abundance of methoxy in the model of Balucani et al. (2015) is more than one order of magnitude larger than the observed value, making it unclear

whether dimethyl ether can be formed solely in the gas phase in cold cores (Vasyunin & Herbst, 2013; Chang & Herbst, 2016). Also, the chemical networks for F and Cl are relatively sparse, introducing further uncertainties; the models of Vasyunin et al. (2017) suggest that OH is instead a more important agent of H-abstraction from dimethyl ether.

Cosmic ray-induced radiolysis models by Shingledecker et al. (2018) appear promising, although it is unclear whether they can account for large abundances of COMs on their own, or whether they require radicals also to be produced by UV photons. For example, those authors suggest an average rate of solid-phase water dissociation by cosmic rays of around  $6 \times 10^{-16} \text{ s}^{-1}$  at the canonical cosmic-ray ionization rate. However, the typically-assumed rate used in astrochemical models for the separate process of UV photo-dissociation of *gas-phase* water by cosmic ray-induced photons is around  $1.3 \times 10^{-14} \text{ s}^{-1}$ . Even if the rates of UV photo-dissociation in the solid phase are around three times lower than those of gas-phase molecules (Kalvāns, 2018), the influence of cosmic ray-induced photons in producing radicals in ice mantles would, on average, appear to be greater than that of direct cosmic-ray impingement by close to an order of magnitude. Other calculations for CR-induced water dissociation (Garrod, 2019) would suggest an even greater discrepancy. The formation of COMs through direct cosmic-ray impacts into icy grains may therefore rely on the presence of pre-existing radicals produced by CR-induced UV.

In order for chemical modeling studies to be directly comparable with observations, they should ideally seek to reproduce the spatio-physical conditions of the target source. In pre-stellar cores such as L1544, strong gradients in physical parameters such as dust temperature, density, and visual extinction may sample a range of chemical regimes. The recent detection of a chemically-active outer shell around the core center of L1544 sheds light on the complexity of its chemical structure (Bizzocchi et al., 2014). Methanol column density in this source appears to peak at a radius around 4000 au distant from the source center. Abundances of other COMs seem to be enhanced at this position also (Jiménez-Serra et al., 2016).

The modeling study by Vasyunin et al. (2017) is notable in its use of an explicit spatio-physical model to perform chemical modeling of L1544, successfully reproducing a similar feature to the observed methanol peak. Those authors used a surface-specific treatment of chemical desorption from grains in which a pure water-ice surface would allow only minimal desorption of newly-formed molecules, while a more CO-rich surface would allow molecules including methanol to desorb more easily. However, the peak fractional abundances of methanol produced in this model appear high ( $\sim 10^{-7}$  with respect to total hydrogen) compared with the usual values observed in cold sources ( $\sim 10^{-9}$ ). The efficiency of the chemical desorption of methanol (which is responsible for its gas-phase abundance) and many other species on water ice is poorly constrained by experiment, with an upper limit of 8% for methanol formed through H addition (Minissale et al., 2016c); thus, there is room for the efficiency of this mechanism to be varied in models to produce the correct observed quantity. However, the Vasyunin et al. (2017) models rely on gas-phase methanol as the feedstock for the production of other, larger COMs. Lower peak abundances of gas-phase methanol would almost certainly render the gas-phase routes investigated by those authors too weak to account for the abundances of DME, MF and AA. Furthermore, using gas-phase reactions between CH and  $\text{CH}_3\text{OH}$  as a mechanism to form  $\text{CH}_3\text{CHO}$ , they erroneously extrapolated experimental reaction rates determined at room temperature (Johnson et al., 2000) down to 10 K; this produces impossibly large rate values that are around 3 orders of magnitude greater than the collisional rates for

neutrals at such temperatures. It is unclear how much influence their alternative route for AA production, the radiative association of  $\text{CH}_3$  and  $\text{HCO}$  radicals, would have on that molecule's peak gas-phase abundance; however, in their network they assume a rate that is on the order of the collisional rate (i.e. high efficiency), based on high-pressure experiments that would in fact be more representative of collisional (rather than radiative) de-excitation, and which therefore say nothing certain about radiative association. Until detailed calculations for this, or indeed for the radiative association of  $\text{CH}_3\text{O}$  with  $\text{CH}_3$ , are available, those rates may be considered to be somewhat optimistic.

Recent laboratory results have added new impetus to understanding the behavior of grain-surface chemistry at very low temperatures. Fedoseev et al. (2015, 2017) considered the co-deposition of  $\text{CO}$  and  $\text{H}$  at low temperatures, resulting in significant production of complex organics such as glycolaldehyde, ethylene glycol, and glycerol. They postulate that reactions between adjacent  $\text{HCO}$  radicals, and/or  $\text{HCO}$  and  $\text{CO}$ , may produce such species with minimal thermal diffusion required – a result not predicted by standard gas-grain chemical models, due to the lack of diffusion involved. So-called microscopic Monte Carlo models, unlike the more usual rate-equation models, are capable of simulating the relative positions of all atoms and molecules on a grain surface at each moment, allowing them automatically to account for this nondiffusive process. Such models seem to indicate that COM production through nondiffusive mechanisms is plausible (Fedoseev et al., 2015; Chang & Herbst, 2016; Dulieu et al., 2019, Ioppolo et al. 2020, *subm.*, Garrod et al. 2020, *in prep.*).

It would appear, therefore, that – regardless of other mechanisms such as gas-phase processes or radiolysis – the standard rate description of grain-surface reactions is insufficient to treat all temperature regimes; there are situations in which reactants may be produced and rapidly meet (and react), either without diffusion of radicals or with some minimal amount of diffusion that does not obey the more general rate treatment.

In this study, we present a relatively simple formulation for nondiffusive chemistry, for use in standard gas-grain chemical models, that allows a newly-formed reaction product to react further with some other chemical species that happens to be in close proximity to the product(s) of the first reaction. Due to the instantaneous nature of this process, we refer to it here as a “three-body reaction mechanism” (3-B). We also consider a similar, related mechanism in which the new product has sufficient excitation energy to allow it to overcome the activation-energy barrier to its reaction with some nearby species; here, specifically with  $\text{CO}$  or  $\text{H}_2\text{CO}$ . This mechanism is referred to here as the “three-body excited formation mechanism” (3-BEF).

A functionally-similar mechanism was included in the recent model of the solid-phase chemistry of cometary nuclei by Garrod (2019), but rather with the initiating process being the production of radicals by UV-induced photo-dissociation. In preliminary versions of that model that did not include that mechanism, it was found that the photo-dissociation of bulk ice molecules at temperatures 5–10 K was capable of producing implausibly high abundances of reactive radicals, which were unable to react due to the lack of bulk thermal diffusion at those temperatures. The Garrod (2019) model includes a new reaction process whereby a newly-formed photo-product may react immediately with a nearby reaction partner in the ice. This mechanism is included in the present model also, which we label as the “photodissociation-induced reaction mechanism” (PDI).

Garrod & Pauly (2011) used a similar mechanism to the 3-body mechanisms to explain the formation of  $\text{CO}_2$  ice at low temperatures. In their treatment, the production of an

OH radical via the reaction of H and O atoms in proximity to a CO molecule could allow the immediate formation of CO<sub>2</sub> (overcoming a modest activation energy barrier). Their models successfully reproduced the observed behavior of CO, CO<sub>2</sub>, and water ice in dense clouds, and showed that such nondiffusive processes could be handled within a standard gas-grain chemical model. More recently, Chang & Herbst (2016) implemented a similar process, which they called a “chain reaction mechanism” in their microscopic Monte Carlo simulation, achieving abundances of gas-phase COMs high enough to reproduce the observational values toward cold cores (at a temperature of  $\sim 10$  K), using a chemical desorption efficiency of 10% per reaction. Dulieu et al. (2019), seeking to explain the surface production of NH<sub>2</sub>CHO in laboratory experiments involving H<sub>2</sub>CO, NO and H deposition, introduced a nondiffusive reaction treatment for a single reaction (see also Sec. 2.2.4).

Finally, a simple treatment for the Eley-Rideal process is included in the present model, in which an atom or molecule from the gas-phase is accreted directly onto a grain-surface reaction partner, resulting in immediate reaction (mediated by an activation-energy barrier, where appropriate). Such processes have been included in similar models before (e.g. Ruaud et al., 2015), but are included here for completeness in the consideration of all mechanisms by which reactants may instantly be brought together without a mediating diffusion mechanism.

The formulations presented here for the above processes also allow, through a repetitive application of the main nondiffusive reaction process (i.e. the three-body mechanism), for the products of each of those processes themselves to be involved in further nondiffusive reaction events (in cases where such processes are allowed by the reaction network). Thus, for example, an Eley-Rideal reaction may be followed by an immediate secondary nondiffusive reaction. The importance of such repetitive processes will diminish with each iteration.

All of the above nondiffusive reaction mechanisms are considered in the model, with a particular emphasis on the production of the O-bearing COMs that are now detected in the gas-phase in cold prestellar cores. The formulations corresponding to each of the new mechanisms presented here are functionally similar to each other, but quite different from the standard diffusive reaction formula used in typical astrochemical models. However, they are fully compatible with the usual treatment and may be used in tandem with it.

With the introduction of the new mechanisms, we run multi-point chemical models of prestellar core L1544 to test their effectiveness in an appropriate environment. A spectroscopic radiative-transfer model is implemented here as a means to evaluate the observable column densities of molecules of interest, allowing the direct comparison of the model results with observations.

This paper is structured as follows. The chemical model and the newly-implemented mechanisms are described in § 2.2. The results of the models are explored in § 2.3, with discussion in § 2.4. Conclusions are summarized in § 2.5.

species, $i$	$n(i)/n_{\text{H}}^{\text{a}}$
H	5.0(-4)
H <sub>2</sub>	0.49975
He	0.09
C	1.4(-4)
N	7.5(-5)
O	3.2(-4)
S	8.0(-8)
Na	2.0(-8)
Mg	7.0(-9)
Si	8.0(-9)
P	3.0(-9)
Cl	4.0(-9)
Fe	3.0(-9)

Notes. <sup>a</sup>  $A(B) = A^B$

Table 2.1: Initial elemental and chemical abundances

## 2.2 Chemical model

We use the astrochemical kinetic code *MAGICKAL* to study new grain-surface/ice-mantle mechanisms that may effectively form complex organic molecules in cold environments. The model uses a three-phase approach, based on that described by Garrod & Pauly (2011) and Garrod (2013), in which the coupled gas-phase, grain/ice-surface and bulk-ice chemistry are simulated through the solution of a set of rate equations. Initial chemical abundances used in the model are shown in Table 2.1, with elemental values based on those used by Garrod (2013). The initial H/H<sub>2</sub> abundances are chosen to agree approximately with the steady-state values appropriate to our initial physical conditions, as determined by the chemical model. Bulk diffusion is treated as described by Garrod et al. (2017). Although the bulk ice is technically chemically active in this model, at the low temperatures employed in this work, diffusive reactions in general are negligibly slow, excluding processes involving H or H<sub>2</sub> diffusion. However, the addition of nondiffusive reactions to the model increases significantly the degree of chemical activity within the bulk.

The model uses the modified-rate treatment for grain-surface chemistry presented by (Garrod, 2008), which allows the stochastic behavior of the surface chemistry to be approximated; the back-diffusion treatment of Willis & Garrod (2017) is also used. Surface diffusion barriers ( $E_{\text{dif}}$ ) are related to desorption (i.e. binding) energies ( $E_{\text{des}}$ ) such that  $E_{\text{dif}}=0.35E_{\text{des}}$  for all molecular species, with bulk diffusion barriers taking values twice as high (Garrod, 2013). However, the recent study by Minissale et al. (2016) estimated surface diffusion barriers for atomic species such as N and O to be  $E_{\text{dif}}=0.55E_{\text{des}}$ . We adopt a similar value  $E_{\text{dif}}/E_{\text{des}}=0.6$  for all atomic species; the impact of this parameter is discussed in §2.4.3. These basic surface diffusion and desorption parameters are also adjusted according to the time-dependent abundance of H<sub>2</sub> in the surface layer, following the method of Garrod & Pauly (2011). All diffusion is assumed to be thermal, with no

tunneling component (see also Sec. 2.4.3).

Chemical desorption, whereby grain-surface reactions allow some fraction of their products to desorb into the gas phase, is treated using the RRK formulation of Garrod et al. (2007) with an efficiency factor  $a_{\text{RRK}} = 0.01$ .

The grain-surface/ice-mantle photodissociation rates used in *MAGICKAL* are based on the equivalent gas-phase rates, in the absence of other evidence (e.g. Garrod et al., 2008), and they likewise assume the same product branching ratios. Following the work of Kalvāns (2018), we adopt photodissociation rates on the grain-surfaces and in the ice mantles that are a factor of 3 smaller than those used for the gas phase. Photodissociation may be caused either by external UV, or by the induced UV field caused by cosmic-ray collisions with  $\text{H}_2$  molecules, and both sources of dissociation are included in the model.

Methanol in cold clouds is mainly formed on the grain surfaces through ongoing hydrogenation of CO (Fuchs et al., 2009). The methanol production network used in the present network follows from that implemented by Garrod (2013), and includes not only forward conversion of CO to methanol but also the backward reactions of each intermediate species with H atoms.

The overall chemical network used here is based on that of Garrod et al. (2017), with a few exceptions. In particular, a new chemical species,  $\text{CH}_3\text{OCH}_2$ , has been added along with a set of associated gas-phase and grain-surface reactions/processes listed in Tables 2.2 (gas-phase) and 2.3 (solid-phase). This radical is a key precursor of DME in our new treatments (see §2.2.5). Its inclusion also allows the addition of a grain-surface H-abstraction reaction from DME, making this species consistent with methyl formate and acetaldehyde.

An additional reaction was included in the surface network, corresponding to H-abstraction from methane ( $\text{CH}_4$ ) by an O atom ( $E_A=4380$  K; Herron & Huie, 1973), as a means to ensure the fullest treatment for the  $\text{CH}_3$  radical in the network.

The final change to the network is the adjustment of the products of  $\text{CH}_3\text{OH}$  photo-desorption to be  $\text{CH}_3+\text{OH}$  rather than  $\text{CH}_3\text{OH}$ , roughly in line with the recent experimental study by Bertin et al. (2016).

Each of the generic nondiffusive mechanisms that we include in the model (as described below) is allowed to operate on the full network of grain-surface and ice-mantle reactions that are already included for the regular diffusive mechanism; reactive desorption, where appropriate, is also allowed to follow on from each of these, in the case of surface reactions. The full model therefore includes around 1600 surface and 1100 bulk-ice reaction processes for each new generic mechanism included in the model (excluding 3-BEF, see Section 2.5). All the grain-surface and bulk-ice reactions allowed in the network are presented in machine-readable format in Table 2.3. The rate formulations for diffusive and nondiffusive reaction mechanisms used in the model are described below.

### 2.2.1 New chemical mechanisms

The standard formulation, as per e.g. Hasegawa et al. (1992), for the treatment of a diffusive grain-surface chemical reaction (also known as the Langmuir-Hinshelwood or L-H mechanism) between species  $A$  and  $B$  is based on: the hopping rates of the two reactants,  $k_{\text{hop}}(A)$  and  $k_{\text{hop}}(B)$ ; the abundances of both species on the grains,  $N(A)$  and

Reaction	Rate coefficient	Ref.	Type
$\text{CH}_3\text{OCH}_2 + \text{H}_3^+ \rightarrow$	$3.21 \times 10^{-9} (T/300 \text{ K})^{-0.5} \text{ cm}^3 \text{ s}^{-1}$	a	ion-neutral
$\text{CH}_3\text{OCH}_3 + \text{H}_2$			
$\text{CH}_3\text{OCH}_2 + \text{H}_3\text{O}^+ \rightarrow$	$1.48 \times 10^{-9} (T/300 \text{ K})^{-0.5} \text{ cm}^3 \text{ s}^{-1}$	a	ion-neutral
$\text{CH}_3\text{OCH}_3 + \text{H}_2\text{O}$			
$\text{CH}_3\text{OCH}_2 + \text{HCO}^+ \rightarrow$	$1.29 \times 10^{-9} (T/300 \text{ K})^{-0.5} \text{ cm}^3 \text{ s}^{-1}$	a	ion-neutral
$\text{CH}_3\text{OCH}_3 + \text{CO}$			
$\text{CH}_3\text{OCH}_2 + \text{C}^+ \rightarrow$	$1.76 \times 10^{-9} (T/300 \text{ K})^{-0.5} \text{ cm}^3 \text{ s}^{-1}$	a	ion-neutral
$\text{CH}_3\text{OCH}_3 + \text{C} + \text{He}$			
$\text{CH}_3\text{OCH}_2 + \text{He}^+ \rightarrow$	$7.06 \times 10^{-10} (T/300 \text{ K})^{-0.5} \text{ cm}^3 \text{ s}^{-1}$	a	ion-neutral
$\text{CH}_2^+ + \text{CH}_3\text{O} + \text{He}$			
$\text{CH}_3\text{OCH}_2 + \text{He}^+ \rightarrow$	$7.06 \times 10^{-10} (T/300 \text{ K})^{-0.5} \text{ cm}^3 \text{ s}^{-1}$	a	ion-neutral
$\text{CH}_3\text{O}^+ + \text{CH}_2 + \text{He}$			
$\text{CH}_3\text{OCH}_2 + \text{He}^+ \rightarrow$	$7.06 \times 10^{-10} (T/300 \text{ K})^{-0.5} \text{ cm}^3 \text{ s}^{-1}$	a	ion-neutral
$\text{CH}_3^+ + \text{H}_2\text{CO} + \text{He}$			
$\text{CH}_3\text{OCH}_2 + \text{He}^+ \rightarrow$	$7.06 \times 10^{-10} (T/300 \text{ K})^{-0.5} \text{ cm}^3 \text{ s}^{-1}$	a	ion-neutral
$\text{H}_2\text{CO}^+ + \text{CH}_3 + \text{He}$			
$\text{CH}_3\text{OCH}_2 + \text{CH}_2\text{OH} \rightarrow$	$1.00 \times 10^{-11} \text{ cm}^3 \text{ s}^{-1}$	b	neutral-neutral
$\text{CH}_3\text{OCH}_3 + \text{H}_2\text{CO}$			
$\text{CH}_3\text{OCH}_2 + \text{CH}_3\text{O} \rightarrow$	$1.00 \times 10^{-11} \text{ cm}^3 \text{ s}^{-1}$	b	neutral-neutral
$\text{CH}_3\text{OCH}_3 + \text{H}_2\text{CO}$			
$\text{CH}_3\text{OCH}_2 + \text{HCO} \rightarrow$	$1.00 \times 10^{-11} \text{ cm}^3 \text{ s}^{-1}$	b	neutral-neutral
$\text{CH}_3\text{OCH}_3 + \text{CO}$			
$\text{CH}_3\text{OCH}_2 + \text{COOH} \rightarrow$	$1.00 \times 10^{-11} \text{ cm}^3 \text{ s}^{-1}$	b	neutral-neutral
$\text{CH}_3\text{OCH}_3 + \text{CO}_2$			
$\text{CH}_3\text{OCH}_2 \xrightarrow{\text{CRUV}} \text{CH}_3 + \text{H}_2\text{CO}$	$5.00 \times 10^2 \times \zeta_0 \text{ s}^{-1}$	c, e	CR-induced PD
$\text{CH}_3\text{OCH}_2 \xrightarrow{\text{CRUV}} \text{CH}_2 + \text{CH}_3\text{O}$	$5.00 \times 10^2 \times \zeta_0 \text{ s}^{-1}$	c, e	CR-induced PD
$\text{CH}_3\text{OCH}_2 \xrightarrow{\text{UV}} \text{CH}_3 + \text{H}_2\text{CO}$	$5.00 \times 10^{-10} \exp(-1.7 A_V) \text{ s}^{-1}$	d, e	external UV PD
$\text{CH}_3\text{OCH}_2 \xrightarrow{\text{UV}} \text{CH}_2 + \text{CH}_3\text{O}$	$5.00 \times 10^{-10} \exp(-1.7 A_V) \text{ s}^{-1}$	d, e	external UV PD

Notes. <sup>a</sup>Ion-molecule rates calculated using the method of Herbst & Leung (1986); <sup>b</sup>Generic rate coefficients are assumed as per Garrod (2013).; <sup>c</sup>The cosmic ray ionization rate,  $\zeta_0$ , is set to  $1.3 \times 10^{-17} \text{ s}^{-1}$ .; generic prefactors are assumed based on like processes.; <sup>d</sup>Generic rate coefficients based on like processes; <sup>e</sup>Same processes are assumed for grain-surface/ice species with a factor 3 smaller rate.

Table 2.2: Gas-phase reactions newly included in chemical network

Reaction	$E_A$ (K)	Width (Å)	Notes
$\text{CH}_3 + \text{CO} \rightarrow \text{CH}_3\text{CO}$	2,870	1.0	a b
$\text{CH}_3 + \text{H}_2\text{CO} \rightarrow \text{CH}_3\text{OCH}_2$	2,870	1.0	a c
$\text{CH}_3\text{O} + \text{CO} \rightarrow \text{CH}_3\text{OCO}$	3,967	1.0	a d
$\text{CH}_2 + \text{CH}_3\text{O} \rightarrow \text{CH}_3\text{OCH}_2$	0	1.0	
$\text{H} + \text{CH}_3\text{OCH}_2 \rightarrow \text{CH}_3\text{OCH}_3$	0	1.0	
$\text{H} + \text{CH}_3\text{OCH}_3 \rightarrow \text{CH}_3\text{OCH}_2 + \text{H}_2$	4,450	1.0	e
$\text{H} + \text{CH}_2\text{CO} \rightarrow \text{CH}_2\text{CHO}$	3050	1.0	f
$\text{H} + \text{CH}_2\text{CO} \rightarrow \text{CH}_3\text{CO}$	1320	1.0	f
$\text{H} + \text{CH}_3\text{CO} \rightarrow \text{CH}_3\text{CHO}$	0	1.0	
$\text{O} + \text{CH}_4 \rightarrow \text{CH}_3 + \text{OH}$	4380	1.0	g

Notes. The full set of the bulk-ice reactions is available in the machine readable format. This version only shows important and/or newly-included reactions; <sup>a</sup>Also treated using the 3-BEF scheme, see § 2.5; <sup>b</sup>Estimate using Evans-Polanyi relation; <sup>c</sup>Estimate based on  $\text{CH}_3 + \text{CO}$  reaction; <sup>d</sup>Huynh & Violi (2008); <sup>e</sup>Takahashi et al. (2007); <sup>f</sup>Senosiain et al. (2013); <sup>g</sup>Westenberg & DeHaas (1967)

Table 2.3: Important and/or newly-included grain-surface and ice-mantle reactions

$N(B)$ , which here are expressed as the average number of atoms or molecules of that species present on an individual grain; the total number of binding sites on the grain surface,  $N_S$ , often assumed to be on the order of 1 million for canonically-sized grains; and an efficiency related to the activation energy barrier (if any),  $f_{\text{act}}(AB)$ , which takes a value between zero and unity. Thus, the total rate of production ( $\text{s}^{-1}$ ) may be expressed in the following form (which is arranged in such a way as to demonstrate its correspondence with the nondiffusive mechanisms discussed later):

$$R_{AB} = f_{\text{act}}(AB) [k_{\text{hop}}(A) N(A)] \frac{N(B)}{N_S} + f_{\text{act}}(AB) [k_{\text{hop}}(B) N(B)] \frac{N(A)}{N_S} \quad (2.1)$$

In the first term, the expression within square brackets corresponds to the total rate at which particles of species  $A$  may hop to an adjacent surface binding site. The ratio  $N(B)/N_S$  gives the probability for each such hop to result in a meeting with a particle of species  $B$ . Multiplying these by the reaction efficiency gives the reaction rate associated solely with the diffusion of species  $A$ . The reaction rate associated with diffusion solely of species  $B$  is given by the second term. The total reaction rate is commonly expressed more succinctly thus:

$$R_{AB} = k_{AB} N(A) N(B) \quad (2.2)$$

$$k_{AB} = f_{\text{act}}(AB) (k_{\text{hop}}(A) + k_{\text{hop}}(B))/N_S \quad (2.3)$$

which provides a more standard-looking second-order reaction rate. The rate coefficient,  $k_{AB}$ , may be further adjusted to take account of random walk, in which a reactant that has yet to meet a reaction partner may re-visit previous, unsuccessful sites. This effect typically reduces the overall reaction rate by no more than a factor of a few (e.g. Charnley, 2005; Lohmar & Krug, 2006; Lohmar et al., 2009; Willis & Garrod, 2017).

The individual hopping rate for some species  $i$  is assumed in this model to be a purely thermal mechanism, given by

$$k_{\text{hop}}(i) = \nu(i) \exp\left(\frac{-E_{\text{dif}}(i)}{T}\right) \quad (2.4)$$

where  $\nu(i)$  is the characteristic vibrational frequency of species  $i$  and  $E_{\text{dif}}(i)$  is the barrier against diffusion in units of K.

The reaction efficiency factor for a reaction between species  $A$  and  $B$  considers the case where, if there is an activation energy barrier, the diffusion of either species *away* from the other may compete with the reaction process itself (see e.g. Garrod & Pauly, 2011), thus:

$$f_{\text{act}}(AB) = \frac{\nu_{AB} \kappa_{AB}}{\nu_{AB} \kappa_{AB} + k_{\text{hop}}(A) + k_{\text{hop}}(B)} \quad (2.5)$$

where  $\nu_{AB}$  is taken as the faster of either  $\nu(A)$  or  $\nu(B)$ , and  $\kappa_{AB}$  is a Boltzmann factor or tunneling efficiency for the reaction (see Hasegawa et al., 1992). The denominator represents the total rate at which an event may occur when species A and B are in a position to react.

In order to formulate rates for *nondiffusive* reaction processes of whatever kind, the total rate must again be decomposed into its constituent parts, which, unlike in Eqs. (2.2) and (2.3), cannot generally be re-combined.

The generic form that we adopt for such processes is:

$$R_{AB} = f_{\text{act}}(AB) R_{\text{comp}}(A) \frac{N(B)}{N_S} + f_{\text{act}}(AB) R_{\text{comp}}(B) \frac{N(A)}{N_S} \quad (2.6)$$

where  $R_{\text{comp}}(i)$  is labeled the ‘‘completion rate’’ for the reaction, corresponding specifically to the ‘‘appearance’’ of species  $i$ . The determination of  $R_{\text{comp}}(i)$  values is explained in more detail in the following subsections for each of the specific reaction mechanisms considered. The above form is essentially the same as that given by Garrod (2019) for photodissociation-induced reactions. The correspondence of Eq. (2.1) (for diffusive reactions) with Eq. (2.6) is clear; the latter may be considered a more general description of a surface reaction rate, which can be applied to both diffusive and nondiffusive processes, according to the chosen form of  $R_{\text{comp}}(i)$ . The regular diffusive mechanism would use  $R_{\text{comp}}(i) = k_{\text{hop}}(i) N(i)$ .

While the general form given in Eq. (2.6) is set up to describe grain-surface processes, it may easily be adapted for bulk-ice processes by substituting  $N_S$  for  $N_M$ , the total number of particles in the ice mantle, with  $N(i)$  now representing the number of atoms/molecules of species  $i$  present in the mantle. In this case, mantle-specific diffusion rates should be used.

The several nondiffusive processes incorporated into the chemical model, based on Eq. (2.6), are described below. Table 2.4 indicates which specific new mechanisms are included in each of the model setups tested in the present study.

### 2.2.2 Eley-Rideal reactions

The Eley-Rideal (E-R) reaction process occurs when some atom or molecule that is adsorbing/accreting from the gas phase onto the grain surface immediately encounters its grain-surface reaction partner as it adsorbs. Ruaud et al. (2015) considered a more intricate treatment than we use here, in which an adsorbing carbon atom could enter into a bound complex with a surface molecule. Here we adopt a more generalized treatment in which we do not differentiate between the binding properties of local surface species.

The rates for the Eley-Rideal process can easily be represented using Eq. (2.6). For reactions that have no activation-energy barrier (and for which  $f_{\text{act}}(AB)$  is therefore close to unity), this is achieved by setting  $R_{\text{comp}}(i) = R_{\text{acc}}(i)$ , the total accretion rate of species  $i$  from the gas phase.

In the interests of completeness, it is necessary also to consider how to treat the kinetics of E-R reactions that have at least some modest activation-energy barrier. To this end, one may consider a hypothetical case where oxygen atoms are slowly accreting onto an otherwise pure CO surface. For purposes of illustration, it is initially assumed here that the surface-diffusion rates of both O and CO are negligible, with the result that  $f_{\text{act}}(\text{O} + \text{CO})=1$ .

The reaction  $\text{O} + \text{CO} \rightarrow \text{CO}_2$  has an activation energy on the order of 1000 K; although the reaction will not be instant, in the absence of all other competing processes it should nevertheless occur on some finite timescale. Thus, the total timescale for the complete E-R process for an individual accreting O atom encountering and reacting with a surface CO molecule would be the sum of: (i) the accretion timescale of the oxygen atom onto the surface and (ii) the lifetime against its subsequent reaction with CO, i.e.  $1/R_{\text{acc}}(\text{O}) + 1/(\nu_{\text{O}+\text{CO}} \kappa_{\text{O}+\text{CO}})$ . This would provide a total completion rate associated with O accretion (to be employed in Eq. 2.6) of:

$$R_{\text{comp}}(\text{O}) = \frac{1}{1/R_{\text{acc}}(\text{O}) + 1/(\nu_{\text{O}+\text{CO}} \kappa_{\text{O}+\text{CO}})}$$

The completion rate  $R_{\text{comp}}(\text{O})$  should be viewed as the rate at which the reaction process occurs *successfully* from the point of view of an individual accreting O atom, taking into account all sequential steps in the completion of the reaction process. Note that, in the full description, the probability of encountering a CO molecule on the surface,  $N(\text{CO})/N_S$ , and the reaction efficiency,  $f_{\text{act}}(\text{O} + \text{CO})$ , should both remain outside of the formula for  $R_{\text{comp}}(\text{O})$ , as per Eq. (2.6). Neither of these values affects the actual *timescale* over which an individual O atom successfully accretes and reacts with a surface CO molecule; rather, they affect the *probability* that a single such event is successful.

This expression for  $R_{\text{comp}}(\text{O})$  could result in one of two important outcomes, depending on the relative rates of accretion and reaction. If accretion of O is very slow, and therefore reaction is comparatively fast, then  $R_{\text{comp}}(\text{O}) \simeq R_{\text{acc}}(\text{O})$ . Since  $N(\text{CO})/N_S \simeq 1$ , this means that the total Eley-Rideal production rate would initially be  $R_{\text{O}+\text{CO}} \simeq R_{\text{acc}}(\text{O})$ . In other words, the overall production rate of  $\text{CO}_2$  is only limited by the rate of O accretion onto the surface, which is as one would expect for this case.

However, if reaction is slower than or comparable to the initiating accretion process, each accretion of O would be followed by some significant lag-time between accretion and reaction, which must be accounted for in the overall rate; the incorporation of the above

expression for  $R_{\text{comp}}(\text{O})$  into Eq. (2.6) indeed does this. Without this expression, and instead using the value  $R_{\text{comp}}(\text{O}) = R_{\text{acc}}(\text{O})$ , the rate of conversion of O and CO into  $\text{CO}_2$  would incorrectly be set to the accretion rate of O. The correct formulation gives a total E-R reaction rate that is less than the total accretion rate, allowing the build-up of O on the surface.

The final adjustment to the barrier-mediated E-R treatment comes into play when one or other surface diffusion rate is non-negligible. If diffusion of (say) O is indeed fast compared to reaction, then the reaction efficiency,  $f_{\text{act}}(\text{O} + \text{CO})$ , becomes small, which reduces the total rate of the reaction as per Eq. (2.6). However, the completion rate  $R_{\text{comp}}(\text{O})$  must also be adjusted, to correspond only to the instances in which the O+CO reaction is actually successful. Successful reactions would have to occur before the diffusive separation of the two reactants could render the process unsuccessful, so the reaction timescale would become shorter, even though the reaction *probability* (i.e.  $f_{\text{act}}$ ) were reduced. For this reason, diffusion rates must also be considered when formulating  $R_{\text{comp}}(\text{O})$ . Using a more general description for reactants  $A$  and  $B$ , the average lifetime against some event occurring (including reaction itself), once the reactants are in a position to react, may be described more fully by the expression:

$$t_{AB} = 1/(\nu_{AB} \kappa_{AB} + k_{\text{hop}}(A) + k_{\text{hop}}(B)) \quad (2.7)$$

which can then be used in the general definitions:

$$R_{\text{comp}}(A) = \frac{1}{1/R_{\text{app}}(A) + t_{AB}} \quad (2.8)$$

$$R_{\text{comp}}(B) = \frac{1}{1/R_{\text{app}}(B) + t_{AB}} \quad (2.9)$$

where  $R_{\text{app}}(i)$  is the ‘‘appearance rate’’ of species  $i$ , which in the case of the E-R mechanism is simply  $R_{\text{acc}}(i)$ .

It should be noted that once diffusion becomes significant, a model even as simple as the one used above to describe pure Eley-Rideal reaction processes would be incomplete; the standard diffusive reactions described by Eq. (2.1) must also be considered (as an entirely separate process) in such a model, to handle the occasions where accreting atoms (e.g. O) do not immediately react with their reaction partners (e.g. CO) before they diffuse away to another binding site, where they may also have the ability to react. In this case, the Eley-Rideal expressions would depend much less strongly on the time-lag effect described above, meaning that  $R_{\text{comp}}$  and  $R_{\text{acc}}$  would be similar in cases where diffusion of either reactant were relatively fast. In practical application to astrochemical models, for nondiffusive reactions whose reactants have slow or negligible diffusion rates, other processes could also act to interfere with the reaction; for example, the UV-induced dissociation of one or other reactant might occur on a shorter timescale than a very slow reaction, or a hydrogen atom might arrive to react with one of other reactant, before the reaction in question could occur. Competition from processes such as these would prevent very slow reactions (i.e. those with large activation barriers) from becoming important, even where diffusion of the reactants were negligible. A yet more complete treatment of reaction competition would include rates for these processes in Eqs. (2.5) and (2.7).

In our chemical model *MAGICKAL*, Eqs. (2.6)–(2.9) are used to set up Eley-Rideal versions of all allowed grain-surface reactions in the network. Because the E-R process is exclusively a surface process, no such processes in the ice mantle are included. Note

that, when incorporating the Eley-Rideal mechanism into a model, no modification of the accretion (adsorption) rates themselves is required, since the Eley-Rideal mechanism does not *replace* any part of the adsorption rate. Rather, the E-R mechanism occurs immediately after adsorption, and therefore acts as a sink on the surface populations of the reactants, even though its rate is driven by the rate of arrival from the gas phase of one or other reactant.

Equations with the general form of Eqs. (2.6)–(2.9) are used also to formalize the remaining nondiffusive reaction mechanisms described below, where  $R_{\text{app}}(i)$  is the only quantity to vary between processes. These formulations can be used equally well for processes with or without activation-energy barriers.

While Eq. (2.6) is still valid for the regular diffusive reaction mechanism with completion rates of  $R_{\text{comp}}(i) = k_{\text{hop}}(i) N(i)$ , no adjustment following Eqs. (2.7)–(2.9) should be used, nor would be needed. The formulation required to model any lag-time for diffusive reactions is different from that of nondiffusive processes (because  $N(i)/N_S$  and  $f_{\text{act}}(AB)$  cannot remain outside the  $R_{\text{comp}}(i)$  expression), but there are no circumstances in which such a lag-time would be significant.

### 2.2.3 Photodissociation-induced reactions

Garrod (2019) suggested that the omission of nondiffusive, photodissociation-induced reactions from models of interstellar ice chemistry may result in the photolytic production of COMs being severely underestimated. Past models of chemistry in star-forming regions (e.g. Garrod et al., 2008, 2017) have allowed photodissociation to contribute to the production of COMs in the surface and bulk-ice phases in only an indirect way, mediated by thermal diffusion. That is, photodissociation of various molecules produces radicals, which are separately allowed to react through the standard diffusive mechanism. Thus, at very low temperatures, no significant COM production is seen via radical-radical recombination, as diffusion of radicals is minimal. However, the presence of radicals in or upon the ice means that in some fraction of photodissociation events, the products may sometimes be formed with other reactive radicals already present nearby. In this case, the immediate products of photodissociation could react with the pre-existing radicals either without diffusion, or following some short-ranged, non-thermal diffusion process (possibly enabled by the excitation of the dissociation products).

Eqs. (2.6)–(2.9) can again be used to describe this process, with an appropriate choice for  $R_{\text{app}}(i)$ , which is simply the total rate of production of photo-product  $i$  caused by all possible photodissociation processes:

$$R_{\text{app}}(i) = \sum_{\text{all } j} R_j(i) \quad (2.10)$$

where  $R_j(i)$  is the production rate of  $i$  via an individual photodissociation process  $j$ . For the radical  $\text{CH}_3$ , for example, this would include the photodissociation of  $\text{CH}_3\text{OH}$ ,  $\text{CH}_4$ , and various larger molecules containing a methyl group.

If one were to consider, for example, the production of dimethyl ether through this mechanism, an important reaction would be  $\text{CH}_3 + \text{CH}_3\text{O} \rightarrow \text{CH}_3\text{OCH}_3$ , which is usually assumed to be barrierless. For this reaction, in Eq. (2.6), species  $A = \text{CH}_3$  and species  $B$

=  $\text{CH}_3\text{O}$ ; the appearance rate of  $\text{CH}_3$  would be as described above. The main contribution to the appearance rate of  $\text{CH}_3\text{O}$  would likely be the photodissociation process  $\text{CH}_3\text{OH} + h\nu \rightarrow \text{CH}_3\text{O} + \text{H}$ . The formulation used for the dimethyl ether-producing reaction simply states that some fraction of  $\text{CH}_3$  produced by photodissociation of various molecules in the ice will immediately meet a  $\text{CH}_3\text{O}$  radical that it can react with, and vice versa.

Reactions affected by this PD-induced mechanism need not only be radical-radical recombination reactions; the production, via photodissociation, of atomic H in close proximity to CO, for example, could enhance the rate of the reaction  $\text{H} + \text{CO} \rightarrow \text{HCO}$ , which has an activation-energy barrier. The treatment of barrier-mediated reactions in the generic Eqs. (2.7)–(2.9) is used again for this purpose.

This treatment does not take into account any explicit consideration of excitation of the photo-products, which could also enhance reaction rates (as per e.g. Shingledecker et al., 2018, in the case of cosmic-ray induced dissociation). It is also implicitly assumed that the rates of photodissociation used in the network represent the rates at which dissociation occurs without immediate recombination of those same photo-products.

It is trivial to adapt the equations used for surface reactions to deal instead with ice-mantle related processes, and this is indeed implemented in the simulations presented here.

## 2.2.4 Three-body reactions

The laboratory results of authors such as Fedoseev et al. (2015, 2017), in which H, CO and/or other species are deposited onto a cold surface, indicate that surface reactions between radicals of low mobility may produce COMs, even at low temperatures and without any energetic processing. The suggested explanation is that pairs of radical species such as HCO may, on occasion, be formed in close proximity to each other, allowing them to react either immediately or after a very small number of surface hops. The HCO radicals themselves would initially be formed through a more typical diffusive (Langmuir-Hinshelwood) process or through an Eley-Rideal process, via the barrier-mediated reaction of H and CO. Fedoseev et al. (2015) suggest that reactions of HCO with CO may also be active, which would require no diffusion of HCO at all, if the HCO itself is formed through the reaction of atomic H and CO on top of a CO-rich surface.

In a similar vein, Garrod & Pauly (2011) found, using chemical kinetics modeling, that the interstellar abundance of solid-phase  $\text{CO}_2$  could be explained by the reaction  $\text{H} + \text{O} \rightarrow \text{OH}$  occurring on a CO-rich dust-grain ice surface. This allows the newly-produced OH to react rapidly with the CO without any intervening thermal diffusion. They introduced into their models a new reaction rate specifically for this process that was functionally similar to Eq. (2.6).

Here, we use Eqs. (2.6)–(2.9) to calculate rates for what may be termed three-body reactions, which include the above examples. This approach is extended to all grain-surface reactions in the network, with a similar treatment for bulk-ice processes. To do this, another dedicated expression for the appearance rate  $R_{\text{app}}(i)$  to be used in Eqs. (2.8) and (2.9) must be constructed specifically for three-body reactions. Eq. (2.10) can again be used, this time where  $R_j(i)$  is the production rate of  $i$  (as determined using Eq. 2.1) resulting from any diffusive (Langmuir-Hinshelwood) reaction, or for any nondiffusive

Eley-Rideal or photodissociation-induced reaction, whose rates are described above. Thus,  $R_{\text{app}}(i)$  includes the production rates of  $i$  for all reactive mechanisms  $j$  that could lead to a subsequent reaction. From a technical point of view, the rates of all such reaction processes must therefore be calculated in advance of the calculations for any three-body reactions.

Using the example of the process considered by Garrod & Pauly (2011), the reaction under consideration as a three-body process would be  $\text{OH} + \text{CO} \rightarrow \text{CO}_2$ ; thus, in Eq. (2.6),  $A = \text{OH}$  and  $B = \text{CO}$ . There are several reactions in our network that could produce OH, but the main one is indeed  $\text{H} + \text{O} \rightarrow \text{OH}$ . The sum of the production rates of OH from all of these reactions would comprise  $R_{\text{app}}(\text{OH})$ . The appearance rate for CO would also be constructed from the CO production rates of all reactions leading to its formation.

In this way,  $\text{CO}_2$  could be formed via a three-body reaction process in which, for example, an H and an O atom diffuse on a surface until they happen to meet in a binding site where CO is in close proximity, they react to form OH in the presence of the CO, and the OH and CO then subsequently react with no further diffusion required. Alternatively, an oxygen atom could be situated in contact with a CO molecule when an incoming H atom from the gas phase initiates an Eley-Rideal process, leading to OH formation, followed by reaction with the CO. Or, a  $\text{CH}_4$  molecule in close proximity to a CO molecule and an O atom could be dissociated to H and  $\text{CH}_3$ , with the H quickly reacting with the O atom to produce OH, which would then react with CO. The prescription above would allow many such scenarios to be included in the overall production rate of  $\text{CO}_2$ , including others relating to the formation of a CO molecule in close proximity to an OH radical. The adoption of this generalized process means that the special-case prescription for the  $\text{OH} + \text{CO}$  reaction introduced by Garrod & Pauly (2011) is no longer required.

In the kind of chemical system considered by Fedoseev et al. (2015, 2017), in which H and CO are deposited onto a surface, complex molecules could be built up via three-body reactions between HCO radicals, initiated either by E-R or L-H production of HCO.

Note that the new treatment does not explicitly differentiate between the case where the newly-formed reactant is immediately in contact with the next reaction partner, and the case where it has sufficient excess energy to allow it to undergo a thermal hop in order to find its next reaction partner. It is in fact highly probable that the products of exothermic reactions (which includes virtually every surface reaction included in the network) would have sufficient energy to allow some degree of non-thermal hopping immediately following formation. The possibility of such energy also allowing barrier-mediated three-body reactions to occur more rapidly is considered in the next subsection.

To go yet a stage further, one may imagine a scenario in which the products of three-body reactions themselves could also be involved in subsequent nondiffusive three-body reactions. This possibility is also included in our model, using the same equations as before, with appearance rates defined by:

$$R_{\text{app}}(i) = \sum_{\text{all } j} R_{j,3\text{B}}(i) \quad (2.11)$$

where  $R_{j,3\text{B}}(i)$  is the production rate of  $i$  caused by the three-body reaction labelled  $j$ . Although these appearance rates will usually be lower than those used in the first round of three-body reactions, the second three-body reaction could be the most important for certain species if they have no more dominant production mechanism. In the present models, we allow a total of three rounds of three-body reactions to take place. Although

this could in theory be increased to any arbitrary number of rounds, the influence of those processes rapidly diminishes beyond the second round.

As with the photodissociation-induced reactions, a similar method is employed also for reactions in the bulk ice. In this case, the appearance rates of reactants in the first round of three-body reactions would generally all be products of photodissociation-induced reactions, as the Eley-Rideal process is exclusively a surface mechanism, while the thermal diffusion of all species in the bulk – excluding arguably H and H<sub>2</sub> – would be very slow at the temperatures considered in the simulations presented here.

### Specific reactions

Although the full model includes a range of three-body (3-B) processes capable of producing acetaldehyde (CH<sub>3</sub>CHO), methyl formate (CH<sub>3</sub>OCHO) and dimethyl ether (CH<sub>3</sub>OCH<sub>3</sub>), the dominant mechanisms for each (based on model results) are presented below.

For acetaldehyde, the most important three-body mechanism is made up of a pair of sequential two-body processes as follows:



The most important sequential mechanisms for the other two COMs are:



Each of these reaction pairs involves the addition of radicals in the second step, and two of them involve the addition of atomic H to a radical in the first step. The production of the COMs through these mechanisms should therefore have a strong dependence on the instantaneous abundances of short-lived reactive radicals.

The full network used in the models includes three-body versions of all the reactions used for regular diffusive chemistry, for all surface and mantle species.

### 2.2.5 Excited three-body reactions

Besides the three-body reaction process described in §2.4, we also consider a mechanism whereby the initiating reaction produces a product that is sufficiently excited that it is able to overcome the activation energy barrier to a subsequent reaction. This is of particular interest if it may allow a reaction with either CO or H<sub>2</sub>CO – both abundant surface species – that would result in the production of a precursor to an important O-bearing COM. In this picture, the energy of formation released by a reaction is held in the vibrational excitation of the product species. That excited species can then immediately react with a contiguous reaction partner.

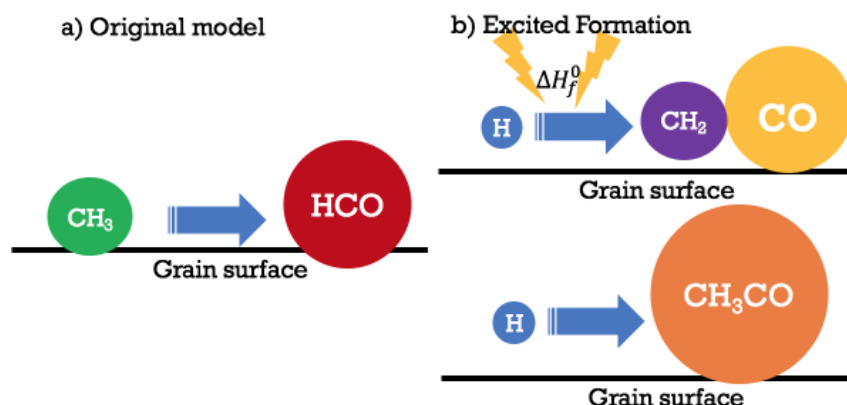
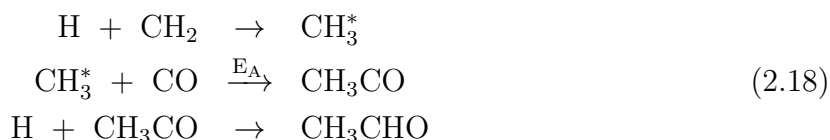
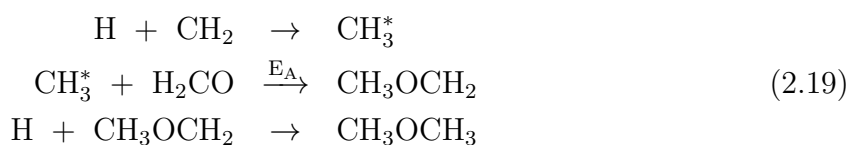


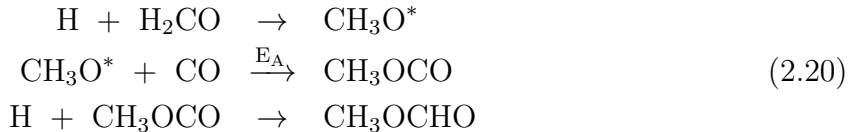
Figure 2.1: Illustration of alternative mechanisms for acetaldehyde formation: (a) the regular diffusive grain-surface reaction between radicals  $\text{CH}_3$  and  $\text{HCO}$ , and (b) a postulated three-body excited-formation mechanism involving  $\text{H}$ ,  $\text{CH}_2$  and  $\text{CO}$ , followed by a regular diffusive reaction between the radical product,  $\text{CH}_3\text{CO}$ , and another  $\text{H}$  atom. In case (a), reaction is slow at low temperatures. In case (b), a rapid initiating reaction between  $\text{H}$  and  $\text{CH}_2$ , with exothermicity  $\Delta H_f^0 = 4.80$  eV, provides enough energy to the product  $\text{CH}_3$  that it may immediately overcome the barrier to reaction with a neighboring  $\text{CO}$  molecule. This produces a precursor to acetaldehyde,  $\text{CH}_3\text{CO}$ , that can easily be hydrogenated by a mobile  $\text{H}$  atom to form  $\text{CH}_3\text{CHO}$ .

Figure 2.1 shows the formation of  $\text{CH}_3\text{CHO}$  via this three-body excited formation (3-BEF) mechanism as an example. The original reaction network included the direct association of  $\text{CH}_3$  and  $\text{HCO}$ , mediated by radical diffusion, as the main formation process for surface  $\text{CH}_3\text{CHO}$ . The chance to form the  $\text{CH}_3\text{CHO}$  in that purely diffusive model is small, because it would require immobile heavy radicals to meet at low temperature. The new 3-body process described above, as well as the photodissociation-induced and Eley-Rideal processes, would allow this reaction to occur nondiffusively. However, the excited production of  $\text{CH}_3$  could also allow reaction with abundant surface  $\text{CO}$ . In the first step, an  $\text{H}$  atom meets and then reacts with a  $\text{CH}_2$  radical that is adjacent to a  $\text{CO}$  molecule. This reaction is exothermic by 4.80 eV ( $\sim 55,700$  K), sufficient to overcome the barrier to the  $\text{CH}_3 + \text{CO}$  reaction (nominally 2,870 K, see below). Once this follow-up reaction has occurred, the product  $\text{CH}_3\text{CO}$ , which is a precursor to acetaldehyde, can easily be converted into a stable species via hydrogenation by another  $\text{H}$  atom. The entire process is described as follows:



where an asterisk indicates an excited species. Similar reactions for the production of  $\text{CH}_3\text{OCH}_3$  and  $\text{CH}_3\text{OCHO}$  through the 3-BEF process are as follows:





The 3-BEF process technically concerns only the first two reactions out of the three, in each case; the final hydrogen-addition step most typically occurs through the usual Langmuir-Hinshelwood mechanism that is already included in the model, although non-diffusive mechanisms may also act to add the final H atom.

Due to the more complicated requirement to consider the energy of formation in each case, the three new 3-BEF processes shown above were individually coded into the model, rather than constructing a generic mechanism. For this reason, the 3-BEF mechanism is included only in the first round of three-body processes. The production rate of the standard diffusive process for the initiating reaction in each case is responsible for the entire value of  $R_{\text{app}}(i)$ , and only one term is required in Eq. (2.6). Crucially, the reaction efficiency for the second reaction in the process (i.e. the reaction whose rate is actually being calculated with the 3-BEF method) is initially set to unity, to signify that the activation energy barrier is immediately overcome.

Unfortunately, the activation energies of the above reactions between the radicals and CO or H<sub>2</sub>CO are not well constrained. The chemical network of Garrod (2013) included the CH<sub>3</sub> + CO and CH<sub>3</sub>O + CO reactions, adopting a generic activation energy barrier of 2,500 K, based on the approximate value for the equivalent reactions of atomic H with CO and H<sub>2</sub>CO. A reaction between CH<sub>3</sub> and H<sub>2</sub>CO was also present in that network, with products CH<sub>4</sub> and HCO, and  $E_A=4440$  K; this reaction is retained here in addition to the new pathway.

For the present network, we calculate an approximate activation energy of 2,870 K for the CH<sub>3</sub> + CO reaction using the Evans-Polanyi (E-P) relation (e.g. Dean and Bozzelli, 2000); this would be well below the energy produced by the initiating reaction ( $\sim 55,700$  K). Due to the lack of comparable reactions for a similar E-P estimate for the activation energy of the CH<sub>3</sub> + H<sub>2</sub>CO reaction, the same value of 2,870 K might be assumed, placing it also comfortably less than the energy produced by the H + CH<sub>2</sub> → CH<sub>3</sub> reaction. Few determinations exist for the activation energy of the CH<sub>3</sub>O + CO reaction, although an experiment places it at 3,967 K (Huynh & Violi, 2008, for temperatures 300-2500 K). This also is less than the energy produced by the initiating reaction, H + H<sub>2</sub>CO → CH<sub>3</sub>O ( $\sim 10,200$  K). In any case, the activation energies involved in each of the three reactions mentioned here are sufficiently large that they should be of no importance without the inclusion of the 3-BEF mechanism to provide the energy required, while the 3-BEF mechanism itself is assumed to go at maximum efficiency. However, the latter assumption may not necessarily be accurate, depending on the form of the energy released by the reaction, and whether there is any substantial loss prior to reaction actually occurring (see §2.3.3).

## 2.2.6 Physical conditions

*MAGICKAL* is a single-point model, but a spatially-dependent picture of the chemistry

Model	E-R	PD-Induced	3-B	3-B+3-BEF	3-BEF	Best
Control						
Eley-Rideal	✓					
Photodissociation-Induced		✓				
Three-body			✓	✓		✓
Three-body Excited Formation				✓		✓
Adjusted 3-BEF efficiency for MF						✓

Table 2.4: nondiffusive mechanisms included in model setups

of L1544 can be achieved by running a set of models with different physical conditions at specific positions within the prestellar core. Recently, Chacón-Tanarro et al. (2019) determined the parameterized density and temperature structure of L1544 as follows, considering the optical properties of dust grains as a function of radius:

$$T(r) [\text{K}] = 12 - \frac{12 - 6.9}{1 + \left(\frac{r}{28.07''}\right)^{1.7}} \quad (2.21)$$

$$n_{\text{H}_2}(r) [\text{cm}^{-3}] = \frac{1.6 \times 10^6}{1 + \left(\frac{r}{17.3''}\right)^{2.6}} \quad (2.22)$$

where  $r$  is measured in arcseconds. Based on this density structure, we determine 15 densities at which the chemical models are to be run, ranging logarithmically from the minimum of  $n_{\text{H}} = 4.4 \times 10^4 \text{ cm}^{-3}$  ( $\sim 11,000 \text{ AU}$ ) to the maximum of  $n_{\text{H}} = 3.2 \times 10^6 \text{ cm}^{-3}$  (core center). An additional eight density points are then placed to achieve better spatial resolution toward the core center (where the density profile is relatively flat). The appropriate temperature for each point is then chosen from the profile, based on density/radius.

In order to take account of the gradual collapse of the gas into this final density profile, the density used for each chemical model in the set is independently evolved using a simple modified free-fall collapse treatment. (The radial position of each model point is thus not explicitly considered during this evolution). Each point begins with a gas density of  $n_{\text{H},0} = 3 \times 10^3 \text{ cm}^{-3}$ , with an initial H/H<sub>2</sub> ratio of  $5 \times 10^{-4}$ . The density evolution stops once each model reaches its specified final density, resulting in a marginally different evolutionary time for each density point. The collapse treatment is based on that used by Rawlings et al. (1992). Magnetic fields can play an important role in the equilibrium of dense cores, significantly slowing down the collapse process. Estimating an accurate collapse timescale is challenging, although the ratio of the ambipolar diffusion time ( $\tau_{\text{ap}}$ ) and the freefall time ( $\tau_{\text{ff}}$ ) is typically assumed to be  $\tau_{\text{ap}}/\tau_{\text{ff}} \sim 10$  (see, e.g., Hennebelle & Inutsuka, 2019). Thus, the magnetic retardation factor for collapse,  $B$ , is adopted here to control the collapse timescale. This parameter takes a value between 0 (static) and 1 (free-fall) and is technically density-dependent. In our model, this value is set for simplicity to 0.3 for all density points, which results in a collapse timescale approximately 3 times longer than the free-fall timescale. A time of a little over  $3 \times 10^6$  year is therefore required to reach the final density at each point, although much of this time is spent under relatively low-density conditions as the collapse gradually ramps up.

The density evolution for each model is accompanied by increasing visual extinction, which evolves according to the expression  $A_{\text{V}} = A_{\text{V},0}(n_{\text{H}}/n_{\text{H},0})^{2/3}$  (Garrod & Pauly,

2011). The initial extinction values are set such that the values at the end of the chemical model runs correspond to the linear integration of the density profile, converted to visual extinction using the relationship  $N_H = 1.6 \times 10^{21} A_V$ . An additional background visual extinction of 2 is added for all positions and times, under the assumption that L1544 is embedded in a molecular cloud (e.g. Vasyunin et al., 2017). In contrast to density and visual extinction, the temperature is held steady throughout the chemical evolution for each density point, with the same value adopted for both the gas and the dust. Temperatures range from approximately 8 to 14 K depending on radius, which is consistent with the observational features (Crapsi et al., 2007).

## 2.3 Results

The time-evolution of the fractional abundances at the core-center position is presented in Fig. 2.2 (gas phase) and Fig. 2.3 (solid phase), for each of the main chemical model setups. In the control model, no new mechanisms are added. In each of the other model setups, a single new mechanism is added to the control model setup, except for model 3-B+3-BEF, in which it is assumed that the 3-BEF mechanism could not occur without the 3-B mechanism also being active.

As seen in Fig. 2.2, every new mechanism introduced here, excluding E-R, significantly increases the abundances of  $\text{CH}_3\text{OCH}_3$  and  $\text{CH}_3\text{OCHO}$  in the gas phase during core evolution, while  $\text{CH}_3\text{CHO}$  is only substantially increased via 3-BEF. However, it should be noted that the increased fractional abundances rapidly drop as density increases toward the end-time of all the models, mostly converging to the control-model values. This indicates that the new mechanisms may hardly affect the gas-phase COMs at the core center, but may be more effective at more distant radii (i.e. lower density regions); this would nevertheless result in higher abundances toward the core-center position when averaged over the line of sight to include lower-density gas.

The presence of the COMs in the gas phase following their formation on grain surfaces is the result of chemical desorption. All surface reactions that form a single product have a small possibility of returning that product to the gas phase. The upper limit on the ejection probability per reaction is 1%.

Similar to the gas phase, every mechanism excluding E-R significantly increases the solid-phase populations of the COMs (Fig. 2.3). Note that the solid-phase population of  $\text{CH}_3\text{CHO}$ , whose gas-phase abundance is only strongly increased by the 3-BEF mechanism, increases even in the 3-B (only) and PD-Induced models. The 3-B and 3-B+3-BEF models converge to essentially the same value at the end-time. Dimethyl ether in the mantle is produced in similar quantities by each of the three effective mechanisms, while 3-BEF and then 3-B are more important than PD-Induced formation in the case of methyl formate. The E-R mechanism produces only marginal increases in mantle abundances of acetaldehyde and methyl formate. The increase in dimethyl ether production caused by E-R is around an order of magnitude throughout most of the evolution, although this is dwarfed by the effects of the other mechanisms.

Fig. 2.4 shows the radial distribution of gas-phase COM abundances using the full radius–density–temperature profile model results; abundances shown correspond to the

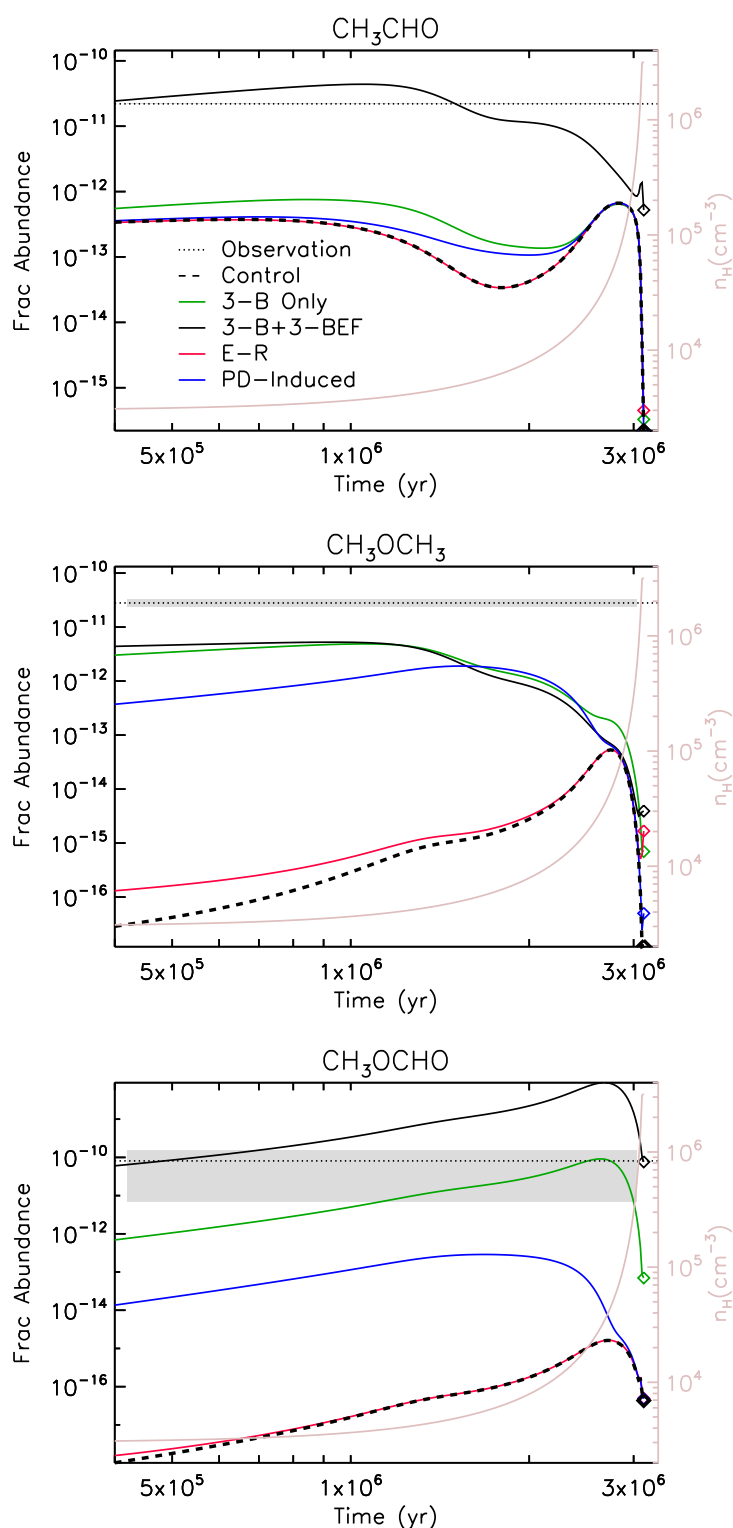


Figure 2.2: Time evolution of the gas-phase abundances of the three O-bearing COMs, at the core center, for models using each of the new mechanisms. The abundance from the control model is denoted as a black dashed line. Diamonds indicate the abundances at the end of each model run. The black dot-dash lines and the gray shaded regions indicate the observational abundances and their uncertainties, obtained from Jiménez-Serra et al. (2016) for L1544. The gas density is indicated by the right-hand vertical axis and the similarly colored line.

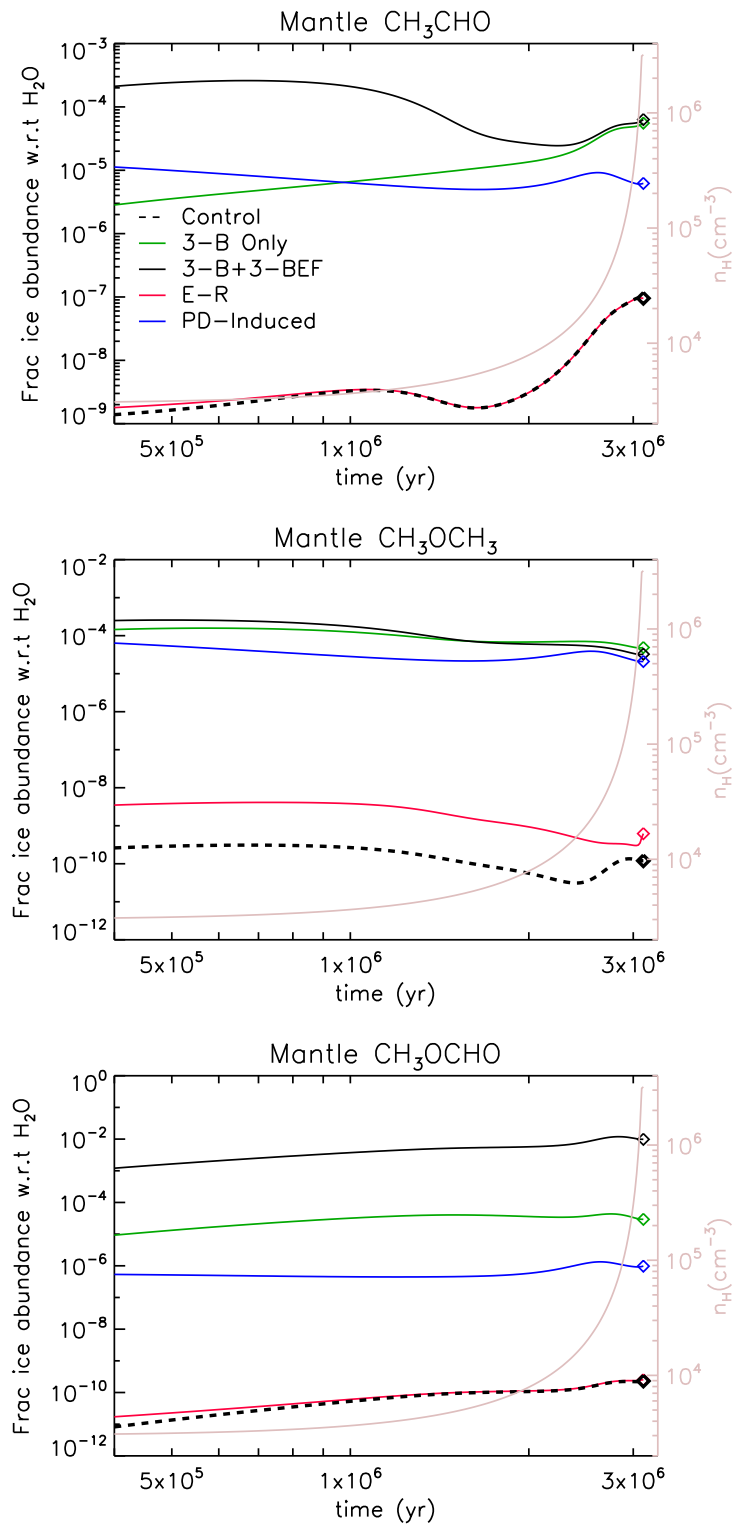


Figure 2.3: Time evolution of the abundances in the dust-grain ice mantles of the three O-bearing COMs at the core center, for models using each of the new mechanisms. The abundance from the control model is denoted as a black dashed line. Diamonds indicate the abundances at the end of each model run. The gas density is included for reference, indicated by the right-hand vertical axis and the similarly colored line.

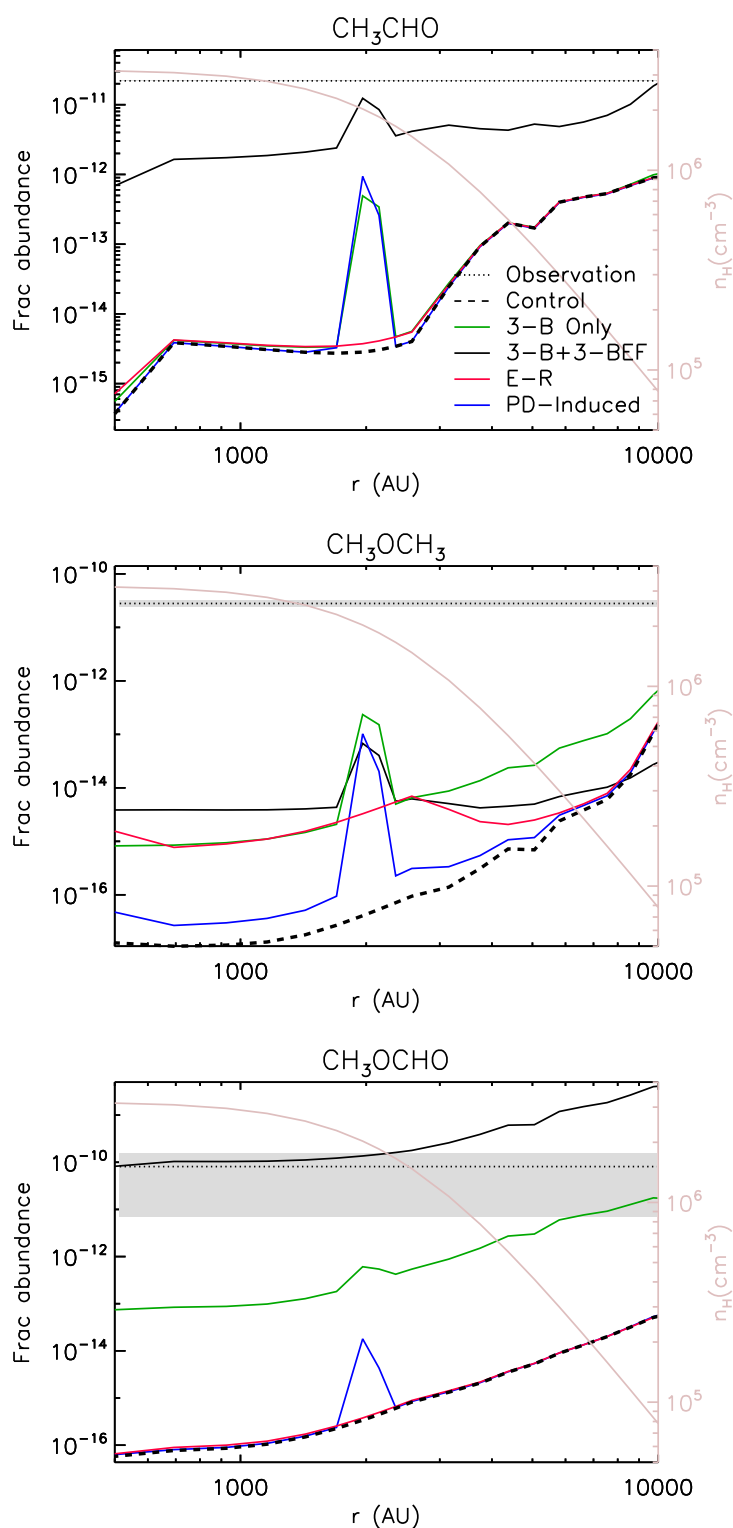


Figure 2.4: Radial distribution of the gas-phase abundances of the three O-bearing COMs depending on the mechanisms. The black dotted line and grey shaded region indicates the abundance from the observation and error, respectively. The observational data and its error is referred from the Jiménez-Serra et al. (2016). The observational error of the  $\text{CH}_3\text{CHO}$  is not provided in the reference. The abundance from the control model is denoted as a black dashed line and a black dotted line, respectively. While the result from the 3-B combined with the 3-BEF is denoted as a black solid line, a green line represent the 3-B only model. The red and blue solid line indicates the abundances from the E-R model and PD-Induced model, respectively.

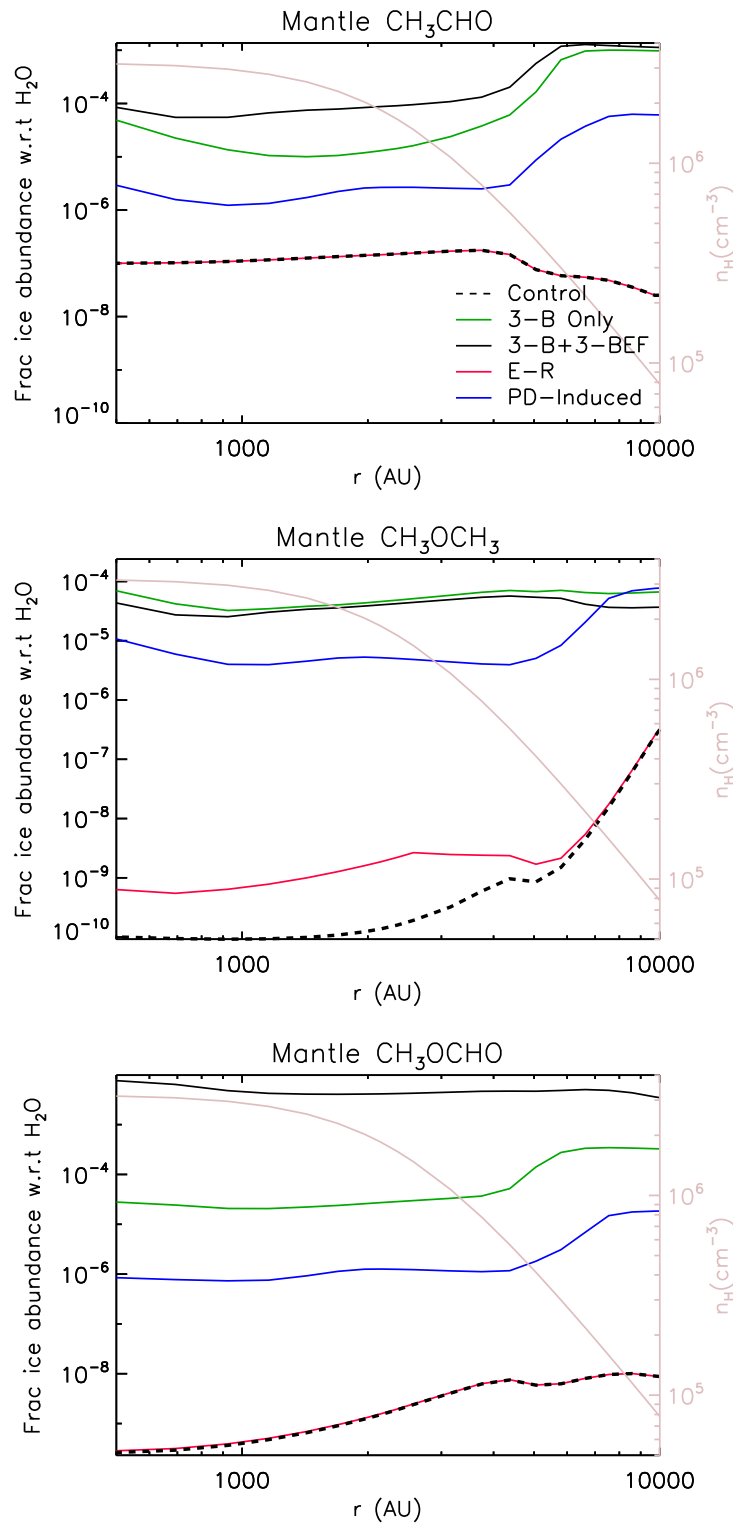


Figure 2.5: Radial distribution of the solid-phase abundances of the three O-bearing COMs depending on the mechanisms. The black dotted line and grey shaded region indicates the abundance from the observation and error, respectively. The observational data and its error is referred from the Jiménez-Serra et al. (2016). The observational error of the  $\text{CH}_3\text{CHO}$  is not provided in the reference. The abundance from the control model is denoted as a black dashed line and a black dotted line, respectively. While the result from the 3-B combined with the 3-BEF is denoted as a black solid line, a green line represent the 3-B only model. The red and blue solid line indicates the abundances from the E-R model and PD-Induced model, respectively.

end-time abundances, at which the final density profile is achieved. The observational values that are also indicated in the figure are for the core-center position; however, those observations correspond to a beam of radius  $\sim 1900$  AU, and would also sample a range of physical conditions along the line of sight – some caution should therefore be taken in directly comparing them with the local fractional abundance values.

It may be seen that the general trend, even for the control model, is for COM abundances to increase toward greater radii. The 3-B+3-BEF model produces maximum molecular abundances for acetaldehyde and methyl formate similar to the observational values. For the latter molecule, the modeled fractional abundance exceeds the observational values at radii greater than around 2500 AU, although the absolute gas density begins to fall off at these positions, so that they should contribute less to the total column density of the molecule. At the largest radii modeled, the 3-B (only) model produces methyl formate sufficient to match the observed abundance (although, again, perhaps with little contribution to total column density). Acetaldehyde also reaches its peak abundance at large radii, although it reaches a similar abundance at smaller radii.

For each of the new models, the local fractional abundance of  $\text{CH}_3\text{OCH}_3$  is greatest at positions away from the core center, but a significant increase in abundance is achieved at almost all positions for every model, versus the control. However, the maximum value achieved (for the 3-B model) is still at least two orders of magnitude lower than the observations, both in the inner regions and at the outer edge. Curiously, for dimethyl ether, the most effective model is the 3-B (only) model, whereas the 3-B+3-BEF model is the most productive for the other two COMs.

In each of the 3-B, 3-B+3-BEF and PD-Induced models, acetaldehyde and dimethyl ether abundances show a prominent peak feature at around 2000 AU. This feature is also present for methyl formate in the PD-Induced and 3-B (only) models. Observations of L1544 by Jiménez-Serra et al. (2016) show higher fractional abundances of  $\text{CH}_3\text{CHO}$  and  $\text{CH}_3\text{OCH}_3$  toward an off-center position at  $r \simeq 4000$  AU, versus those at the core-center, with  $\text{CH}_3\text{OCHO}$  arguably showing similar behavior. Our 3-B, 3-B+3-BEF and PD-Induced models all show this general behavior (methyl formate in the 3-B+3-BEF model notwithstanding), albeit at a somewhat different radius from the observations. The origin of this peak and its similarity to the observations are discussed in more detail in § 2.4.2.

Figure 2.5 shows the radial distribution of the ice-mantle abundances at the end-time of each model, plotted as a function of the water abundance in the ice at each position. In contrast with the gas-phase, all the new mechanisms but E-R significantly increase the solid-phase abundances of COMs at all radii. This is partly because the ice mantle preserves the earlier surface layers during the evolution of the prestellar core, when significant enhancement of the COM abundances in the gas-phase is found (see Fig. 2.2), which is itself caused by increased efficiency in the production of COMs on the grain surfaces. However, the PD-Induced model permits substantial ongoing processing of mantle material itself.

While COM production is not especially important in the control or E-R models, the others attain substantial COM abundances in the ices, comparable with gas-phase values observed in *hot* molecular cores. The maximum abundance achieved by methyl formate in the 3-B+3-BEF model is close to 1% of water abundance at the core center, i.e. around  $10^{-6}$  with respect to total hydrogen. This value may thus be *too* high to agree with observations of hot cores/corinos, if the abundances achieved in the prestellar stage

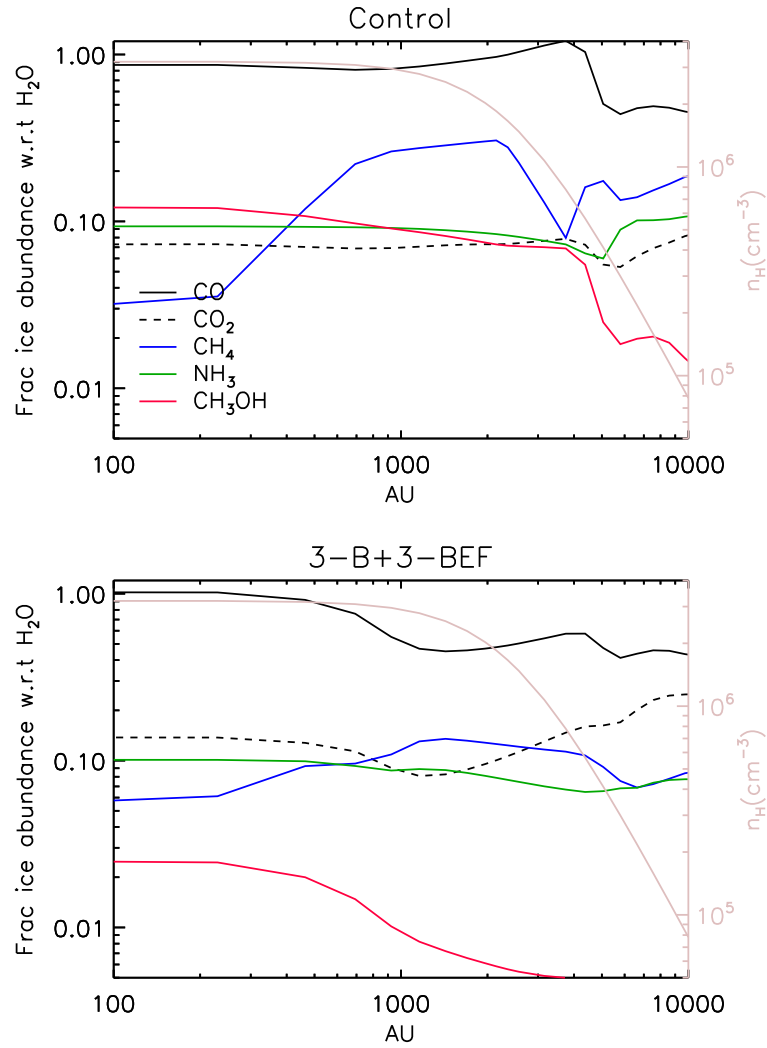


Figure 2.6: Radial distribution of the ice abundances of the main ice constituents. The abundance of CO and CO<sub>2</sub> is denoted as a black solid and a black dashed line, respectively. A blue, green, and red solid line represents the abundances of CH<sub>4</sub>, NH<sub>3</sub>, and CH<sub>3</sub>OH, respectively.

should be preserved intact to the later, warmer stages of evolution.

It is also noteworthy that the COM fraction in the ices is in general somewhat greater at larger radii, although the dimethyl ether abundance is fairly stable through the core in the 3-B and 3-B+3-BEF models, and methyl formate is also stable throughout in the 3-B+3-BEF model.

Figure 2.6 shows the final radial distribution of the main ice constituents as a fraction of the local water ice abundance, for the control model and for the 3-B+3-BEF model. The absolute abundance of profile of water ice is fairly constant across the profiles. The latter is taken as representative of all the new models, due to their similarity, except for the E-R model, which is rather similar to the control. Based on the absolute abundance profiles, column densities for each ice species are derived by integrating along the line of sight (without beam convolution); the resulting abundances with respect to H<sub>2</sub>O ice column density are summarized in Table 2.5. Comparable observational ice abundances are also shown, taken from Boogert et al. (2015), who provided median values with respect to H<sub>2</sub>O,

Model	CO	CO <sub>2</sub>	CH <sub>4</sub>	NH <sub>3</sub>	CH <sub>3</sub> OH
Observation <sup>a</sup>	0.21 <sup>0.85</sup> <sub>(&lt;0.03)</sub>	0.28 <sup>0.50</sup> <sub>0.12</sub>	0.05 <sup>0.11</sup> <sub>0.01</sub>	0.06 <sup>0.10</sup> <sub>0.03</sub>	0.06 <sup>0.25</sup> <sub>(&lt;0.01)</sub>
Control	0.83	0.07	0.19	0.09	0.07
3-B+3-BEF	0.57	0.12	0.11	0.08	0.01

Notes. <sup>a</sup> Boogert et al. (2015); values correspond to low-mass YSOs.

Table 2.5: Abundances relative to the H<sub>2</sub>O ice column density.

along with the full range of the observed abundances (from subscript to superscript value). Both of our model setups produce a centrally-peaked distribution of CH<sub>3</sub>OH ice, while CO ice is approximately as abundant as H<sub>2</sub>O ice, especially toward inner radii where the most extreme depletion occurs. With the new mechanisms, a more gently-sloped distribution appears, and a better match with observational abundances of CO and CO<sub>2</sub> is achieved. The other ice components in the 3-B+3-BEF model are within the observational range as well.

### 2.3.1 Column density analysis

Observational abundances may not accurately represent the true local abundances within a source. This is because the observational intensities are not only averaged over the line of sight, but are also affected by the excitation characteristics of each observed species, and by the response of the telescope beam. Considering this, it is indispensable to perform spectral simulations for better comparison with the observations. The spectral model used here simulates molecular lines (of COMs) that are expected to be observable, and uses chemical abundances shown in Fig. 2.4 as the underlying distribution. The 1-D chemical/physical model is treated as spherically symmetric, so that molecular emission can be simulated along lines of sight passing through the core at various offsets (including directly on-source), assuming local thermodynamic equilibrium. Each line of sight passes through a range of gas densities, temperatures and chemical abundances. The resulting 2-D simulated intensity maps for each frequency channel are then convolved with a Gaussian telescope beam of appropriate size, dependent on frequency and the telescope in question. (For a more detailed description of the spectral model, see Garrod, 2013). The FWHM of the molecular lines is assumed here to be 1 km/s, with a spectral resolution of 250 kHz, although the simulations are quite insensitive to the precise choice of parameters.

The integrated intensities of the ensemble of molecular lines is used in a rotational diagram analysis (Goldsmith & Langer, 1999) to obtain column densities ( $N_{\text{tot}}$ ) and rotational temperatures ( $T_{\text{rot}}$ ) for each molecule. These quantities can then be compared directly with those obtained from observations. Beam sizes were assumed to be  $\sim 28''$ - $31''$  between 79-87 GHz and  $\sim 24''$ - $26''$  between 94-103 GHz, based on the size of the observing beam of the IRAM 30 m telescope. The distance to the model prestellar core is assumed to be 140pc (Elias, 1978).

The radiative transfer and rotational diagram analysis is performed toward the on-source position, and toward two offset positions: (i) the peak of the COM abundances (2000 AU), and (ii) the low-density outer-shell (9000 AU). By considering these three

Molecule	Transition	Frequency (GHz)	$E_{\text{up}}$ (K)	$A_{ij}$ ( $\text{s}^{-1}$ )
A-CH <sub>3</sub> CHO	2 <sub>1,2</sub> -1 <sub>0,1</sub>	84.21976	4.96	$2.4 \times 10^{-6}$
E-CH <sub>3</sub> CHO	5 <sub>0,5</sub> -4 <sub>0,4</sub>	95.94744	13.9	$3.0 \times 10^{-5}$
A-CH <sub>3</sub> CHO	5 <sub>0,5</sub> -4 <sub>0,4</sub>	95.96346	13.8	$3.0 \times 10^{-5}$
E-CH <sub>3</sub> CHO	5 <sub>1,4</sub> -4 <sub>1,3</sub>	98.86331	16.6	$3.0 \times 10^{-5}$
*A-CH <sub>3</sub> CHO	5 <sub>1,4</sub> -4 <sub>1,3</sub>	98.90094	16.5	$3.0 \times 10^{-5}$
AA-CH <sub>3</sub> OCH <sub>3</sub>	3 <sub>2,1</sub> -3 <sub>1,2</sub>	84.63680	11.0	$4.4 \times 10^{-6}$
AA-CH <sub>3</sub> OCH <sub>3</sub>	2 <sub>2,0</sub> -2 <sub>1,1</sub>	86.22872	8.36	$3.5 \times 10^{-6}$
AA-CH <sub>3</sub> OCH <sub>3</sub>	2 <sub>2,1</sub> -2 <sub>1,2</sub>	89.70281	8.36	$3.8 \times 10^{-6}$
AA-CH <sub>3</sub> OCH <sub>3</sub>	6 <sub>0,6</sub> -5 <sub>1,5</sub>	90.93754	19.0	$5.7 \times 10^{-6}$
AA-CH <sub>3</sub> OCH <sub>3</sub>	3 <sub>2,2</sub> -3 <sub>1,3</sub>	91.47931	11.1	$4.9 \times 10^{-6}$
AA-CH <sub>3</sub> OCH <sub>3</sub>	4 <sub>2,3</sub> -4 <sub>1,4</sub>	93.85964	14.7	$5.6 \times 10^{-6}$
AA-CH <sub>3</sub> OCH <sub>3</sub>	5 <sub>2,4</sub> -5 <sub>1,5</sub>	96.85246	19.3	$6.2 \times 10^{-6}$
*AA-CH <sub>3</sub> OCH <sub>3</sub>	4 <sub>1,4</sub> -3 <sub>0,3</sub>	99.32600	10.2	$8.8 \times 10^{-6}$
A-CH <sub>3</sub> OCHO	7 <sub>2,6</sub> -6 <sub>2,5</sub>	84.45475	19.0	$8.0 \times 10^{-6}$
A-CH <sub>3</sub> OCHO	7 <sub>3,4</sub> -6 <sub>3,3</sub>	87.16129	22.6	$7.8 \times 10^{-6}$
A-CH <sub>3</sub> OCHO	8 <sub>1,8</sub> -7 <sub>1,7</sub>	89.31664	20.1	$1.0 \times 10^{-5}$
A-CH <sub>3</sub> OCHO	7 <sub>2,5</sub> -6 <sub>2,4</sub>	90.15647	19.7	$9.8 \times 10^{-6}$
A-CH <sub>3</sub> OCHO	9 <sub>1,9</sub> -8 <sub>1,8</sub>	100.0805	24.9	$1.5 \times 10^{-5}$
A-CH <sub>3</sub> OCHO	8 <sub>1,7</sub> -7 <sub>1,6</sub>	100.4907	22.8	$1.5 \times 10^{-5}$
A-CH <sub>3</sub> OCHO	9 <sub>0,9</sub> -8 <sub>0,8</sub>	100.6834	24.9	$1.5 \times 10^{-5}$
*A-CH <sub>3</sub> OCHO	8 <sub>2,6</sub> -7 <sub>2,5</sub>	103.4787	24.6	$1.5 \times 10^{-5}$

Notes. Acetaldehyde line data from JPL catalogue based on the data set of Bauder et al. (1976). Dimethyl ether line data from JPL catalogue based on the data set of Lovas et al. (1979); Neustock et al. (1990). Methyl formate line data from JPL catalogue based on the data set of Ilyushin et al. (2009); Plummer et al. (1984). The representative molecular transition used for the normalized convolved intensity analysis in § 2.3.4 is denoted with \*.

Table 2.6: List of targeted transitions with their spectroscopic properties

Model	CH <sub>3</sub> CHO (cm <sup>-2</sup> )	CH <sub>3</sub> OCH <sub>3</sub> (cm <sup>-2</sup> )	CH <sub>3</sub> OCHO (cm <sup>-2</sup> )
Observation <sup>a</sup>	1.2×10 <sup>12</sup>	1.5×10 <sup>12</sup> (4.0×10 <sup>11</sup> )	4.4×10 <sup>12</sup> (8.0×10 <sup>12</sup> )
Control	2.6×10 <sup>10</sup> (4.3×10 <sup>7</sup> )	1.2×10 <sup>10</sup> (1.9×10 <sup>7</sup> )	1.1×10 <sup>9</sup> (9.9×10 <sup>6</sup> )
3-B	3.8×10 <sup>10</sup> (1.1×10 <sup>8</sup> )	2.6×10 <sup>10</sup> (1.8×10 <sup>8</sup> )	4.7×10 <sup>11</sup> (4.4×10 <sup>9</sup> )
3-B+3-BEF	1.2×10 <sup>12</sup> (4.1×10 <sup>9</sup> )	2.6×10 <sup>9</sup> (7.0×10 <sup>7</sup> )	1.1×10 <sup>14</sup> (1.3×10 <sup>12</sup> )
E-R	2.7×10 <sup>10</sup> (4.5×10 <sup>7</sup> )	1.3×10 <sup>10</sup> (1.1×10 <sup>7</sup> )	1.1×10 <sup>9</sup> (9.8×10 <sup>6</sup> )
PD-Induced	4.0×10 <sup>10</sup> (1.2×10 <sup>8</sup> )	1.4×10 <sup>10</sup> (6.0×10 <sup>7</sup> )	1.3×10 <sup>9</sup> (9.6×10 <sup>6</sup> )

Notes. <sup>a</sup> Jiménez-Serra et al. (2016) ; Values in parentheses indicate observational or rotational diagram line-fitting (model) errors.

Table 2.7: The molecular column densities of the COMs at the core center

positions, we may compare the modeled COM peaks with the observational ones, and determine the dependence of the chemical reactions on the local physical conditions in the prestellar core.

One strategy to apply this radiative transfer and rotational diagram technique would be to simulate precisely the same molecular lines used in individual observational datasets for L1544. However, since the present aim is to determine a well-defined column density (and rotational temperature) based on the models, with which observed column densities may be directly compared, we instead choose a selection of lines that may plausibly be (or indeed have been) detected toward cold sources, and which include a range of upper energy levels. Emission lines of CH<sub>3</sub>CHO and CH<sub>3</sub>OCHO recently detected toward the cold dark cloud B5 (Taquet et al., 2017) are chosen for this analysis. While Taquet et al. (2017) detected a relatively large number of molecular lines for CH<sub>3</sub>CHO and CH<sub>3</sub>OCHO, only four transitions of CH<sub>3</sub>OCH<sub>3</sub> with a limited range of  $E_{\text{up}}$  (10–11 K) were detected by those authors. Our adoption of *only* those lines could therefore cause substantial uncertainty in the determination of  $N_{\text{tot}}(\text{CH}_3\text{OCH}_3)$ . For this reason, we choose eight bright (i.e. high  $A_{ij}$ ) AA-transitions of CH<sub>3</sub>OCH<sub>3</sub> with  $E_{\text{up}}$  ranging from 8–19 K, using the *Splatalogue* web tool <sup>1</sup>. The spectroscopic data originate from the JPL line list <sup>2</sup> (Bauder et al., 1976; Lovas et al., 1979; Neustock et al., 1990; Ilyushin et al., 2009; Plummer et al., 1984); the COM transitions considered in this analysis are listed in Table 2.6.

### 2.3.2 Column densities of O-bearing COMs toward the core center

Tables 2.7 – 2.9 (core center, 2000 AU, 9000 AU) compare the molecular column densities obtained from the RD analysis of different chemical models with observational values from the literature; observational errors and rotational diagram line-fitting error estimates are given in parentheses. Figure 2.7 shows the molecular column densities for each model at three different positions as histograms. The observed value (a solid horizontal line) and its error bounds (dashed horizontal lines) are presented together for comparison. While

<sup>1</sup><http://www.cv.nrao.edu/php/splat>

<sup>2</sup><https://spec.jpl.nasa.gov>

Model	CH <sub>3</sub> CHO (cm <sup>-2</sup> )	CH <sub>3</sub> OCH <sub>3</sub> (cm <sup>-2</sup> )	CH <sub>3</sub> OCHO (cm <sup>-2</sup> )
Observation <sup>a</sup>	3.2×10 <sup>12</sup>	7.7×10 <sup>11</sup> (3.2×10 <sup>11</sup> )	2.3×10 <sup>12</sup> (2.8×10 <sup>12</sup> )
Control	3.3×10 <sup>10</sup> (3.7×10 <sup>7</sup> )	2.8×10 <sup>10</sup> (3.6×10 <sup>7</sup> )	1.4×10 <sup>9</sup> (6.9×10 <sup>6</sup> )
3-B	3.6×10 <sup>10</sup> (4.2×10 <sup>7</sup> )	4.2×10 <sup>10</sup> (5.7×10 <sup>7</sup> )	5.3×10 <sup>11</sup> (2.1×10 <sup>9</sup> )
3-B+3-BEF	1.1×10 <sup>12</sup> (4.6×10 <sup>9</sup> )	1.8×10 <sup>9</sup> (1.2×10 <sup>7</sup> )	1.3×10 <sup>14</sup> (1.3×10 <sup>12</sup> )
E-R	3.3×10 <sup>10</sup> (3.9×10 <sup>7</sup> )	2.9×10 <sup>10</sup> (2.9×10 <sup>7</sup> )	1.4×10 <sup>9</sup> (6.8×10 <sup>6</sup> )
PD-Induced	3.3×10 <sup>10</sup> (3.7×10 <sup>7</sup> )	2.8×10 <sup>10</sup> (3.6×10 <sup>7</sup> )	1.5×10 <sup>9</sup> (7.3×10 <sup>6</sup> )

Notes. <sup>a</sup> Jiménez-Serra et al. (2016) ; The off-position for the observations is 4000 AU, corresponding to the observational methanol peak of L1544 (Jiménez-Serra et al., 2016). In the models, the fractional abundance peak occurs around 2000 AU. Values in parentheses indicate observational or rotational diagram line-fitting (model) errors.

Table 2.8: The molecular column densities of the COMs toward the off-center COM peak

Model	CH <sub>3</sub> CHO (cm <sup>-2</sup> )	CH <sub>3</sub> OCH <sub>3</sub> (cm <sup>-2</sup> )	CH <sub>3</sub> OCHO (cm <sup>-2</sup> )
Control	2.5×10 <sup>10</sup> (3.8×10 <sup>6</sup> )	3.9×10 <sup>10</sup> (8.8×10 <sup>7</sup> )	1.3×10 <sup>9</sup> (1.4×10 <sup>7</sup> )
3-B	3.0×10 <sup>10</sup> (3.1×10 <sup>6</sup> )	5.7×10 <sup>10</sup> (4.4×10 <sup>7</sup> )	3.7×10 <sup>11</sup> (3.5×10 <sup>9</sup> )
3-B+3-BEF	7.5×10 <sup>11</sup> (2.0×10 <sup>8</sup> )	1.5×10 <sup>9</sup> (2.2×10 <sup>5</sup> )	9.5×10 <sup>13</sup> (6.0×10 <sup>11</sup> )
E-R	2.6×10 <sup>10</sup> (3.8×10 <sup>6</sup> )	4.0×10 <sup>10</sup> (8.7×10 <sup>7</sup> )	1.3×10 <sup>9</sup> (1.4×10 <sup>7</sup> )
PD-Induced	2.5×10 <sup>10</sup> (3.7×10 <sup>6</sup> )	3.9×10 <sup>10</sup> (8.8×10 <sup>7</sup> )	1.5×10 <sup>9</sup> (1.5×10 <sup>7</sup> )

Notes. Values in parentheses indicate rotational diagram line-fitting errors.

Table 2.9: The molecular column densities of the COMs toward the outer-shell (radius 9000 AU)

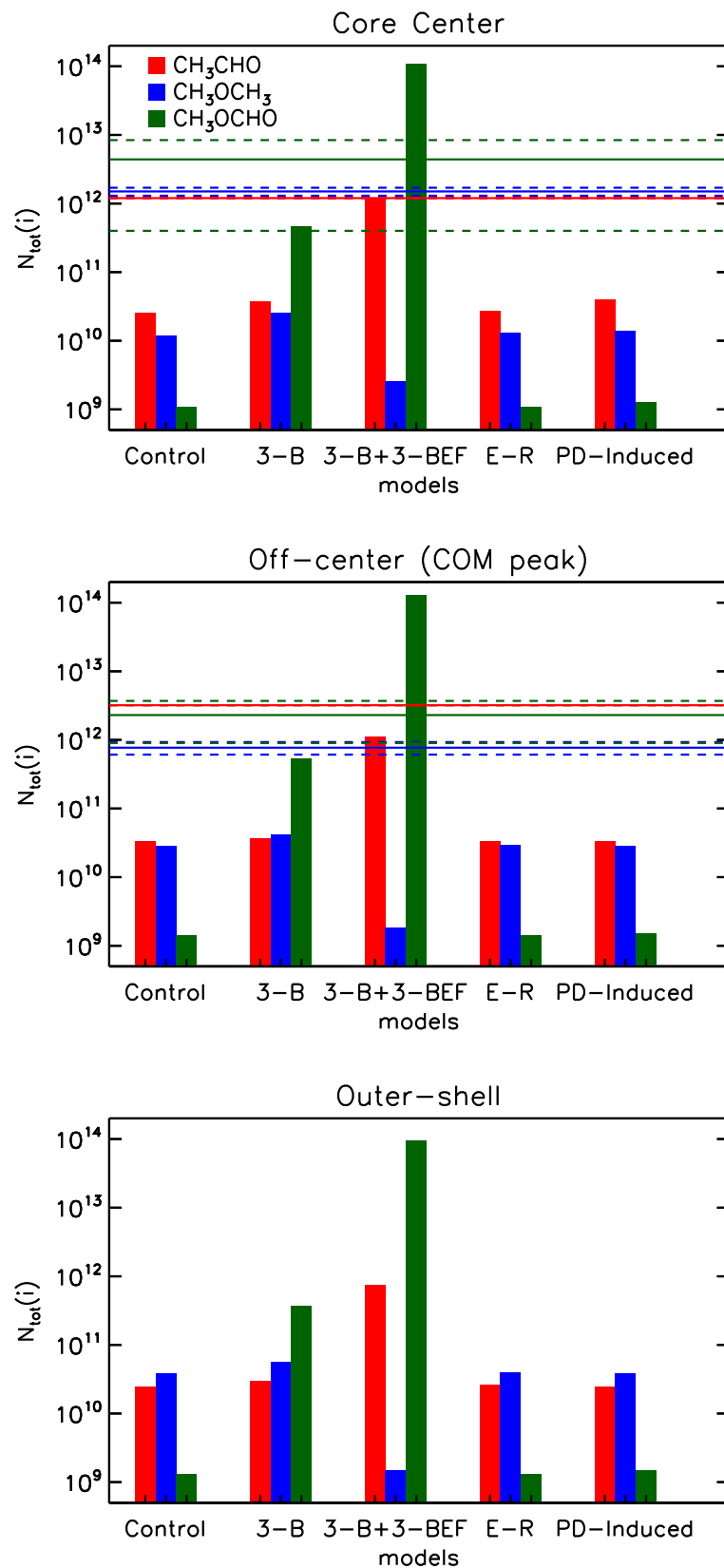


Figure 2.7: Column densities calculated from each model. Red, blue, and green histogram represents the molecular column densities of AA, DME, and MF, respectively. The errors of the modeled column densities are not presented here as those values are relatively small ( $< 3\%$ ) compared to the bar size. The observed value and its error bound are presented together with solid and dashed horizontal lines respectively. For the COM peak position (middle panel), the the observations was performed towards 4000 AU, corresponding to the observational methanol peak of L1544 (Jiménez-Serra et al., 2016), while the off-position for the model is 2000 AU, where fractional abundance peak occurs.

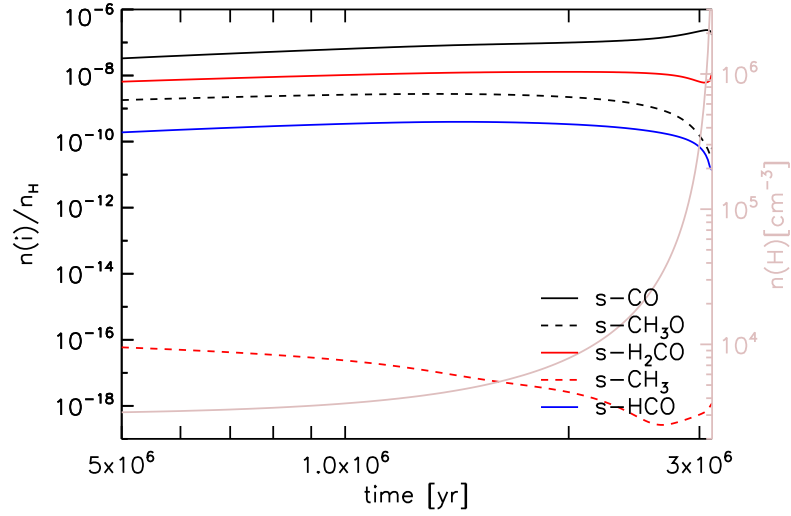


Figure 2.8: Time evolution of the fractional ice composition of the reactants on the grain-surface related to the 3-B+3-BEF mechanisms forming  $\text{CH}_3\text{OCH}_3$  (red lines) and  $\text{CH}_3\text{OCHO}$  (black lines). Note that the abundances shown refer specifically to species on the outer grain/ice surface and not within the ice mantles. A fractional abundance of  $\sim 1.3 \times 10^{-12}$  corresponds to one particle per grain.

every chemical model introduced here significantly underproduces  $\text{CH}_3\text{OCH}_3$ , both the 3-B and 3-B+3-BEF models result in meaningful differences from the control model for the other two COMs at the core center (Table 2.7). One thing to note is that the COMs are more actively formed via 3-BEF than solely by the 3-B mechanism. For example, while 3-B+3-BEF significantly increases the column density of  $\text{CH}_3\text{CHO}$  as well as  $\text{CH}_3\text{OCHO}$ , 3-B substantially increases  $\text{CH}_3\text{OCHO}$  only. Furthermore, even though both the 3-B and 3-B+3-BEF mechanisms enhance the  $\text{CH}_3\text{OCHO}$  population significantly, the increment is much higher in the 3-B+3-BEF model (3-B+3-BEF even substantially overproduces  $\text{CH}_3\text{OCHO}$  – see also § 2.3.3).

In either the 3-B or 3-BEF models, the key quantities through which the production rates of COMs (on the grains or in the gas phase) may be understood are the surface abundance of reactants, and the production (i.e. *appearance*) rates of their reaction partners. The latter quantity is an explicit component of the new expressions for nondiffusive processes, whereas in the regular L-H formulation it does not appear. The higher formation rates in the 3-BEF model can be explained by the fact that this mechanism involves the addition of radicals to stable compounds (which are thus more abundant on the grain surface) in the second step of the consecutive reaction chain (Eqs. 2.18-2.20), while the 3-B process involves the addition of sparse radicals (Eqs. 2.13, 2.15, and 2.17).

The greater rate of formation of  $\text{CH}_3\text{OCHO}$  over that of  $\text{CH}_3\text{CHO}$  in either the 3-B or 3-BEF model can also be understood in the same context. In the 3-B model, the reactants  $\text{CH}_3$  and  $\text{CH}_3\text{O}$  are technically competing with each other to form either  $\text{CH}_3\text{CHO}$  or  $\text{CH}_3\text{OCHO}$  by reacting with  $\text{HCO}$  radicals on the grain surface. As seen in Fig. 2.8, the fractional grain-surface abundance of  $\text{CH}_3\text{O}$  (shown for the core-center position) is much higher than that of  $\text{CH}_3$ . The production rate of  $\text{CH}_3\text{O}$  is also much greater than that of  $\text{CH}_3$ , which is partly why its surface abundance is higher. Similarly, in the 3-BEF model,  $\text{CH}_3^*$  and  $\text{CH}_3\text{O}^*$  are competing with each other to react with  $\text{CO}$  on the grain surface to

form either  $\text{CH}_3\text{CHO}$  or  $\text{CH}_3\text{OCHO}$ ; CO is abundant, and the appearance rates of  $\text{CH}_3^*$  and  $\text{CH}_3\text{O}^*$  directly determine the formation rates of  $\text{CH}_3\text{CHO}$  and  $\text{CH}_3\text{OCHO}$ .

Note that only a fraction of newly-formed methyl radicals can take part in the formation of the COMs through the 3-BEF mechanism, because only the excited methyl radicals formed via hydrogenation of  $\text{CH}_2$  have this mechanism available; abstraction of H from  $\text{CH}_4$  by other H atoms is slightly endothermic, so it should not produce  $\text{CH}_3^*$ .

Thus, the radical  $\text{CH}_3$  acts as a bottleneck to the formation of the COMs in the nondiffusive models. Also, the gradual depletion of C and related hydrocarbons from the gas phase, while CO remains abundant, means that production of  $\text{CH}_3$  cannot keep up with the production of CO-related radicals. The reaction of  $\text{CH}_3$  with H or  $\text{H}_2$  from the gas phase to re-form  $\text{CH}_4$  also keeps the average grain-surface  $\text{CH}_3$  abundance low. The production of HCO and  $\text{CH}_3\text{O}$  radicals continues to be effective as methanol builds up; while the net direction of the CO chemistry is to convert it gradually to methanol, there are backward reactions at every step, including H-abstraction from  $\text{CH}_3\text{OH}$ , that allow the intermediate radicals to maintain some level of surface coverage and a sustained rate of production/appearance.

Given that the formation of  $\text{CH}_3\text{OCH}_3$  is related to  $\text{CH}_3$  in both the 3-B or 3-BEF models, the lower column density of  $\text{CH}_3\text{OCH}_3$  in those models can be explained. CO and  $\text{H}_2\text{CO}$  are competing to form either  $\text{CH}_3\text{CHO}$  or  $\text{CH}_3\text{OCH}_3$  by reacting with the excited methyl radicals on the grain surface, but CO is much more abundant than  $\text{H}_2\text{CO}$  (Fig. 2.8). The small amount of excited methyl radicals on the surface are thus preferentially consumed to form  $\text{CH}_3\text{CHO}$ .

The E-R mechanism does not make a substantial difference to the gas-phase abundances versus the control (see Fig. 2.4 and Table 2.7). This is because the E-R process requires high surface coverage of the reactive species on the grains to be effective. This result is not exactly consistent with the results from Ruaud et al. (2015). They find that the combination of E-R and their complex-induced reaction mechanisms is efficient enough to reproduce the observed COM abundances at temperatures as low as 10 K. Beyond the uncertainty in the level of contribution of either mechanism, the different model parameters of both studies should be noted: Ruaud et al. (2015) mainly focus on the accretion of carbon atoms and assume a much higher binding energy (3600–8400 K) than ours (800 K). This may cause higher concentration of reactive species on the grain surface, allowing the E-R process to be efficient.

The PD-induced reaction process is ineffective in increasing the population of COMs in the gas phase at the core center. However, the PD-induced model significantly increases (more than 2 orders of magnitude) the amount of COMs in the ice mantles throughout the core's evolution (see figure 2.5). Other studies suggest indeed that the bulk ice is where the majority of physico-chemical changes caused by radiation chemistry are likely to occur (Johnson, 1990; Spinks & Woods, 1990; Shingledecker et al., 2017). The enhanced population of the COMs in the ice mantle does not actively affect the population in the gas phase, because the COM products are preserved in the mantle rather than diffusing to the grain-surface, which is directly coupled to the gas phase. Even though this process does not make a prominent difference in the gas-phase abundance for the prestellar core, it would significantly affect the chemistry during the warm-up period of a protostellar core in which accumulated mantle material is ejected from the grains.

### 2.3.3 Optimization of the 3-BEF model

As discussed in §2.3.2, the formation of methyl formate ( $\text{CH}_3\text{OCHO}$ ) through the 3-BEF mechanism is so efficient that  $\text{CH}_3\text{OCHO}$  is significantly overproduced, while this is not the case for acetaldehyde ( $\text{CH}_3\text{CHO}$ ). The 3-BEF mechanism as described in §2.2.5 is assumed to proceed with 100 % efficiency; however, the appropriate value in individual cases could be lower if the exothermic energy available from the initiating reaction ( $E_{\text{reac}}$ ) is similar in magnitude to the activation energy barrier ( $E_{\text{A}}$ ) of the subsequent reaction. Assuming the energy is initially released into the vibrational modes of the excited species, it may not be available in the required mode for reaction with an adjacent species to occur before that energy is lost to the surface, or indeed that the excited species diffuses away entirely from its reaction partner. If the excited product has  $s$  internal vibrational modes, the 3-BEF process would be expected to have substantially sub-optimal efficiency in the case where  $E_{\text{A}} > E_{\text{reac}}/s$ , while it would not occur at all in the case where  $E_{\text{A}} > E_{\text{reac}}$ . The former condition would appear to hold for the reactions shown in Eqs. (2.20), in which methyl formate is produced; here,  $s(\text{CH}_3\text{O})=9$ ,  $E_{\text{reac}} \simeq 10, 200$  K, and  $E_{\text{A}}=3,967$  K for the  $\text{CH}_3\text{O} + \text{CO} \rightarrow \text{CH}_3\text{OCO}$  reaction (Huynh & Violi, 2008).

Rice-Ramsperger-Kassel (RRK) theory may be introduced to obtain a statistical estimate of the efficiency. Using the same formulation that is employed to determine the probability of chemical desorption in the model (Garrod et al., 2007), the probability of a successful 3-BEF process would be:

$$P = \left[1 - \frac{E_{\text{A}}}{E_{\text{reac}}}\right]^{s-1} \quad (2.23)$$

where  $s$  now includes an additional vibrational mode representing the reaction coordinate (i.e.  $s(\text{CH}_3\text{O})=10$ ). For the reactions forming  $\text{CH}_3\text{OCHO}$ , the values provided above give a probability of 1.2%, while for the reactions producing  $\text{CH}_3\text{CHO}$  and  $\text{CH}_3\text{OCH}_3$  the probability would be 73%. This shows that the  $P(\text{CH}_3\text{OCHO})$  of 1 originally introduced in our 3-B+3-BEF model was too high, explaining the overproduction of that species.

For the present models, in which only three 3-BEF processes are explicitly considered, we empirically test a selection of efficiencies for the reaction to form  $\text{CH}_3\text{OCHO}$  ranging incrementally from 100% to 0.1% in factors of 10; the other two 3-BEF reactions are assumed to operate at maximum efficiency. It is found that a probability of 0.1% best reproduces the molecular column densities from the observations.

The empirically-determined optimal efficiency is clearly lower than the simple RRK treatment above would suggest. However, the latter does not include competition between reaction and diffusion of the excited species, which could account for at least a factor of a few, representing several diffusion directions. Likewise, additional translational degrees of freedom of the excited species could be considered in Eq. (2.23), rather than just one reaction coordinate. We note also that these modifications would reduce the efficiency of the other two 3-BEF reactions considered here, perhaps bringing them closer to around 10%. The molecular dynamics study by Fredon et al. (2017) of reaction-induced non-thermal diffusion would indeed suggest that translational motion would be a necessary factor to consider in a detailed treatment of the 3-BEF process (although it should be noted that those authors assumed all of the energy to be immediately released into translational modes, rather than distributed also into internal vibration and/or rotation).

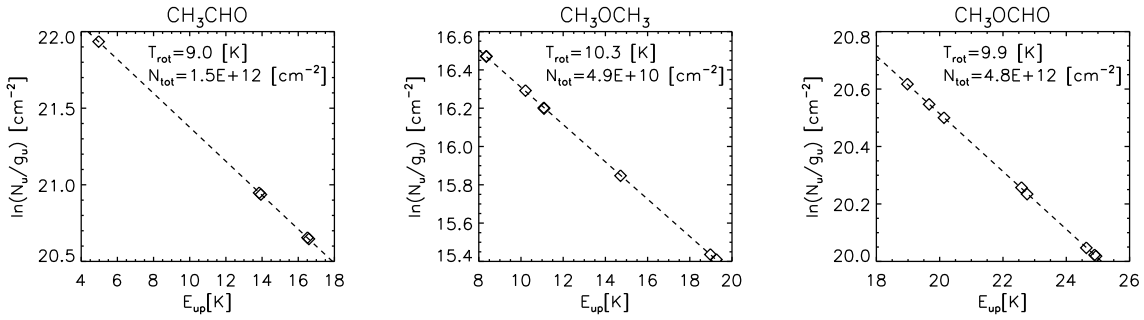


Figure 2.9: Rotation diagrams for the three O-bearing COMs at the core center. The black dashed lines represent the fit.

Species	CH <sub>3</sub> CHO (cm <sup>-2</sup> )	CH <sub>3</sub> OCH <sub>3</sub> (cm <sup>-2</sup> )	CH <sub>3</sub> OCHO (cm <sup>-2</sup> )
Observation <sup>a</sup> (Core Center)	$1.2 \times 10^{12}$	$1.5 \times 10^{12} (2.0 \times 10^{11})$	$4.4 \times 10^{12} (4.0 \times 10^{12})$
Core Center	$1.7 \times 10^{12} (5.7 \times 10^9)$	$3.4 \times 10^{10} (3.3 \times 10^8)$	$4.0 \times 10^{12} (2.7 \times 10^{10})$
2000 AU	$1.4 \times 10^{12} (5.4 \times 10^9)$	$4.8 \times 10^{10} (1.1 \times 10^8)$	$4.8 \times 10^{12} (1.1 \times 10^{10})$
9000 AU	$8.5 \times 10^{11} (3.3 \times 10^8)$	$5.7 \times 10^{10} (3.0 \times 10^7)$	$4.0 \times 10^{12} (3.8 \times 10^{10})$

Notes. <sup>a</sup> Jiménez-Serra et al. (2016); Values in parentheses indicate observational or rotational diagram line-fitting (model) errors.

Table 2.10: Column densities of COMs in the 3-BEF Best model

Figure 2.9 shows rotational diagrams obtained from LTE radiative transfer calculations based on the 3-BEF Best model molecular profiles, with the beam directed toward the core center. Table 2.10 compares the molecular column densities towards the core center from this model with the observational literature values. The errors (in parentheses) for modeled column densities are derived from the standard deviation of linear regression fitting in rotation diagrams. The three-body mechanisms introduced here are efficient enough to reproduce the amount of CH<sub>3</sub>OCHO and CH<sub>3</sub>CHO in the prestellar core when an appropriate efficiency for the 3-BEF mechanism is adopted.

Figure 2.10 compares the chemical distribution of the 3-BEF Best results (solid lines) with those of the control (dotted lines) and the normal 3-BEF (dashed lines) models. While the amount of CH<sub>3</sub>OCHO is significantly reduced in the 3-BEF Best model compared to the normal 3-BEF in both gas- and solid-phase, the population of CH<sub>3</sub>OCH<sub>3</sub> increases (by roughly an order of magnitude in the gas); the weakening of the 3-BEF mechanism for methyl formate production leaves more of the CH<sub>3</sub>O radical available to participate in other reactions, including the regular 3-B mechanism (CH<sub>3</sub> + CH<sub>3</sub>O) that produces dimethyl ether. A commensurate increase is seen in the column density values.

The adjustment to the efficiency of MF production through the 3-BEF process also reduces the solid-phase abundance of that molecule with respect to water back to more plausible values that are in line with the maximum typical values observed in hotter sources (i.e. around  $10^{-8}$  with respect to H<sub>2</sub>). The fraction is higher beyond around 5,000 AU, but the total ice abundance at these positions would also be somewhat lower.

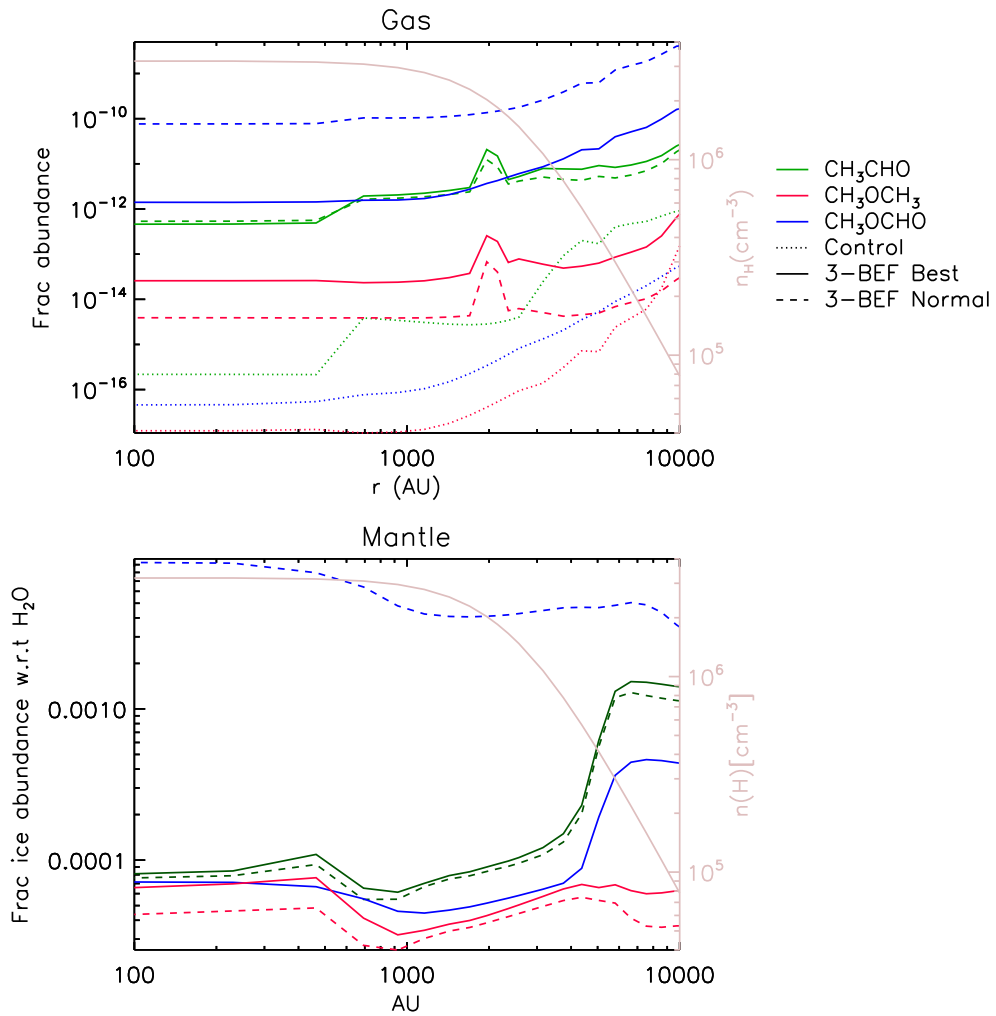


Figure 2.10: Comparison of chemical distribution of the 3-BEF Best (solid lines) in the gas with those of the normal 3-B+3-BEF (dashed lines). Control model results are also shown (dotted lines).

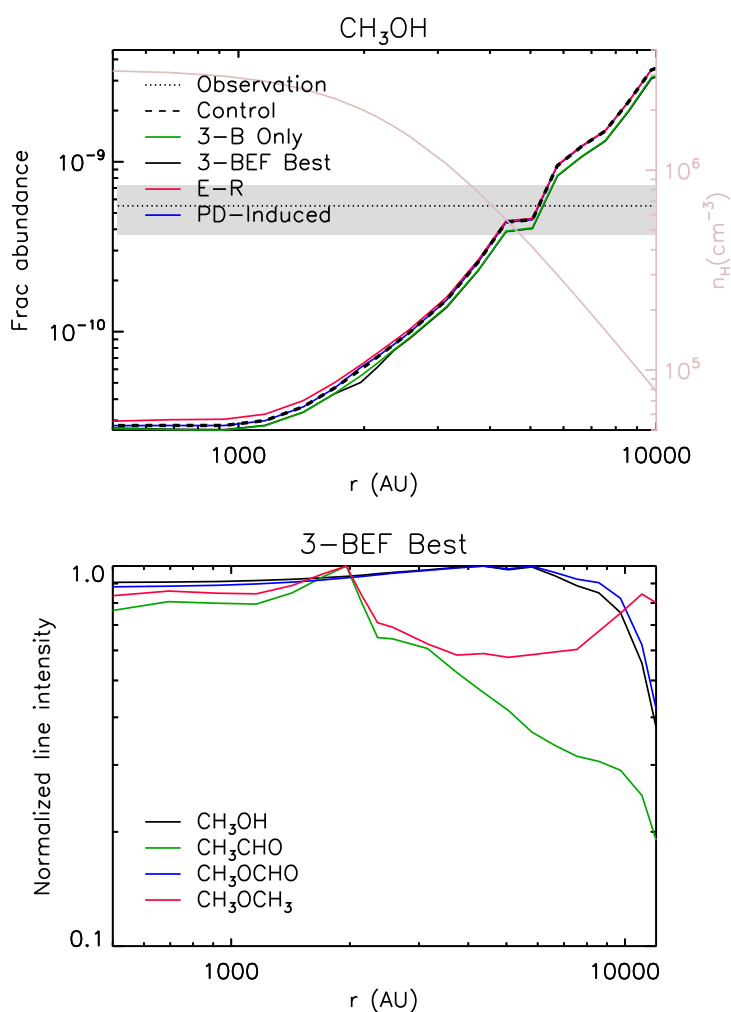


Figure 2.11: (a) Radial distribution of fractional abundance of  $\text{CH}_3\text{OH}$  for each model. The abundance value from the observations toward the core center is denoted a black dotted line. Gas density as a function of radius is also indicated. (b) The normalized, convolved intensity of a representative emission line for methanol and for each of the three COMs of interest, shown as a function of the offset of the beam from the on-source position.

### 2.3.4 CO hydrogenation and $\text{CH}_3\text{OH}$ abundances

The  $\text{CH}_3\text{OH}$  map of Bizzocchi et al. (2014) shows a highly asymmetric non-uniform ring surrounding the dust peak of L1544. This morphology is consistent with central depletion and preferential release of methanol in the region where CO starts to freeze out significantly. Jiménez-Serra et al. (2016) shows that COMs are actively formed and already present in this methanol peak.

The upper panel of Fig. 2.11 shows the radial distribution of  $\text{CH}_3\text{OH}$  fractional abundance for each of the chemical models; abundances are very similar for all models at all positions. Methanol in the gas is mainly formed as the result of the hydrogenation of grain-surface CO all the way to  $\text{CH}_3\text{OH}$ , followed by chemical desorption. The radial distribution of the *fractional abundance* of gas-phase methanol has its peak well beyond where the observations would suggest. However, it should be noted that the gas density

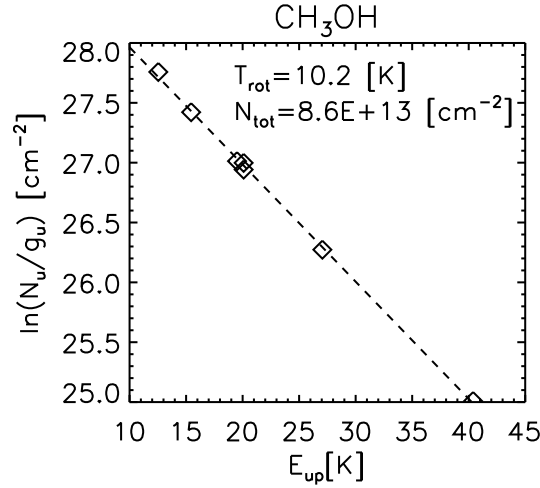


Figure 2.12: The rotation diagram for CH<sub>3</sub>OH. The black dashed lines represent the fit.

Molecule	Transition	Frequency (GHz)	$E_{\text{up}}$ (K)	$A_{ij}$ (s <sup>-1</sup> )
E-CH <sub>3</sub> OH	5 <sub>-1</sub> -4 <sub>0</sub>	84.52117	40.4	$2.0 \times 10^{-6}$
E-CH <sub>3</sub> OH	2 <sub>-1</sub> -1 <sub>-1</sub>	96.73936	12.5	$2.6 \times 10^{-6}$
E-CH <sub>3</sub> OH	2 <sub>0</sub> -1 <sub>0</sub>	96.74455	20.1	$3.4 \times 10^{-6}$
E-CH <sub>3</sub> OH	3 <sub>0</sub> -2 <sub>0</sub>	145.09375	27.1	$1.2 \times 10^{-5}$
E-CH <sub>3</sub> OH	3 <sub>-1</sub> -2 <sub>-1</sub>	145.09744	19.5	$1.1 \times 10^{-5}$
E-CH <sub>3</sub> OH	1 <sub>0</sub> -1 <sub>-1</sub>	157.27083	15.4	$2.2 \times 10^{-5}$
*E-CH <sub>3</sub> OH	2 <sub>0</sub> -2 <sub>-1</sub>	157.27602	20.1	$2.2 \times 10^{-5}$

Notes. Methanol line data from JPL catalogue based on the data set of Xu et al. (2008). The representative molecular transition used for the normalized convolved intensity analysis in § 2.3.4 is denoted with \*.

Table 2.11: List of methanol transitions with their spectroscopic properties

in these more distant regions drops off significantly, according to the physical profile. The location of the peak in *absolute* abundance would provide a better comparison directly with observations, although the best method is to consider the column density structure of methanol explicitly.

The lower panel of Fig. 2.11 shows the normalized convolved intensity of a representative emission line of methanol, as a function of the beam offset from the center, using the radiative transfer model already described with the 3-BEF Best model data. Since the lines are optically thin and are well represented by an LTE treatment (see Fig. 2.12 and Table 2.11), the line intensity profile scales well with the column density profile along each line of sight. The modeled methanol emission shows a peak near to 4000 AU as reported in the observations, even though this feature is not so obvious, as the slope is quite gentle. The same treatment is shown for the other three COMs of interest. Methyl formate shows a fairly similar distribution of emission to that of methanol, while the other two COMs show peaks at 2000 AU as seen in the fractional abundances. The representative molecular transition used for this analysis is denoted with an asterisk in Tables 2.6 and 2.11.

The full RD analysis is performed for methanol as for the other COMs. The seven E-transition lines of  $\text{CH}_3\text{OH}$  that were detected by Taquet et al. (2017) are chosen for this (Table 2.11). A single fit to all lines provides a column density  $8.6 \times 10^{13} \text{ cm}^{-2}$  at the core center. This value is roughly consistent with the observation ( $2.6 \times 10^{13} \text{ cm}^{-2}$ , Bizzocchi et al., 2014). The precise value, as with those of the other COMs, will be dependent on the fidelity of the chemical desorption treatment used here.

## 2.4 discussion

Of the several new nondiffusive processes tested here, the Eley-Rideal mechanism appears to have the least effect, due largely to the low surface coverage of reactive species. Those reactive species that might benefit from the spontaneous arrival of a reaction partner from the gas phase always maintain low fractional surface coverage due to their reactivity with highly diffusive surface species e.g. atomic H. Species that do build up a large surface coverage, like CO, tend to have large barriers to reaction, so that incoming species are more likely to diffuse away than to react spontaneously. The importance of the E-R process to typical surface reactions is unlikely to be substantial under any physical conditions as long as atomic H remains mobile.

Photodissociation-induced reactions, in which the PD process acts spontaneously to bring a reactive radical into contact with some other species, has no significant influence on the gas-phase abundances of complex organics, but has a strong effect on the COM content of the ice mantles. The basic three-body process provides substantial improvement in the gas-phase abundances of COMs, notably methyl formate and dimethyl ether, by allowing the products of diffusive reactions (in some fraction of cases) to find a reaction partner themselves without requiring further diffusion. However, the excited formation mechanism, which allows the reaction of excited, newly-formed radicals with stable species (in spite of activation energy barriers) has the strongest effect, and is again most important for methyl formate and acetaldehyde. An adjustment to the efficiency of these processes, based on the available energy from the initiating reaction, appears to provide the best match with observational column densities of those molecules.

It is important that the process that seems to reproduce most effectively the gas-phase abundances of the COMs (3-BEF) is one that occurs on the grain/ice surface itself, rather than deep within the mantle, allowing chemical desorption to return some fraction of the product to the gas phase. The details of the various mechanisms and their implications are discussed in more detail below.

### 2.4.1 H-abstraction/recombination as an amplifier of chemical desorption

The models show substantial success in reproducing observed gas-phase column densities, through molecular production mechanisms operating on the surfaces of the icy dust grains. Consideration should therefore be given to the efficiency of the desorption mechanism that

Species	All on	CH <sub>3</sub> OH + H	CH <sub>3</sub> CHO + H	CH <sub>3</sub> OCHO + H	CH <sub>3</sub> OCH <sub>3</sub> + H
CH <sub>3</sub> OH	$2.9 \times 10^{-11}$	$5.4 \times 10^{-12}$	$2.9 \times 10^{-11}$	$2.8 \times 10^{-11}$	$2.9 \times 10^{-11}$
CH <sub>3</sub> CHO	$4.5 \times 10^{-13}$	$4.5 \times 10^{-13}$	$3.8 \times 10^{-14}$	$4.5 \times 10^{-13}$	$4.5 \times 10^{-13}$
CH <sub>3</sub> OCHO	$1.4 \times 10^{-12}$	$5.5 \times 10^{-13}$	$1.4 \times 10^{-12}$	$7.2 \times 10^{-14}$	$1.4 \times 10^{-12}$
CH <sub>3</sub> OCH <sub>3</sub>	$2.6 \times 10^{-14}$	$8.4 \times 10^{-15}$	$2.6 \times 10^{-14}$	$2.6 \times 10^{-14}$	$1.4 \times 10^{-15}$

Table 2.12: Local fractional abundances of COMs at the core center when the H-abstraction reaction listed is *switched off* in the 3-BEF Best.

releases surface molecules into the gas phase. Although photo-desorption is included in all of the models presented here (with the explicit assumption of fragmentation of methanol as the result of this process), the most important ejection mechanism for grain-surface COMs is chemical desorption. In these models, this occurs with a *maximum* efficiency per reaction of 1%; this efficiency is further lowered according to the RRK-based treatment described by Garrod et al. (2007).

Thus the formation of, for example, acetaldehyde, through Eqs. 2.18, culminating in the addition of an H-atom to the CH<sub>3</sub>CO radical, may sometimes produce gas-phase CH<sub>3</sub>CHO. However, the immediate desorption following its formation is not the only factor in ejecting those molecules into the gas. The chemical desorption effect is considerably amplified by the *abstraction* of H atoms from existing surface COMs, followed rapidly by recombination of the resulting radical with another H atom, inducing the ejection into the gas of some fraction of the product molecules. In the case of methanol, for instance, once it is formed on the grain surface through the repetitive addition of H to CO, the abstraction of H from CH<sub>3</sub>OH by another H-atom allows it to be transformed back to its precursor (CH<sub>3</sub>O/CH<sub>2</sub>OH), providing additional chances for chemical desorption – indeed, this process of addition and abstraction was suggested by Minissale et al. (2016) as a mechanism by which the depletion of CO from the gas phase could be slowed and its grain-surface conversion to methanol delayed. Similar H-abstraction/addition processes are present for each of the larger COMs of interest in our models.

To understand how significantly this process takes part in the overall chemical desorption scheme, four additional test models were run for conditions appropriate to the core center, turning off the H-abstraction reaction for each molecule (the three larger COMs plus methanol). The local fractional abundances of COMs from each test model are compared with the control in Table 2.12. When the H-abstraction reaction of a specific COM is turned off, the gas-phase abundance of that molecule decreases by  $\sim 1$  order of magnitude. Furthermore, when H abstraction from methanol is switched off, it reduces the fractional abundance of other COMs such as CH<sub>3</sub>OCHO and CH<sub>3</sub>OCH<sub>3</sub>, whose surface production is closely related to the CH<sub>3</sub>O radical. The abstraction of H from methanol by other H atoms in fact strongly favors the production of the CH<sub>2</sub>OH radical; the network employed here uses surface reaction rates for these processes calculated by F. Goumans and S. Andersson (see Garrod, 2013) based on harmonic quantum transition state theory. However, as per the network of Garrod (2013), the recombination of CH<sub>2</sub>OH with H is assumed to produce either methanol or H<sub>2</sub>CO+H<sub>2</sub> with a branching ratio of 1:1. The production of formaldehyde in this way can then lead to reaction with H atoms again; this forward process strongly favors production of the CH<sub>3</sub>O radical, thus influencing the production of DME and MF.

## 2.4.2 COM distribution and COM peaks

As seen in Fig. 2.10 for the 3-BEF Best model, the COMs in the gas phase have their lowest fractional abundances at the core center, gradually increasing toward the outer shell of the prestellar core. This general feature is observed regardless of model type (Fig. 2.4). Interestingly, a local fractional abundance peak for COMs is found at around 2000 AU, especially for  $\text{CH}_3\text{CHO}$  and  $\text{CH}_3\text{OCH}_3$ . This result suggests at least qualitative agreement with the observational result of Jiménez-Serra et al. (2016); those authors performed deep observations of the COMs toward the low-density outer shell (4000 AU) as well as the core center of L1544. While they observed higher abundances for all three COMs at the outer position, the level of enhancement for  $\text{CH}_3\text{OCHO}$  was ambiguous, due to its large observational error.

The behavior seen in the models indicates that there are *two* possible peak features (or two plausible causes for observed peaks) that could become apparent in column densities or line intensities (e.g. lower panel of Fig. 2.11) as opposed to fractional abundances. The first of these relates simply to the increased fractional abundances of COMs at large radii, combined with the drop-off in overall gas density at the greatest extents, producing a peak in the *absolute* molecular abundances that manifests in the resulting column density or line intensity profiles. This behavior is especially apparent for methyl formate (which does not show the bump-like feature at around 2000 AU). This peak seems to be in reasonably good agreement with the observational peak position; Fig. 2.11 indicates peak line intensities around 4000–6000 AU. A major cause of the lack of COMs in the gas phase at small radii (in terms of fractional abundance, e.g. Fig. 2.10) is that most of the gas-phase material at those locations has already accreted onto the grains and become locked into the ice mantles by the end-time of the models; little CO exists in the gas phase (on the order  $10^{-7}$  with respect to total H), thus grain-surface chemistry involving CO-related products is limited. At the greatest radii, freeze-out is incomplete and CO chemistry is still active with the accretion of new CO. Somewhat greater gas-phase abundances of atomic H at large radii, caused by the density slope, also encourage H-abstraction from COMs on the surfaces, followed by recombination and chemical desorption.

The local peak at 2000 AU in the fractional abundances of acetaldehyde and dimethyl ether occurs particularly in models that use the 3-B and 3-BEF processes, and manifests also in the resultant column density profiles of those molecules (lower panel of Fig. 2.11). The gas density at the 2000 AU position is at least three times higher than at the outer-peak region (4000–6000 AU), so the inner peak tends to dominate over the outer in its contribution to column densities, for the models/molecules in which that inner peak occurs.

What is the origin of the inner peak at 2000 AU? It is related to the freeze-out of gas-phase material through the core. It traces a position at which the net rate of accretion of gas-phase material onto the grains is close to zero, caused by the high degree of depletion that has already occurred for most major gas-phase species other than hydrogen. For example, the gas-phase abundance of CO reaches a local minimum at this position. At radii internal and external to the 2000 AU peak region, there is slightly more gas-phase material remaining to be accreted onto dust grains at the end of the model runs, thus the ice mantles still continue (slowly) to grow. This local peak in freeze-out is due to the combined density and temperature profiles used in the models. The adsorption rates of neutrals scale with gas density, which is greatest at the core center, but they also scale

with the square root of the gas temperature, which is greater at larger radii. The 2000 AU position is the point where the two profiles combine to give the largest total adsorption rate. The position of the maximum freeze-out position is thus strongly dependent on the density and temperature profiles. Furthermore, given a slightly longer model run time, the freeze-out peak would likely widen, as other positions reached a state of near-zero net accretion onto grains.

The stronger production of COMs (acetaldehyde and dimethyl ether) around this 2000 AU position peak is a consequence of the changing freeze-out conditions described above. Once the net rate of freeze-out reaches zero, it indeed undergoes a reversal in which there is a small, net rate of *loss* of material from the grains. This loss is caused by the desorption of molecular hydrogen from the grain surface, which is slowly replenished by the gradual outward diffusion of H<sub>2</sub> molecules embedded deep in the ice mantles. This H<sub>2</sub>-loss process occurs throughout all the model runs, but is of little importance until the adsorption of non-volatile species diminishes, when gas-phase species become depleted. Once this net loss of material from the grains starts to occur, some molecules embedded in the upper layer of the ice mantles are “uncovered”, becoming available for surface chemical processing. Most importantly, this includes CH<sub>4</sub>, from which an H-atom may be chemically abstracted through several mechanisms, increasing both the production rate of CH<sub>3</sub> and its surface abundance. This drives up the three-body production of acetaldehyde and dimethyl ether (Eqs. 2.12–2.15), which are chemically desorbed into the gas phase – either directly, or as the result of H-abstraction and recombination on the surface.

The behavior of the inner peak in certain COMs should therefore be treated with a degree of skepticism. Not only does its position depend on the interplay of the observationally-determined physical profiles, but its strength must be time-dependent. Furthermore, the ability of the chemical model to treat accurately the return (“uncovering”) of mantle material to the ice surface is limited by the use of only a single mantle phase, rather than the consideration of distinct layers within the ice (cf. Taquet et al., 2014). If most of the methane residing in the mantles is present mainly in the deepest layers, the inner-peak effect described above would be overestimated here. It is also the case that, even with this mechanism in play, the gas-phase abundance of dimethyl ether is insufficient to reproduce observed column densities in L1544 (although see § 4.6). If such a mechanism is active, considering the uncertainty in its precise position (based on models), it may not be easily distinguished from the outer peak at 4000+ AU.

The peak in methanol column density occurs at the outer peak position, caused again by a peak in *absolute* abundance of that molecule. It is noteworthy that in the present models, the local fractional abundance of methanol does not need to exceed a value of a few 10<sup>-9</sup> to be able to reproduce the observed column density. Again, the strength of the methanol peak will be dependent on the efficiency of chemical desorption for that molecule, which is not well constrained through purely experimental means.

### 2.4.3 The effect of diffusion barriers

In many astrochemical models including *MAGICKAL*, chemistry on the grains is governed by the diffusion of surface species via thermal hopping (any nondiffusive processes notwithstanding). The energy required for a particular species to hop from one surface

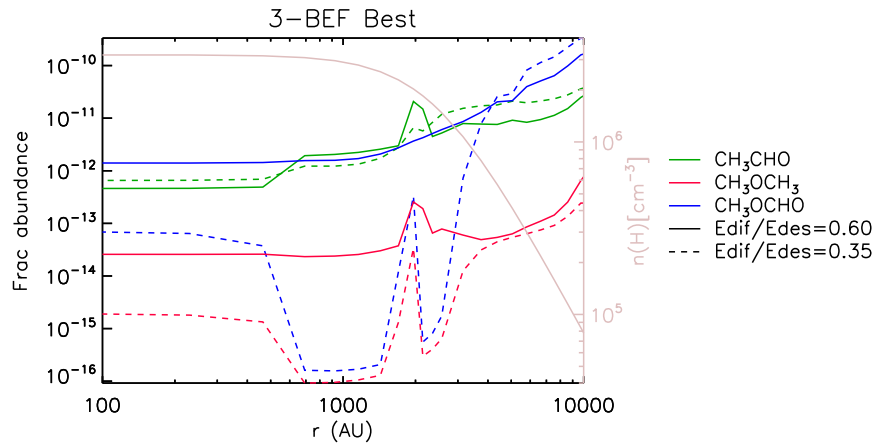


Figure 2.13: Comparison of chemical distribution of the COMs in the 3-BEF Best models with different values of  $E_{\text{dif}}:E_{\text{des}}$  for atoms.

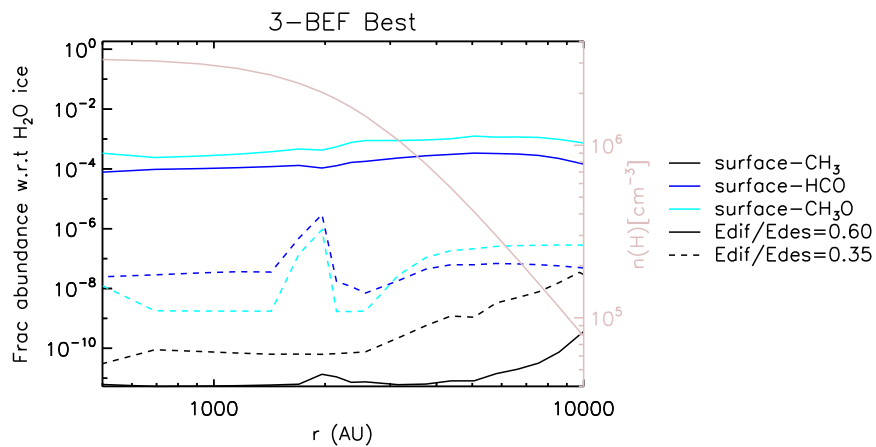


Figure 2.14: Comparison of chemical distribution of the reactants in the 3-BEF Best models with different values of  $E_{\text{dif}}:E_{\text{des}}$  for atoms.

binding site to another is given by the diffusion barrier  $E_{\text{dif}}$ ; this value is parameterized in the chemical model as some fraction of the desorption energy, i.e.  $E_{\text{dif}}/E_{\text{des}}$ . Even though this is a key parameter to describe the mobility of species on grain surfaces, the exact value has not historically been well constrained, broadly ranging from 0.3 to 0.8. In the present models, this parameter was set to  $E_{\text{dif}}/E_{\text{des}}=0.6$  for all atomic species, which leans toward a high value based on recent experimental estimates by Minissale et al. (2016), who suggested 0.55 for atoms. In our past models (e.g. Garrod 2013), atoms and molecules were assigned the same fractional barrier value of 0.35, based on the optimum value for CO. All *molecular* species in the present models retain the 0.35 value.

At the very low surface temperatures that are found in prestellar cores, the diffusion of atoms in particular is of great importance. For this reason, test models were also run using the previous fractional diffusion barrier of 0.35 for atoms. Figure 2.13 shows a comparison of COM abundances for the two cases, shown for the end-time of the 3-BEF Best model run using the L1544 physical profiles as before. Using the higher  $E_{\text{dif}}/E_{\text{des}}$  ratio, the COMs typically show much higher abundances at positions near the core center. This result is somewhat contradictory to the expectations of Vasyunin et al. (2017), who suggest that the  $E_{\text{dif}}/E_{\text{des}}$  ratio would not play a crucial role in cold environments, as diffusion of H and H<sub>2</sub> via tunneling is dominant. In our model, while tunneling through chemical barriers is included, surface diffusion via tunneling is not, as the barriers are assumed to be too broad for tunneling to be effective. In this case, the higher diffusion barrier for the atomic species means that the time taken for H atoms to reach and react with surface radicals is increased. This consequently raises the lifetimes of those radicals on the surface (see Fig. 2.14), which in turn renders the non-thermal mechanisms explored here more effective, increasing the production of COMs.

It should be noted that the higher  $E_{\text{dif}}/E_{\text{des}}$  ratio does not always result in a larger amount of COMs (or radicals) on the grain surface. For example, the discrepancy in the COM abundances between the two models decreases at large radii, and methyl formate and acetaldehyde here are even a little more abundant in the case where atomic diffusion barriers are lower, due to slightly more effective H-abstraction from methane to produce CH<sub>3</sub>.

The variation of the  $E_{\text{dif}}/E_{\text{des}}$  ratios thus has an important effect on the chemical model results; the higher value for atomic species, and for H in particular, reproduces COM abundances more effectively, through the increase in radical lifetimes. Senevirathne et al. (2017) calculated the distribution of binding energies and diffusion barriers for H on an amorphous water surface, suggesting representative values for each; although their H binding energy (661 K) is higher than the value used in our models (450 K), their diffusion barrier (243 K) is close to the value we use here (270 K) for the  $E_{\text{dif}}/E_{\text{des}}=0.6$  models. We note also that Senevirathne et al. (2017), based on their calculations of diffusion rates using quantum transition-state theory, aver that tunneling (as opposed to the thermal mechanism) is likely of limited importance under most temperature conditions in dark clouds; our use of purely thermal diffusion rates in *MAGICKAL* is thus broadly consistent with that work.

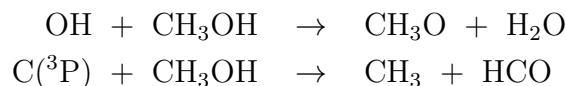
In other models, in which nondiffusive chemical processes were *not* included, the variation of the H diffusion barrier might have less of an effect, as most of the active chemistry in that case would involve *only* atomic H. The lifetime of the radicals would therefore be of less relevance, since H would still be the dominant reaction partner. In the present models, the mobility of atomic hydrogen is a major determinant of the effectiveness of

non-thermal processes in producing complex species.

## 2.4.4 Gas-phase processes

Due perhaps to the generally low abundances of DME that our chemical models provide, they do not appear to reproduce the correlation between  $\text{CH}_3\text{OCHO}$  and  $\text{CH}_3\text{OCH}_3$  sometimes observed in various evolutionary stages of star-forming regions (Jørgensen et al., 2011; Brouillet et al., 2013; Jaber et al., 2014). As a means by which such a relationship might arise, Brouillet et al. (2013) suggested protonated methanol  $\text{CH}_3\text{OH}_2^+$  in the gas-phase as the common precursor to form  $\text{CH}_3\text{OCHO}$  and  $\text{CH}_3\text{OCH}_3$  via reactions with  $\text{HCOOH}$  and  $\text{CH}_3\text{OH}$ . As a test, the proposed reactions were incorporated into our chemical network; however, they were too slow to be effective in producing  $\text{CH}_3\text{OCHO}$  and  $\text{CH}_3\text{OCH}_3$  in our model, due to the low abundance of protonated methanol in the gas.

Recently, potentially influential gas-phase reactions were proposed by Shannon et al. (2013, 2014), who found that reactions of either  $\text{OH}$  or  $\text{C}(^3\text{P})$  with methanol are efficient at low temperatures, due to quantum tunneling:

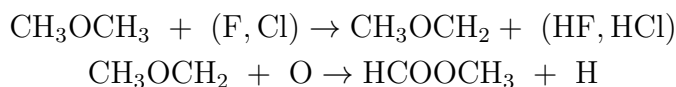


The gas-phase methanol reactions could act not only as an efficient loss process for gas-phase methanol, but also produce more radicals that would be available as reactants to form other COMs when they accrete onto grain surfaces, or directly in the gas phase if such processes are efficient. Vasyunin & Herbst (2013) suggested a gas-phase radiative association reaction between the radicals that are produced by the above mechanisms, to form DME:



To understand how significantly these reactions would affect the overall formation of COMs in our chemical model, we ran a test model that included all three (with rate coefficients on the order of  $10^{-10} \text{ cm}^{-3}$ ). However, gas-phase methanol was still predominantly destroyed by ion-molecule reactions at the core center. The contribution of the above neutral-neutral reactions to the loss of gas-phase methanol was minor ( $\sim 2\%$ ), hardly changing the abundances of methanol and the three COMs, while the radiative association reaction also showed minimal influence.

Balucani et al. (2015) proposed a gas-phase mechanism that would form methyl formate from dimethyl ether through the radical  $\text{CH}_3\text{OCH}_2$ . The dimethyl ether itself would form through the efficient radiative association of the radicals  $\text{CH}_3$  and  $\text{CH}_3\text{O}$  :



Although our network does not include fluorine, the incorporation of the other reactions into our model did not make a meaningful difference to the results, because they involve a one-way process where  $\text{CH}_3\text{OCH}_3$  is converted into  $\text{CH}_3\text{OCHO}$ . In our chemical model,

neither the radiative association of the radicals  $\text{CH}_3$  and  $\text{CH}_3\text{O}$  nor any other processes were efficient enough to form abundant  $\text{CH}_3\text{OCH}_3$ . As such, several key reactions concerning gas-phase chemistry of COMs do not affect our chemical model significantly.

Thus, at least under the conditions tested in our physical model, we found no efficient gas-phase mechanisms that could produce either DME or MF.

### 2.4.5 Other surface processes

The 3-body excited-formation mechanism included here is especially efficient for the initiating reaction  $\text{H} + \text{CH}_2 \rightarrow \text{CH}_3$ , which is highly exothermic, but which also results in a small product,  $\text{CH}_3$ , that has only a limited number of vibrational modes in which the resulting energy may be stored. The models suggest that when this is coupled with highly abundant CO on the grain surface, the subsequent reaction between the two proceeds at a sufficient pace to produce enough  $\text{CH}_3\text{CO}$  (and thence  $\text{CH}_3\text{CHO}$ ) to be able to explain the gas-phase abundance of the latter molecule (given an adequate desorption mechanism). The production of  $\text{CH}_3\text{O}$  via the hydrogenation of formaldehyde is also exothermic, but not sufficiently so to allow the subsequent reaction with abundant CO to proceed at high efficiency. Nevertheless, this low-efficiency mechanism is capable of producing enough  $\text{CH}_3\text{OCO}$  (and thence  $\text{CH}_3\text{OCHO}$ ) to account for the presence of methyl formate in the gas phase.

As noted in Section 3.3, a more detailed treatment of the 3-BEF mechanism should include not only the energy partition between bonds, but also translational degrees of freedom of the excited species. This would impact the RRK calculation, but could also provide an alternative outcome to the process. The RRK treatment as formulated in Section 3.3 assumes that the efficiency of the process is determined solely by the competition between energy going into the “reaction mode” and energy being lost to the surface. However, if diffusion spontaneously occurred, moving the two reactants apart, then the process would automatically end (unless another reactant were present in this new site), regardless of the energy status of the excited species. We would expect this effect to reduce efficiency by a factor of say 4 (on the basis of there being four available diffusion directions), even for the otherwise efficient 3-BEF mechanism that produces  $\text{CH}_3\text{CO}/\text{CH}_3\text{CHO}$ . The production of  $\text{CH}_3\text{CHO}$  may therefore be somewhat less efficient than the simple 100% approximation used in the treatment presented here.

It is also of interest to consider specifically the possible effects of reaction-induced diffusion, such as that studied by Fredon et al. (2017) for stable molecules including methane. If reactive species like  $\text{CH}_3$  were able to undergo some non-thermal diffusion as the result of excitation caused by their formation, they could react with other radicals that they could not otherwise reach under low-temperature (i.e. nondiffusive) conditions. In fact, as we allude in Section 2.4, the standard (non-excited) 3-B mechanism that we already implement in the models will automatically include such processes to a first approximation. The treatment that we construct for 3-B processes does not explicitly require the reactants to be immediately contiguous, but rather to become so immediately following the initiating reaction. If one were to consider a newly-formed radical species,  $A$ , taking some finite and approximately straight-line trajectory across an ice surface, the probability of it encountering some reaction partner,  $B$ , along its path would still

be given, to first order, by  $N(B)/N_S$ , as already included in Eq. (2.6). The simple 3-B mechanism is therefore broad enough to cover this specific case also.

While the 3-BEF mechanism for the production of the dimethyl ether precursor,  $\text{CH}_3\text{OCH}_2$ , should be highly efficient based on the statistical calculations in § 2.3.3, the lower abundance of  $\text{H}_2\text{CO}$  on the grain surfaces appears to be too low to allow this mechanism to account for gas-phase DME. It should also be noted that in this work it was assumed that DME is the only product of this reaction. It is possible, and perhaps favorable, for ethanol ( $\text{C}_2\text{H}_5\text{OH}$ ) also ultimately to be formed, if the methyl radical attaches to the carbon atom in formaldehyde, producing a radical  $\text{C}_2\text{H}_5\text{O}$ . This would naturally limit the yield of DME through the suggested excited-formation mechanism.

Are there alternative surface processes that might produce sufficient dimethyl ether if the reactants could be brought together through some nondiffusive process? One possibility might be the reactions of the carbene  $\text{CH}_2$  with methanol ( $\text{CH}_3\text{OH}$ ). Methylene,  $\text{CH}_2$ , is a diradical in its ground (triplet) state. Reactions of triplet  $\text{CH}_2$  with methanol could involve the abstraction of hydrogen from  $\text{CH}_3\text{OH}$ , followed by immediate radical-radical addition of the resultant  $\text{CH}_3$  to the remaining  $\text{CH}_3\text{O}$  or  $\text{CH}_2\text{OH}$ . The review of Tsang (1987) suggests gas-phase rate coefficients for the abstraction processes (without the subsequent recombination); the activation barrier for the  $\text{CH}_3\text{O}$  branch is marginally lower than that for  $\text{CH}_2\text{OH}$ , indicating that  $\text{CH}_3\text{O}$  (and thence DME) might be the preferred product. On a dust-grain/ice surface, the production of  $\text{CH}_2$ , either by H-addition to CH or by the barrier-mediated reaction of  $\text{H}_2$  with atomic C, would likely be exothermic enough to allow the subsequent abstraction barriers to be overcome. However, abstraction might be fast in any case, even without (vibrationally) excited  $\text{CH}_2$ , due to hydrogen tunneling through the activation-energy barrier.

Another possibility is that the higher-energy *singlet*  $\text{CH}_2$  could undergo a direct, barrierless insertion into the methanol molecule, producing either dimethyl ether or ethanol. Bergantini et al. (2018) investigated the action of singlet  $\text{CH}_2$ , produced through the irradiation of a mixed  $\text{CH}_4/\text{CH}_3\text{OH}$  ice, to produce DME and ethanol in this way; they found essentially equal production of the two branches. If, instead of the dissociation of methane, the hydrogenation of carbon on the grain surfaces were the means by which singlet  $\text{CH}_2$  were produced, then this mechanism could occur effectively as a nondiffusive (i.e. three-body) process, although the short lifetime of the singlet methylene might make a diffusive meeting of the reactants unlikely. Although the dissociation of methane, as per those experiments, is an entirely plausible starting point for the production of COMs within ice mantles, it is an unlikely explanation for the *gas-phase* detection of COMs.

A further consideration, relating to the production of  $\text{CH}_3\text{CHO}$  via the 3-BEF mechanism, is the possible production of ketene,  $\text{CH}_2\text{CO}$ , through the reaction  $\text{CH}_2 + \text{CO} \rightarrow \text{CH}_2\text{CO}$ . This process could also occur through the 3-BEF mechanism, following production of methylene through exothermic surface reactions. The more complex nature of the coding of the 3-BEF mechanism required us to include only the three 3-BEF mechanisms directly related to MF, MDE and AA in the present work, but the application of this mechanism to the full chemical network might impact ketene production. An immediate question would be whether the ketene production might also preclude the production of acetaldehyde, as the  $\text{CH}_2$  used to produce ketene would otherwise be required to produce the  $\text{CH}_3$  needed for AA production. Furthermore, one could argue that the production of  $\text{CH}_3$  in the presence of CO, as needed for our 3-BEF route to AA, would first require contiguous  $\text{CH}_2$  and CO, and that this  $\text{CH}_2$  would also have to be formed in the presence

of CO, making ketene the preferred product *instead* of AA. Such a view implicitly assumes that there is no reaction-induced diffusion occurring, when in fact, due to the large exothermicities of the reactions in question, it is highly likely that there is some form of diffusion following each reaction. As mentioned above, this diffusion does not make either the 3-B nor the 3-BEF treatments any less accurate, as we do not explicitly rule out such occurrences. Rather, it might be better to assume that, on a surface at least, such reaction-induced diffusion is the rule, rather than the exception, and thus that there is no expectation nor requirement that any newly-formed reaction product considered in the 3-B mechanisms necessarily meets its own reaction partner within its immediate surroundings. In that case, any conditionality in the production of one species from another, based on location, would be lost. On the topic of ketene in particular, it is also possible that it may be hydrogenated to acetaldehyde anyway; the reaction  $\text{H} + \text{CH}_2\text{CO} \rightarrow \text{CH}_3\text{CO}$  is assumed in our network to have a barrier of 1320 K (Senosiain et al., 2006), which is lower than, for example, the typically-assumed barrier to hydrogenation of CO. In future work, we will apply the 3-BEF process to the entire surface network, allowing the relationship between acetaldehyde and ketene to be explored more deeply.

Fedoseev et al. (2015) conducted experiments investigating the production of COMs, specifically glycolaldehyde and ethylene glycol, through nondiffusive surface reactions of HCO radicals produced through H and CO co-deposition. Those experiments did not detect any methyl formate production, but follow-up work by Chuang et al. (2016), who co-deposited various combinations of CO, H<sub>2</sub>CO, CH<sub>3</sub>OH and H, demonstrated methyl formate production in the setups that involved direct deposition of formaldehyde (H<sub>2</sub>CO). Thus, under the conditions of their experiments, the HCO and CH<sub>3</sub>O radicals required for the radical-radical reactions to produce CH<sub>3</sub>OCHO derived mainly or uniquely from H<sub>2</sub>CO reactions with atomic H (either H addition or H-abstraction by H atoms). In the case of CO and H deposition alone, they suggested that the reaction between two HCO radicals dominates, producing glyoxal (HCOCHO) that can be further hydrogenated to glycolaldehyde (CH<sub>2</sub>(OH)CHO) and ethylene glycol (HOCH<sub>2</sub>CH<sub>2</sub>OH).

The reaction network we use here includes HCO–HCO reaction routes (Garrod et al., 2008), with one branch producing glyoxal, and an equal branch producing CO and H<sub>2</sub>CO through a barrierless H-abstraction process. Our network does not include the further hydrogenation of glyoxal, but the removal of HCO radicals should be well enough treated.

In our astrochemical models (in which the overall system is much more complicated than the laboratory setups, with many more species and processes), grain-surface formaldehyde and methanol are produced through CO hydrogenation by H atoms; in the experiments, the CO + H system does not produce enough formaldehyde to allow substantial production of CH<sub>3</sub>O and thence methyl formate. The outcomes of the models, which are run over astronomical timescales, should not therefore be expected to correspond directly with the experimental outcomes. However, the mechanism of nondiffusive radical chemistry that seems to produce methyl formate in the experiments (via HCO + CH<sub>3</sub>O) is present in our models (the basic three-body mechanism).

The key comparison with the experiment concerns our implementation of the excited three-body formation mechanism for the reaction of CH<sub>3</sub>O with CO (the other 3-BEF mechanisms tested in this work involve CH<sub>3</sub> and are therefore not tested in the laboratory experiments). The very low efficiency that we require (0.1%) for immediate reaction is likely to be too small to have an important effect in a laboratory regime where the regular three-body process is presumably efficient (unlike in our prestellar core models).

In this sense, it seems superficially consistent with the experiments, since there are no experimental setups in which methyl formate was not found in which our excited formation mechanism would predict it to be highly abundant. Indeed, our mechanism should only become important if other means of production (such as the regular three-body process) are already weak. Thus, it may be difficult to test the excited-formation mechanism for methyl formate through experimental means.

Another possibility exists for the production of all three COMs considered here: that is, that they are produced in the ice mantles, through UV processing (or some other means). The ice mantle material would then have to be removed by some violent process such as sputtering by cosmic rays. (Such a process would also result in some degree of complex molecule production, e.g. Shingledecker et al., 2018). However, it is unclear whether such mechanisms would be capable of maintaining gas-phase abundances of COMs at the required levels.

A separate point of discussion concerns the experimental evidence surrounding the interaction of H atoms specifically with solid-phase acetaldehyde. Bisschop et al. (2007) studied the deposition of H onto a pre-deposited surface of pure  $\text{CH}_3\text{CHO}$  at temperatures ranging from 12.4 – 19.3 K. They found reaction products  $\text{C}_2\text{H}_5\text{OH}$ ,  $\text{H}_2\text{CO}$ ,  $\text{CH}_3\text{OH}$ , and  $\text{CH}_4$ , which they posited to be formed either through repetitive hydrogenation (ethanol), or fragmentation into a stable molecule and a radical, which may be further hydrogenated to a stable species. In our model, it is assumed that H atoms interact with  $\text{CH}_3\text{CHO}$  by abstracting another hydrogen atom from the aldehyde end of the molecule. If the alternative mechanisms measured in the laboratory should compete strongly with this process, then the mechanism described in Section 2.4.1, in which H-abstraction and re-hydrogenation work together to enhance reactive desorption, could become less effective, and the acetaldehyde produced on the surface could be converted to entirely different species.

The Bisschop et al. (2007) data suggest production yields for ethanol of  $\sim 20\%$ , with other products also on the order of 10%. However, these yields are provided as a fraction of the acetaldehyde initially available in the surface layer of the ice; they do not indicate yields per hydrogen atom or per H- $\text{CH}_3\text{CHO}$  interaction. Furthermore, the experiments would not appear to be sensitive to processes in which acetaldehyde were converted to  $\text{CH}_3\text{CO}$ , then re-hydrogenated to  $\text{CH}_3\text{CHO}$ . As a result, it is not possible to determine how strongly H-abstraction may dominate over hydrogenation or fragmentation, or vice versa. However, each of these processes would involve an activation energy barrier, and it is found that abstraction from aldehyde groups occurs more readily than H-addition. Hippler & Viskolcz (2002) calculated barriers to such processes, including the  $\text{H} + \text{CH}_3\text{CHO} \rightarrow \text{C}_2\text{H}_5\text{O}$  addition reaction, finding an activation energy of  $22.4 \text{ kJ mol}^{-1}$  (2690 K), versus the literature value for abstraction of  $17.6 \text{ kJ mol}^{-1}$  (2120 K Warnatz, 1984). Assuming the simple rectangular-barrier tunneling treatment used in our models, and assuming a  $1 \text{ \AA}$  barrier width, the abstraction process should go around 350 times faster than hydrogenation. The preferred gas-phase value in the more recent review by Curran (2006) suggests an even higher barrier to hydrogenation of  $26.8 \text{ kJ mol}^{-1}$  (3220 K), which would provide an abstraction/hydrogenation ratio closer to  $10^5$ . Fragmentation is more sparsely studied in the literature, but based on the Bisschop et al. study we presume those mechanisms to occur at similar rates to the hydrogenation mechanism. Since chemical desorption in our model is calculated to proceed in a little less than 1% of cases, we would not expect our results for acetaldehyde to be strongly affected by the inclusion of

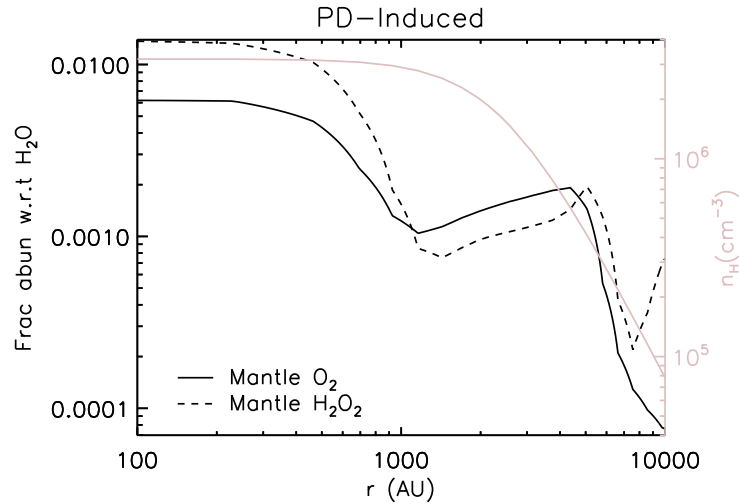


Figure 2.15: Radial distribution of the solid-phase abundances of  $\text{O}_2$  (solid lines) and  $\text{H}_2\text{O}_2$  (dashed lines) in the PD-Induced model.

alternative reaction branches, either on the grains or in the gas-phase.

## 2.4.6 $\text{O}_2$ production

Aside from its effect on COM abundances in the ice mantles, the PD-induced reaction mechanism also produces a significant increase in  $\text{O}_2$  ice abundance; this effect is noteworthy, as it may provide a clue to the origin of  $\text{O}_2$  in comets. Gas-phase  $\text{O}_2$  was recently observed toward comet 67P/C-G, as part of the Rosetta mission (Bieler et al., 2015). It was found that  $\text{O}_2$  achieves a fractional abundance as high as  $\sim 4\%$  with respect to water, indicating this compound as one of the most dominant species in cometary material. While the origin of molecular oxygen is still controversial because of its difficulty in observation, the strong correlation with  $\text{H}_2\text{O}$  implies a connection to dust-grain ice chemistry rather than gas-phase chemistry in the coma.

Many studies directly or indirectly suggest a primordial nature for  $\text{O}_2$  in comets. For example, Rubin et al. (2015) confirmed the presence of  $\text{O}_2$  in the Oort cloud comet 1P/Halley at a level similar to that seen in the Jupiter-family comet 67P/C-G. This suggests that  $\text{O}_2$  may be common, regardless of dynamical history, indicating a primordial origin. Mousis et al. (2016) proposed that the radiolysis of water-containing interstellar ices in low-density environments such as molecular clouds could produce  $\text{O}_2$  in high abundance. Meanwhile, Taquet et al. (2016) conducted a range of astrochemical models based on diffusive grain-surface chemistry, to investigate three possible origins for  $\text{O}_2$  in comets: (i) dark cloud chemistry; (ii) formation in protostellar disks; and (iii) luminosity outbursts in disks. They concluded that dark clouds are the most plausible regime in which to form the  $\text{O}_2$ , through diffusive O-atom addition on grain/ice surfaces at temperatures around 20 K. However, as they noted, the temperature required in their models is rather higher than typical dark cloud values. Garrod (2019) suggested that the upper layers of cold-storage comets could be processed to increase their  $\text{O}_2$  content, as the result of photolysis and radiolysis by the galactic UV and cosmic ray fields. The chemical models presented

by Garrod included the same PD-induced mechanism used in the present study.

Here, we propose nondiffusive, photodissociation-induced processing of interstellar ice mantles as the possible origin of the abundant  $O_2$  in comets; this avoids the requirement for higher-temperature diffusive chemistry on dust-grain surfaces.

Fig. 2.15 shows the radial distribution of the  $O_2$  ice (solid lines) in our model of L1544 with the PD-induced process activated. The fractional abundance of  $O_2$  ice in this model is as high as 0.6 % with respect to water ice toward the core center, which is 1-2 orders of magnitude higher than in the other models. The abundance of  $O_2$  ice has been suggested to be low in prestellar core material, because  $O_2$  is efficiently hydrogenated to form  $H_2O$  and  $H_2O_2$  ices at low temperature (Ioppolo et al., 2008). However, the PD-Induced process induces the association of O-atoms in the icy mantle (sourced from water molecules), resulting in the production of large amounts of  $O_2$ . The other models (without PD-induced reactions) accumulate the  $O_2$  ice on the grain-surface over time rather than directly synthesizing it within the ice mantles. If interstellar  $O_2$  ice formed via the PD-induced process were locked in until such ices were incorporated into comets, it could remain there to contribute to the  $O_2$  population observed in 67P/C-G.

It should be noted that  $H_2O_2$  ice in the PD-induced model is more abundant than  $O_2$  ice (dashed line; Fig. 2.15), in contrast to observations. The  $H_2O_2/O_2$  ratio found in 67P/C-G by ROSINA was as low as  $6.0 \pm 0.7 \times 10^{-3}$  (Bieler et al., 2015). The same discrepancy was found by Garrod (2019), and is related to the relative formation rates of other compounds in the ice as well as  $O_2$ . Photodissociation of water leads first to OH; two such radicals may recombine through the PD-induced processes to form  $H_2O_2$  in high abundance. The present chemical network may be missing some chemical reactions related to the destruction of  $H_2O_2$ , or may overestimate the efficiency to form  $H_2O_2$  via the PD-Induced process. The efficiency of H-atom diffusion within the bulk ice to abstract another H atom from  $H_2O_2$  may also be an important factor; Fig. 2.15 shows that the  $H_2O_2$  abundance strongly dominates  $O_2$  in the coldest (inner) regions of the core. The sum of the  $O_2$  and  $H_2O_2$  abundances collectively reach a value on the order of 1% in total at the core center. Inclusion of  $O_3$  and  $O_2H$  boosts this total further. The photodissociation that leads to  $O_2$ ,  $H_2O_2$  and other species' production from  $H_2O$  in these models is the result of the secondary, cosmic ray-induced UV field. Thus, the abundances of each would likely be enhanced by the adoption of a somewhat larger cosmic-ray ionization rate. A longer evolutionary timescale, or further processing of the ices during the later disk stage, could also lead to enhancement. Radiolysis, i.e. direct cosmic-ray impingement on the ice mantles could also act in concert with the photodissociation effect.

Further modeling to reproduce the amount of  $O_2$  and  $H_2O_2$  seen in 67P/C-G is outside the scope of this work, but may be a fruitful means to elucidate the origins of cometary  $O_2$ . The vast majority of this  $O_2$  could indeed be interstellar, produced by photolysis.

## 2.5 Conclusions

Here we have introduced new rate formulations that allow astrochemical models to simulate a number of new, nondiffusive chemical mechanisms on interstellar dust-grain surfaces and within bulk ices. These formulations are fully compatible with existing model treat-

ments for diffusive chemistry. Some of the nondiffusive mechanisms considered here, such as the Eley-Rideal process and three-body reactions, are automatically taken into account in microscopic Monte Carlo kinetics models of the same systems, but must be explicitly added in rate-based treatments such as the one used here. Others, such as the three-body excited-formation mechanism and photodissociation-induced reactions, are entirely new.

Crucially, it is shown that nondiffusive processes can affect the bulk-ice, the ice-surface, and – indirectly – the gas-phase composition, through a cyclic H-abstraction and addition process that amplifies the efficiency of chemical desorption. Eley-Rideal reaction processes appear not to have a strong effect in our implementation.

To place the new nondiffusive mechanisms into a context in which they could be directly tested, a physical model approximating the prestellar core L1544 was adopted, with a focus on reproducing the observed gas-phase abundances of the complex organic molecules (COMs) acetaldehyde, dimethyl ether, and methyl formate. Reactions involving excited radicals (recently produced by other surface or bulk reactions) appear to be influential in producing COMs, although their influence is likely limited to reactions involving the highly-abundant CO molecule on the grain surfaces, and/or the excited radical  $\text{CH}_3$ , whose production through the addition of H to  $\text{CH}_2$  is especially exothermic. In the three-body excited formation model, the efficiency of the 3-BEF mechanism for methyl formate production must indeed be optimized, as this mechanism is otherwise more efficient than is required to agree with observations. Although the gas-phase dimethyl ether abundance in particular remains difficult to reproduce, the models presented here tested only three plausible excited-formation mechanisms; alternative surface-formation processes for this molecule could be active.

Further application of the new mechanisms and formulations presented here into astrochemical models of the later stages of star formation, such as the hot core/corino stage, is currently underway.

The main conclusions of our study are enumerated below:

1. nondiffusive reactions between newly-formed radicals and nearby species on dust grains, which we label three-body reactions, appear to influence strongly the production of complex organics and other species on interstellar dust grains and in their ice mantles, producing abundances similar to those detected in the gas phase toward hot star-forming sources.
2. We propose a new surface/bulk mechanism in which the energy of formation of a newly-formed radical allows it to overcome an activation energy barrier against reaction with a nearby, stable species (the three-body excited-formation process, 3-BEF). For key molecules/processes, especially reactions between excited radicals and abundant grain-surface CO, this mechanism appears strongly to influence production, beyond the effects of the regular three-body mechanism. Except for these key processes, the 3-BEF process is expected to be inefficient in most cases.
3. Grain-surface molecule production is enhanced by the three-body excited-formation mechanism sufficiently to explain observed *gas-phase* abundances of methyl formate and acetaldehyde in prestellar core L1544. Chemical desorption allows these grain surface-formed molecules to enter the gas phase.
4. Dimethyl ether is still under-produced in the model, when compared with observations of L1544. Other plausible grain-surface production mechanisms, such as

reactions between  $\text{CH}_2$  and methanol, remain to be tested in the models.

5. Repetitive H-abstraction by H atoms from COMs on grain surfaces, followed by recombination with another H atom and the possible desorption of the product into the gas phase, gives chemical desorption a greater influence than its basic efficiency of around 1% would otherwise suggest. This cyclic amplification effect brings the required surface-formed COMs into the gas phase effectively enough to reproduce abundances as described above. The effect should be especially important in regions where gas-phase H abundances remain relatively high.
6. Specific to the L1544 models, the position of the methanol peak is located further outward than observation, but it is still associated with the region where CO starts to freeze out significantly. The off-center peaks in COM column densities toward L1544 are most likely related to the interplay between rising COM fractional abundances at larger radii and rising gas density at smaller radii.
7. The surface-diffusion rate of atomic H is important to radical lifetimes, which affects the efficiency of nondiffusive mechanisms that rely on reactive radicals being available on the grain surfaces. Thus the choice of diffusion barrier for H has a strong effect on the production of COMs in chemical models that consider nondiffusive chemistry.
8. Photodissociation-induced nondiffusive chemistry within the bulk ices produces abundances of  $\text{O}_2$  and related species on the order of 1% of water. This suggests that interstellar (and perhaps later) UV-processing of grain-surface ices may be sufficient to reproduce observed cometary values, regardless of the precise temperature of the dust grains.
9. The broader inclusion of various nondiffusive grain-surface/ice chemical reactions in interstellar chemical models now seems imperative.

## Acknowledgement

We thank the anonymous referees for helpful comments and suggestions. We are grateful to E. Herbst and P. Caselli for useful discussions. This work was partially funded by a grant from the National Science Foundation (Grant number AST 19-06489).

# 3

## Spatial distribution of acetaldehyde in Orion KL: Observations and chemical modeling

### Contents

---

<b>3.1</b>	<b>Introduction</b>	<b>70</b>
<b>3.2</b>	<b>Methods</b>	<b>71</b>
3.2.1	Observations and data reduction	71
3.2.2	Chemical Model	72
<b>3.3</b>	<b>Data analysis and Results</b>	<b>74</b>
3.3.1	Emission map	74
3.3.2	Line identification and spectra	77
3.3.3	Derivation of physical parameters	78
<b>3.4</b>	<b>Discussions</b>	<b>78</b>
3.4.1	Spatial distribution of acetaldehyde and other HCO-bearing species	78
3.4.2	Aldehyde chemistry and chemical modeling	81
3.4.3	Searching for other aldehyde species	90
<b>3.5</b>	<b>Summary</b>	<b>90</b>

---

### 3.1 Introduction

The Orion molecular cloud complex is one of the most well-studied high-mass star forming regions due to its proximity ( $388 \text{ pc} \pm 5 \text{ pc}$ ; Kounkel et al., 2017). It shows highly structured star-forming regions with visible hierarchy, hosting many substructures such as Orion molecular cloud (OMC) 1-4. The Orion Kleinmann-Low Nebula (Orion KL) in OMC-1 has received particular attention because of its unique features. The enormously high IR luminosity ( $\sim 10^5 L_{\odot}$  Wynn-Williams et al., 1984) and chemical complexity on various scales (Blake et al., 1987, 1996; Liu et al., 2002; Friedel & Snyder, 2008; Favre et al., 2011; Pagani et al., 2017; Tercero et al., 2018; Peng et al., 2019) are attributed to a recent ( $\sim 500 \text{ yr}$ ) explosive event; investigations of the proper motions of infrared/radio sources BN, I, and n (Menten & Reid, 1995; Lonsdale et al., 1982) reveal that they are moving away from a common central region (Gómez et al., 2005). Orion KL thus provides a unique laboratory for studying a rich interstellar chemistry driven by a very recent and energetic event at the heart of the nebula.

Orion KL is classically described as being host to four large-scale components that show a distinctive systemic velocity; these are the hot core (HC), compact ridge (CR), extended ridge and plateau (Blake et al., 1987). In particular, the HC and CR are known as major emission regions of organic molecules. Observations of O- and N-bearing species toward these two regions show an apparent chemical segregation; the N-bearing molecules tend to peak to the north of the HC, while O-bearing molecules cover both HC and CR (Guélin et al., 2008; Beuther et al., 2005; Friedel & Snyder, 2008). The HC is believed to be externally heated; its heating source is possibly either an impact of the explosive event or the shocks from the source I outflow. The CR would also be externally heated, but is not directly affected by the impact of the explosion (Pagani et al., 2017).

Complex organic molecules (COMs) are typically defined as carbon-bearing molecules composed of six or more atoms. The high angular resolution achieved by interferometric observations allows us to understand the spatial scales and the distributions of many COMs in Orion KL. For example, many methyl formate ( $\text{CH}_3\text{OCHO}$ ; MF) peaks are identified (Favre et al., 2011), and Tercero et al. (2018, TCR18) reported a clear segregation of complex O-bearing species depending on their different functional groups. Furthermore, the deeper observations with interferometry reveals many new species not previously detected in Orion KL. For example, Pagani et al. (2017) present the detection of new species such as propyl cyanide ( $\text{C}_3\text{H}_7\text{CN}$ ), while Favre et al. (2017) reported the first detection of gGg' ethylene glycol ( $(\text{CH}_2\text{OH})_2$ ; EG) and acetic acid ( $\text{CH}_3\text{COOH}$ ). Peng et al. (2019) searched for ethyl formate ( $\text{C}_2\text{H}_5\text{OCHO}$ ; EF) motivated by the extended distribution of MF in Orion KL and reported the clear detection of many EF lines throughout the two main emission regions.

Despite its chemical complexity, however, none of the large interstellar aldehydes including the ubiquitous aldehydes – acetaldehyde ( $\text{CH}_3\text{CHO}$ ; AA) has been clearly identified toward this region. An aldehyde is an organic compound containing a functional group with the structure  $-\text{CHO}$ , where the carbon atom is also bonded to any generic alkyl or side chain R group. So far, five COMs bearing an aldehyde group have been found in the interstellar medium – acetaldehyde ( $\text{CH}_3\text{CHO}$ ; AA), glycolaldehyde ( $\text{CH}_2\text{OHCHO}$ ; GA), propynal ( $\text{C}_2\text{HCHO}$ ), propenal ( $\text{C}_2\text{H}_3\text{CHO}$ ), and propanal ( $\text{C}_2\text{H}_5\text{CHO}$ ). AA in particular, the simplest of the five, was among the earliest molecules to be detected in space.

This species is of great prebiotic significance, being a possible precursor for several carbohydrates, and for larger intermediates that can form various amino acids (Vazart et al., 2020, and references therein).

Since the first detection of AA was reported toward Sgr B2 (Gottlieb, 1973; Fourikis et al., 1974), it has been identified in various star-forming regions: from cold ( $\sim 10$  K) environments such as prestellar cores and outer envelopes of protostars (Bacmann et al., 2012; Vastel et al., 2014; Scibelli & Shirley, 2020) to warm regions including inner protostellar envelopes and outflows (Belloche et al., 2013; Cazaux et al., 2003; Bianchi et al., 2019; De Simone et al., 2020). All these detections were made by single-dish observation, and the rotational temperature estimated from those studies were quite low ( $< 40$  K) except for Sgr B2 (60 K-100 K; Belloche et al., 2013). The recent interferometer observation with ALMA traces more compact and warmer ( $> 100$  K) emission of AA but the detection has been successful only for a few sources (Lykke et al., 2017; Csengeri et al., 2019; Lee et al., 2019).

There have been many attempts to detect AA towards Orion KL regions (Blake et al., 1987; Turner, 1991; Ziurys & McGonagle, 1993; Ikeda et al., 2001). In many cases, however, the reported spectra suffered from low S/N ratios and/or a lack of accurate spectroscopic information. Although two bright transitions of AA presented by Ikeda et al. (2001) are notable, the large observing beam size (16 ") and the transitions discriminatorily detected to the very low  $E_u$  (16 K) implies that this emission may come from a foreground layer of ISM rather than Orion KL, which is cold and dense enough to be seen. Other bright transitions with higher  $E_u$  (72K - 93 K) therein were not detected.

Despite its potential prebiotic importance and its presence in a range of sources, our understanding of AA formation has been limited. The observational bias toward large-scale detection possibly implies its origin is related to cold environments, such as icy grain surfaces, but deeper investigation with a wide range of spatial scales is required to better understand the chemistry. Considering this, Orion KL is one of the potential sources which is open to the new exploration of AA.

In this study, we investigate an extensive ALMA archive dataset to search for AA and other undetected aldehydes. Chemical modeling is also employed in this work in order to understand better the aldehyde chemistry. In § 2, we briefly provide a summary for the investigated archive datasets. Data reduction process and chemical modeling are described as well. The observational results and derivation of physical parameters are presented in § 3. The model results and discussion are provided in § 4 and § 5, respectively.

## 3.2 Methods

### 3.2.1 Observations and data reduction

Because many studies have been already made with the ALMA scientific verification (SV) data of Orion KL, we investigated four new ALMA archive datasets with an improved observation specification. They cover band 4 (2017.1.01149) and band 7 (2013.1.01034, 2016.1.00297, and 2016.1.01019) of which frequency coverage spreads between 142 – 355 GHz with a spectral resolution of 488.28 KHz ( $\sim 0.5$ km/s). Table 3.1 compares the

ALMA Band	6 (SV)	4	7
Angular resolution (")	1.2	0.5	0.2
sensitivity at 10 km/s (mJy)	0.00015	1.0	0.5
Maximum Recoverable Scale (")	8.9	4.5	3.6
The number of 12m antenna	16	49	41

Notes. The observation specification is based on the project 2011.0.00009.SV (band 6), 2017.1.01149.S (band 4), and 2016.1.00297.S (band 7).

Table 3.1: Comparison of the observation specification

observational specification of the ALMA archive data under consideration to SV data. The data was re-calibrated using the publicly provided python script (`scriptforPI.py`) Data reduction was performed through the Common Astronomy Software Applications (CASA) software (McMullin et al., 2007). The continuum emission was subtracted in the maps by carefully selecting line-free channels. The line maps were cleaned using auto-masking feature (Kepley et al., 2020) based on the `hogbom` algorithm (Hogbom & Brouw, 1974).

### 3.2.2 Chemical Model

We model the chemical evolution of the main emission region in Orion KL using the astrochemical kinetic code *MAGICKAL*. This code solves a set of rate equations describing a fully coupled gas-phase, grain-surface, and ice-mantle chemistry under time-dependent physical conditions appropriate to the source (Garrod & Pauly, 2011; Garrod, 2013); modified rate equations are used to simulate the stochastic behavior of the grain-surface chemistry, where required (Garrod, 2008).

Notably, the chemical model used here includes not only the typical diffusive grain-surface/ice chemistry, but also a range of nondiffusive mechanisms by which reactants on the grain/ice surface or in the bulk ice may meet each other and react (Jin & Garrod, 2020). The new nondiffusive mechanisms considered in the model are: three-body (3-B) reactions, in which a preceding surface/bulk reaction is immediately followed by the reaction of the product with some nearby species; photodissociation-induced (PDI) reactions, in which a radical produced by photodissociation meets its reaction partner in the immediate vicinity as soon as dissociation occurs; and the Eley-Rideal process, in which gas-phase species may adsorb directly onto a grain-surface reaction partner. The model uses the updated “PDI2” treatment of Garrod et al. (2021), in which the recombination of photodissociation products in the bulk ice is allowed, in cases where no immediate reaction partner is available. Jin & Garrod (2020) also proposed a three-body excited-formation (3-BEF) mechanism, in which chemical energy produced by an initiating reaction in the 3-B process could allow an activation energy barrier to be overcome; this was found to be important for the grain-surface production of methyl formate, in order to explain its presence in the gas phase in cold, prestellar sources. The generic 3-BEF method provided by Garrod et al. (2021) is used here, which is based on a statistical treatment of the chemical energy available from the preceding reaction to overcome the barrier to a specific subsequent reaction.

Another major change from past versions of the *MAGICKAL* code, as employed here and in the models of Garrod et al. (2021), is the elimination of bulk diffusion for all species but atomic and molecular hydrogen. Much of the chemistry within the bulk is thus driven either directly by photodissociation (via the PDI mechanism) or indirectly, as the result of H-atom production within the ice followed by diffusion of H and its reaction with existing bulk species; this can include reactions with radicals or with relatively stable species like CO. The combination of the switch-off of bulk diffusion and the use of the nondiffusive PDI mechanism means that COM production caused by photodissociation in the bulk is no longer diffusion-driven and thus has far weaker dependence on the dust temperature.

Following Garrod et al. (2021), and based on the modeling study of Kalvāns (2018), the photodissociation rates of grain-surface/bulk species is assumed to be a factor of 3 lower than the corresponding gas-phase processes, although the other rate coefficients and the photoproducts are the same. The final binding energy and diffusion barrier treatments used by Garrod et al. (2021) are also adopted here. The chemical network is also the same, and includes a selection of new methylene- and methyldiyne-related reactions on the grains, a more complete glycolaldehyde-related chemistry, and some key gas-phase reactions for COMs, such as the reaction of atomic O and the radical  $\text{CH}_3\text{OCH}_2$  to produce MF (Balucani et al., 2015), and the radiative association of  $\text{CH}_3$  and  $\text{CH}_3\text{O}$  radicals to form dimethyl ether (Tennis et al., 2021).

The chemical evolution is initiated from the typical elemental and chemical abundances of dark clouds (Table 4.1). The physical evolution in this model is described with a two-stage approach, in which (i) an initial, cold core is formed and then (ii) it is warmed up to a high temperature representative of a hot core. During the first stage, the gas density ( $n_{\text{H}}$ ) rises from a value of  $3000 \text{ cm}^{-3}$  to the value measured toward the main emission region in Orion KL ( $n_{\text{H}} \sim 8 \times 10^8 \text{ cm}^{-3}$ ). This density evolution basically follows the free-fall collapsing timescale, but it can slow down by employing a magnetic field retardation factor,  $B$ . The dust temperature ( $T_{\text{d}}$ ) hardly changes at this stage because a central heating source has not yet been formed. Rather, the dust temperature is determined by the balance between heating by external photons and thermal cooling;  $T_{\text{d}}$  during the collapse stage is calculated according to the visual extinction-dependent formula provided by Garrod & Pauly (2011). This results in a gradual fall in dust temperature from  $\sim 16 \text{ K}$  to  $8 \text{ K}$  as gas density and visual extinction rise. The gas temperature is held steady at  $10 \text{ K}$  throughout the collapse stage.

The visual extinction during the collapse takes an initial value of 2 mag, and is scaled with the density according to the expression  $A_{\text{V}} \propto n_{\text{H}}^{2/3}$ . An additional background visual extinction ( $A_{\text{V,BAC}}$ ) can be considered under the assumption that the collapse is initiated in the deeply embedded position in the molecular cloud.

$$A_{\text{V}} = \frac{3.1}{5.8 \times 10^{21}} N_{\text{H}} + A_{\text{V,BAC}}. \quad (3.1)$$

Once the density reaches the final value specified for the source under consideration, it is followed by a static warm-up stage which resembles the vicinity of a central heat source. The warm-up characteristics such as maximum temperature and warm-up timescale can be tuned depending on the source properties. The gas density is assumed to be high enough for the gas and dust temperatures to be well coupled at this stage.

species, $i$	$n(i)/n_{\text{H}}^{\text{a}}$
H	5.0(-4)
H <sub>2</sub>	0.49975
He	0.09
C	1.4(-4)
N	2.1(-5)
O	3.2(-4)
S	8.0(-8)
Na	2.0(-8)
Mg	7.0(-9)
Si	8.0(-9)
P	3.0(-9)
Cl	4.0(-9)
Fe	3.0(-9)

Notes. <sup>a</sup>  $A(B) = A^B$

Table 3.2: Initial elemental and chemical abundances

## 3.3 Data analysis and Results

### 3.3.1 Emission map

To identify AA emission, we select bright transitions of AA by using the Splatalogue web tool <sup>1</sup> with the following line selection criteria: Einstein coefficient  $\log(A_{ij}) > -5$  and upper level energy  $E_{\text{up}} < 350$  K. CDMS and JPL database are used for this selection process. A total of 31 bright AA transitions fulfilling this criteria are found within the frequency coverage. For each bright transition line, a cleaned channel map is generated for 80 channels of 0.5 km/s starting at -10km/s defined in the LSRK frame. One of the brightest transition of acetaldehyde at 312.78377 GHz ( $16_{1,15} - 15_{1,14}$ ,  $A$ ;  $E_{\text{up}} = 131$  K,  $S_{ij}\mu^2 = 201$  D<sup>2</sup>) is found to be little contaminated by nearby molecular lines. This transition is used to manually identify AA components, then the deeper investigation is performed for the identified regions.

Moment 0 map is generated by integrating velocity channel of the representative AA transition from  $v_{\text{LSR}} = 4.0$  km/s to  $v_{\text{LSR}} = 8.5$  km/s (figure 3.1). Four emission peaks (AA1 to AA4; black contour) are determined with  $5\sigma$  criteria, and three peaks above  $3\sigma$  (yellow contour) are additionally presented in the figure. All of them are associated with the previously reported sources – HC-SW/Ethanol Peak (AA1), HC-N/MF10 (AA2), IRc7 (AA3), MF3 (AA4), CR/MF1, HC, and IRc21. The main emission peak AA1 is located about  $4''.5$  southwest of the hot core. This HC-SW region is known as the most abundant chemical inventory of organic materials in Orion KL, and it hosts many COM sources such as ethylene glycol peak (EGP) and ethanol peak (EtP) (Tercero et al., 2015). In particular, AA1 corresponds to EtP, implying the chemical correlation between AA and ethanol. All but AA3 components are characterized with a single  $v_{\text{LSR}}$  while AA3 hosts

<sup>1</sup><http://www.cv.nrao.edu/php/splat>

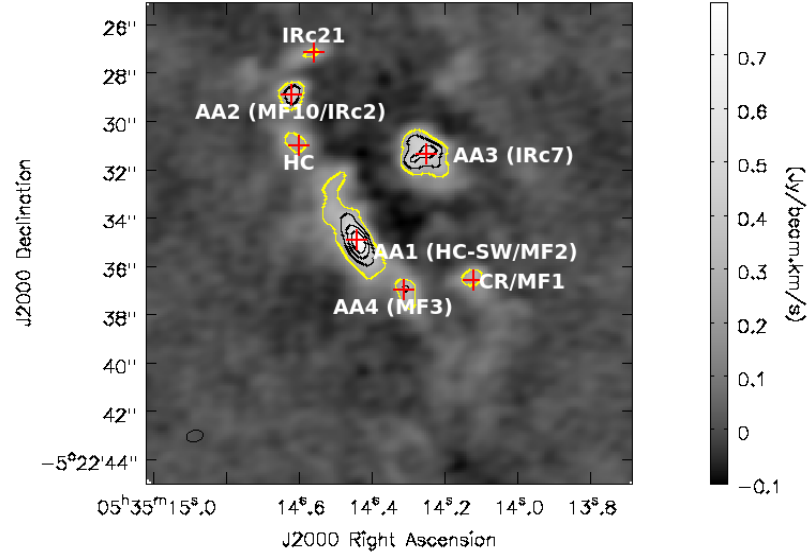


Figure 3.1: Acetaldehyde integrated intensity map at 312.78377 GHz. The synthesized beam is shown in the bottom right corner. The contour levels are  $(3,5,7,9) \times \sigma$  ( $\sigma=0.07$  Jy/beam km/s; uncorrected for primary beam). Yellow contour is at  $3\sigma$  while black contours are at above  $5\sigma$ . The cross mark the AA peak positions above  $3\sigma$ .

four different velocity components ( $v_{\text{LSR}}=4.5, 5, 6,$  and  $8$  km/s) overlapping each other.

AA source parameters are estimated by using a 2-D Gaussian fitting method, and the result is summarized in Table 3.3. It should be noted that the substructures within AA3 are not resolved here. We fit the substructures of AA3 altogether by integrating a relatively wide velocity interval ( $v_{\text{LSR}}$  from 4.0 km/s to 8.5 km/s). Fitting the substructures separately with a narrow interval of velocity integration was unfavored because of the complex spatial and kinematic structure of AA3. The resolved kinematic structure of AA3 can be more clearly seen in the channel map (figure 3.2).

AA component	position name	RA (J2000) 05 <sup>h</sup> 35 <sup>m</sup> ...	Dec (J2000) -05 <sup>o</sup> 22' <sup>...</sup>	$V_{\text{LSR}}$ (km/s)	source size ("×")
1	HC-SW (Ethanol Peak; EtP)	14.44	34.91	7.5	2.8×1.1
2	HC-N (MF10/IRc2)	14.62	28.88	7.5	1.2×0.9
3	HC-W(the vicinity of IRc7)	14.25	31.36	4.5-8	1.8×1.4
4	MF3	14.31	36.97	7.5	2.0×0.9
	CR (MF1)	14.12	36.61	6.5	1.2×1.0
	HC	14.61	30.85	4.5	1.5×1.1
	IRc21	14.58	27.19	6	1.7×0.7

Table 3.3: Source parameters characterized by 2-D Gaussian map fitting

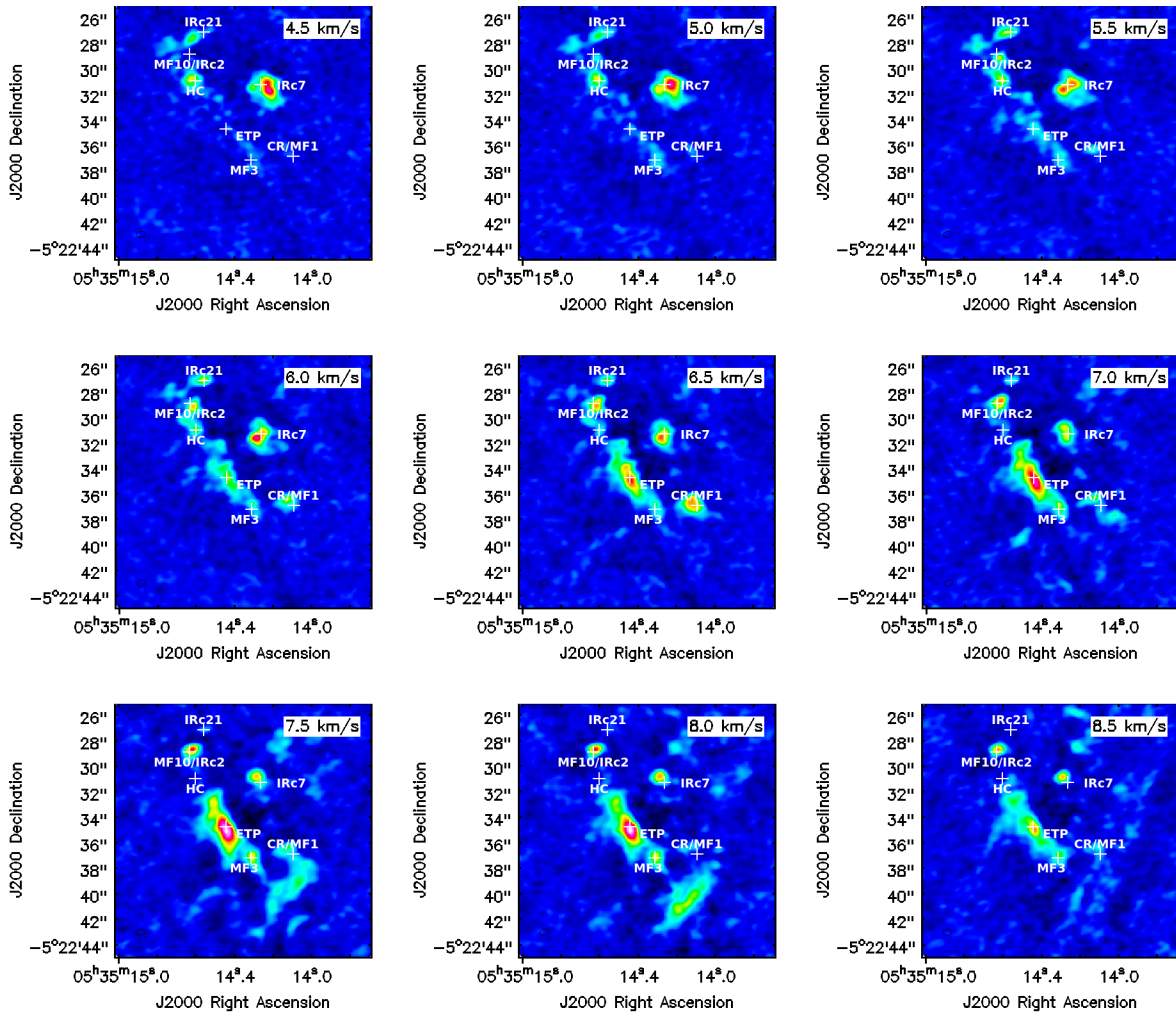


Figure 3.2: Channel map of the representative AA transition (312.78377 GHz)

Frequency (GHz)	154.32220	288.00382	312.71061	312.78377	354.81294
Band	4	7	7	7	7
Transition	8( 3, 6)- 7( 3, 5) E	16( 0,16)- 15( 1,15) A	16( 1,15)- 15( 1,14) E	16( 1,15)- 15( 1,14) A	18( 2,16)- 17( 2,15) E
$S_{ij}\mu^2$ ( $D^2$ )	86.96	27.53	201.19	201.10	225.04
$\log(A_{ij})$ ( $s^{-1}$ )	-3.96	-3.93	-2.96	-2.96	-2.80
$E_{up}$ (K)	53.60	123.53	130.73	130.68	169.65
$T_{peak}$ (mJy/beam)	13.3 (1.5)	75 (14)	312 (27)	380 (15)	593 (29)
$\Delta v$ (km/s)	2.27 (0.30)	1.09 (0.24)	2.49 (0.24)	2.02 (0.10)	1.10 (0.06)
Integral (mJy/beam km/s)	32.1 (5.6)	87 (25)	853 (109)	817 (51)	693 (52)
rms (mJy/beam)	2	9	39	26	34
comment	a-type	b-type	a-type	a-type	a-type

Table 3.4: Line parameters for the detected transitions for AA1

### 3.3.2 Line identification and spectra

Other AA transitions are investigated by analyzing their spectra extracted from the four intensity peaks of AA (table 3.3). The spectral peaks are compared with rms noise levels ( $\sigma$ ) to determine line detection. We performed 1-D Gaussian fitting for the collected spectra by using a specfit task in CASA. The rms is measured using an imstat task of CASA across the field for a specific channel where the spectral peak exists. This line detection analysis is performed without correction for primary beam attenuation to achieve a consistent noise across the field of view.

Five AA transitions including the AA representative line are detected out of 31 bright AA transitions above  $5\sigma$  level without severe blending. AA1 is the only region where all the five transitions are clearly identified above the detection limit (see figure 3.3). Table 3.4 summarize their line parameters and  $\sigma$  values determined from the the spectra collected from the intensity peak pixel of AA1. The detected transitions are found in the two project data – 2016.1.00297 (band 7) and 2017.1.01149 (band 4) out of four projects under investigation. All of them are a-type ( $\Delta\kappa_p = 0$ ,  $\Delta\kappa_o = \pm 1$ ) transitions, except for one b-type ( $\Delta\kappa_p = \pm 1$ ,  $\Delta\kappa_o = \pm 1$ ) transition at 288.003816 GHz. All the a-type lines are characterized to be bright compared to other non-detected transitions ;  $S_{ij}\mu^2 \sim 90 D^2$  and  $E_{up} \sim 60$  K at band 4,  $S_{ij}\mu^2 > 200 D^2$  and  $E_{up} < 170$  K at band 7.

### 3.3.3 Derivation of physical parameters

Molecular lines from the main emission region AA1 are modeled by using eXtended CASA Line Analysis Software Suite (XCLASS) (Möller et al., 2017). The observations are compared with the synthesized spectra to find the column densities ( $N_{\text{tot}}$ ) and the rotational temperatures ( $T_{\text{rot}}$ ) that best fit the observation. Figure 3.3 shows the best-fit results of the AA lines. It takes into account the beam dilution, the line opacity, and line blending under the assumption of local thermodynamical equilibrium (LTE). The line modeling results will be discussed in §4 by comparing with other HCO-bearing species from the literature (Tercero et al., 2015, 2018).

Main input parameters are hydrogen column density  $N(\text{H})$ , systemic velocity  $v_{\text{LSR}}$ , source size, line FWHM  $\Delta v$ , rotational temperature  $T_{\text{rot}}$ , and column density  $N_{\text{tot}}$ . We assume  $N(\text{H})=2.0 \times 10^{24} \text{ cm}^{-2}$  and  $v_{\text{LSR}}=7.5 \text{ km/s}$  while the other four parameters are left as free parameters. The spectrum of AA is first computed with an initial guess of parameter vectors; source size of  $1''$ ,  $\Delta v$  of  $2.0 \text{ km/s}$ ,  $v_{\text{off}}$  of  $1 \text{ km/s}$ ,  $T_{\text{rot}}$  of  $120 \text{ K}$ , and  $N_{\text{tot}}$  of  $2.0 \times 10^{15} \text{ cm}^{-2}$ . The model then find minima of  $\chi^2$  distribution varying the source size between  $0.5''$  and  $100''$ , the line FWHM between  $1.0 \text{ km/s}$  and  $3.5 \text{ km/s}$ ,  $v_{\text{off}}$  between  $-1.5 \text{ km/s}$  and  $1.5 \text{ km/s}$ , column density between  $10^{14} \text{ cm}^{-2}$  and  $10^{17} \text{ cm}^{-2}$ , and rotational temperature between  $80 \text{ K}$  and  $150 \text{ K}$ .

To provide appropriate spectra to be compared with the model, primary beam correction is performed for the AA detected channel maps. Spectra are then re-extracted by averaging over  $1'' \times 1''$  around the AA1 peak. The region chosen for the spectral extraction is the same with TCR18 for consistent comparison. Flux density is converted to an antenna temperature using the conversion factor appropriate to its spectral window. The AA1 observation can be best described with  $N_{\text{tot}}(\text{CH}_3\text{CHO}) = 3.18 \times 10^{15} \text{ cm}^{-2}$  and  $T_{\text{rot}}=150 \text{ K}$ . Source size is estimated to be  $\sim 1''$ , which is consistent with the region size for spectra extraction.

## 3.4 Discussions

### 3.4.1 Spatial distribution of acetaldehyde and other HCO-bearing species

The spatial distribution of AA is compared with EtOH and other aldehyde-like species from the literature. TCR18 investigated many O-bearing COMs in Orion KL including EtOH and three HCO-bearing species (MF, GA, and FA) using ALMA SV data. They found the spatial segregation between the species depending on their functional groups. Ether (the species containing C-O-C) generally shows an extended V-shape morphology that links HC, CR, and BN objects, showing the brightest peak toward CR. In contrast, the species not bearing C-O-C but hydroxyl (C-O-H) group (alcohols and carboxylic acids) shows missing or relatively weak emission toward CR, and its brightest emission peak is associated with HC-SW. For example, MF emission follows a typical V-shape distribution of ether while the other two HCO-bearing species show their main emission peak toward

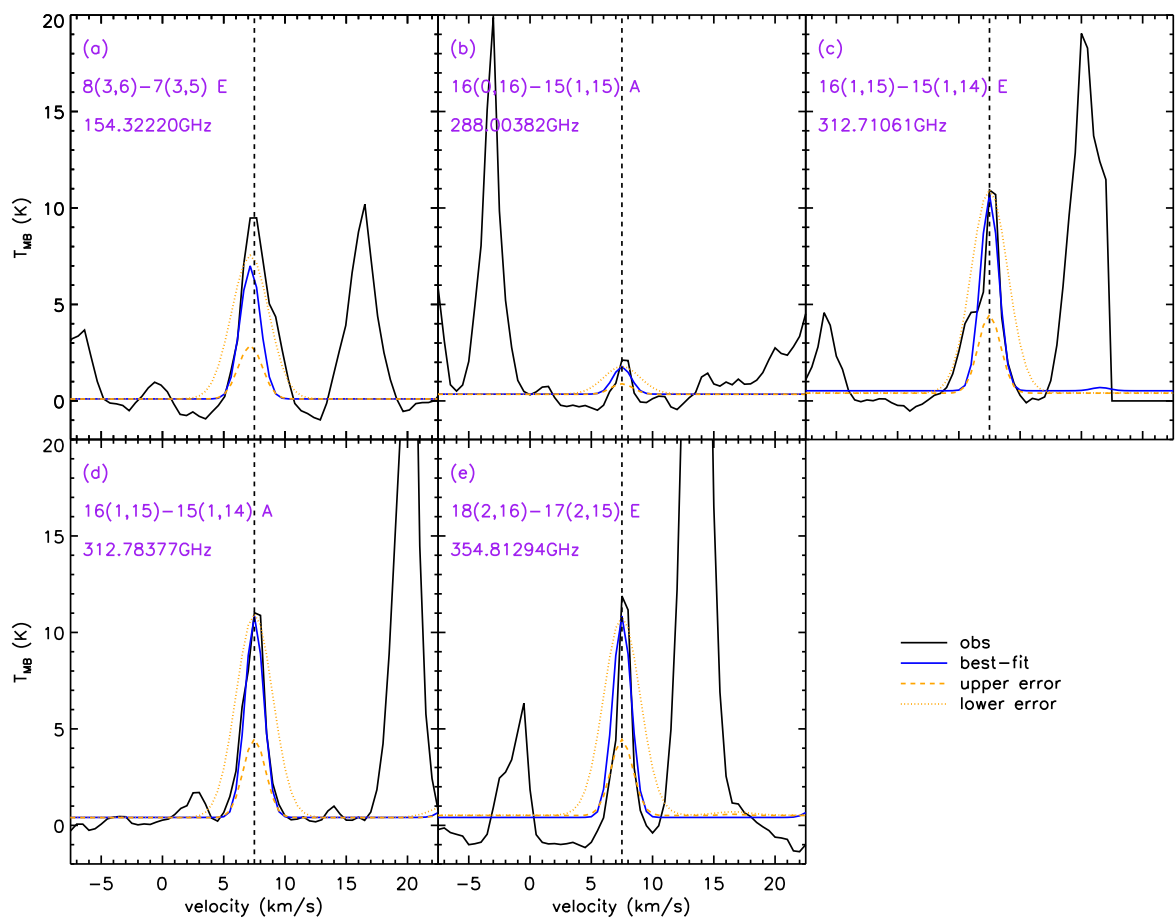


Figure 3.3: The XCLASS model spectra of acetaldehyde (blue) overlaid with ALMA observations toward AA1 (black solid)

HC-SW (see figure 1 in TCR18).

TCR18 well explains the chemical segregation with a grain-surface formation scenario, although they did not rule out the potential contribution of gas-phase chemistry. According to the grain-surface chemistry, methanol can be efficiently formed on the grain surface even at low temperature through ongoing hydrogenation of accreted materials. The products from this process can be broken down into radicals through energetic processes. This process is followed by radical-radical recombinations to form larger COMs on grain surfaces. TCR18 propose that different radicals, methoxy ( $-\text{CH}_3\text{O}$ ) and hydroxymethyl ( $-\text{CH}_2\text{OH}$ ) is dominating the radical-radical reactions of CR and HC-SW, respectively, driving different chemical complexity of the region.

The spatial distribution of AA is more consistent with the two non-ether HCO-bearing species – GA and FA ; the brightest AA emission (AA1) is found at HC-SW but the emission toward CR is weak not fulfilling the  $5\sigma$  criterion. Particularly, we note the coincidence in the emission peaks between FA and AA. FA also shows the second brightest peak at AA2, and another relatively weak component is found at AA4. Even though FA peak is not clearly identified toward AA3, this discrepancy can be caused by the different range of velocity integration to generate the moment 0 map, considering the complex kinematic structure of AA3 region. FA is the only species that shows the distinctive peak at AA2 among the thirteen O-bearing species investigated by TCR18. This obviously indicates the close chemical relation between FA and AA. The weak AA emission toward CR is consistent with the proposition of TCR18 in that AA is not bearing C-O-C functional group. However, the bright AA emission towards HC-SW despite the absence of C-O-H structure indicates that other chemical processes without involving either methoxy or hydroxymethyl radical are efficiently contributing to the chemical complexity toward this region as well.

It is interesting that no chemical segregation is selectively found for general HCO-bearing species. Even though the aforementioned species are all bearing HCO, the morphologies of those species are different, except for the spatial coincidence between FA and AA. This lack of correlations between the HCO-bearing species can imply the ubiquitous characteristic of HCO radical. If the HCO radical is abundant on the grain-surface regardless of physical environments, the other counterpart consisting of the molecule would be the bottleneck to determine the chemical segregation between the species. This hypothesis is consistent with the fact that the HCO radical is the first species that could be formed through the CO hydrogenation reaction chain ( $\text{CO} - \text{HCO} - \text{H}_2\text{CO} - \text{CH}_3\text{O}/\text{CH}_2\text{OH} - \text{CH}_3\text{OH}$ ) on the grain-surface.

Under the assumption that surface processes dominated the chemistry, the chemical status of each region can be characterized as follows.

- HC-SW (The richest in chemistry - ether / alcohols / carboxylic acids / AA abundant) : both methoxy and hydroxymethyl are contributing to the chemical complexity. Other chemical processing related to the simpler functional groups are active as well.
- CR (Moderate rich in chemistry - only ether abundant) : only methoxy is driving chemical complexity, and hydroxymethyl radical may not exist.
- HC-N (Relatively simple COMs exist) : Relatively small radicals are contributing to the chemistry of the region.

Species	$N_{\text{tot}}(\text{i})$ ( $\text{cm}^{-2}$ )	$\frac{N_{\text{tot}}(\text{i})}{N_{\text{tot}}(\text{FA})}$
HCOOH; FA	1.0E+15	1
CH <sub>3</sub> CHO; AA	3.0E+15	3
HCOOCH <sub>3</sub> ; MF	2.4E+17	240
CH <sub>2</sub> OHCHO; GA	< 3.0E+14	<0.3
C <sub>2</sub> H <sub>5</sub> OH; EtOH	6.4E+16	64

Table 3.5: Column densities of HCO-bearing species

Species	$N_{\text{tot}}(\text{i})$ ( $\text{cm}^{-2}$ )	$\frac{N_{\text{tot}}(\text{i})}{N_{\text{tot}}(\text{FA})}$
FA	1.4E-07	1
AA	5.5E-09	<0.1
MF	1.2E-07	0.9
GA	3.0E-08	0.2
EtOH	3.3E-07	2.4

Table 3.6: Ice abundances of the control model at the end of prestellar phase

### 3.4.2 Aldehyde chemistry and chemical modeling

Relative abundance ratios between the HCO-bearing species and EtOH at AA1 are determined based on the results from this work and from TCR18; GA:FA:AA:EtOH:MF = <0.3:1:3:60:240. The observed column densities are significantly different depending on the species, showing a wide range of the relative abundance ratios with respect to FA column density from <0.3 to 240. Table 3.5 lists the estimated column densities for each species. Because these values are derived based on various datasets, it is important to compare the observational specifications to achieve reliable comparison between them. Angular resolution and maximum recoverable scale (MRS) of the archive data investigated here are about two times smaller than those of SV data that used by TCR18. This means that the large scale structure previously seen in the SV data can be resolved out in the recent archive data. To our best knowledge, however, AA emission has not been clearly detected toward Orion KL with single-dish observation despite many attempts. This implies the flux contribution from the large scale AA structure is minor, and the effect of resolving out would be negligible. In addition, the region size for the spectral extraction is smaller enough than the MRS.

The observed relative abundance ratios (GA:FA:AA:EtOH:MF) are investigated with a chemical model to understand the chemistry related to the aldehyde-like species and EtOH. We perform an one-point chemical model for HC-SW which is associated with the brightest AA emission peak, AA1. We assume that density increases from  $n_{\text{H}} = 2.0 \times 10^3 \text{ cm}^{-3}$  to the maximum value of  $n_{\text{H}} = 8.0 \times 10^8 \text{ cm}^{-3}$  during the collapse stage. The warm-up stage then follows with a timescale of 550 years based on the assumption that this region is externally heated by the recent explosion.  $T_{\text{kin}}$  increases from 8 K to

Species	$N_{\text{tot}}(\text{i})$ ( $\text{cm}^{-2}$ )	$\frac{N_{\text{tot}}(\text{i})}{N_{\text{tot}}(\text{FA})}$
FA	9.3E-10	1
AA	5.6E-11	0.1
MF	1.3E-08	14.0
GA	1.9E-12	<0.1
EtOH	2.2E-11	<0.1

Table 3.7: Gas-phase abundances of the control model at the end of warm-up ( $T_{\text{kin,max}}=120$  K)

a range of maximum temperatures (100K-150K) to understand the effect of temperature on chemistry. The assumed physical conditions are based on Pagani et al. (2017) and references therein.

We first set up a control model, then how the various physical/chemical model inputs affect the chemistry is further explored to find the best model. The essential model setup and a chemical reaction network for the control is consistent with a hot core model described by Garrod et al. (2021, in prep). A free-fall collapsing timescale (no magnetic retardation) is assumed, and the collapse is initiated at an initial visual extinction of  $A_{V,0}=2$ . Table 3.6 summarizes the modeled ice abundances at the end of density evolution, while table 3.7 lists the gas-phase abundances of the species when the temperature reaches  $T_{\text{max}}$  after the warm-up. In this control model, the gas-phase abundances of the species after the warm-up are far off from the observation, implying the necessity of fine-tuning of the model. The relative abundance ratios between the species in gas are significantly different from the ones in ice mantles, nevertheless little chemical processing is expected after the ice species come off the grains due to the short warm-up timescale. This discrepancy between gas- and solid-phase chemistry is caused by the different thermal desorption behaviors of the species that sensitively change at the “luke-warm” temperature regime. To disentangle the effect of thermal desorption during the warm-up phase, we focus on examining the impact of different model parameters on ice chemistry during the prestellar phase. After that, the parameters governing the desorption of the species such as binding energies and  $T_{\text{max}}$  are further investigated.

By comparing the results of the control model with the observation, we could summarize several aspects to improve in the control as follows; 1) given the low AA ice abundance in the model, some chemical/physical processes to form AA could be necessary in the control, 2) considering the high ice abundances of FA and EtOH, the formation of FA and EtOH on the ice surface would be too efficient, or additional sink reactions should have considered in the control, 3) given that EtOH abundance in gas is significantly low despite its high ice abundance, the adjustment of binding energies might be necessary. Here, we examined four different model inputs, focusing on improving the three aforementioned aspects – chemical reaction networks, visual extinction, collapsing timescale, and binding energies of the species. Through this modeling work, we aim to 1) explain the observed GA:FA:AA:MF ratio in AA1 region, 2) explore dominant formation and destruction reactions for each species, 3) understand chemical relation between FA and AA, 4) examine the spatial coincidence between EtP and AA1.

Related species	Reaction ( $\text{cm}^3/\text{s}$ )	$k_{\text{OH}}(T)$	$k_{\text{OH}}(120\text{K})$	Notes
MF	$\text{OH} + \text{HCOOCH}_3 \rightarrow$ $\text{COOCH}_3 + \text{H}_2\text{O}$		5.0E-13	<sup>a</sup>
FA	$\text{OH} + \text{HCOOH} \rightarrow$ $\text{COOH} + \text{H}_2\text{O}$		5.0E-13	<sup>b</sup>
AA	$\text{OH} + \text{CH}_3\text{CHO} \rightarrow$ $\text{CH}_3\text{CO} + \text{H}_2\text{O}$	$1.2 \times 10^{-11}(T/300 \text{ K})^{-1.8} e^{-28.7/T}$	5.0E-11	<sup>c</sup>
EtOH	$\text{OH} + \text{C}_2\text{H}_5\text{OH} \rightarrow$ $\text{C}_2\text{H}_4\text{OH} + \text{H}_2\text{O}$	$2.0 \times 10^{-11}(T/300 \text{ K})^{-0.71}$	4.0E-11	<sup>d</sup>

Notes. <sup>a</sup> Jiménez et al. (2016); Le Calvé. (1997) – 22-64 K, 233-372 K; <sup>b</sup> The  $k_{\text{MF}}(120\text{K})$  is adopted; <sup>c</sup> Blázquez et al. (2020) – 11.7-115 K; <sup>d</sup> – 21-107 K

Table 3.8: Updated / newly-included gas-phase reactions

### chemical network

To explain the relative abundance ratios from the observation, we add or update the reactions related to the HCO-bearing species and EtOH by using the chemical network of Garrod et al. (2021) as the basis. The new/updated reactions in gas- and solid-phase are summarized in table 3.8-3.9, respectively. The gas-phase reactions newly included here are the neutral-neutral reactions between the aforementioned molecules and OH radicals. The molecules are destroyed through the H-abstraction by OH. The rate coefficients of these reactions are recently estimated for EtOH, AA, and MF at astrophysical relevant temperature, and it is found that the reaction rate coefficients are particularly high for EtOH and AA due to quantum tunneling (Ocaña et al., 2018; Blázquez et al., 2020). The rate coefficient for MF is not parameterized so that the experimental results were not directly applicable to the chemical model. Instead, we extrapolate the measurement from two different range of temperature (22-64 K; Ocaña et al. 2018 and 233-372 K; Le Calve 1997), and adopt the constant  $k_{\text{MF}}=5 \times 10^{-13} \text{ cm}^3/\text{s}$  which roughly represent the rate coefficient at  $100 \text{ K} < T < 150 \text{ K}$  (see figure 3.4). The neutral-neutral reaction for FA and GA has not been measured at low temperature. We adopted the same  $k_{\text{MF}}$  for these two species, because the rate coefficient measured at  $T > 200 \text{ K}$  behaves similar to MF.

Table 3.10 (model B) shows the change in gas-phase abundances of the species with the updated gas-phase reaction network. The inclusion of new gas-phase reactions little affects the chemistry because the warm-up timescale ( $\sim 500 \text{ yr}$ ) is too short for these reactions to affect the chemistry after ice species come off the grains. However, if the chemical model were running with a typical warm-up timescale for hot corinos ( $\sim 10^5 \text{ yr}$ ), these gas-phase reactions could play important roles. Considering the high  $k_{\text{MF}}$  measurement at  $T < 60\text{K}$  (figure 3.4), assuming the constant  $k$  value for a wide range of temperature can result in a significant underestimation of the impact of the reactions in cold environments. To examine this, higher  $k$  values are tested in the prestellar model. It is found that the new gas-phase reactions little affect the chemistry regardless of the assumed reaction rate coefficients. This is because most of the volatile species have not come off the grains yet in the prestellar environment. These results show that the observed relative abundance

Related species	Reaction	$E_A$ (K)	Width ( $\text{\AA}$ )	Notes
FA	$\text{CO} + \text{OH} \rightarrow$ $\text{CO}_2 + \text{H} / \text{COOH}$	800	1.0	branching ratio updated - 99:1 $\rightarrow$ 99.9:0.1
EtOH	$\text{H} + \text{C}_2\text{H}_2 \rightarrow$ $\text{C}_2\text{H} + \text{H}_2$	1300	1.0	new <sup>a</sup>
	$\text{H} + \text{C}_2\text{H}_3 \rightarrow$ $\text{C}_2\text{H}_2 + \text{H}_2$	0	1.0	new, 50% fractionation against hydrogenation
	$\text{H} + \text{C}_2\text{H}_4 \rightarrow$ $\text{C}_2\text{H}_4 + \text{H}_2$	1410	1.0	$E_A$ updated - 605 K $\rightarrow$ 1300 K <sup>b</sup>
	$\text{O} + \text{C}_2\text{H}_5 \rightarrow$ $\text{C}_2\text{H}_4 + \text{OH}$	0	1.0	new, 50% fractionation against hydrogenation
	$\text{OH} + \text{C}_2\text{H}_5 \rightarrow$ $\text{H}_2\text{O} + \text{C}_2\text{H}_4$	0	1.0	new, 50% fractionation against hydrogenation
AA	$\text{H} + \text{CH}_3\text{CO} \rightarrow$ $\text{CH}_2\text{CO} + \text{H}_2$	0	1.0	new, 50% fractionation against hydrogenation
EtOH, AA	$\text{H} + \text{C}_2\text{H}_4\text{OH} \rightarrow$ $\text{CH}_3\text{CHO} + \text{H}_2$	0	1.0	new, 5% fractionation against other reaction channels.

Notes. <sup>a</sup> The same values for  $\text{H} + \text{C}_2\text{H}_2 \rightarrow \text{C}_2\text{H}_3$  – 1992BAU/COB411-429; <sup>b</sup> 1972KER/PARB

Table 3.9: Updated / newly-included grain-surface and ice-mantle reactions

Model	A	B	C	D	E	F
	control	A + gas reac	A + surf reac	B + C + high $A_{V,0}$	B + C + $B=0.3$	D+E
FA	1.4E-07	1.4E-07	1.0E-07	9.6E-08	1.6E-08	1.4E-08
AA	5.5E-09	5.5E-09	1.1E-08	2.6E-08	1.1E-09	2.3E-08
MF	1.2E-07	1.2E-07	1.2E-07	1.1E-07	1.0E-07	1.1E-07
GA	3.0E-08	3.0E-08	3.0E-08	2.9E-08	2.6E-08	2.5E-08
EtOH	3.3E-07	3.3E-07	1.9E-07	5.2E-07	1.0E-08	2.0E-07

Table 3.10: Ice abundances ( $n(i)/n_{\text{H}}$ ) with the model update

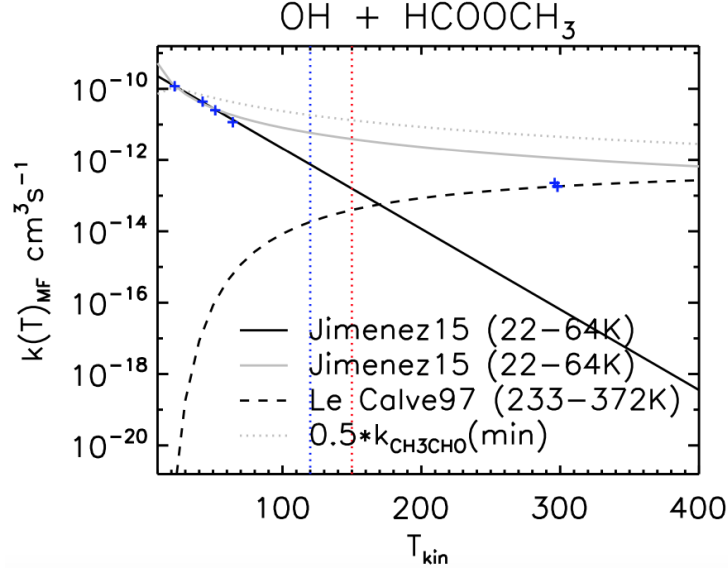


Figure 3.4: Extrapolation of  $k$  from two different experimental data for MF

ratios are mainly governed by the ice compositions as a result of ice chemistry and thermal desorption.

The solid-phase reactions updated here are related to FA, EtOH, and AA. As for FA, two reactions on grain surfaces mainly contribute to the formation of FA as follows



In the latter, the small fractionation of  $\text{CO} + \text{OH}$  reaction products can form  $\text{COOH}$ , which can be transformed to FA through hydrogenation. The branching ratio (BR) to form  $\text{COOH}$  against  $\text{CO}_2 + \text{H}$  has not been constrained well, and we assumed in the control that 1% of the  $\text{CO} + \text{OH}$  reaction products would form  $\text{COOH}$ . However, the high ice abundance of FA seen in the control shows that the BR of 1% might be still aggrandized. Thus we empirically adjusted the BR to be 10 times lower (0.1%) in the new network.

The update of the solid-phase reactions are particularly focused on EtOH. This is because the chemical network related to EtOH was biased to the formation pathways. In the control, two reactions mainly contribute to the formation of EtOH.



The  $\text{C}_2\text{H}_4\text{OH}$  and  $\text{C}_2\text{H}_5\text{O}$  radicals in the latter are formed by ongoing hydrogenation of hydrocarbon in the model;  $\text{C}_2\text{H} - \text{C}_2\text{H}_2 - \text{C}_2\text{H}_3 - \text{C}_2\text{H}_4 - \text{C}_2\text{H}_5 - \text{C}_2\text{H}_6$ . We found that only forward reactions are considered in the previous chemical network, resulting in the overproduction of EtOH ice. The backward reactions of this reaction chain are newly included. In addition to that, we consider that the small fractionation of  $\text{H} + \text{C}_2\text{H}_4\text{OH}$  reaction products can result in AA. This reaction can affect both EtOH and AA abundances in the ice.

The surface reaction network related to AA in the control is visualized in figure 3.5. The hydrogen abstraction of  $\text{CH}_3\text{CO}$  (red arrow in figure 3.5) is newly included as another

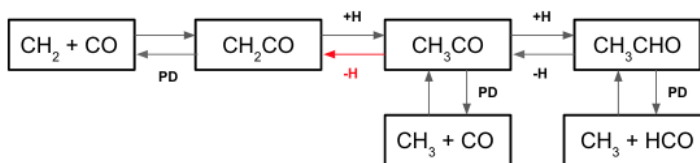


Figure 3.5: Surface reaction diagram for the formation of acetaldehyde

competitive channel against  $\text{CH}_3\text{CO} + \text{H} \rightarrow \text{CH}_3\text{CHO}$  to provide more complete surface network for AA.

Table 3.10 (model C) summarizes the changes in the ice abundances at the end of the prestellar phase with the updated chemical network. All the three species related to the network update show considerable changes. The fractionation adjustment for  $\text{CO} + \text{OH}$  reaction to form  $\text{COOH}$  results in 25% lower FA ice abundance. The EtOH ice abundance decreases by a factor of  $\sim 2$  because of the new sink fractionation of  $\text{C}_2\text{H}_4\text{OH}$  to form AA. Interestingly, the inclusion of the backward reactions for hydrocarbon reaction chains does not change ice abundances of EtOH a lot. Rather, the population of hydrocarbons has been rebalanced. The hydrogen and carbon budget was previously crowded in the higher order of  $\text{C}_2\text{H}_n$  such as  $\text{C}_2\text{H}_6$ . With the new network, however, the abundances of the intermediate  $\text{C}_2\text{H}_n$  increases while  $\text{C}_2\text{H}_6$  abundance decreases. This change can further affect the surface chemistry involving the intermediate hydrocarbon radicals. AA ice abundance increases by a factor of  $\sim 2$  with the update of surface network. Although the inclusion of H-abstraction of  $\text{CH}_3\text{CO}$  into the chemical network effectively reduces AA abundance in the ice, the increment of AA ice from the new formation channel ( $\text{H} + \text{C}_2\text{H}_4\text{OH}$ ) dominates over the decrement. This efficient formation of AA from the precursor of EtOH might explain the spatial coincidence between EtP and AA1. Even though there is somewhat improvement in describing the observed ratios (GA:FA:AA:EtOH:MF) with the update of the chemical network, the modeled ratios are still far off from the observations. This implies that other explanations are needed to more completely understand the chemistry in AA1.

### Collapsing timescales and visual extinction

The chemistry in star-forming regions is governed by three physical factors – density, temperature, and visual extinction. By varying the model parameters related to them, we examined how the ice composition is affected by different physical conditions. We first set a high visual extinction model by adopting an initial visual extinction of  $A_{V,0}=3$ . The model with the updated chemical network is used as a basis. Table 3.10 (model D) compares the ice composition in the new model with the control. The higher  $A_V$  environment significantly increases EtOH and AA abundances in the ice while the other three species slightly decreases. The disparity between the two models arises at early times of collapse, where interstellar radiation fields play an important role in chemistry. In such low-density environments, the dust temperature of the high  $A_V$  model is lower than the control, because heating by the external UV photons is suppressed. This results in the slower diffusion of atomic hydrogen on grain surfaces, which ultimately retard driving chemical complexity. However, it should be noted that the destruction of large ice species via UV photodissociation (PD) is also suppressed in the high  $A_V$  model. Thus, the new ice composition is determined by the balance between the slower formation of large ice

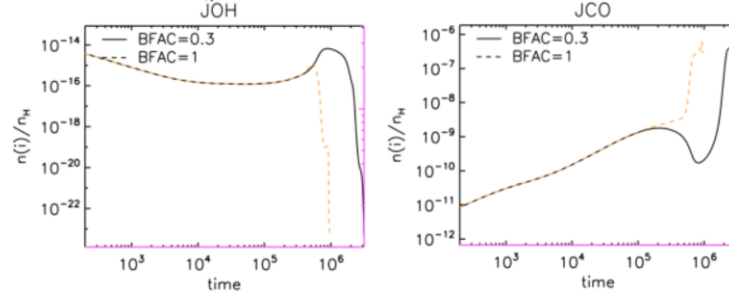


Figure 3.6: Time-dependent ice abundances of CO and OH on the grain surface

species through H diffusion and the slower PD destruction of the species. EtOH and AA ice would be more vulnerable to PD, so that the ice abundances in the high  $A_V$  model (low UV flux) increase despite the lower H diffusion rate. As for the other three species, the two chemical processes balance well, resulting in little changes in the ice abundances.

The repercussion of slower collapsing timescale is examined in another experimental model. The magnetic retardation factor for collapse,  $B$ , is adopted here to control the collapse timescale. This parameter takes a value between 0 (static) and 1 (free-fall), and we set  $B=0.3$  for the experimental setup. This results in a collapse timescale approximately 3 times longer than the free-fall timescale. Table 3.10 (model E) summarizes the ice composition in the slower collapse model. Ice abundances of EtOH, AA, and FA significantly decrease. Considering that PD is a dominant chemical process governing the destruction of EtOH and AA, decrease of these species can be explained by the longer exposure time to external UV photons due to slow density evolution. In the case of FA, however, different mechanisms might be needed. Figure 3.6 shows the evolution of ice abundances of CO and OH on the grain surface during the prestellar phase, which are the main reactants to form the precursor of FA, COOH. CO abundance in the experimental model abruptly decreases at late times of collapse ( $\sim 10^6$  yr), while in the free-fall collapse model it does not. This is when the OH ice is the most abundant on the surface during the collapse. The predominance of the OH ice on the grain surface, when CO is depressed, would result in inefficient formation of FA in the slower collapse model.

Table 3.10 (model F) shows the ice abundances of the model adopting the slower collapsing timescale as well as the higher visual extinction. AA abundance in the ice increases effectively while those of EtOH and FA decrease, which better reproduces the observational features. This model is then used as a basis for the further exploration of desorption behaviors of the species.

### Desorption energies

The update of chemical networks and/or the different physical parameters employed in the model does not fully explain the observed abundance ratios in the gas despite the improvements in description of ice compositions. Especially, the distinctively high abundance of EtOH and MF compared to others in the observations (e.g.  $MF/FA \sim 240$ ) is hardly reproduced. The chemistry in the gas and on the grain-surface are coupled through desorption / accretion process, and we could expect that the different treatment for the desorption of ice species would be necessary. Binding energies ( $E_{des}$ ) are governing these processes within the model but are bearing high uncertainties for the moment. In this section, a different set of  $E_{des}$  is adopted based on the previous literature, and its impact

Species	$E_{\text{des, prev}}$ (K)	$E_{\text{des, new}}$ (K)	Notes
H <sub>2</sub> O	5700	4815	a
CH <sub>3</sub> CHO; AA	2775	5400	b
C <sub>2</sub> H <sub>5</sub> OH; EtOH	6259	5400	b
HCOOCH <sub>3</sub> ; MF	4210	–	
HCOOH; FA	5570	–	
CH <sub>2</sub> OHCHO; GA	5630	–	

Notes. <sup>a</sup> Sandford & Allamandola (1990); <sup>b</sup> Wakelam et al. (2017)

Table 3.11: The update of binding energies of species

Species	FA	AA	MF	GA	EtOH
100 K	1.7E-14	5.0E-13	7.6E-09	2.1E-17	2.0E-12
110 K	1.1E-11	3.6E-11	1.3E-08	5.8E-15	7.9E-10
115 K	1.2E-10	1.6E-10	1.5E-08	2.9E-13	5.2E-09
120 K	8.0E-10	9.9E-10	2.0E-08	5.4E-11	1.7E-08
130 K	2.8E-09	3.6E-09	3.3E-08	2.8E-09	4.2E-08
140 K	3.7E-09	5.6E-09	4.1E-08	5.2E-09	5.5E-08
150 K	5.9E-09	1.0E-08	6.0E-08	9.6E-09	8.7E-08

Table 3.12: Gas-phase abundances at different warm-up temperature

on the estimated abundances in the gas is discussed.

Table 3.11 summarizes the updated set of  $E_{\text{des}}$  under consideration. The lower binding energy for water  $E_{\text{des}}(\text{H}_2\text{O})$  is newly assumed based on the experimental study for the amorphous solid water (ASW) surfaces by Sandford & Allamandola (1990), although a wide range of values have been estimated for  $E_{\text{des}}(\text{H}_2\text{O})$  depending on methodology and/or experimental setup (e.g. Wakelam et al., 2017; Fraser et al., 2001). This new value for water is also consistent with the DFT calculations by Wakelam et al. (2017). The EtOH binding energy previously used in the model was estimated assuming a crystalline ice surface (Lattalais et al., 2011). We use the lower EtOH binding energy based on the recent DFT calculations for ASW (Wakelam et al., 2017). The binding energy of AA in the new model has changed because the previous value was significantly low compared to other COMs of similar molecular weights. The new  $E_{\text{des}}(\text{AA})$  is measured from the DFT calculations for ASW (Wakelam et al., 2017).

The model with this new set of binding energies are tested with a range of  $T_{\text{kin,max}}$  from 100 K to 150 K. Table 3.12-3.13 shows the new abundances of the species in the gas and its abundance ratios with respect to (w.r.t.) FA column densities, respectively. It is notable that the modeled chemical compositions sensitively change depending on temperatures, in particularly for MF. This high variability of MF/FA ratios seen in the new models is related to the high volatility of MF compared to other species. The adjustment of water binding energy in the new model is related to this. Water is the most abundant ice constituents, and the change in  $E_{\text{des}}(\text{H}_2\text{O})$  can affect the general desorption features within the model. In particular, the ice species with binding energies lower than  $E_{\text{des}}(\text{H}_2\text{O})$  more

Species	AA	MF	GA	EtOH
100 K	30.0	>1000	<0.1	117
110 K	3.3	>1000	<0.1	71
115 K	1.3	125	<0.1	42
120 K	1.2	25	0.1	22
130 K	1.3	12	1.0	15
140 K	1.5	11	1.4	15
150 K	1.8	10	1.6	15

Table 3.13: Relative abundance ratios w.r.t. FA column densities at different warm-up temperature

easily co-desorb with water, otherwise the ice species desorb relatively slowly until high enough thermal energies are provided. As the water binding energy is adjusted to the lower value in the new model, MF become the only species of which binding energy is smaller than water among the five ice species under investigation, achieving the high volatility compared to others. This distinctive characteristic of MF well explains its observational features such as extended morphologies and high column densities.

The observed abundance ratios between the species are adequately consistent with the model results at  $T_{\text{kin,max}}=115$  K (GA:FA:AA:EtOH:MF = <0.1:1:1:42:125). However, it should be noted that the observed ratios is not necessarily represented by a single chemical model. This is because the chemical model represents the chemistry at one single density point while observation does not. The dependency of chemical composition on temperature can be characterized as follows,

$$\begin{aligned} &\text{at } T_{\text{kin}} < 115\text{K}, (\text{MF/FA})_{\text{model}} > (\text{MF/FA})_{\text{obs}} \\ &\text{at } T_{\text{kin}} > 115\text{K}, (\text{MF/FA})_{\text{model}} < (\text{MF/FA})_{\text{obs}}. \end{aligned}$$

Considering the high variability of chemical compositions, the observed ratios can be interpreted as a result of integration of chemistry throughout the line of sight with temperature gradient.

### Acetaldehyde Chemistry

Due to the short warm-up timescale of HC-SW, the observed relative abundance ratios between the aldehyde-like species are determined by the ice compositions as a result of ice chemistry and thermal desorption. The observed chemistry towards AA1 is the results of the integration of chemistry throughout the line of sight with temperature gradient. The lower binding energy of MF than water as well as other species is needed for reasonable description of desorption behavior of the species depending on temperature.

The main formation / destruction pathways of AA on the grain-surface is described in figure 3.5. The net sources of this species are radical-radical recombination ( $\text{CH}_3 + \text{HCO}$ ) and nondiffusive reactions between CO and radicals ( $\text{CH}_2 + \text{CO} / \text{CH}_3 + \text{CO}$ ) followed by hydrogenation (Jin & Garrod, 2020). Because the thermal diffusion of heavy radicals on grain surfaces is inefficient in prestellar environments, the latter would predominantly contribute to the formation of AA. In addition to that, the H-abstraction reaction of the precursor of EtOH ( $\text{H} + \text{C}_2\text{H}_4\text{OH}$ ) considered here would be another important formation pathway of AA. This well explains the spatial coincidence between EtP and AA1. The

H-diffusion reactions in this chemical network are not contributing to the net formation / destruction of AA, but rather involving the chemical cycle between AA and its precursor. The recurrent formation of AA through hydrogenation is an important mechanism for AA ice to chemically desorb at low temperature. As discussed in § 3.4.2, the destruction of AA ice dominated by PD, showing the high ice abundance in low UV flux environments. This vulnerability of AA ice to PD might explain the predominance of AA detection toward quiescent environments in the literature.

### 3.4.3 Searching for other aldehyde species

Propynal ( $C_2HCHO$ ), propenal ( $C_2H_3CHO$ ), and propanal ( $C_2H_5CHO$ ) are the aldehydes with three carbon atoms derived from propyne, propene and propane. They make up three of the five large ( $n_{\text{atom}} \geq 6$ ) aldehydes that have been detected in molecular clouds (McGuire, 2018b). Only tentative detections for propanal and propenal have been reported toward Orion KL using ALMA SV data (Pagani et al., 2017). Motivated by this, we searched for the three  $C_2H_nCHO$  species from our new archive data, following the same analysis in § 3.3.2. However, this attempt was not successful because the number of bright transitions of  $C_2H_nCHO$  species was low, and all the investigated transitions did not fulfill the detection criteria. The non-detection of  $C_2H_nCHO$  in Orion KL can be explained by the combination of their weak line properties and/or low abundances of the species.

After the first detection towards TMC-1 (Irvine et al., 1988, propynal only) and Sgr B2 (N) (Hollis et al., 2004), these three  $C_2H_nCHO$  have been investigated towards other interstellar environments. Although a single detection of warm propanal ( $\sim 125$  K) has been reported towards IRAS16293-2422 with ALMA (Lykke et al., 2017), successful detections of these species were mostly made towards cold components (Irvine et al., 1988; Hollis et al., 2004; Requena-Torres et al., 2008; Loison et al., 2016). This temperature-sensitive detection of  $C_2H_nCHO$  may indicate the formation of  $C_2H_nCHO$  favored in cold environments. Further investigation of  $C_2H_nCHO$  combined with a chemical model would be interesting to verify this proposition. The laboratory and quantum mechanical studies for these aldehydes would be necessary to kept pace with the recent astronomical discoveries and to construct the robust chemical network for these species.

## 3.5 Summary

Thanks to the significant improvement of sensitivity and angular resolution of ALMA, we can report the distinct detection of acetaldehyde towards Orion KL for the first time. The main conclusions of our study are enumerated below:

1. Four emission components of AA are identified with a  $5\sigma$  criterion, and three weaker peaks are additionally found with a  $3\sigma$  criterion. All of them are associated with the previously known sources. The brightest AA source, AA1, is consistent with EtP at HC-SW.

2. Spatial distributions of AA are compared with other HCO-bearing species. It follows the general morphologies of non-ether COMs; the main emission peak is associated with HC-SW but the emission toward another chemical rich region, CR, is faint. Although the morphology of AA correlates with FA, there was no general chemical segregation for HCO-bearing species. This can indicate the ubiquity of HCO radicals in the ISM.
3. Deeper investigation of aldehyde chemistry is performed toward AA1; AA abundances are estimated using LTE line modeling, and the results are compared with other aldehyde-like species and EtOH from literature. The relative abundance ratios between the species are estimated to be GA:FA:AA:EtOH:MF = <0.3:1:3:60:240.
4. Chemical model is performed to explain the observed abundance ratios towards AA1. The contribution of gas-phase chemistry in this model was minor because of the very short warm-up timescale. Ice composition and desorption behavior of species critically determine the observed ratios. To explain the observation, the desorption energy of water should be higher than MF but lower than other species under consideration.
5. The larger aldehyde species with three carbon atoms ( $C_2H_nCHO$ ) is not detected from this investigation. This possibly implies the formation of  $C_2H_nCHO$  favored in cold environments.



# 4

## Chemo-dynamical modeling to predict new ice species for detection with JWST

### Contents

---

<b>4.1</b>	<b>Introduction</b>	<b>94</b>
<b>4.2</b>	<b>Chemo-dynamical Model</b>	<b>96</b>
4.2.1	Chemical model	97
4.2.2	Radiative-hydrodynamics simulations	101
<b>4.3</b>	<b>Results &amp; Discussions</b>	<b>102</b>
4.3.1	Physical/dynamical behavior	102
4.3.2	Main ice constituents	104
4.3.3	Other volatiles expected to be abundant in the ice mantles	108
4.3.4	Calculated ice column densities	112
4.3.5	Synthesis of model ice spectra and diagnostic detectability of new ice species with JWST	115
4.3.6	Gas-phase abundances	122
4.3.7	High ice column density of H <sub>2</sub> O	124
4.3.8	The effect of nondiffusive chemical mechanisms	124
4.3.9	Implications of this study and future perspectives	126
<b>4.4</b>	<b>Conclusions</b>	<b>127</b>

---

## 4.1 Introduction

Over the past decades, the rich chemistry of the interstellar medium (ISM) has been unveiled largely through dedicated ground-based microwave and sub-mm observations of molecular rotational transitions. Complex organic molecules (COMs), typically defined as carbon-bearing molecules containing 6 or more atoms, are found to be ubiquitous in the gas throughout various evolutionary stages of star formation, from extremely cold prestellar cores to chemically-rich sources such as hot corinos (e.g. Blake et al., 1987; Arce et al., 2008; Bottinelli et al., 2010; Öberg et al., 2010; Bacmann et al., 2012; Jørgensen et al., 2012; Fayolle et al., 2015; Jørgensen et al., 2016). In particular, the unprecedented sensitivity of the ALMA (Atacama Large Millimeter/submillimeter Array) telescope has allowed the identification of a variety of new interstellar COMs (McGuire, 2018b). The spatial distribution of molecules within individual sources has also been more finely resolved, providing clues to how the chemistry changes with the underlying spatio-physical conditions. However, while the inventory of gas-phase COMs has continued to expand, our understanding on ice-mantle composition in interstellar clouds and star-forming sources has been limited to the most abundant, simple ice species. Several absorption features have been attributed to frozen COMs, although the identification with particular molecular species remains a hotly debated topic, in contrast to gas phase studies.

Although not directly detected, the presence of highly complex molecules on grain surfaces has frequently been inferred, based on a variety of evidence. For example, many laboratory studies indicated that UV and energetic radiation of ices results in the formation of COMs (e.g. Gerakines et al., 1996; Bernstein et al., 2002). The chemical richness revealed in hot cores by gas-phase observations may also indirectly indicate the presence of COMs in interstellar ices; in this scenario, as an embedded protostar heats up the surrounding envelope, the ensuing thermal release of simple solid-phase molecules would be accompanied by the release of complex species that are also present in the ice (see the review of Jørgensen, Belloche & Garrod, 2020). While the gas-phase chemistry induced by the release of simple species could in principle produce some of the molecules observed, the timescales available for gas-phase COM production have been argued to be too short (Aikawa et al., 2008), suggesting that they must already have been formed prior to ice-mantle sublimation. Until recently, the grain-surface/ice chemistry driving the development of chemical complexity was believed to be related to the warming of the dust, with intermediate temperatures ( $T_{\text{dust}} \approx 30$  K) being sufficient to allow heavy radicals on the grains to become thermally mobile and thus reactive (Garrod & Herbst, 2006). However, recent detection of COMs toward prestellar cores shows that large species can be synthesized during the very cold, early phase of star formation in which thermal diffusion of radicals is highly inefficient. Laboratory studies, and now gas-grain chemical models, show that the formation of COMs appears to be possible in such cold and quiescent envi-

ronments through nondiffusive reactions, and/or radiolysis within ice mantles (Fedoseev et al., 2015; Chuang et al., 2016; Shingledecker et al., 2018; Garrod, 2019; Jin & Garrod, 2020). This new picture of grain-surface/ice chemistry during star formation suggests that much of the gas-phase COM material observed under hot conditions may have been formed during the very earliest stages of ice-mantle growth (Garrod et al., 2021), although some processing likely occurs at later times and higher temperatures. A recent laboratory study shows that species as complex as glycine ( $\text{NH}_2\text{CH}_2\text{COOH}$ ) may also be formed under cold, prestellar conditions, given an appropriate ice composition (Ioppolo et al., 2021).

So far, however, the observational determination of ice-mantle compositions in interstellar clouds and star-forming sources has been limited to the most abundant, simple ice species ( $\text{H}_2\text{O}$ ,  $\text{CO}$ ,  $\text{CO}_2$ ,  $\text{NH}_3$ ,  $\text{CH}_4$ ,  $\text{H}_2\text{CO}$ , and  $\text{CH}_3\text{OH}$ ) in absorption from 3 to 15  $\mu\text{m}$ . The observational identification of larger ice species is challenging; in addition to the lack of infrared (IR) spectroscopic data from the laboratory, the spectral resolution and sensitivity of past astronomical instruments were insufficient to identify the weak and complicated IR bands of COMs, and to distinguish them from the deep, broad features presented by the abundant simple molecules. Furthermore, the detection of various ice species (see Figure 7 of Boogert et al., 2015) requires a line of sight of sufficiently high visual extinction, thus narrowing the number of sources in which COMs could plausibly be detected.

With the launch of the James Webb Space Telescope (JWST) in the near future, our limited observational knowledge of solid-phase COMs is expected to expand rapidly, particularly through the approved JWST Early Release Science (ERS) program *Ice Age*. This program will trace the evolution of pristine and complex ice chemistry during different evolutionary stages of low-mass star formation, from prestellar cores to protoplanetary disks, through observations of the Ced 110 region of the Chamaeleon molecular cloud I (Cha I) complex, located at a distance of 192 pc (Dzib et al., 2018). Many background stars exist within this field, providing more than 140 lines of sight, which would allow the determination of spatial profiles for ice abundances. In particular, four of these lines of sight probe the ice within 10,000 AU of the Class 0 protostar “Chamaeleon-MMS1” (Cha-MMS1) which is a main target of this study. Due to the benefits of observing ice formation in this field, one of the main science goals of the *Ice Age* project is to identify new COM species within ice mantles. If successful, such identifications would provide a direct observational link between the well-known gas-phase presence of COMs in warm/hot sources and their expected production on dust grains at earlier times.

In preparation for the *Ice Age* project, we have modeled the time-dependent chemical evolution and structure of one of its target sources, Cha-MMS1, to guide the observational study of solid state COMs towards this object. This very young star-forming core is an interesting source from an astrophysical perspective. Since Reipurth et al. (1996) first identified this source, it has drawn attention as a promising candidate for the first hydrostatic core (FHSC) stage of evolution due to its weak mid-IR emission at 24  $\mu\text{m}$  and 70  $\mu\text{m}$  (Belloche et al., 2006). The FHSC is defined as an adiabatic core in a quasi-hydrostatic equilibrium state where the gravity is balanced by the thermal pressure gradient (Larson, 1969). Because of the short lifetime of this stage, only one FHSC candidate, Barnard 1b-N (Gerin et al., 2015), has so far been successfully identified as such. High-resolution observations toward Cha-MMS1 have recently become available with ALMA, but the evolutionary stage of this source remains highly debated. Busch et al. (2020)

detected a CO outflow towards Cha-MMS1 with high angular resolution observations. The deprojected outflow velocities exceed the range of the expected values from a FHSC outflow, implying that Cha-MMS1 has already gone through the FHSC phase; those authors suggest a dynamical age of 200–3000 yr post-FHSC. However, another recent paper, Maureira et al. (2020), reported weak or missing emission of  $\text{HCO}^+$ , HCN, and  $\text{CH}_3\text{OH}$  toward the Cha-MMS1 envelope. ALMA observations of CO, CS,  $\text{H}_2\text{CO}$ , and  $\text{CH}_3\text{OH}$  towards an outflow associated with Cha-MMS1 also show that the outflow is weaker than the ones produced by Class 0 objects (Allen et al., 2020). However, regardless of whether Cha-MMS1 is in the FHSC stage or is a young Class 0 source, we would expect the state of the ice mantles, especially in the more extended regions, to be largely unaffected by this change.

In this work, the chemical structure of Cha-MMS1 is modeled by using an astrochemical model combined with a radiative hydrodynamics simulation (RHD) of FHSC with a simple 1-D approach. This chemo-dynamical modeling method enables us to explore the chemical responses to the dynamical change, achieving a more realistic chemical picture of the source, and to build up simulated profiles of gas- and solid-phase species through the core that may ultimately be compared with new data from the JWST *Ice Age* project. This paper is structured as follows: The chemical model and its implementation within a dynamical simulation are described in § 4.2. The results of the models are discussed in § 4.3. Conclusions are summarized in § 4.4.

## 4.2 Chemo-dynamical Model

The main modeling focus of this study involves the coupling of a three-phase chemical kinetics model to the outputs of a radiation hydrodynamics simulation (RHD) of the formation of the first hydrostatic core, in order to investigate the chemistry of Cha-MMS1. The approach is broadly similar to that of Barger et al. (2021), who applied a 1-D RHD method to the evolution of high-mass hot cores (note also that the gas-grain chemical model used by those authors included only diffusive grain-surface/ice-mantle chemistry, whereas the present model also employs nondiffusive chemistry).

Firstly, a one-dimensional collapse from a flat density profile ( $n_{\text{H}} \simeq 6.3 \times 10^4 \text{ cm}^{-3}$ ) to a self-supported FHSC is simulated using the hydrodynamic code *Athena++* (Stone et al., 2020). The model setup is very similar to that presented by Masunaga et al. (1998). Lagrangian particles are placed throughout the initial density profile, which then evolve over time to track the motions of mass-conserved fluid parcels, or shells, as the core collapses. The time-dependent physical conditions and radial positions of each particle (which we refer to as trajectories) determined by the dynamical code are then fed into the chemical model, *MAGICKAL*, to build up a corresponding chemical picture of the core. The chemical model is run independently for each trajectory, after the RHD simulation is complete; thus, there is no direct chemical interaction between the different trajectories, and the chemistry does not affect the dynamics in any way.

A total of 47 trajectories were selected to describe the time-dependent 1-D physical structure, for each of which the chemical evolution was calculated. Each trajectory has its own set of time-dependent density, temperature, visual extinction and radius values.

Due to the 1-D nature of the simulations, the radial ordering of the trajectories is maintained. The visual extinction for each trajectory throughout its physical evolution (which is needed for the chemical rates and to determine the dust temperature) is calculated in post-processing, by evaluating the one-dimensional integral of the total hydrogen density profile to determine the total H column density, then applying the relation of Bohlin et al. (1978), i.e.

$$A_V = \frac{3.1}{5.8 \times 10^{21}} N_H. \quad (4.1)$$

Here,  $N_H$  is the column density from the instantaneous position of a particular trajectory to the outer edge of the core. To this value for  $A_V$ , an assumed background visual extinction provided by material surrounding the core,  $A_{V,\text{bac}}$ , is added, to account for external material that is not explicitly considered in the RHD calculations. A value of  $A_{V,\text{bac}} = 2.5$  mag is adopted, which corresponds to the observed visual extinction threshold of 5 mag for starless cores in the Cha I cloud (Belloche et al., 2011), within which Cha MMS-1 resides.

The initial conditions of the RHD simulation are intended to represent a gravitationally-bound dense condensation within the dark cloud (slightly more massive than the Jeans mass). The chemistry of this initial state should be expected already to have evolved somewhat; thus, a prior stage of collapse is also modeled, allowing the chemistry to evolve from that appropriate to a translucent cloud to that of the dense core from which the RHD model begins. This pre-RHD chemical model (referred to hereafter as the “pre-model”) is run individually for each RHD-model trajectory, and consists of a simple (0-D) freefall collapse treatment, in which the gas density evolves from  $3 \times 10^3 \text{ cm}^{-3}$  to the (uniform) starting density of the dense core of  $\sim 6.3 \times 10^4 \text{ cm}^{-3}$  over a period of approximately 1 Myr (see e.g. Nejad et al., 1990). The visual extinction at each position is scaled during the pre-model evolution according to  $A_V \propto n_H^{2/3}$ , in keeping with past implementations of the collapse treatment (e.g. Garrod et al., 2021), such that the visual extinction profile that is present at the initiation of the RHD simulations is attained at the end of the pre-model. The additional background extinction is added to all calculated values, as described above.

Gas temperatures in the pre-model and main chemical model are set to 10 K or to the RHD model-calculated value, whichever is greater. The dust temperature used in the chemical models is chosen as the greater of the RHD-model value and the visual extinction-dependent value obtained from the relation provided by Garrod & Pauly (2011). Both dust temperature treatments assume a minimum value of 8 K. The details of the RHD simulation are described in § 4.2.2. A more detailed description of the chemistry used in the model is provided in § 4.2.1.

### 4.2.1 Chemical model

The chemical simulations conducted for each of the dynamical trajectories use the astrochemical gas-grain kinetics code *MAGICKAL*. The coupled gas-phase, grain-surface, and icy mantle chemistry are simulated by solving a set of rate equations (Garrod & Pauly, 2011; Garrod, 2013), supplemented by the modified rate-equation treatment presented by Garrod (2008).

Following Jin & Garrod (2020) and Garrod et al. (2021), the chemical model includes both the typical diffusive grain-surface/ice chemistry and a range of nondiffusive mechanisms by which grain/ice surface or bulk-ice species may meet and thence react. These mechanisms are important to treat accurately the production of COMs at low temperatures. The model includes the following nondiffusive mechanisms: three-body (3-B) reactions, in which a preceding surface/bulk reaction is followed by the immediate reaction of the product with some pre-existing nearby species; photodissociation-induced (PDI) reactions, in which a radical produced through photodissociation of a precursor instantly meets a reaction partner in its immediate vicinity; and the Eley-Rideal process, in which gas-phase species adsorb directly onto a grain-surface reaction partner. The “PDI2” treatment of Garrod et al. (2021) is employed, in which (non-hydrogenic) photodissociation products in the bulk ice that do not find an immediate reaction partner are allowed to recombine with each other. The three-body excited-formation (3-BEF) mechanism proposed by Jin & Garrod (2020), in which the chemical energy released by a preceding reaction allows the energized product to overcome the activation energy barrier to the follow-on reaction, is also used, adopting the generalized treatment of Garrod et al. (2021). All chemical reactions included in the surface/bulk network are able to occur through both diffusive and nondiffusive mechanisms (excluding the 3-BEF mechanism, which occurs only in cases where the initiating reaction produces sufficient energy to overcome the barrier to the subsequent reaction). A discussion of the effects of nondiffusive processes in the model is provided in § 4.3.8.

Importantly, the present model (following Garrod et al., 2021) eliminates bulk diffusion in the ice for all species but atomic and molecular hydrogen. Although this means that thermally-driven, diffusive bulk-ice reactions between radicals do not occur, those radicals may still react through the nondiffusive mechanisms described above. H atoms may also react diffusively with those radicals, as well as with more stable species such as CO via activation energy barrier-mediated reactions. Those diffusive hydrogen atoms are typically produced via photodissociation of molecules. Thus, both the direct photodissociation-driven “PDI” chemistry and the indirect reactions between atomic H and other species are ultimately the result of UV-induced photodissociation of bulk-ice molecules.

Following Garrod et al. (2021), and based on the modeling study of Kalvāns (2018), the photodissociation rates of grain-surface/bulk species is assumed to be a factor 3 lower than the corresponding gas-phase processes, although the other rate coefficients and the photoproducts are the same. The final binding energy and diffusion barrier treatments used by Garrod et al. (2021) are also adopted here.

Initial elemental abundances used in the chemical model are shown in Table 4.1. These values are partially based on those used by Wakelam & Herbst (2008) and Jin & Garrod (2020). However, here we adopt the “low-metal” value (Graedel et al., 1982) for nitrogen. In the dark clouds that should provide the starting point for low-mass star formation, metals (all elements other than hydrogen and helium) are depleted in the gas compared to diffuse clouds, because heavy elements have already been incorporated into solids as the density evolves. Jenkins (2009) suggests a relationship to describe the degree of depletion of each metal element with density, and Wakelam & Herbst (2008) define the initial elemental abundances for chemical models by applying Jenkins’ relation to a typical density of dense clouds ( $2 \times 10^4 \text{ cm}^{-3}$ ). Previously, we did not use the low-metal value only for nitrogen, because nitrogen is the element that does not show distinctive depletion with density evolution (Jenkins, 2009). Here, we assume some depletion for nitrogen in dense

species, $i$	$n(i)/n_{\text{H}}^{\text{a}}$
H	5.0(-4)
H <sub>2</sub>	0.49975
He	0.09
C	1.4(-4)
N	2.1(-5)
O	3.2(-4)
S	8.0(-8)
Na	2.0(-8)
Mg	7.0(-9)
Si	8.0(-9)
P	3.0(-9)
Cl	4.0(-9)
Fe	3.0(-9)

Notes. <sup>a</sup>  $A(B) = A^B$

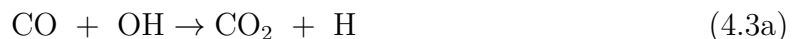
Table 4.1: Initial elemental and chemical abundances

clouds, consistent with other elements; as argued by Jenkins, observational bias could be possibly involved in measuring the nitrogen depletion. The newly adopted initial abundance for nitrogen is around 3 times lower than the values found in the  $\zeta$  Oph diffuse cloud (Hincelin et al., 2011). In the models, this change has the effect of reducing the ultimate solid-phase ammonia abundance to a value in keeping with observations of interstellar ice features, ensuring that COMs whose production derives from ammonia also will not be overproduced for this reason. The same issue with ammonia was also found in past models (e.g. Garrod et al., 2021).

### Chemical reaction updates

The underlying chemical network used in these models is based on that presented by Garrod et al. (2021), with a number of additions and changes made to the grain-surface/bulk-ice portion of the network. Particular adjustments are made to the reaction schemes involving the formation of formic acid (HCOOH, FA) and ethanol (C<sub>2</sub>H<sub>5</sub>OH, EtOH), which are summarized in Table 4.2.

Two reactions on grain surfaces mainly contribute to the formation of FA:



Reaction (2) has two equally weighted branches resulting in stable products, one of which is formic acid. Reaction (3), which is mediated by a modest activation energy barrier, typically leads to carbon dioxide production, but may also produce the radical COOH, which can easily be transformed into FA through hydrogenation by mobile atomic H. The

Reaction	$E_A$ (K)	Notes
$\text{CO} + \text{OH} \rightarrow \text{CO}_2 + \text{H} / \text{COOH}$	80	Branching ratio (BR) updated - 99:1 $\rightarrow$ 199:1
$\text{H} + \text{C}_2\text{H}_2 \rightarrow \text{C}_2\text{H} + \text{H}_2$	1300	<sup>a</sup> 50% branching ratio versus hydrogenation
$\text{H} + \text{C}_2\text{H}_3 \rightarrow \text{C}_2\text{H}_2 + \text{H}_2$	0	50% BR versus hydrogenation
$\text{H} + \text{C}_2\text{H}_4 \rightarrow \text{C}_2\text{H}_5$	1040	$E_A$ updated - 605 K $\rightarrow$ 1040 K <sup>b</sup>
$\text{H} + \text{C}_2\text{H}_5 \rightarrow \text{C}_2\text{H}_4 + \text{H}_2$	0	50 % BR versus the formation of EtOH
$\text{O} + \text{C}_2\text{H}_5 \rightarrow \text{C}_2\text{H}_4 + \text{OH}$	0	100% BR versus hydrogenation
$\text{OH} + \text{C}_2\text{H}_5 \rightarrow \text{H}_2\text{O} + \text{C}_2\text{H}_4$	0	50% BR versus the formation of EtOH
$\text{H} + \text{C}_2\text{H}_4\text{OH} \rightarrow \text{C}_2\text{H}_3\text{OH} + \text{H}_2$	0	50% BR versus hydrogenation

Notes. <sup>a</sup> The same  $E_A$  assumed for  $\text{H} + \text{C}_2\text{H}_2 \rightarrow \text{C}_2\text{H}_3$  based on Baluch et al. (1992); <sup>b</sup> Lee et al. (1978); The simple rectangular-barrier tunneling treatment is used in our models, and a barrier width of 1 Å is assumed.

Table 4.2: Updated and/or newly-included grain-surface and ice-mantle reactions

branching ratio (BR) to form COOH versus  $\text{CO}_2 + \text{H}$  is not well constrained. Garrod et al. (2021) proposed a 1% conversion, although the resulting gas-phase formic acid in those hot core models, derived from grain-surface production, was overproduced by a factor 2 compared with well-observed sources Sgr B2(N2) and IRAS 16293-2422 (high- and low-mass hot core/corino sources, respectively). We here adjust the ratio for COOH production downward by a factor 2, to 0.5%.

The production of ethanol on the grains in this model is strong, and can occur early in the evolution. As a result, we paid particular attention to ensuring that the grain-surface network is as complete as possible. Two reactions mainly contribute to the formation of EtOH in our chemical model:



The first of these involves the barrier-mediated abstraction of an H-atom from the methyl end of the methanol molecule, by methylene,  $\text{CH}_2$ . This is allowed either to form simply two radicals, or for those radicals to immediately recombine to produce ethanol. A branching ratio of 50% is assumed, following the approach of Garrod et al. (2021).

In reaction (5), the  $\text{C}_2\text{H}_4\text{OH}$  and  $\text{C}_2\text{H}_5\text{O}$  radicals are formed through ongoing hydrogenation of surface and bulk-ice hydrocarbons;  $\text{C}_2\text{H} - \text{C}_2\text{H}_2 - \text{C}_2\text{H}_3 - \text{C}_2\text{H}_4 - \text{C}_2\text{H}_5 - \text{C}_2\text{H}_6$ . However, in the previous chemical network, only addition reactions were considered, rendering the efficient hydrogenation of unsaturated hydrocarbons inevitable and providing a bias toward EtOH production. To avoid overproduction, a number of backward reactions were also included, some of which have activation energy barriers (Table 4.2).

### 4.2.2 Radiative-hydrodynamics simulations

The radiative-hydrodynamic equations are solved as described by Barger et al. (2021) with an additional cosmic-ray heating term. For reference, the equations are

$$\frac{\partial \rho}{\partial t} + \nabla \cdot (\rho \mathbf{v}) = 0, \quad (4.6)$$

$$\rho \frac{\partial \mathbf{v}}{\partial t} + \nabla \cdot (\rho \mathbf{v} \mathbf{v} + P) = \rho \mathbf{g} - \mathbf{G}_r, \quad (4.7)$$

$$\frac{\partial E}{\partial t} + \nabla \cdot [(E + P) \mathbf{v}] = \rho \mathbf{v} \cdot \mathbf{g} - G_r^0 + \rho \epsilon_{\text{CR}}, \quad (4.8)$$

$$\frac{\partial I}{\partial t} + c \mathbf{n} \cdot \nabla I = S(I, \mathbf{n}). \quad (4.9)$$

Here,  $\mathbf{g}$  is the gravitational acceleration, and  $\epsilon_{\text{CR}}$  is the cosmic-ray heating rate per unit mass of gas.  $\mathbf{G}_r$  and  $G_r^0$  are respectively the radiative force and heating/cooling term that couple the hydrodynamics with the radiative transfer equation. The total energy density  $E$  is related to the gas pressure  $P$  by

$$E = \frac{P}{\gamma - 1} + \frac{1}{2} \rho \mathbf{v}^2, \quad (4.10)$$

where  $\gamma = 5/3$  is the adiabatic index. The source term  $S(I, \mathbf{n})$  in the radiative transfer equation (9) is defined by

$$S(I, \mathbf{n}) = c\rho \left[ \kappa_{a,P} \left( \frac{ca_r T^4}{4\pi} - J \right) + \kappa_{a,R} (J - I) \right], \quad (4.11)$$

where  $\kappa_{a,P}$  and  $\kappa_{a,R}$  are the Planck and Rosseland mean opacity,  $T = \rho k_B T / \mu$  is the gas temperature calculated with the mean molecular weight  $\mu = 2.33$  u, and  $J = \int I d\Omega / 4\pi$  is the mean intensity. The rest of the symbols carry their usual meanings.

The set of equations is solved in spherical coordinates assuming 1-D symmetry in the *Athena++* framework (Stone et al., 2020). The radiative transfer equation is solved as described by Jiang et al. (2019) except that the equation is solved covariantly as described by Chang et al. (2020) with additional geometric terms to account for spherical geometry following Davis & Gammie (2020).

The RHD simulation starts with a stationary cloud core with uniform density and temperature. A setup similar to model M1a from Masunaga et al. (1998) is adopted. The computational domain from  $r = 0.1$  to  $10^4$  AU is resolved by 128 logarithmically spaced cells. A total mass of  $1 M_\odot$  with an initial temperature of  $T_0 = 8$  K (as opposed to 10K in Masunaga et al., 1998) is enclosed in the domain. To maintain constant temperature in the initial isothermal phase, the cosmic-ray heating rate  $\epsilon_{\text{CR}}$  is set to  $c\kappa_{a,P} a_r T_0^4$  where the opacity  $\kappa_{a,P}$  is evaluated at the initial density  $\rho_0$  and temperature  $T_0$  to account for the radiative cooling. We adopted the same density- and temperature-dependent prescription for frequency-averaged opacity as in Kuiper et al. (2010). To speed up the simulation without sacrificing accuracy, the reduced speed of light approximation (see, e.g., Chang et al., 2020) with a reduction factor of  $10^4$  is used. Reflecting boundary conditions are employed at both the inner and outer radial boundaries for hydrodynamic variables to

prevent gas from exiting the computational domain and conserve the total mass. This is a good approximation at the inner boundary because we are interested in the early phase of the star formation up to the thermally supported FHSC, before the formation of a central protostellar object. Reflecting and vacuum boundary conditions are implemented at the inner and outer boundaries respectively for radiation to both prevent radiation from leaking through the inner boundary while allowing radiation to exit through the outer boundary. The system is evolved for 255.1 kyr, up to the moment when the central temperature reaches 2000 K, at which point the dissociation of molecular hydrogen that triggers the collapse of the FHSC is expected. However, it should be noted that the chemical modeling is performed for infalling parcels for which final temperatures do not exceed 400 K, beyond which the description of the chemistry could become inaccurate, due in part to some of the measured gas-phase reaction rate coefficients used in the network exceeding their recommended temperature range. Thus, 1 AU is the minimum radius resolved within the chemo-dynamical model at the end of the dynamical evolution (which corresponds to a parcel of gas with a minimum radius of 2700 AU when the collapse begins). This is small enough to resolve the effective radius of the FHSC ( $\sim 5$  AU). Overall, the dynamical results are consistent with Masunaga et al. (1998).

## 4.3 Results & Discussions

### 4.3.1 Physical/dynamical behavior

Figure 4.1 shows snapshots of the gas density and temperature as functions of radius at four different evolutionary times in the RHD model of FHSC formation; these correspond to a moment early in the simulation, to the end-time of the simulation, and to two intermediate moments during the collapse, which becomes rapid at late times. The collapsing cloud core is initially optically thin to the thermal emission from dust grains, and it collapses isothermally for a long evolutionary time because the compressional heating rate is much smaller than the radiative cooling rate. During this time, the density develops an  $r^{-2}$  profile, which resembles the Larson-Penston solution for the isothermal infalling envelope (Larson, 1969; Penston, 1969). As the density evolves, the collapsing cloud becomes optically thick, forming the adiabatic FHSC in the central region. Once the adiabatic core is formed, the warm-up timescale is very short, showing a step-like profile for the temperature as a function of time (see figure 4.2, which indicates the temperature behavior for an individual trajectory). Considering that the second collapse (which terminates the FHSC phase) begins when the central temperature reaches about 2000 K, such rapid evolution of temperature explains well the short lifetime of FHSC. This process is discussed in further detail by Masunaga et al. (1998).

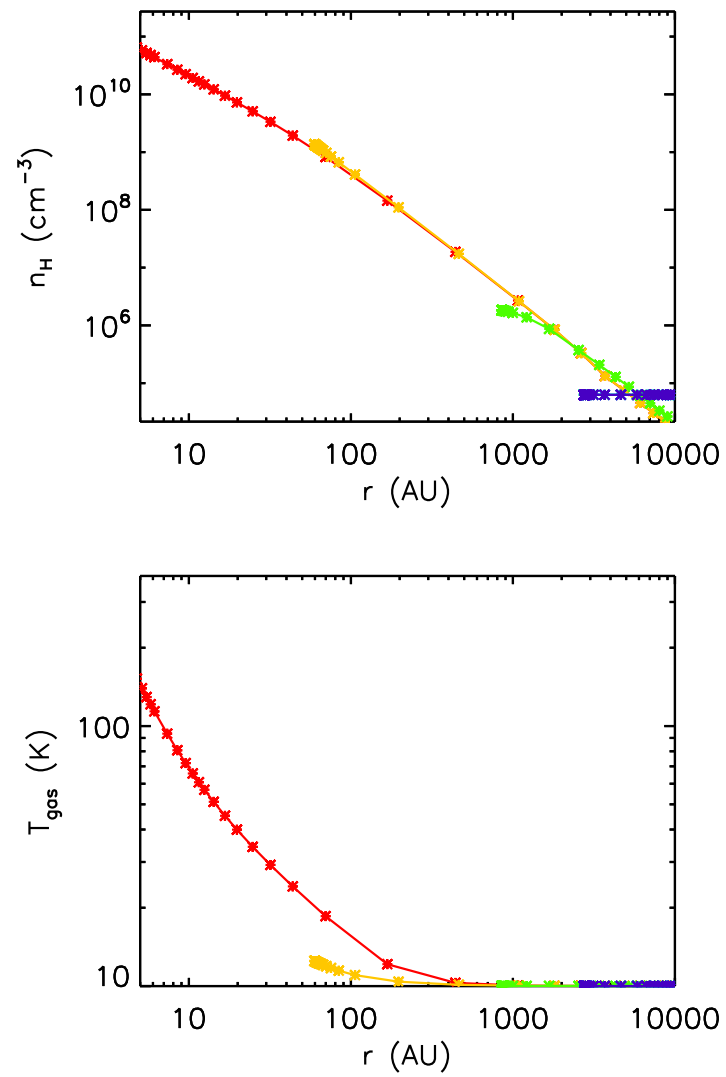


Figure 4.1: Snapshots of the physical conditions as functions of radius at four different evolutionary times in the RHD model ; 1 yr (blue), 192,400 yr (green), 254,800 yr (yellow), and 255,100 yr (red)

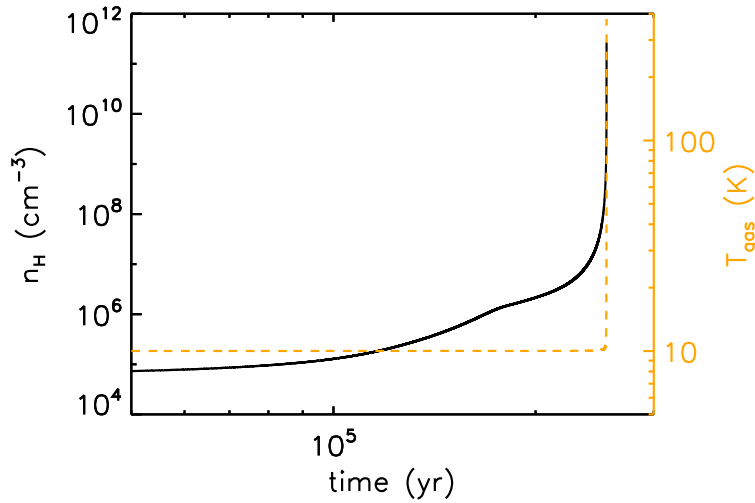


Figure 4.2: Physical evolution of the innermost trajectory as a function of time during the RHD model. The black solid line and the yellow dashed line indicates the evolution of density and temperature, respectively.

### 4.3.2 Main ice constituents

Figure 4.3 shows the four snapshots of the radial distribution of main ice constituents at the same evolutionary times presented in figure 4.1, i.e. 1, 192,400, 254,800, and 255,100 yr. Abundances are shown as a fraction of total hydrogen in the gas. Although ice species are formed throughout the whole collapsing core, the chemical evolution is presented only for the infalling parcels with initial radius  $r_{\text{init}} > 2700$  AU; this ensures that their final radii are no smaller than  $\sim 1$  AU, and thus that their final temperatures do not exceed the nominal 400 K maximum temperature of the chemical model.

Figure 4.4 again shows the final spatial distribution of the main ice components, here with the gas and dust temperature profiles shown. The divergence of the gas and dust temperatures at radius  $> 200$  AU occurs because  $T_{\text{gas}}$  is following the results from the RHD simulation, while  $T_{\text{dust}}$  is governed by visual extinction. They converge when the RHD-derived temperature exceeds, and thus overrides, the extinction-derived dust temperature. The gas and dust temperatures should be expected to be well coupled at this point, due to the substantial gas density.

The ice abundances within the effective radius of the FHSC ( $\sim 5$  AU; Masunaga et al., 1998) significantly decrease due to active thermal desorption of ice species. The distribution of main ice constituents generally shows a locally-peaked structure, peaking between 10 AU and 1000 AU. This can be explained by a centrally condensed density profile combined with high temperature toward the core center. However, this locally-peaked structure is not always seen. For example, the ice abundance of  $\text{CO}_2$  increases with radius, and the abundances of  $\text{NH}_3$  and  $\text{CH}_4$  in the ice mantles change little outside of the 5 AU effective radius of the FHSC. This implies the involvement of chemistry depending on ice species.

From the abundance data, ice column densities are calculated by integrating the number density ( $\text{cm}^{-3}$ ) of each ice species through a line of sight toward the core center

	CO	CO <sub>2</sub>	CH <sub>4</sub>	NH <sub>3</sub>	CH <sub>3</sub> OH
	%	%	%	%	%
model	31.5	38.9	4.1	6.1	3.7
observed median value (LYSO) <sup>a</sup>	21 <sup>35</sup> <sub>12</sub> (18)	28 <sup>37</sup> <sub>23</sub>	4.5 <sup>6</sup> <sub>3</sub> (3)	6 <sup>8</sup> <sub>4</sub> (4)	6 <sup>12</sup> <sub>5</sub> (5)
observed range	(<3) - 85	12 - 50	1 - 11	3 - 10	(<1) - 25

Notes. <sup>a</sup> Öberg et al. (2011) ; For each molecule, the second row gives the median and lower and upper quartile values of the detections, and in brackets the median including upper limits. The third row gives the full range of abundances.

Table 4.3: The relative abundances of the main ice constituents with respect to water ice column density

(technically, 1AU offset from the core center). In this case, the protostar itself would be the background source; the column densities are thus derived by integrating the number density from the core center to the edge of the core.

Table 4.3 summarizes ice abundance with respect to water ice column density toward the core center. The relative abundances reproduce well the main ice composition of clearly identified species from past observations towards low-mass YSOs (Boogert et al., 2015). The relative abundances of all main ice species are within the observational range. The CO:CO<sub>2</sub> abundance ratio from the model (0.81) shows a good match with the observations based on median values of CO and CO<sub>2</sub> abundances (0.75), although the relative abundance of CO<sub>2</sub> with respect to water exceeds the upper quartile value from the observations. The broad consistency suggests that the Cha-MMS1 model presented here should provide a reliable basis for the chemical investigation. The peak water ice abundances with respect to total hydrogen ( $\sim 10^{-4}$ ) in the model (see figure 4.3) are higher than required to reproduce the highest abundances seen in the observations, by a factor of around 2. This suggests that column densities of other ice species could be overproduced by a similar factor. For this reason, we further investigate the model results with a focus on the relative abundances with respect to water ice rather than on the ice abundances relative to atomic hydrogen; the possible causes of the higher ice abundances produced by the model are discussed in § 4.3.7. The influence of this effect on synthesized observational spectra is also tested in § 4.3.5.

Figure 4.5 shows the radial distribution of abundances for the main ice constituents (with respect to water ice) at the end of the model run, i.e., once the FHSC is formed. The following three features may be identified in the distribution:

(1) An anti-correlation between CO and CO<sub>2</sub> at  $r > 2000$  AU – the CO:CO<sub>2</sub> ratio is almost constant ( $\sim 0.8$ ) at  $r < 100$  AU, while the ratio rapidly decreases in the outer regions. This also results in the CO<sub>2</sub>/H<sub>2</sub>O ratio exceeding 1 at  $r > 3000$  AU (which is improbable given that no observational sightline has ever revealed such a ratio). The latter effect is related to the efficient conversion of CO to CO<sub>2</sub> ( $\text{OH} + \text{CO} \rightarrow \text{CO}_2 + \text{H}$ ) on grain-surfaces and within ice mantles. On the grain surface, this is a diffusive reaction due to the high dust temperatures at outer regions while nondiffusive reaction dominates within the mantles. Thus, OH radicals produced as a result of PD of water ices quickly react with nearby CO (which is one of the most abundant ice species after water). The rate at which this instantaneous reaction mechanism occurs depends on the photodissociation rate of water ice, thus more efficient conversion appears at outer regions. Although

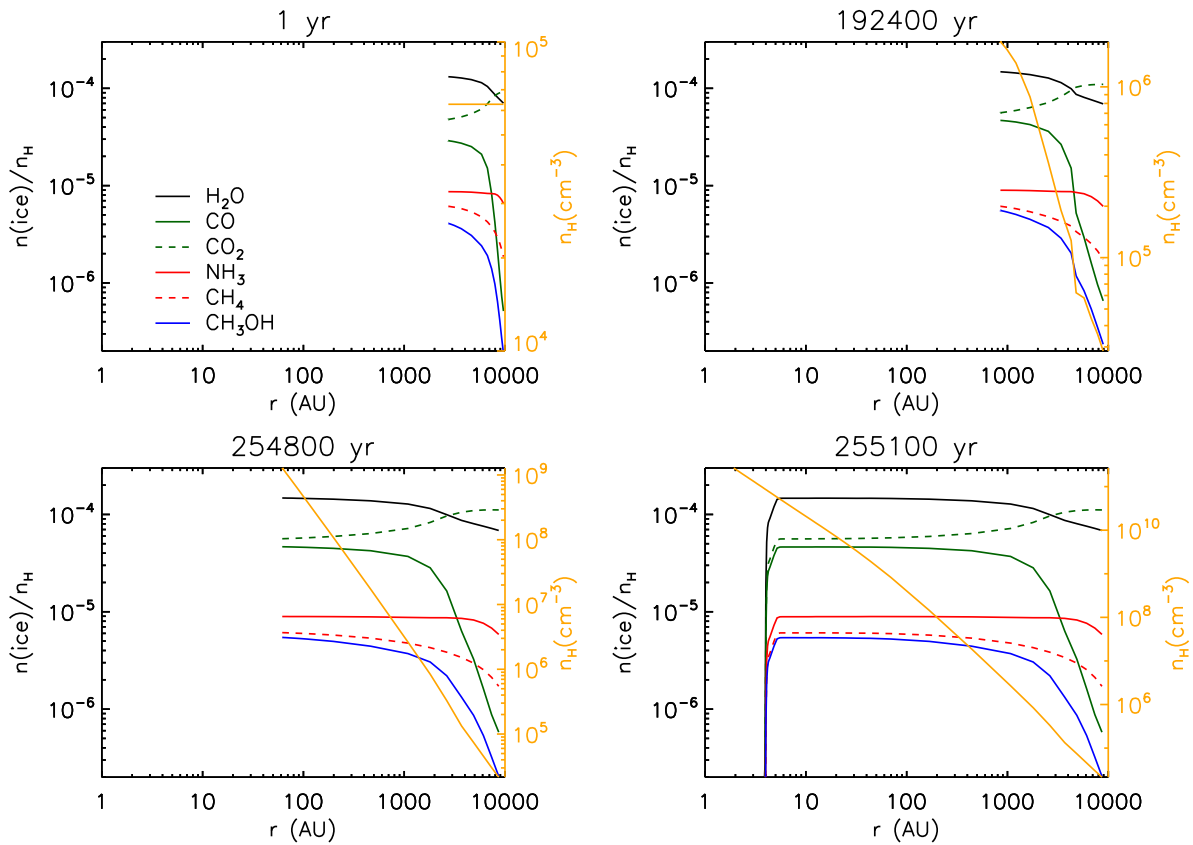


Figure 4.3: Radial distribution of the main ice constituent abundances during the evolution of Cha-MMS1; H<sub>2</sub>O (solid black), CO (solid green), CO<sub>2</sub> (dashed green), NH<sub>3</sub> (solid red), CH<sub>4</sub> (dashed red) and CH<sub>3</sub>OH (solid blue). The yellow lines indicate density profile within the source obtained from the RHD simulation.

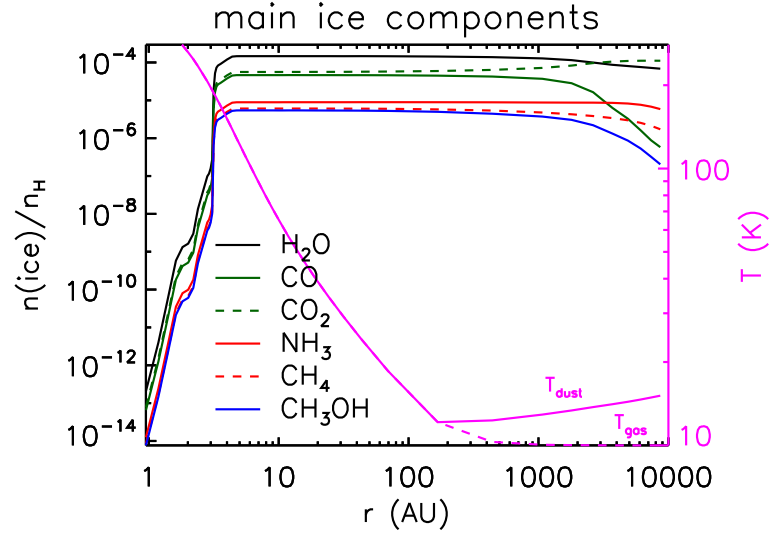


Figure 4.4: Final distribution of the main ice constituent abundances within Cha-MMS1; H<sub>2</sub>O (solid black), CO (solid green), CO<sub>2</sub> (dashed green), NH<sub>3</sub> (solid red), CH<sub>4</sub> (dashed red) and CH<sub>3</sub>OH (solid blue). The magenta lines indicate the temperature profile within the source obtained from the RHD simulation.

category	species
main ice constituent	H <sub>2</sub> O, CO, CO <sub>2</sub> , CH <sub>4</sub> , NH <sub>3</sub> , CH <sub>3</sub> OH
CO hydrogenation	HCO, H <sub>2</sub> CO, CH <sub>3</sub> O, CH <sub>2</sub> OH
O-bearing	HCOOH (formic acid; FA), CH <sub>3</sub> CHO (acetaldehyde; ACTD)
large	CH <sub>3</sub> OCH <sub>3</sub> (dimethylether; DME), HCOOCH <sub>3</sub> (methyl formate; MF)
( $n_{\text{atom}} \geq 5$ )	CH <sub>2</sub> OHCHO (glycolaldehyde; GA), CH <sub>3</sub> COOH (acetic acid; AA)
astronomical	CH <sub>3</sub> OCH <sub>2</sub> OH (methoxy methanol; MM), (CH <sub>3</sub> ) <sub>2</sub> CO (acetone; ACTN)
species	C <sub>2</sub> H <sub>5</sub> OH (ethanol; EtOH), (CH <sub>2</sub> OH) <sub>2</sub> (ethylene glycol; EG)

Table 4.4: Ice species investigated in this study

photodissociation of CO<sub>2</sub> acts as a backward reaction to form CO (CO<sub>2</sub> → CO + H), the formation of CO<sub>2</sub> through the nondiffusive process dominates over its destruction. Thus, the formation of CO<sub>2</sub> is sensitive to the description of visual extinction in the model, as this parameter governs dust temperature and photodissociation rates at the same time. Our simple assumption for the single isolated core could cause the underestimation of visual extinctions in the outer regions, resulting in the conversion of CO to CO<sub>2</sub> which might be too efficient (see the discussion in § 4.3.4). However, the effect will have only a very minor influence on the column densities calculated below.

(2) The correlation between CO and CH<sub>3</sub>OH ice distribution; this indicates that CH<sub>3</sub>OH ice is mainly formed by ongoing CO hydrogenation on grain surfaces.

(3) Minor spatial changes in NH<sub>3</sub> and CH<sub>4</sub> ice abundances; the chemistry related to these two saturated species is fairly insensitive to the physical variations with radius. The gradual increases of their ice abundances with respect to water ice seen at outer radii is caused by the faster accretion of NH<sub>3</sub> and CH<sub>4</sub> than H<sub>2</sub>O, as the gas-phase budget of C and N has not run down yet at those outer radii (Garrod et al., 2021).

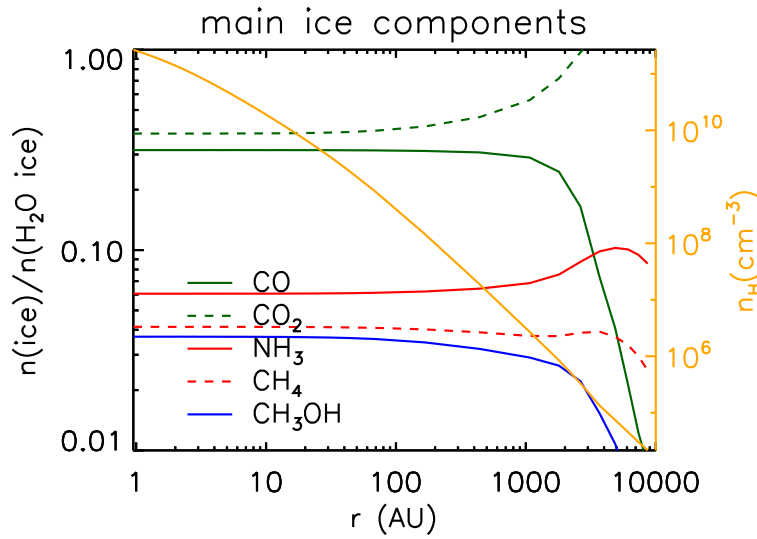


Figure 4.5: Final distribution of the main ice constituent abundances w.r.t. water ice within ChMMS1; H<sub>2</sub>O (solid black), CO (solid green), CO<sub>2</sub> (dashed green), NH<sub>3</sub> (solid red), CH<sub>4</sub> (dashed red) and CH<sub>3</sub>OH (solid blue). The yellow lines indicate the density profile within the source determined by solving the RHD equations.

### 4.3.3 Other volatiles expected to be abundant in the ice mantles

We have investigated other volatiles expected to be abundant in the ice mantles, including CO-hydrogenation intermediates and well known O-bearing hot-core species; species of interest are listed in Table 4.4, along with their abbreviations. Figure 4.6 shows the spatial distribution of these ice species with respect to the local fractional abundance of water ice,  $X(\text{H}_2\text{O})$ , at the end of the evolution. The two upper panels show large ( $n_{\text{atom}} \geq 5$ ) O-bearing species that have been detected toward hot cores while the lower panel shows the intermediates related to CO hydrogenation.

The results from this model predict high ice abundances for the CO-hydrogenation intermediates, including radicals ( $10^{-3} \times X(\text{H}_2\text{O})$ ). For more complex O-bearing species, their solid-phase abundances are typically on the order of  $10^{-5}$ – $10^{-4} \times X(\text{H}_2\text{O})$ , while EtOH shows distinctively high solid-phase abundances of  $10^{-3} \times X(\text{H}_2\text{O})$ . The five O-bearing species presented in the upper-left panel of figure 4.6 also show relatively high abundances. Observations of these species have, either directly or indirectly, implied their presence within the ice mantles. Three of them (ACTD, MF, and DME) have been identified in the gas phase in cold, prestellar environments (Bacmann et al., 2012; Vastel et al., 2014; Cernicharo et al., 2012; Scibelli & Shirley, 2020), with grain-surface formation being suggested as an explanation. In addition, the analysis of the mid-IR spectrum of the massive protostar W33A – one of the few sources for which a high quality mid-IR spectrum is currently available – identified three prominent features that have been attributed to EtOH, FA, and ACTD, although their identification in the ices remains uncertain (Schutte et al., 1999; Boogert et al., 2008; Öberg et al., 2011). Terwisscha van Scheltinga et al. (2018) re-analyzed the same spectrum with more accurate spectroscopic laboratory data, deriving upper limits for ice abundances with respect to water of 1.9 % and 2.3 % for EtOH and ACTD, respectively. This is 1-2 orders of magnitude more than predicted by our model. AA and MM have not been identified from the ice observations

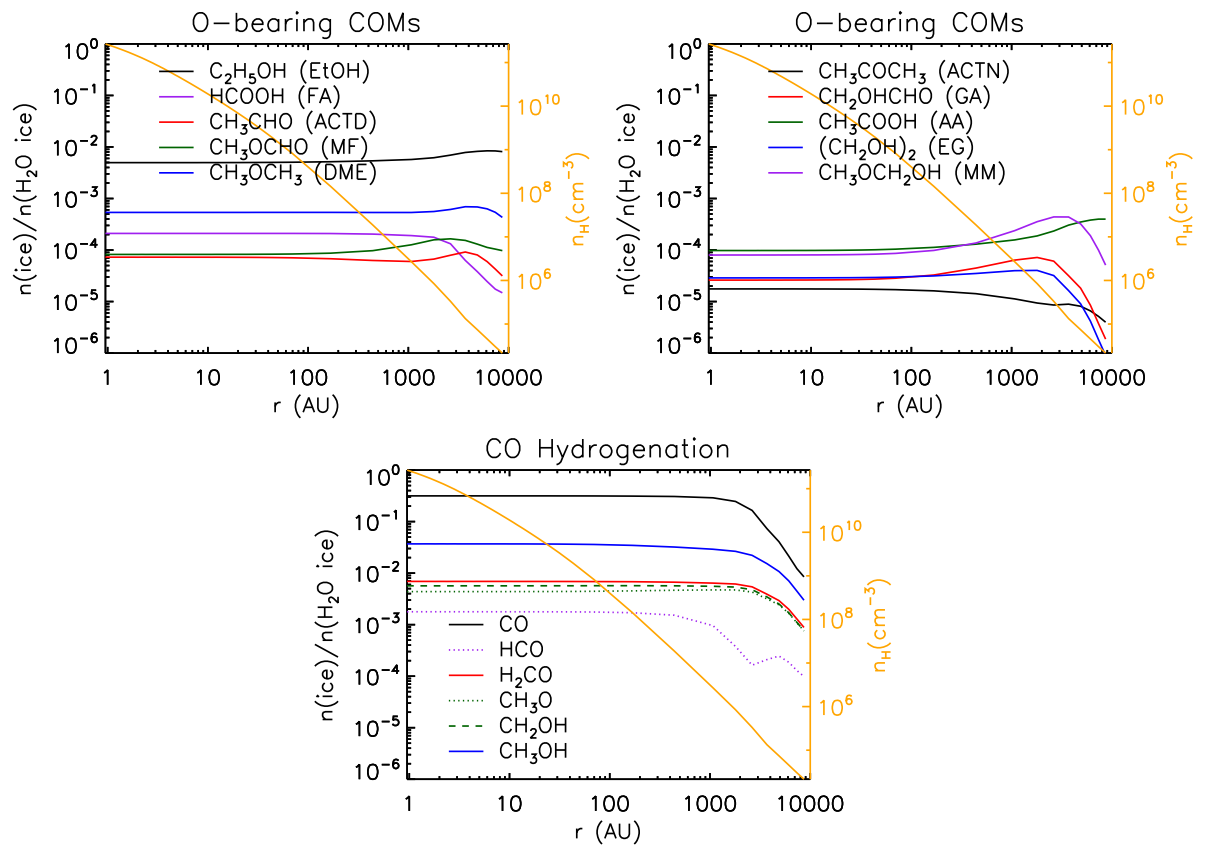


Figure 4.6: Radial distribution of the ice abundances with respect to water ice abundances at the end of the evolution. The yellow lines indicate the density profile within the source determined by solving the RHD equations.

so far, but their large abundances in the model suggests them to be plausible candidates for solid-phase detection, their spectral characteristics notwithstanding. In particular, those species could be enhanced at the outer radius (in low-density regions) by almost one order of magnitude compared to the core center.

We categorize the spatial distribution of the species shown in figure 4.6 into three types: 1) pudding shape, i.e. flattened center, decreasing at large radii; 2) bowl shape, i.e. flattened center, increasing at larger radii; and 3) locally-peaked, with  $X(i)/X(\text{H}_2\text{O})$  peaking at a few thousand AU. Table 4.5 shows the shape with which we identify each of the ice species shown in the figure. Interestingly, aside from the three aforementioned COMs (ACTD, MF, and DME) detected in cold environments, the chemical species following each type of distribution can be linked back to a specific radical or molecule involving their formation. For example, the CO ice distribution is a pudding shape, and most of the ice species whose formation is directly related either to the CO $\rightarrow$ FA conversion pathway (see equations 1 and 2) or to the hydrogenation products of CO show similar distributions.

The main factor that determines the radial distribution of ice species is the  $A_V$  distribution, dominantly during the pre-model. At the beginning, the visual extinction ranges from 3.0 mag (innermost) to 2.5 mag (outermost), and it evolves to the ranges from 6.2 mag to 2.7 mag with the density evolution during the pre-model. The chemical differentiation of many species (e.g. EtOH) are determined by the balance between formation and destruction processes that both become more efficient further out from the central core. In outer regions, low  $A_V$  and/or higher dust temperatures can drive the formation of these species through PDI nondiffusive reactions and/or diffusive reactions, while destruction via PD also becomes active. However, the formation of some species such as MF becomes rather efficient when the density is higher, indicating that the  $A_V$  has increased as well. The formation of this type of species is not strongly dependent on the PDI processes in the bulk ice, but on the build up through direct surface production via 3-B nondiffusive reactions, when radicals become more abundant on the grain surfaces (see figure 13 in Garrod et al. 2021).

As for the larger species, whose formation pathways are more complex, the abundance profiles are nevertheless found to depend on which functional groups are present. All species with bowl-shaped distributions contain a methyl group ( $-\text{CH}_3$ ), while all species containing the hydroxymethyl radical ( $-\text{CH}_2\text{OH}$ ) exhibit locally-peaked distributions peaking at a few thousand AU. ACTD, MF, and DME show locally-peaked distributions despite each containing a methyl group, but in the test model of a moderately higher extinction environment their distributions converge to the bowl-shape distribution. This result shows that  $-\text{CH}_3$  (which perhaps may include  $-\text{CH}_3\text{O}$ ) and  $-\text{CH}_2\text{OH}$  might be the key functional groups determining the spatial profiles of solid-phase species. Such spatial segregation has been also reported from the observations. For example, O-bearing COMs in Orion KL show different morphology depending on which functional group is present in the molecule (Tercero et al., 2018). To explain this, Tercero et al. (2018) propose that different radicals, methoxy ( $-\text{CH}_3\text{O}$ ) and hydroxymethyl ( $-\text{CH}_2\text{OH}$ ), may dominate, driving the different chemical complexity of the regions.

shape	species
pudding	CO, HCO, H <sub>2</sub> CO, CH <sub>3</sub> O, CH <sub>2</sub> OH, CH <sub>3</sub> OH, HCOOH
bowl	CH <sub>3</sub> COOH, C <sub>2</sub> H <sub>5</sub> OH
locally-peaked	CH <sub>2</sub> OHCHO, CH <sub>3</sub> OCH <sub>2</sub> OH, (CH <sub>2</sub> OH) <sub>2</sub> , HCOOCH <sub>3</sub> , CH <sub>3</sub> OCH <sub>3</sub> , CH <sub>3</sub> CHO

Table 4.5: Spatial distribution of ice abundance of COMs w.r.t. water ice within Cha-MMS1

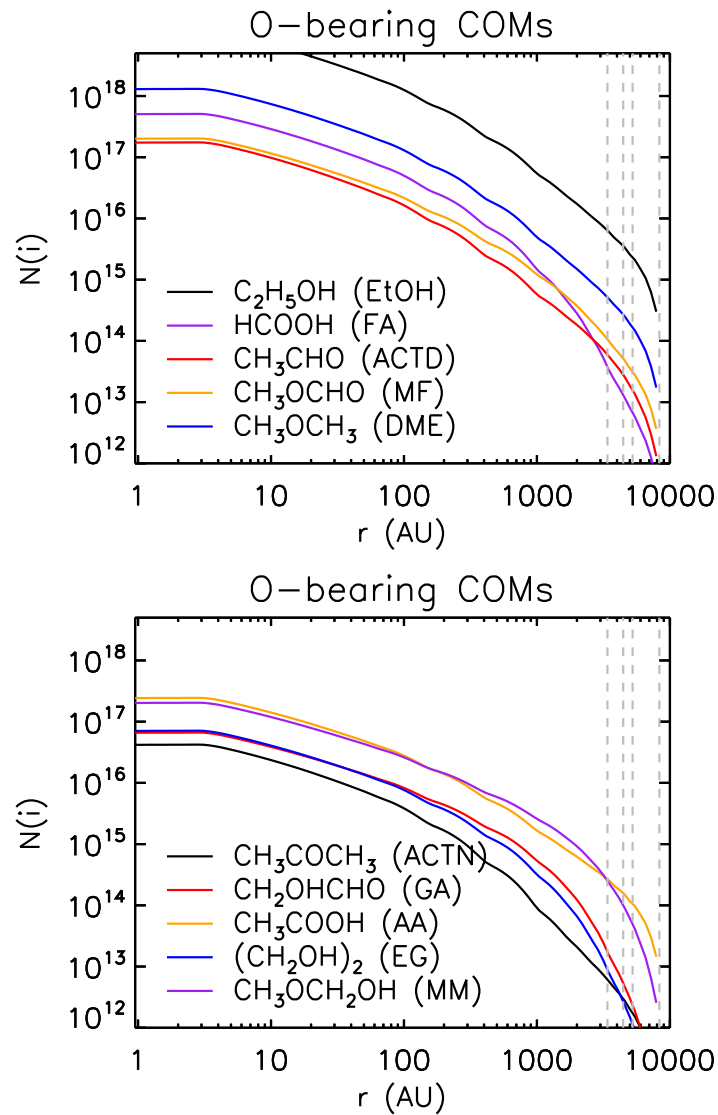


Figure 4.7: Radial distribution of the column density produced by our model of Cha-MMS1 for large O-bearing ice species. Gray dashed lines indicate the observed radial offsets from the center of Cha-MMS1 for the lines of sight toward a selection of background stars.

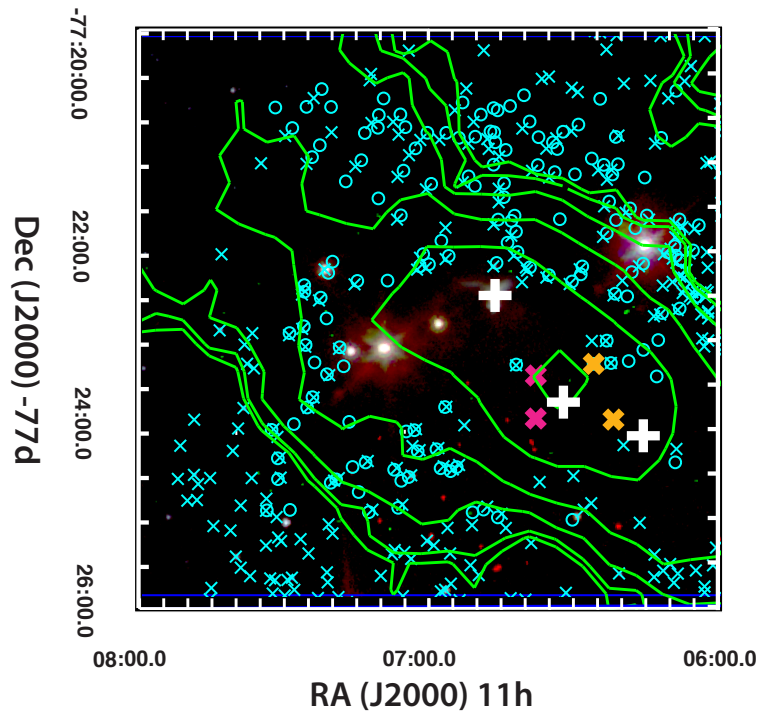


Figure 4.8: Map field of ice mapping in the ice age project. Green contours indicates high- $A_V$  870  $\mu\text{m}$  dust continuum emission (Belloche et al., 2011). The targets of ice age are denoted as large white crosses. From the left, Ced 110 IRS4 (Class I protostar), Cha-MMS1 (Class 0 protostar), and C2 (prestellar core).

#### 4.3.4 Calculated ice column densities

Figure 4.7 shows the column density profiles produced by our model of Cha-MMS1 for large solid-phase molecules. These are calculated by integrating the number density of each species along parallel lines of sight intercepting different offsets from the core center. For comparison, the gray dashed lines indicate the observed radial offsets from the center of Cha-MMS1 of the lines of sight toward a selection of background (BG) stars. These lines of sight are showing high- $A_V$  in the *Ice Age* field. Considering the high  $A_V$  threshold expected for the detection of complex ice species, these lines of sight would be the most probable to identify icy COMs, of those BG stars yet known that lie near on the sky to Cha-MMS1. The two outer BG stars (orange crosses in figure 4.8 – NIR 38 and J110621.63-772354.1 – will be observed both with NIRSPEC’s fixed slit mode (0.6 to 5 microns) and MIRI’s low resolution spectroscopy (LRS) mode (5-14 microns) which operate in the near-IR and mid-IR, respectively. The core center and the other two inner positions (pink crosses in figure 4.8)– J110637.01 and J110637.34 – will be observed with NIRCAM / Wide Field Slitless Spectroscopy (WFSS) only (2.4 to 5  $\mu\text{m}$ ). The combination of these five lines of sight will provide a spatial profile of ice composition possibly including COMs.

The extinction towards the two MIRI LRS targets, NIR 38 and SSTSL2J110621.63-772354.1, was calculated for the *Ice Age* ERS program using the observed photometric color taken between the K bandpass at 2.2  $\mu\text{m}$  and Spitzer IRAC band 1 at 3.6  $\mu\text{m}$  taken from Persi et al. (2001) and the IPAC Gator database. The calculation assumed

an intrinsic K-IR1 color for background giant stars of 0.03 from Majewski et al. (2011) and the highest extinction  $A_\lambda/A_V$  curve for molecular clouds from McClure (2009). The other two background stars were only observed at WISE bands 1 and 2. Therefore we assumed an intrinsic background giant W1-W2 color of -0.08 from Schlafly et al. (2016) and the  $A_{W1}/A_{W2}$  extinction of 0.463 from Xue et al. (2016). The final extinctions in  $A_V$  are listed in table 4.6. From comparing the variation in  $A_V$  derived for other, less reddened stars from both this set of colors and other colors, we estimate a conservative 20% systematic uncertainty in our final  $A_V$  measurements.

To see how well the density structure described in the model matches with the observations, an observational column density of total hydrogen toward each background star is compared with a calculation of the column density along a line of sight in the model that lies at the appropriate radial separation from the core center. A similar comparison is made between the observed column density of total H toward the center of Cha-MMS1 and the same line of sight toward the model of the source.

For each background star, the column density of total hydrogen,  $N_{\text{H,obs}}$ , is calculated based on the observational visual extinction information, using the relation  $N_{\text{H,obs}}=1.8 \times 10^{21} A_V \text{ cm}^{-2}$ . To take some account of observational effects in the comparison, the corresponding model values,  $N_{\text{H,model}}$ , are obtained by convolving the column density profiles with the spatial resolution of Spitzer IRAC (2''), using a Gaussian beam profile.

For the core center,  $N_{\text{H,obs}}$  derived from 870  $\mu\text{m}$  dust continuum is also available from the literature (Belloche et al., 2011). This value is compared with the model by convolving the modeled column density profile with the beam size of the dust continuum map ( $\theta_{\text{HPBW}}=21.2''$ ). As seen in table 4.6, the column density derived from the model is roughly consistent with the observation at the core center. However, the disparity in total column density between model and observation grows at larger radii, where  $N_{\text{H,model}}$  falls more than two orders of magnitude below the observational value for the outermost BG position.

The main reason for this discrepancy is that the physical evolution of Cha-MMS1 in the model is described as a single isolated object with the RHD simulation, while Cha-MMS1 is actually one of nine young, low-mass star-forming cores within a distance of 0.2 pc in the plane of the sky (Maureira et al., 2020). For example, another *Ice Age* target – prestellar core C2 (right white cross in figure 4.8)– exists near the outermost BG position, and it is even closer to this BG position than Cha-MMS1. This explains the much higher column density toward this line of sight in the observation than the model. Thus, the model is unlikely to produce meaningful predictions for ice abundances for the nearest BG stars yet detected in the vicinity of Cha-MMS1. However, it is expected that the JWST observations will reveal new background stars that are closer to the core center and therefore may provide a better constraint on the model.

In addition to the density structure, we also compare the modeled water-ice column density with values previously reported for observations. There is no direct measurement of water ice column density for this source, but values toward various other low-mass YSOs are available for comparison. This allows the compatibility of the modeled ice compositions with the observations to be determined. Considering the correlation between water ice column density and visual extinction, which has been found for a range of visual extinctions  $0 < A_V < 30$  mag (reviewed in Boogert et al., 2015), water-ice column densities on the order of  $10^{19} \text{ cm}^{-2}$  would be expected, given the high visual extinction of Cha-MMS1. The corresponding value from the model is simply derived by integrating the

source name	Cha-MMS1	J110637.01	J110637.34	NIR 38	J110621.64	
RA (J2000)	11:06:33.46	11:06:37.74	11:06:37.80	11:06:26.69	11:06:21.64	
Dec (J2000)	-77:23:34.52	-77:23:23.83	-77:23:52.80	-77:23:18.6	-77:23:54.12	
radius (AU)	0	3386	4447	5240	8330	
$A_V$ (mag)	>100 <sup>a</sup>	106 <sup>d</sup>	95 <sup>d</sup>	60	95	
$N_{H,obs}$ ( $10^{23} \text{ cm}^{-2}$ )	1.80	0.92 <sup>b</sup>	1.91	1.71	1.08	1.71
$N_{H,model}$ ( $10^{23} \text{ cm}^{-2}$ )	5.20	0.26 <sup>c</sup>	0.04	0.02	0.01	<0.01
$\frac{N_{H,obs}}{N_{H,model}}$	0.3	4	48	86	108	>171

Notes. <sup>a</sup> M.K. McClure, Priv. Comm.; This estimation is based on the  $A_V$  towards the surrounding background stars. There is a systematic uncertainty of  $\sim 20\%$  on this estimation. See § 4.3.4 for more details. <sup>b</sup> Belloche et al. (2011) –  $N_{H,obs}$  is derived from the  $870 \mu\text{m}$  dust continuum emission map. <sup>c</sup>  $N_{H,model}$  is derived by convolving the modeled chemical distribution with the same observing beam size (21.1") of the  $870 \mu\text{m}$  dust continuum emission map in Belloche et al. (2011). <sup>d</sup> only two WISE photometric bands are available for the estimation of  $A_V$ .

Table 4.6: The information on background stars near to Cha-MMS1

number density of water ice along a pencil beam toward the core center (In observations, the water ice column density is generally measured from the optical depth of the  $3\ \mu\text{m}$  band relative to the dust continuum, which is expected to be confined within a very small radius for a deeply embedded object). This calculation results in the value of  $1.2 \times 10^{21}\ \text{cm}^{-2}$ , which is around two orders of magnitude higher than the expected observational one. This discrepancy could be caused by the model having too high a local density near the core center in particular; the  $N_{\text{H,model}}$  value obtained without beam convolution is overproduced by a similar factor as the water column density, while the maximum water ice fractional abundance of  $\sim 10^{-4}$  in the model (see Figure 4.4) is just a factor of 2 higher than the measured abundances previously reported for observations (Boogert et al., 2013).

Figure 4.4 indicates also that the modeled dust-grain ice mantles are present to an inner radius of just a few AU, with the temperatures inside this radius being too great for ices to be maintained on the dust grains. A more extended final temperature profile would push the ices out to a region of lower density, reducing the column densities of solid-phase species. Test calculations that curtail the line-of-sight integration of ice column densities to a minimum inner radius on the order of 100 AU indeed reduces the calculated values by an appropriate factor.

These proposed influences on density and temperature could be explained by the presence of a protostellar outflow carving out the central region of the core, as long as the sightline passed through the outflow cavity before reaching the central star. Furthermore, much of the material settles in a disk even at this early stage. The observations typically don't cover the high disk columns because edge-on disks have such high columns that we don't detect the central star anymore. Such a disk and an outflow has actually been identified toward Cha-MMS1 (Busch et al., 2020), but is not included in the 1-D dynamical model used here.

The possibility that the chemical model itself is still overproducing the ice abundances in general cannot be completely ruled out, and the simple method of column density calculation used here could be related to this discrepancy as well. Further discussion of this topic is provided in § 4.3.7. Here, for the purposes of further comparison of the modeled ices with observations, we make a further uniform, empirical adjustment to the modeled ice abundances, scaling all the modeled ice column densities down by a factor of 100, i.e.  $f = 0.01$ . The water-ice column density after scaling roughly corresponds to a value that can be derived via extrapolation of Figure 7 in Boogert et al. (2015) to 100 mag ( $1.9 \times 10^{19}\ \text{cm}^{-2}$ ).

### 4.3.5 Synthesis of model ice spectra and diagnostic detectability of new ice species with JWST

Ice absorption spectra will be obtained toward the core center of Cha-MMS1 with the NIRCAM/WFSS instrument, as a part of the *Ice Age* program. In preparation for these observations, the near-IR spectrum expected from the core center is synthesized based on the modeled ice composition. By doing so, we are able to provide a practical diagnosis of the detectability of new ice species with JWST, as well as to get a sense of the order

of magnitude of solid-phase COM abundances that would be required in order for them to be identified. A simple synthetic ice-spectrum simulation script has been developed for this purpose, with input data provided by members of the *Ice Age* team. The main inputs for the simulation are the retrieved modeled ice column densities and three spectral parameters for the characterization of each absorption feature (i.e. frequency, width, and apparent band strength  $A'$ ).

Until recently, laboratory studies for the quantitative measurement of IR spectra of interstellar ice COMs had scarcely kept pace with astronomical discoveries. Fortunately, more and more effort has been expended on this type of study in recent years, although it has typically been focused on the mid-IR regime as this is considered the fingerprint region for solid-state vibrational spectroscopy (see e.g., Terwisscha van Scheltinga et al., 2018; Hudson et al., 2018; Rachid et al., 2020; Hudson & Ferrante, 2020; Hudson et al., 2020; Terwisscha van Scheltinga et al., 2021). For example, Terwisscha van Scheltinga et al. (2018) present ice spectra ( $2.5\mu\text{m} - 20\mu\text{m}$ ) for ACTD, EtOH, and DME in astronomically relevant environments, and they characterize the key absorbance features at  $\lambda > 5\mu\text{m}$  from these reference spectra. Hudson et al. (2018), Hudson & Ferrante (2020) and Hudson et al. (2020) also provide direct measurements of apparent band strengths and absorption coefficients from the mid-IR spectra for amorphous ices of ACTN, DME and ACTD, respectively. From the aforementioned literature, we could directly collect the absorption feature characteristics relevant to NIRCAM/WFSS coverage ( $2.4\mu\text{m} - 5\mu\text{m}$ ) for ACTN, ACTD and DME. In the case of EtOH, only the band information of absorption features at  $\lambda > 5\mu\text{m}$  are readily available. However, the reference spectrum of pure EtOH ( $2.5\mu\text{m}$  to  $20\mu\text{m}$ ) ice is publicly available on the Leiden Ice Database <sup>1</sup>. This allowed us to derive the spectral parameters for the shorter wavelength region ( $2.5\mu\text{m} - 5\mu\text{m}$ ). The unknown apparent band strengths were estimated by using the ratio between the integrated areas of an absorption feature with different absorbance within a single IR spectrum.

In general the column density of a particular ice species,  $N_{\text{species}}$ , is determined according to

$$N_{\text{species}} = \ln(10) \frac{\int_{\text{band}} I_{\lambda}}{A'_{\lambda}} \quad (4.12)$$

where  $\int_{\text{band}} I_{\lambda}$  is the integrated absorbance of the IR band under consideration and  $A'_{\lambda}$  the apparent band strength. The ice column density derived from different absorption features in a single IR spectrum should correspond to each other. Thus the unknown band strengths in the near-IR region for EtOH can be constrained by using the representative absorption band for EtOH at  $9.514\mu\text{m}$  as a reference (Terwisscha van Scheltinga et al., 2018). Table 4.7 summarizes the spectral parameters used in this simulation. The SynthIceSpec are assuming Gaussian for each absorption feature while the complex absorption features of pure ice spectrum from experiments are often not easily characterized by simple Gaussian shapes. For simplicity, here we assumed the center and the half of the integrated interval for the derivation of the integrated absorbance as peak position and FWHM of the absorption band, respectively.

Ice spectra derived from the chemodynamical models are calculated for the main simple ice constituents and the four aforementioned COMs for which IR bands are characterized. Two sets of ice column densities are tested: the regular ice composition (setup A) which is derived by directly integrating the spatial distribution of the species from the core edge to the core center, and the ice composition scaled down by factor  $f = 0.01$  (as discussed

<sup>1</sup><https://icedb.strw.leidenuniv.nl>

in § 4.3.4; setup B.1). Table 4.8 shows the two sets of ice composition for the synthesis of spectra.

species	wavenumber ( $\text{cm}^{-1}$ )	wavelength ( $\mu\text{m}$ )	FWHM		$A'$ ( $\text{cm molecule}^{-1}$ )
			( $\text{cm}^{-1}$ )	( $\mu\text{m}$ )	
$\text{H}_2\text{O}$	3280.0	3.05	335.0	0.31	2.0E-16
	1660.0	6.02	160.0	0.58	1.0E-17
	760.0	13.16	240.0	4.26	3.0E-17
CO	2140.0	4.67	5.0	0.01	1.1E-17
$^{13}\text{CO}$	2092.0	4.78	1.5	0.003	1.3E-17
$\text{CO}_2$	2343.0	4.27	18.0	0.03	7.6E-17
	660.0	15.15	18.0	0.41	1.2E-17
$^{13}\text{CO}_2$	2282.0	4.38	3.0	0.01	7.8E-17
$\text{CH}_4$	3010.0	3.32	7.0	0.01	7.0E-18
	1302.0	7.68	8.0	0.05	7.0E-18
$\text{NH}_3$	3375.0	2.96	45.0	0.04	2.3E-17
	1630.0	6.13	60.0	0.23	5.0E-18
$\text{CH}_3\text{OH}$	1070.0	9.35	70.0	0.61	1.7E-17
	3250.0	3.08	235.0	0.22	1.1E-16
	2982.0	3.35	100.0	0.11	2.1E-17
	2828.0	3.54	30.0	0.04	8.0E-18
	1460.0	6.85	90.0	0.42	1.0E-17
	1130.0	8.85	34.0	0.27	1.4E-18
	1030.0	9.71	29.0	0.27	1.4E-17
EtOH	700.0	14.29	200.0	4.17	1.6E-17
	707.0	14.14	157.0	3.18	9.0E-18
	889.0	11.25	26.0	0.33	3.8E-18
	1034.0	9.67	34.0	0.32	1.4E-17
	1092.0	9.16	24.0	0.20	8.4E-18
	1400.0	7.14	200.0	1.03	1.8E-17
	2805.0	3.57	145.0	0.18	3.2E-17
ACTD	2979.0	3.36	29.0	0.03	1.4E-17
	3314.0	3.02	306.0	0.28	1.3E-16
	3416.0	2.93	40.0	0.03	6.3E-19
	2917.0	3.43	17.0	0.02	3.8E-19
	2858.0	3.50	53.0	0.06	5.4E-18
	1768.0	5.66	32.0	0.10	1.3E-18
	1721.0	5.81	27.0	0.09	3.0E-17
	1428.0	7.00	50.0	0.25	1.1E-17
	1350.0	7.41	25.0	0.14	7.1E-18
	1122.0	8.91	30.0	0.24	5.3E-18
ACTN	2950.0	3.39	150.0	0.17	3.9E-18
	1710.0	5.85	30.0	0.10	2.7E-17
	1440.0	6.94	60.0	0.29	9.2E-18
	1358.0	7.36	22.5	0.12	1.4E-17
	1230.0	8.13	20.0	0.13	7.4E-18

species	$N(i)_{\text{model}}$	$0.01N(i)_{\text{model}}$	
	Setup A	Setup B.1	Setup B.2
H <sub>2</sub> O	1.21E+21	1.21E+19	1.21E+19
CO	3.81E+20	3.81E+18	3.81E+18
CO <sub>2</sub>	4.69E+20	4.69E+18	4.69E+18
CH <sub>4</sub>	4.98E+19	4.98E+17	4.98E+17
NH <sub>3</sub>	7.36E+19	7.36E+17	7.36E+17
CH <sub>3</sub> OH	4.41E+19	4.41E+17	4.41E+17
EtOH	6.05E+18	6.05E+16	1.51E+17
ACTD	8.68E+16	8.68E+14	2.17E+15
ACTN	2.09E+16	2.09E+14	5.23E+14
DME	6.49E+17	6.49E+15	1.62E+16

Table 4.8: Ice compositions for the synthesis of IR spectra

species	wavenumber	wavelength	FWHM		$A'$
	(cm <sup>-1</sup> )	( $\mu\text{m}$ )	(cm <sup>-1</sup> )	( $\mu\text{m}$ )	(cm molecule <sup>-1</sup> )
DME	1090.0	9.17	10.0	0.08	1.6E-18
	890.0	11.24	50.0	0.63	8.3E-19
	790.0	12.66	30.0	0.48	1.6E-19
	535.0	18.69	10.0	0.35	2.1E-18
	2985.0	3.35	93.0	0.10	2.2E-17
	2814.0	3.55	25.0	0.03	6.8E-18
	2075.0	4.82	40.0	0.09	3.7E-19
	2002.0	5.00	28.0	0.07	3.0E-19
	1459.0	6.85	50.0	0.23	4.8E-18
	1248.0	8.01	23.0	0.15	7.8E-19
	1163.0	8.60	23.0	0.17	1.1E-17
	1093.0	9.15	20.0	0.17	9.0E-18
	920.0	10.87	18.0	0.21	5.6E-18

Table 4.7: Ice spectral parameters assumed for the synthesis of ice spectrum

<sup>13</sup>CO and <sup>13</sup>CO<sub>2</sub> are known as two rarer isotopologues of which ice absorption features are clearly detected in interstellar environments. As the chemical model considers the chemistry involving the main isotopologues only, the contribution of the two aforementioned species to the IR absorption features is considered by scaling the column densities of <sup>12</sup>CO and <sup>12</sup>CO<sub>2</sub> with the ratios as follow; <sup>12</sup>CO/<sup>13</sup>CO=70 and <sup>12</sup>CO<sub>2</sub>/<sup>13</sup>CO<sub>2</sub>=86. The former is adopted from Boogert et al. (2002), and the latter is derived from the solid state <sup>13</sup>CO<sub>2</sub>/<sup>12</sup>CO<sub>2</sub> ratio as a function of Galactocentric radius (Boogert et al., 2000).

Figure 4.9 shows the IR spectra for the NIRCAM/WFSS coverage for the two different setups of the ice composition. For each setup, a control spectrum is additionally synthesized (blue dashed line) assuming zero contribution of COMs larger than CH<sub>3</sub>OH to the spectrum for comparison. The IR band at NIRCAM/WFSS coverage is dominated by water features and a mixture of methyl (CH<sub>3</sub>) functional group vibrational stretching

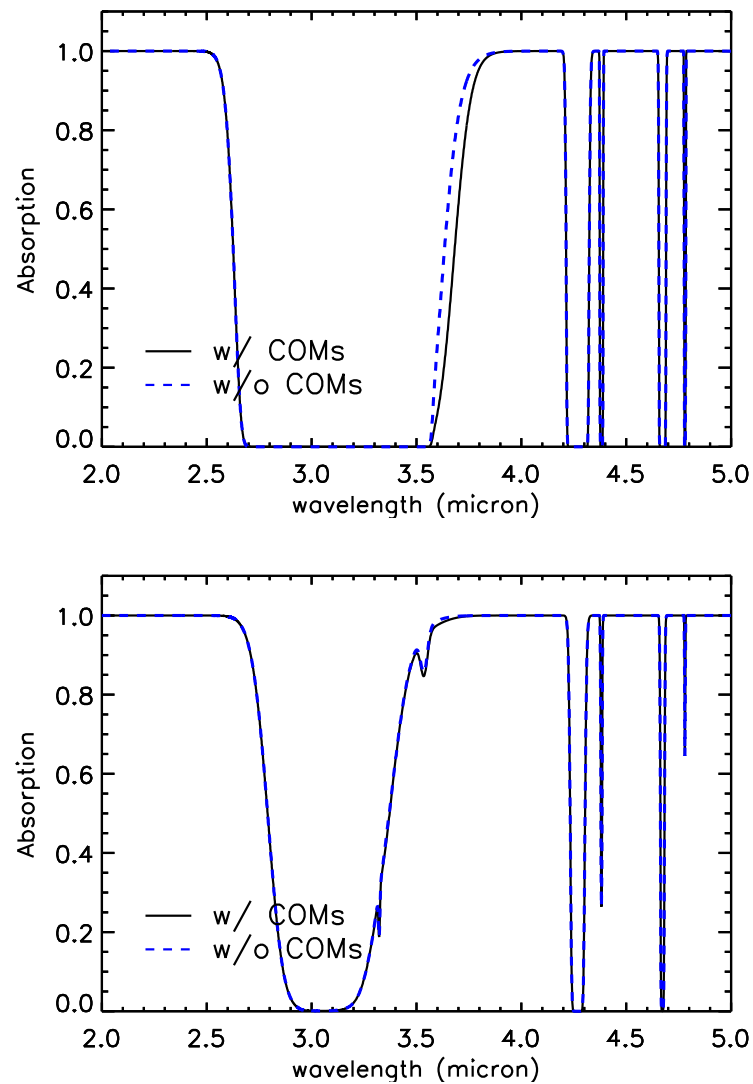


Figure 4.9: Simulated IR spectrum at NIRCAM/WFSS coverage. The left panel shows the one based on the regular ice composition without scaling (setup A) while the right panel shows the one from scaled down ice composition ( $0.01 \times N_i$ ; setup B.1).

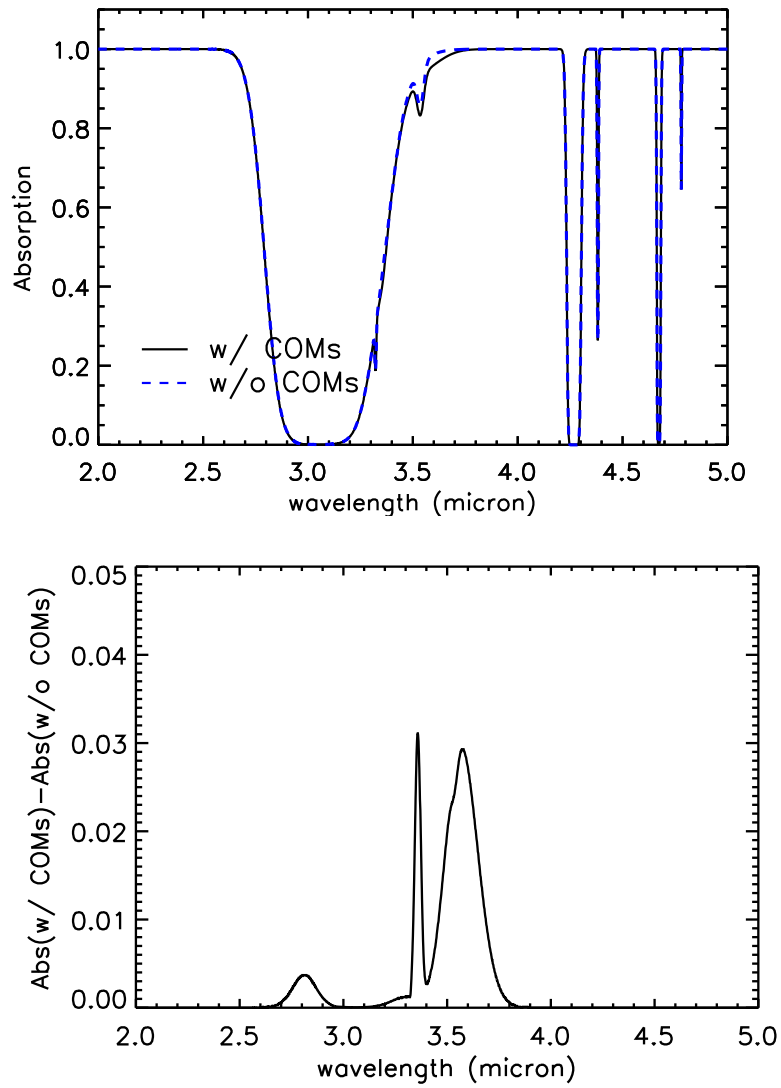


Figure 4.10: Simulated IR spectrum at NIRCAM/WFSS coverage when 2.5 times higher ice abundances for COMs are assumed (setup B.2). The left panel shows the spectrum including all ice species, while the right panel has the contribution by the main ice constituents subtracted.

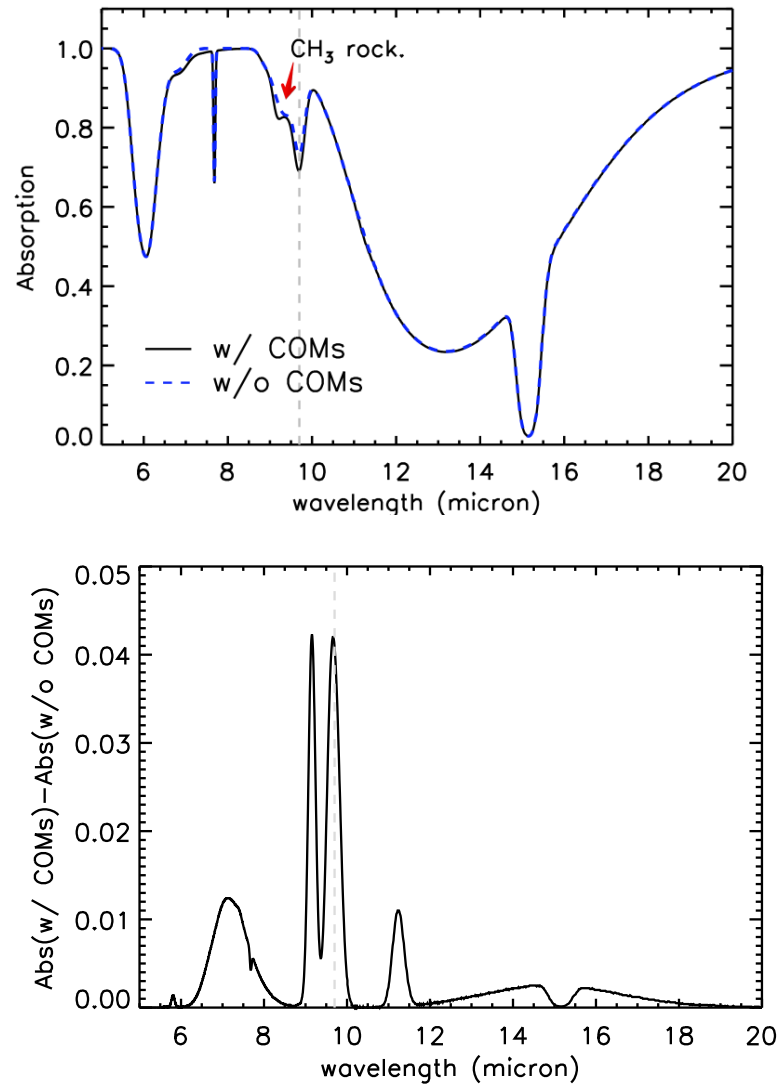


Figure 4.11: Simulated IR spectrum at MIRI coverage when 2.5 times higher ice abundances for COMs are assumed (setup B.2) The left panel shows the spectrum including all ice species, while the right panel has the contribution by the main ice constituents subtracted. The grey dashed line indicates the position of  $9.7\mu\text{m}$  silicate dust absorption band which is assumed to be already subtracted.

modes from the different ice constituents in the simulation. In particular, the spectrum of regular ice composition without scaling (setup A - left panel) is highly saturated by these features, making it hard to identify IR absorption peaks around 3.4 and 3.6  $\mu\text{m}$ , which are distinctively seen in setup B.1 (right panel). However, regardless of whether or not the ice composition is scaled down, the contribution of icy COMs to the IR absorption is either negligible or would not be distinguishable in the case of real observations.

To determine the approximate COM ice abundances required for them to be detected observationally, we again simulate ice spectra based on setup B.1, but this time with the ice abundances of the four COMs increased with respect to the water-ice column density by a factor of 2.5 (setup B.2). Figure 4.10 shows the near-IR absorption spectra for setup B.2. The absorption from COM ices is more notable in this case, adding up to three absorption peaks at 2.8, 3.4 and 3.6  $\mu\text{m}$  to the control IR absorption spectra. However, even if the ice abundances of EtOH are increased to as high as 1% with respect to icy H<sub>2</sub>O in this case, the COM absorption features are still minor. Furthermore, the absorption peaks overlap with the absorption IR band of the main ice constituents. This would introduce additional uncertainty in the identification of COM features in actual observational spectra.

Although only near-IR spectra will be obtained toward the core center as part of the *Ice Age* project, we may extend our investigation to the mid-IR regime (5  $\mu\text{m}$  - 14  $\mu\text{m}$ ; MIRI/LRS coverage) with the same ice composition to seek any distinctive ice feature from COMs; MIRI observations will be performed towards the two high- $A_V$  lines of sight located in the outer envelope of Cha-MMS1.

Figure 4.11 shows the resulting mid-IR absorption spectra with setup B.2. The IR band at 9.2  $\mu\text{m}$ , which is mainly attributed to the CH<sub>3</sub> rocking mode of EtOH, could be a prospective IR band for COM detection (Terwisscha van Scheltinga et al., 2018). Although such high abundance of COMs might not be easily achieved in typical star-forming environments, the model shows that the environment with a high UV flux could enhance the EtOH ice abundance by around five times of magnitude (see figure 4.6). Considering this, the identification of COM ice might be possible with MIRI observations of COM-rich environments.

It should be noted that dust features were not considered for our calculations but only absorption features from species within ice mantles. Silicates will produce deep dust-continuum baselines around 9.7  $\mu\text{m}$  (see L1014 IRS in figure 1; Öberg et al., 2011), and this could make the absorption features of COMs from 8-11 microns more difficult to detect. Here we assume that the dust continuum baseline will be constrained well and already subtracted. By observing multi lines-of-sight within a single source with the *Ice Age* project, we expect the dust continuum baseline would be determined with unprecedented accuracy. MIRI is expected to have at most a signal-to-noise ratio of 300. This corresponds to the detection of an absorption feature at 1% with respect to the continuum flux at  $3\sigma$ .

### 4.3.6 Gas-phase abundances

Gas-phase molecules have been detected in many single-dish observational studies of Cha-MMS1. For example, Kontinen et al. (2000) observed a selection of simple species, carbon-

species	observation	model	references and analytic methods
HC <sub>3</sub> N	1.50E-08	5.91E-13	Kontinen et al. (2000, LTE calculation)
CH <sub>3</sub> OH	2.27E-09	2.03E-09	Kontinen et al. (2000, LTE calculation)
C <sub>2</sub> S	1.03E-09	2.32E-11	Kontinen et al. (2000, LTE calculation)
HCN	6.67E-10	1.72E-09	Tennekes et al. (2006, Monte Carlo modeling)
HNC	2.00E-09	1.76E-09	Tennekes et al. (2006, Monte Carlo modeling)
SO	6.67E-10	1.90E-09	Kontinen et al. (2000, LTE calculation)
N <sub>2</sub> H <sup>+</sup>	4.67E-10	9.60E-11	Kontinen et al. (2000, LTE calculation)

Table 4.9: Comparison of the abundances of gas-phase species between the model and the observation

chain molecules, and methanol using the Swedish ESO Submillimeter Telescope (SEST), while Tennekes et al. (2006) determined the HCN/HNC relative abundance ratio by mapping the HCN and HNC emission with the same instrument. Belloche et al. (2006) measured the deuterium fractionation for molecular ions with the APEX telescope, and Cordiner et al. (2012) performed 7mm observation with the ATNF Mopra telescope for a selection of species including polyynes, sulphuretted carbon chains and methanol.

Although the chemical modeling presented here is focused on solid-phase abundances, the models indeed produce fractional abundance profiles for gas-phase species. In order to compare these with the observational values, column densities must be produced. Molecular column densities through the model core are produced for various offsets from the core center. These raw values are then convolved with a beam size appropriate to the observations, with the beam centered on the core.

Cordiner et al. (2012) provide the most extensive dataset of observed molecular lines. However, when compared with the results from Cordiner et al. (2012), the column densities derived from our model are significantly lower, by more than one order of magnitude. The large observing beam size of the Mopra telescope is attributed to this discrepancy; the observational beam size (96'' at 36 GHz and 77'' at 45 GHz) is comparable to the final radius of the outermost trajectory ( $r \sim 8660$  AU). However, the two nearby sources – Ced 110 IRS4 (class I protostar) and C2 (prestellar core) – contaminate the observing field (see figure 4.8), contributing to the higher molecular column densities, while the model assumes an isolated single FHSC. This may be a major factor in the poor comparison between models and observations with such a large observing beam size.

The abundances measured in SEST observations (FWHM=55'' at 91GHz) are roughly consistent with the modeled abundances for key species within one order of magnitude (table 4.9); methanol is in fact well reproduced, and HCN and HNC are quite adequate. The observed abundances are still generally higher than the model values, perhaps because contamination from nearby objects is still not negligible. The observed abundances of the cyanopolyne HC<sub>3</sub>N and of sulfuretted carbon species are particularly poorly reproduced with the chemical model, although the abundance of sulfur in general is poorly constrained in astrochemical models as discussed in Laas & Caselli (2019). HC<sub>3</sub>N is traditionally considered an “early-time” molecule that becomes prevalent while substantial amounts of atomic carbon are still available in the gas phase. Conversely, our model specifically corresponds to a more chemically-evolved state of the gas; thus the substantial abundance of this molecule could in practice originate from a spatial scale beyond that included in our model. Ultimately, an accurate comparison of gas-phase species toward the Cha-MMS1

source may require high-resolution observations. Although there have been a few studies performing ALMA observation toward this source, it is more focused on the dynamics of the outflow, and/or quantitative measurements of the chemical composition were not fully available (Busch et al., 2020; Allen et al., 2020; Maureira et al., 2020).

### 4.3.7 High ice column density of H<sub>2</sub>O

As discussed in § 4.3.4, the high density regions at the very center of the core may be particularly poorly represented using our simple assumption for the density structure and integration technique. The divergence of the modeled ice column densities from values for comparable sources could indicate the presence of an outflow cavity or other structural differences that are poorly represented by a one-dimensional dynamical treatment.

Furthermore, this divergence between the model and generally-observed values may also be related to the long-standing mystery of the oxygen budget. The water abundance (gas and ice) estimated from observations of various star-forming regions is much lower than the one expected from the known oxygen elemental abundance. This conundrum is reviewed by van Dishoeck et al. (2021), who discuss two possible explanations: (i) The missing oxygen is locked up in an unidentified refractory component. If this is the case, the high abundance of water in the model is caused by a lack of gas-grain chemical network for the unidentified refractory component, which results in the oxygen budget converging to the formation of water ice. If one assumes that all volatile oxygen is locked in water, the water abundance is expected to be around  $4.0 \times 10^{-4}$  (van Dishoeck et al., 2021). This value is just a few times higher than the water-ice abundance in our model in cold environments ( $\sim 1.0 \times 10^{-4}$ ). (ii) Water ice abundance estimated from ice observations can be underestimated if the missing oxygen is locked up in larger  $\mu\text{m}$ -sized grains that do not contribute to infrared ice absorption. Much observational evidence for grain growth to  $\mu\text{m}$  sizes has been published (e.g. Boogert et al., 2013); the toy model with two dust populations (0.1  $\mu\text{m}$ - and 10  $\mu\text{m}$ -sized grain) shows that a fraction  $f_{\text{large}} = 0.01\%$  of the grain population in 10  $\mu\text{m}$ -sized grains would catch 50% of the atomic oxygen during freeze-out and make it invisible (van Dishoeck et al., 2021). However, one argument against water ice being hidden on very large grains is that after sublimation in hot cores or grain sputtering in a shocked region, the gas phase H<sub>2</sub>O abundance along with the abundance of other O-bearing species does still not add up to the cosmic O abundance (van Dishoeck et al., 2021). Possibly the 40  $\mu\text{m}$  H<sub>2</sub>O lattice mode can shed some light on this, though it lies beyond wavelength range available to JWST.

### 4.3.8 The effect of nondiffusive chemical mechanisms

Past astrochemical models have relied on the thermal diffusion of surface or bulk-ice radicals to drive reactions that form COMs (Garrod & Herbst, 2006; Garrod et al., 2008; Garrod, 2013). As thermal diffusion plays a critical role in this process, those models have found that COMs start to be formed efficiently when star-forming cores heat up ( $T_{\text{dust}} > 30$  K). However, the formation of COMs now appears also to be possible in colder environments through nondiffusive reactions or radiolysis (Chang & Herbst, 2016; Jin &

$N(i)/N(\text{H}_2\text{O})$	all on (A)	three-body off (B)	PD-induced off (C)	A/B	A/C
CO	3.15E-01	3.60E-01	4.10E-01	0.81	0.79
CO <sub>2</sub>	3.88E-01	2.82E-01	2.66E-01	1.28	1.51
CH <sub>4</sub>	4.12E-02	4.24E-02	9.81E-02	0.90	0.43
NH <sub>3</sub>	6.09E-02	5.62E-02	6.37E-02	1.01	0.99
CH <sub>3</sub> OH	3.65E-02	3.98E-02	3.60E-02	0.85	1.05

Table 4.10: The effect of the nondiffusive mechanisms on the main ice constituents

Garrod, 2020; Garrod, 2019; Shingledecker et al., 2018). Also, laboratory studies have shown that the hydrogenation of CO and related species on surfaces can produce COMs (Fedoseev et al., 2015; Chuang et al., 2016), as the newly-formed radicals may sometimes react with each other if they happen to be in close proximity, without the need either for surface diffusion to bring them together or radiative processing to produce them.

The recent astrochemical models by Jin & Garrod (2020) introduced general formulations for the numerical simulation of nondiffusive processes involved in grain-surface and bulk-ice chemistry; they show that multiple complex organic molecules may be formed on grain surfaces in prestellar cores, as the result of surface radical production in close proximity to pre-existing radicals. In addition, nondiffusive treatments were introduced for reactions that follow immediately from photo-dissociation of molecules within the bulk ice, which also can occur without the need for bulk diffusion (Garrod, 2019). Applications of these new models to hot-core chemistry indicate that nondiffusive processes may be dominant in COM formation in such sources, and can be active at the very earliest stages of ice-mantle formation (Garrod et al., 2021), although some processing also likely occurs at later times/higher temperatures.

The chemo-dynamical model used here employs the two aforementioned nondiffusive mechanisms – three-body (3-B) (Jin & Garrod, 2020) and photodissociation-induced (PDI) mechanisms (Garrod, 2019). In this section, we discuss the effect of those nondiffusive mechanisms on the composition of icy mantles by turning off either mechanism. However, it should be noted that the change in chemical behavior produced by such changes can be non-linear; when one strong mechanism is removed, a weaker one may take over to replace (partially) what would otherwise be done by the stronger mechanism.

Table 4.10 summarizes the results of the analysis for the main ice constituents. The relative abundances in this table are derived from the ratios of column densities, which are calculated by integrating the number density of each ice species through a line of sight toward the core center. Both nondiffusive mechanisms transfer more of the oxygen budget from CO to CO<sub>2</sub>, through the reaction  $\text{OH} + \text{CO} \rightarrow \text{CO}_2 + \text{H}$ , which results in a better reproduction of generic observations. The modeled ice abundance of CH<sub>4</sub> significantly increases with the PDI mechanism switched off. This implies that with the PDI mechanism, a significant fraction of PD products of methane ice such as CH<sub>3</sub> on the grain consecutively react with nearby ice species to form larger species such as methylamine rather than reforming CH<sub>4</sub>, while the effect of the three-body mechanism is negligible in this case. This PDI production of methyl-group bearing molecules occurs mainly in the ice mantle, due to the much larger quantities of material stored beneath the ice surface. The solid-phase abundances of CH<sub>3</sub>OH and NH<sub>3</sub> barely change regardless of the choice of nondiffusive mechanism, reproducing the observed abundances well. Aside

$N(i)/N(\text{H}_2\text{O})$	all on (A)	three-body off (B)	PD-induced off (C)	A/B	A/C
EtOH	5.01E-03	5.21E-03	6.14E-04	0.89	8.42
FA	2.10E-04	1.43E-04	2.89E-04	1.36	0.75
ACTD	7.18E-05	4.49E-05	2.11E-04	1.49	0.35
MF	8.31E-05	6.67E-06	6.88E-05	11.58	1.25
DME	5.37E-04	4.44E-04	2.23E-04	1.12	2.49
ACTN	1.73E-05	1.42E-05	1.26E-05	1.13	1.42
GA	2.73E-05	4.57E-06	3.54E-06	5.54	7.95
AA	1.01E-04	2.65E-05	3.07E-05	3.53	3.38
EG	2.92E-05	5.88E-06	7.64E-06	4.61	3.95
MM	8.38E-05	1.13E-05	9.17E-06	6.89	9.43

Table 4.11: The effect of the nondiffusive mechanisms on the O-bearing ice species

from the above-mentioned effects, the influence of nondiffusive mechanisms on the main, simple ice constituents is very minor.

Table 4.11 shows the results for solid-phase O-bearing COMs. The inclusion of the nondiffusive mechanisms increases the abundances of these species in general, as it provides additional pathways to form large compounds without a temperature dependence. It is hard to tell which nondiffusive mechanism is more influential to develop the chemical complexity in general, because the chemical behavior of the species in the various nondiffusive setups is different. For example, MF is efficiently formed via 3-B excited formation (see Jin & Garrod (2020) for further detail). The PD-Induced mechanism also promotes the formation of COMs, especially EtOH and MM (methoxymethanol), to increase their ice abundances by a few times, while FA and ACTD ice abundances decrease with the PD-Induced mechanism switched on. This is because OH and CH<sub>2</sub> radicals – which are the photodissociation products of H<sub>2</sub>O and CH<sub>4</sub>, respectively, at early times in the model evolution – are consumed in various nondiffusive reactions, to form larger species. The main formation routes for FA and ACTD involve OH and CH<sub>2</sub> radicals, respectively: FA is synthesized either by the reaction CO + OH → COOH, followed by hydrogenation, or by the addition of OH and HCO radicals. The two-stage reaction between CH<sub>2</sub> and H<sub>2</sub>CO, in which CH<sub>2</sub> abstracts an H-atom from formaldehyde with the product radicals then immediately recombining, is one of the main formation routes for CH<sub>3</sub>CHO. Thus, the PDI mechanism is critical to transfer the CNO budget to various species at early times, developing the chemical complexity of the bulk ice.

### 4.3.9 Implications of this study and future perspectives

Motivated by the imminent observational improvements to be provided by JWST, laboratory experiments have recently been undertaken to characterize the spectroscopic behavior of larger species in the ice (Terwisscha van Scheltinga et al., 2018; Rachid et al., 2020; Hudson & Ferrante, 2020; Hudson et al., 2020; Terwisscha van Scheltinga et al., 2021). As these quantitative measurements have accumulated, the demand has increased for the application of the experimental outputs into a chemical model; this combined method can

more practically probe the strategy needed to identify new ice species with JWST. As ice spectra are influenced by the ice composition as well as the physical structure of the solid (ices and dust grains), it is important to obtain a plausible estimate for the ice composition with a chemical model. This initial study begins to meet this demand. However, our results show that even if ice abundances of COMs are predicted to be as high as 0.5% with respect to water ice, the absorption features of these species are not distinguishable from the water absorption features. This is a good example highlighting the importance of a comprehensive study: the detectability of the ice species can be securely diagnosed with careful consideration of spectroscopic characteristics as well as molecular content before observations follow.

Based on the combination of outstanding features such as a relatively strong IR band, high ice abundance, and the potential to be enhanced in high UV-flux environments, this study indicates EtOH as a good candidate for a new ice detection with MIRI observations, given an appropriate ice abundance. So far, EtOH has not been securely identified in ice observations, but this species is one of the three COMs (MF, ACTD, and EtOH) that is considered to be a tentatively identified species (e.g. Terwisscha van Scheltinga et al., 2018, 2021), which supports the finding of this study. Only gas-phase detections of EtOH in hot core regions has been reported in the Milky Way, indirectly implying a possible origin for this species in the sublimated ices. However, if EtOH were to be detected in cold gas at a cloud edge, perhaps as the result of photodesorption from the icy grain surfaces, this would separately indicate the richness of EtOH in the ice. Such an observational probe could be a reasonable diagnostic to find candidate regions for new EtOH ice detection with JWST in the future.

The results of this study show that the detection of new ice species may be demanding even with JWST. However, it is noteworthy that the IR spectroscopic considerations in this study were only possible for a handful of COMs, due to a lack of quantitative measurements of IR data. Spectroscopic behavior can be significantly different between species, and some molecules that are not covered in this study yet could be “IR-bright” (strong IR absorption band). For example, a recent study found that the infrared absorbance of propynal’s alkyne bond is about 30,000% stronger than the corresponding feature in acetylene (Hudson & Gerakines, 2019). Although propynal’s ice abundance is not high enough in our FHSC chemical model, further IR investigation of other larger interstellar species may unveil new IR bright COMs that are also abundant in the chemical model. With the interplay between laboratory work and chemical modeling studies, physical environments where such IR-bright COMs are efficiently synthesized can be also examined. This comprehensive study provides firm ground to further explore new ice species in the future.

## 4.4 Conclusions

Chemical complexity within interstellar ice mantles has been indirectly implied by dedicated observations of rotational lines of gas-phase complex organic molecules at (sub)millimeter wavelengths. With the upcoming launch of JWST, the chemical compositions within icy mantles are expected to be more deeply explored, perhaps identifying COMs within the

dust-grain ice mantles. To provide a timely diagnosis of the detectability of the new ice species with JWST, we use a 1-D coupled chemo-dynamical model to predict the chemistry toward the young star-forming core Cha-MMS1, and synthesize the expected IR spectrum with the JWST observation based on the given ice composition. The main conclusions of our study are enumerated below:

1. In the chemo-dynamical model, the relative abundances of the main ice constituents with respect to water toward the core center match well with generic observational values, providing a firm basis to further explore the ice chemistry. The absolute ice column densities expected from the models is higher than observational values in general. This could be caused by an inaccurate local density assumed for the very center of the core.
2. The model predicts relatively high solid-phase abundances (i.e.  $> 0.01\%$  with respect to water ice column density) of seven large oxygen-bearing species (ethanol, acetaldehyde, methyl formate, dimethyl ether, acetic acid, methoxy methanol, and formic acid). Three of them (ethanol, acetaldehyde, and formic acid) have been tentatively identified in past ice observations. The abundant solid-phase of acetaldehyde, methyl formate, dimethyl ether, and formic acid produced in the models is in circumstantial agreement with their recent gas-phase detection in prestellar environments.
3. For the large molecules, the abundance profiles in the model are found to depend on which functional groups are present;  $-\text{CH}_3$  and  $-\text{CH}_2\text{OH}$  might be the key functional groups delineating the spatial distributions of solid-phase species.
4. The IR spectrum is synthesized based on the modeled ice column densities of four COMs where IR band information is known, as well as the main ice constituents. Every COM absorption peak in the NIR overlaps with an absorption IR band of one of the main ice constituents. The contribution of COMs to IR absorption is minor compared to the main ice constituents, making the identification of COMs with the NIRCAM/WFSS instrument unlikely.
5. Mid-IR observations of COM-rich environments in which solid-phase COM abundances exceed  $1\%$  w.r.t. the water ice column density could reveal distinctive ice features of COMs. The IR band at  $9.2\mu\text{m}$  which is mainly attributed to the  $\text{CH}_3$  rocking mode of ethanol, could be a prospective IR band for the first firm COM detection. As this ice feature overlaps with silicate features from dust grains at around  $9.7\mu\text{m}$ , accurate treatment for the continuum subtraction is critical.
6. The results of this study show that the detection of new icy COMs with JWST could still be challenging. However, the IR spectroscopic calculations in this study were only possible for a few COMs, due to the lack of quantitative laboratory measurements of IR data. Spectroscopic behavior can be significantly different between the species, and some species that have not been covered in this study yet could have strong IR absorption features. Further IR investigation of other larger interstellar species may unveil new IR bright COMs that are also abundant enough within the ice mantles to be identified.

---

## Acknowledgements

We thank V. Wakelam and P. Caselli for helpful discussions about initial elemental abundances and the calculation of water ice column densities. We thank P. Gratier and A. Taillard for developing and providing an early version of their synthetic ice spectrum simulator within the IceAge consortium, which informed the code used in this study. We also gratefully acknowledge the input spectral data provided by E. Dartois and V. Wakelam for use with the simulator. MJ and RTG thank the Space Telescope Science Institute for funding through grant JWST-ERS-01309.020-A. Chemical model development was funded by the National Science Foundation through the Astronomy & Astrophysics program (grant No. AST 19-06489). Development of the coupled chemical and dynamical modeling treatment was funded by the NASA Astrophysics Theory program (grant number 80NSSC18K0558) and is supported in part by NASA NSSC20K0533, NSF AST-1815784, and NSF AST-1716259.



# 5

## Conclusions

In this thesis we have developed an advanced astrochemical model to provide a general means to understand the underlying chemistry in various star-forming regions. The non-diffusive mechanisms is introduced that promotes the formation of COMs without thermal diffusion of heavy species. Since the production of COMs through the nondiffusive mechanism is reported in the Monte Carlo simulation by Chang & Herbst (2016), this thesis presents the first implementation of the mechanism into a rate equation model with new generic formulations. Based on this advanced model, we investigated the chemistry in various star-forming regions from a prestellar core (L1544; Chapter 2) to an active star-forming region (Orion KL; Chapter 3). Besides the interpretations of the observations, we also provide the prediction of the ice composition for a young and deeply embedded protostar (Cha-MMS1; Chapter 4) to assess the detectability of new ice species with JWST. The results of the chapters of this thesis are summarized as follows :

Chapter 2 provides the details of the construction and implementation of the formalism for the three nondiffusive mechanisms - three-body reactions, Eley-Ridel (E-R) mechanisms, and PD-Induced reactions – into the rate equation gas-grain chemical model to revolves around the unexplained detection of saturated COMs in cold and quiescent prestellar environments. The chemical richness in cold environments can be possibly explained by these mechanisms as all of them show little dependency on temperature. We found that the new mechanisms significantly enhance cold COM abundances, successfully reproducing key observational results for prestellar core L1544. This model provides the firm basis to further explore the formation and destruction of large COMs in various environments.

Chapter 3 investigates an extensive ALMA archive dataset to search for acetaldehyde toward Orion KL. Despite the chemical richness of Orion KL, this ubiquitous interstellar aldehyde has not been securely identified yet. Four emission components of acetaldehyde are clearly identified toward Orion KL, showing a main emission peak consistent with the ethanol peak in hot core-SW (HC-SW). The column densities of acetaldehyde and its kinetic temperatures are determined toward this main emission region, assuming molecular excitation under local thermodynamic equilibrium conditions. The chemical compositions toward the ethanol peak are investigated with a chemical model. The model shows that a relatively long cold collapse timescale and the adjustment of binding energy are needed

to explain the observations.

Chapter 4 presents the prediction of new candidate species for JWST detection toward the young star-forming core Cha-MMS1, using a coupled chemo-dynamical model. With this model, the relative abundances of the main ice constituents with respect to water toward the core center match well with typical observational values, providing a firm basis to explore the ice chemistry. Based on the modeled ice composition, the infrared spectrum is synthesized to diagnose the detectability of the new ice species. The contribution of COMs to IR absorption bands is minor compared to the main ice constituents, and the identification of COM ice at NIR (2.4-5.0  $\mu\text{m}$ ) may be unlikely. However, MIRI observations (5-28  $\mu\text{m}$ ) towards COM-rich environments in which solid-phase COM abundances exceed 1 % with respect to the water ice column density might reveal the distinctive ice features of COMs.

The major scientific questions addressed in chapter 1.5 can be answered through this thesis as follows :

**1. What chemical mechanisms are in charge of the formation of COMs in prestellar environments? Is the nondiffusive mechanism efficient enough to explain the chemistry therein?**

In prestellar environments, nondiffusive chemical mechanisms, in particular, three-body and PD-Induced processes take over to synthesize COMs that would otherwise be done through diffusive chemistry. A careful modeling investigation shows that the nondiffusive mechanism is efficient enough to explain the observed abundance of key COMs such as methyl formate in the prestellar core L1544.

**2. Can one generalized scenario explain the chemistry in all temperature regimes for both in the gas and on within ice?**

The nondiffusive model generally explains well the observed chemistry throughout various evolutionary phases of star-forming regions; the cold and quiescent environment of L1544 as well as the active and energetic environment of Orion KL. Furthermore, a recent modeling study by Garrod et al. (2021) shows that nondiffusive mechanisms are indispensable to explain the general chemistry in hot cores. However, some COMs such as dimethyl ether still need other chemical pathways to explain the observed abundances in prestellar cores.

**3. How does chemistry change with the underlying physical condition? Can we define a best tracer for a specific physical condition through chemical modeling?**

It is found that the chemical behavior of some species sensitively changes depending on the underlying physical condition. In particular, the visual extinction can substantially affect a chemical complexity as this parameter governs both dust temperature and photodissociation rate. For example, the strength of ISRF would be well traced by an ice abundance ratio of CO/CO<sub>2</sub>; it quickly decreases with an increasing UV flux due to the efficient conversion of CO to CO<sub>2</sub> (OH + CO → CO<sub>2</sub> + H) on grain-surfaces and within ice mantles. Other potential tracers could be explored further by observing how the chemistry changes within the model.

**4. What are the dominant formation and destruction pathways of the COMs of interest – on dust grain surfaces or in the gas phase?**

Modeling results in this thesis show that the production of many COMs are largely

---

relevant to the chemistry taking place on the surface or within ice mantles. However, it should be noted that all the three sources covered in this thesis are prestellar phase or the sources undergoing very short warm-up timescale. This bias of source selection may result in the representation of the limited case where its chemistry is readily determined by early ice chemistry. According to a recent nondiffusive modeling study by Garrod et al. (2021), another production regime for COMs also occurs during the warm-up phase of hot cores.

5. **What is the chemical composition of the ice within the young star-forming core?**

The model in this thesis predicts the high degree of chemical complexity within icy mantles of young star-forming cores. In particular, seven large oxygen-bearing species (ethanol, acetaldehyde, methyl formate, dimethyl ether, acetic acid, methoxy methanol, and formic acid) are expected to be as abundant as  $> 0.01\%$  with respect to water ice column density.

6. **Can COMs within the icy mantle be detected with JWST? To what degree the ice abundance is required for the secure identification?**

This study shows that the detection of new icy COMs with JWST could still be challenging. Mid-IR observations of COM-rich environments in which solid-phase COM abundances exceed  $1\%$  w.r.t. the water ice column density could reveal distinctive ice features of COMs.



# Bibliography

- Aikawa, Y., Wakelam, V., Garrod, R. T., et al. 2008, *ApJ*, 674, 984. doi:10.1086/524096
- Allen, V., Cordiner, M. A., Adande, G., et al. 2020, arXiv:2010.01151
- Álvarez-Barcia, S., Russ, P., Kästner, J., et al. 2018, *MNRAS*, 479, 2007
- Altwegg, K., Balsiger, H., Bar-Nun, A., et al. 2016, *Science Advances*, 2, e1600285
- Arce H. G., Santiago-Garcia J., Jørgensen J. K., Tafalla M., & Bachiller R. 2008, *ApJ*, 681, L21
- Bacmann A., Taquet V., Faure A., Kahane C., & Ceccarelli C. 2012, *A&A*, 541, L21
- Balucani N., Ceccarelli C., & Taquet V. 2015, *MNRAS*, 449, L16
- Baulch, D. L., Cobos, C. J., Cox, R.A, et al. 1992, *J. Phys. Chem. Ref. Data*, 21, 411
- Bauder A., Lovas F. J., & Johnson D. R. 1976, *J. Phys. Chem. Ref. Data* 5, 53
- Barger, C. J., Lam, K. H., Garrod, R. T., Li, Z. Y., Davis, S. W. & Herbst, E. 2021, *A&A*, *accepted*
- Belloche, A., Parise, B., van der Tak, F. F. S., et al. 2006, *A&A*, 454, L51
- Belloche, A., Parise, B., Schuller, F., et al. 2011, *A&A*, 535, A2. doi:10.1051/0004-6361/201117276
- Belloche, A., Müller, H. S. P., Menten, K. M., et al. 2013, *A&A*, 559, A47. doi:10.1051/0004-6361/201321096
- Belloche, A., Garrod, R. T., Müller, H. S. P., et al. 2014, *Science*, 345, 1584. doi:10.1126/science.1256678
- Belloche, A., Müller, H. S. P., Garrod, R. T., et al. 2016, *A&A*, 587, A91. doi:10.1051/0004-6361/201527268
- Belloche, A., Garrod, R. T., Müller, H. S. P., et al. 2019, *A&A*, 628, A10. doi:10.1051/0004-6361/201935428
- Beltrán, M. T., Codella, C., Viti, S., et al. 2009, *ApJ*, 690, L93
- Bergantini, A., Góbi, S., Abplanalp, M. J., et al. 2018, *ApJ*, 852, 70

- Bergin, E. A. & Tafalla, M. 2007, *ARA&A*, 45, 339.  
doi:10.1146/annurev.astro.45.071206.100404
- Bergner J. B., Öberg K. I., Garrod R. T., & Graninger D. M. 2017, *ApJ*, 841, 120
- Bergner, J. B., Öberg, K. I., & Rajappan, M. 2017, *ApJ*, 845, 29
- Bergner, J. B., Öberg, K. I., & Rajappan, M. 2019, *ApJ*, 874, 115. doi:10.3847/1538-4357/ab07b2
- Bernstein, M. P., Dworkin, J. P., Sandford, S. A., et al. 2002, *Nature*, 416, 401.  
doi:10.1038/416401a
- Bertin, M., Romanzin, C., Doronin, M., et al. 2016, *ApJ*, 817, L12
- Bianchi, E., Codella, C., Ceccarelli, C., et al. 2019, *MNRAS*, 483, 1850.  
doi:10.1093/mnras/sty2915
- Bieler, A., Altwegg, K., Balsiger, H., et al. 2015, *Nature*, 526, 678
- Bisschop, S. E., Jørgensen, J. K., van Dishoeck, E. F., & de Wachter, E. B. M. 2007, *A&A*, 465, 913
- Bizzocchi, L., Caselli, P., Spezzano, S., & Leonardo, E. 2014, *A&A*, 569, A27
- Blake G. A., Sutton E. C., Masson C. R., & Phillips T. G. 1987, *ApJ*, 315, 621
- Blake, G. A., Mundy, L. G., Carlstrom, J. E., et al. 1996, *ApJ*, 472, L49.  
doi:10.1086/310347
- Blázquez S., González, D., Neeman, E. M., et al. 2020, *Phys. Chem. Chem. Phys.*, 2020,22, 20562-20572 doi:10.1039/D0CP03203D
- Boogert, A. C. A., Ehrenfreund, P., Gerakines, P. A., et al. 2000, *A&A*, 353, 349
- Boogert, A. C. A., Blake, G. A., & Tielens, A. G. G. M. 2002, *ApJ*, 577, 271.  
doi:10.1086/342176
- Boogert, A. C. A., Pontoppidan, K. M., Knez, C., et al. 2008, *ApJ*, 678, 985.  
doi:10.1086/533425
- Boogert, A. C. A., Huard, T. L., Cook, A. M., et al. 2011, *ApJ*, 729, 92
- Boogert, A. C. A., Chiar, J. E., Knez, C., et al. 2013, *ApJ*, 777, 73. doi:10.1088/0004-637X/777/1/73
- Boogert, A. C. A., Gerakines, P. A., & Whittet, D. C. B. 2015, *ARA&A*, 53, 541
- Blake G. A., Sutton E. C., Masson C. R., & Phillips T. G. 1987, *ApJ*, 315, 621
- Bohlin, R. C., Savage, B. D., & Drake, J. F. 1978, *ApJ*, 224, 132. doi:10.1086/156357
- Bottinelli S., Boogert A. C. A., Bouwman J. et al 2010, *ApJ*, 718, 1100
- Brouillet, N., Despois, D., Baudry, A., et al. 2013, *A&A*, 550, A46

- Busch, L. A., Belloche, A., Cabrit, S., et al. 2020, *A&A*, 633, A126
- Beuther, H., Zhang, Q., Greenhill, L. J., et al. 2005, *ApJ*, 632, 355. doi:10.1086/432974
- Cazaux, S., Tielens, A. G. G. M., Ceccarelli, C., et al. 2003, *ApJ*, 593, L51. doi:10.1086/378038
- Caselli, P., Walmsley, C. M., Tafalla, M., et al. 1999, *ApJ*, 523, L165
- Cernicharo, J., Marcelino, N., Roueff, E., et al. 2012, *ApJ*, 759, L43
- Chacón-Tanarro, A., Pineda, J. E., Caselli, P., et al. 2019, *A&A*, 623, A118
- Chandler C. J., & Richer, J. S. 2000, *ApJ*, 530, 851
- Chang, Q., & Herbst, E. 2016, *ApJ*, 819, 145
- Chang, P., Davis, S. W., & Jiang, Y.-F. 2020, *MNRAS*, 493, 5397. doi:10.1093/mnras/staa573
- Charnley, S. B. 2005, *Advances in Space Research*, 36, 132
- Chuang, K.-J., Fedoseev, G., Ioppolo, S., et al. 2016, *MNRAS*, 455, 1702
- Cordiner, M. A., Charnley, S. B., Wirström, E. S., et al. 2012, *ApJ*, 744, 131. doi:10.1088/0004-637X/744/2/131
- Crapsi, A., Devries, C. H., Huard, T. L., et al. 2005, *A&A*, 439, 1023
- Crapsi, A., Caselli, P., Walmsley, M. C., & Tafalla, M. 2007, *A&A*, 470, 221
- Csengeri, T., Belloche, A., Bontemps, S., et al. 2019, *A&A*, 632, A57. doi:10.1051/0004-6361/201935226
- Cuppen, H. M., Walsh, C., Lamberts, T., et al. 2017, *Space Sci. Rev.*, 212, 1. doi:10.1007/s11214-016-0319-3
- Curran, H. J. 2006, *Int. J. Chem. Kinet.*, 38, 250
- Davis, S. W. & Gammie, C. F. 2020, *ApJ*, 888, 94. doi:10.3847/1538-4357/ab5950
- Dean A.M., Bozzelli J.W. 2000, *Combustion Chemistry of Nitrogen*. In: Gardiner W.C. (eds) *Gas-Phase Combustion Chemistry*. Springer, New York, NY
- De Simone, M., Codella, C., Ceccarelli, C., et al. 2020, *A&A*, 640, A75. doi:10.1051/0004-6361/201937004
- Dulieu, F., Nguyen, T., Congiu, E., et al. 2019, *MNRAS*, 484, L119
- Dzib, S. A., Loinard, L., Ortiz-León, G. N., et al. 2018, *ApJ*, 867, 151
- Elias, J. H. 1978, *ApJ*, 224, 857
- Elsila, J. E., Glavin, D. P., & Dworkin, J. P. 2009, *Meteoritics and Planetary Science*, 44, 1323

- Favre, C., Despois, D., Brouillet, N., et al. 2011, *A&A*, 532, A32. doi:10.1051/0004-6361/201015345
- Favre, C., Pagani, L., Goldsmith, P. F., et al. 2017, *A&A*, 604, L2. doi:10.1051/0004-6361/201731327
- Fayolle E. C., Öberg K. I., Garrod R. T., van Dishoeck E. F., & Bisschop S. E. 2015, *A&A*, 576, A45
- Fayolle, E. C., Öberg, K. I., Jørgensen, J. K., et al. 2017, *Nature Astronomy*, 1, 703. doi:10.1038/s41550-017-0237-7
- Fedoseev, G., Cuppen, H. M., Ioppolo, S., et al. 2015, *Monthly Notices of the Royal Astronomical Society*, 448, 1288
- Fedoseev, G., Chuang, K.-J., Ioppolo, S., et al. 2017, *The Astrophysical Journal*, 842, 52
- Feng, S., Beuther, H., Henning, T., et al. 2015, *A&A*, 581, A71. doi:10.1051/0004-6361/201322725
- Fraser, H. J., Collings, M. P., McCoustra, M. R. S., et al. 2001, *MNRAS*, 327, 1165. doi:10.1046/j.1365-8711.2001.04835.x
- Fredon, A., Lamberts, T., & Cuppen, H. M. 2017, *ApJ*, 849, 125
- Friedel, D. N. & Snyder, L. E. 2008, *ApJ*, 672, 962. doi:10.1086/523896
- Fourikis, N., Sinclair, M. W., Robinson, B. J., et al. 1974, *Australian Journal of Physics*, 27, 425. doi:10.1071/PH740425
- Fuchs, G. W., Cuppen, H. M., Ioppolo, S., et al. 2009, *A&A*, 505, 629
- Garrod, R. T. & Herbst, E. 2006, *A&A*, 457, 927. doi:10.1051/0004-6361:20065560
- Garrod, R. T., Wakelam, V., & Herbst, E. 2007, *A&A*, 467, 1103. doi:10.1051/0004-6361:20066704
- Garrod, R. T., Widicus Weaver, S. L., & Herbst, E. 2008, *ApJ*, 682, 283
- Garrod, R. T. 2008, *Astronomy and Astrophysics*, 491, 239
- Garrod, R. T. & Pauly, T. 2011, *ApJ*, 735, 15
- Garrod, R. T. 2013, *ApJ*, 765, 60
- Garrod, R. T., Belloche, A., Müller, H. S. P., et al. 2017, *Astronomy and Astrophysics*, 601, A48
- Garrod, R. T. 2019, *ApJ*, 884, 69. doi:10.3847/1538-4357/ab418e
- Garrod, R. T., Jin, M., Matis, K. A., Jones, D., Willis, E. R. & Herbst, E. 2021, *ApJS*, *in press*
- Gerakines, P. A., Schutte, W. A., & Ehrenfreund, P. 1996, *A&A*, 312, 289

- Gerakines, P. A. & Hudson, R. L. 2020, *ApJ*, 901, 52. doi:10.3847/1538-4357/abad39
- Gerin, M., Pety, J., Fuente, A., et al. 2015, *A&A*, 577, L2. doi:10.1051/0004-6361/201525777
- Gillett, F. C. & Forrest, W. J. 1973, *ApJ*, 179, 483. doi:10.1086/151888
- Graedel, T. E., Langer, W. D., & Frerking, M. A. 1982, *ApJS*, 48, 321
- Goldsmith, P. F., & Langer, W. D. 1999, *ApJ*, 517, 209
- Gómez, L., Rodríguez, L. F., Loinard, L., et al. 2005, *ApJ*, 635, 1166. doi:10.1086/497958
- Gottlieb C. A., 1973, in Gordon M. A., Snyder L. E., eds, *Molecules in the Galactic Environment*. p. 181
- Guélin, M., Brouillet, N., Cernicharo, J., et al. 2008, *Ap&SS*, 313, 45. doi:10.1007/s10509-007-9684-4
- Hasegawa, T. I., Herbst, E., & Leung, C. M. 1992, *The Astrophysical Journal Supplement Series*, 82, 167
- Hatchell, J., Fuller, G. A., Richer, J. S., Harries, T. J., & Ladd, E. F. 2007, *A&A*, 468, 1009
- He, J., Emtiaz, S. M., & Vidali, G. 2017, *ApJ*, 851, 104
- Hennebelle, P., & Inutsuka, S.-I. 2019, *Frontiers in Astronomy and Space Sciences*, 6, 5
- Herbst, E., & Leung, C. M. 1986, *ApJ*, 310, 378
- Herbst, E., & van Dishoeck, E. F. 2009, *ARA&A*, 47, 427
- Herron, J.T. & Huie, R.E. 1973, *J. Phys. Chem. Ref. Data*, 2, 467
- Hincelin, U., Wakelam, V., Hersant, F., et al. 2011, *A&A*, 530, A61
- Hippler, H., & Viskolcz, B. 2002, *Physical Chemistry Chemical Physics (Incorporating Faraday Transactions)*, 4, 4663
- Hogbom, J. A. & Brouw, W. N. 1974, *A&A*, 33, 289
- Hollis, J. M., Lovas, F. J., & Jewell, P. R. 2000, *ApJ*, 540, L107
- Hollis, J. M., Lovas, F. J., Jewell, P. R., et al. 2002, *ApJ*, 571, L59
- Hollis, J. M., Jewell, P. R., Lovas, F. J., et al. 2004, *ApJ*, 610, L21.
- Hudson, R. L. Gerakines, P. A. & Ferrante, R. F. 2018, *Spectrochimica Acta Part A: Molecular and Biomolecular Spectroscopy*, 193, 33. doi:10.1016/j.saa.2017.11.055
- Hudson, R. L. & Ferrante, R. F. 2020, *MNRAS*, 492, 283. doi:10.1093/mnras/stz3323
- Hudson, R. L. & Gerakines, P. A. 2019, *MNRAS*, 482, 4009. doi:10.1093/mnras/sty2821

- Hudson, R. L., Yarnall, Y. Y. & Coleman, F. M. 2020, *Spectrochimica Acta Part A: Molecular and Biomolecular Spectroscopy*, 233, 118217. doi:10.1016/j.saa.2020.118217
- Huynh, L. K., & Violi, A. 2008, *J. Org. Chem.*, 73, 94
- Ilyushin V., Kryvda A., Alekseev E. 2009, *J. Mol. Spectrosc.*, 255, 32
- Ikeda, M., Ohishi, M., Nummelin, A., et al. 2001, *ApJ*, 560, 792. doi:10.1086/322957
- Ioppolo, S., Cuppen, H. M., Romanzin, C., et al. 2008, *ApJ*, 686, 1474
- Ioppolo, S., Fedoseev, G., Chuang, K.-J., et al. 2021, *Nature Astronomy*, 5, 197. doi:10.1038/s41550-020-01249-0
- Irvine, W. M., Brown, R. D., Cragg, D. M., et al. 1988, *ApJ*, 335, L89.
- Ivlev, A. V., Röcker, T. B., Vasyunin, A., & Caselli, P. 2015, *ApJ*, 805, 59
- Jaber, A. A., Ceccarelli, C., Kahane, C., et al. 2014, *ApJ*, 791, 29
- Jenkins, E. B. 2009, *ApJ*, 700, 1299
- Jiang, Y.-F., Blaes, O., Stone, J. M., et al. 2019, *ApJ*, 885, 144. doi:10.3847/1538-4357/ab4a00
- Jiménez, E., Antinolo, M., Ballesteros, B., et al. 2016, *Phys. Chem. Chem. Phys.*, 2016,18, 2183-2191 doi:10.1039/C5CP06369H
- Jiménez-Serra, I., Vasyunin, A. I., Caselli, P., et al. 2016, *ApJ*, 830, L6
- Jin, M., Lee, J.-E., & Kim, K.-T. 2015, *ApJS*, 219, 2
- Jin, M. & Garrod, R. T. 2020, *ApJS*, 249, 26
- Johnson, R. E. 1990, *Energetic Charged-particle Interactions with Atmospheres and Surfaces* (Berlin: Springer)
- Johnson, D. G., Blitz, M. A., & Seakins, P. W. 2000, *Physical Chemistry Chemical Physics* (Incorporating Faraday Transactions), 2, 2549
- Jørgensen, J. K., Schöier, F. L., & van Dishoeck, E. F. 2002, *A&A*, 389, 908
- Jørgensen, J. K., Bourke, T. L., Nguyen Luong, Q., et al. 2011, *A&A*, 534, A100
- Jørgensen, J. K., Favre, C., Bisschop, S. E., et al. 2012, *ApJ*, 757, L4
- Jørgensen, J. K., van der Wiel, M. H. D., Coutens, A., et al. 2016, *A&A*, 595, A117
- Jørgensen, J. K., Belloche, A., & Garrod, R. T. 2020, *ARA&A*, 58, 727
- Kalvāns, J. 2018, *Monthly Notices of the Royal Astronomical Society*, 478, 2753
- Kepley, A. A., Tsutsumi, T., Brogan, C. L., et al. 2020, *PASP*, 132, 024505. doi:10.1088/1538-3873/ab5e14

- Kontinen, S., Harju, J., Heikkilä, A., et al. 2000, *A&A*, 361, 704
- Kounkel, M., Hartmann, L., Loinard, L., et al. 2017, *ApJ*, 834, 142. doi:10.3847/1538-4357/834/2/142
- Kuiper, R., Klahr, H., Dullemond, C., et al. 2010, *A&A*, 511, A81. doi:10.1051/0004-6361/200912355
- Kvenvolden, K., Lawless, J., Pering, K., et al. 1970, *Nature*, 228, 923
- Laas, J. C. & Caselli, P. 2019, *A&A*, 624, A108. doi:10.1051/0004-6361/201834446
- Lamberts T., de Vries X., & Cuppen H. M. 2014, *Faraday Discuss*, 168, 327
- Larson, R. B. 1969, *MNRAS*, 145, 271. doi:10.1093/mnras/145.3.271
- Lattalais, M., Bertin, M., Mokrane, H., et al. 2011, *A&A*, 532, A12. doi:10.1051/0004-6361/201016184
- Le Calvé S., Le Bras G., & Mellouki A. 1997, *The Journal of Physical Chemistry A* 1997 101 (48), 9137-9141 doi: 10.1021/jp972369p
- Lee, J. H., Michael, J. V., Payne, W. A., & Stief, L. J., *J. Chem. Phys.*, 68
- Lee, J.-E., Evans, N. J., II, Shirley, Y. L., & Tatematsu, K. 2003, *ApJ*, 583, 789
- Lee, C.-F., Codella, C., Li, Z.-Y., et al. 2019, *ApJ*, 876, 63. doi:10.3847/1538-4357/ab15db
- Lehtinen, K., Harju, J., Kontinen, S., et al. 2003, *A&A*, 401, 1017. doi:10.1051/0004-6361:20030185
- Liu, S.-Y., Girart, J. M., Remijan, A., et al. 2002, *ApJ*, 576, 255. doi:10.1086/341620
- Lohmar, I., & Krug, J. 2006, *Monthly Notices of the Royal Astronomical Society*, 370, 1025
- Lohmar, I., Krug, J., & Biham, O. 2009, *Astronomy and Astrophysics*, 504, L5
- Loison, J.-C., Agúndez, M., Marcelino, N., et al. 2016, *MNRAS*, 456, 4101.
- Lonsdale, C. J., Becklin, E. E., Lee, T. J., et al. 1982, *AJ*, 87, 1819. doi:10.1086/113272
- Lovas F. J., Lutz H., & Dreizler H. 1979, *J. Phys. Chem. Ref. Data* 8
- Lykke, J. M., Coutens, A., Jørgensen, J. K., et al. 2017, *A&A*, 597, A53. doi:10.1051/0004-6361/201629180
- Majewski, S. R., Zasowski, G., & Nidever, D. L. 2011, *ApJ*, 739, 25. doi:10.1088/0004-637X/739/1/25
- Martín-Doménech, R., Öberg, K. I., & Rajappan, M. 2020, *ApJ*, 894, 98. doi:10.3847/1538-4357/ab84e8
- Masunaga, H., Miyama, S. M., & Inutsuka, S.-I. 1998, *ApJ*, 495, 346.

- Maureira, M. J., Arce, H. G., Dunham, M. M., et al. 2020, MNRAS, doi:10.1093/mnras/staa2894
- Maury, A. J., Belloche, A., André, P., et al. 2014, A&A, 563, L2
- McClure, M. 2009, ApJ, 693, L81. doi:10.1088/0004-637X/693/2/L81
- McGuire, B. A., Carroll, P. B., Loomis, R. A., et al. 2016, Science, 352, 1449. doi:10.1126/science.aae0328
- McGuire, B. A., Burkhardt, A. M., Kalenskii, S., et al. 2018, Science, 359, 202. doi:10.1126/science.aao4890
- McGuire, B. A. 2018, ApJS, 239, 17. doi:10.3847/1538-4365/aae5d2
- McGuire, B. A. 2021, arXiv:2109.13848
- McMullin, J. P., Waters, B., Schiebel, D., et al. 2007, Astronomical Data Analysis Software and Systems XVI, 376, 127
- Meinert, C., Myrgorodska, I., de Marcellus, P., et al. 2016, Science, 352, 208
- Menten, K. M. & Reid, M. J. 1995, ApJ, 445, L157. doi:10.1086/187913
- Minissale, M., Moudens, A., Baouche, S., et al. 2016, MNRAS, 458, 2953
- Minissale, M., Congiu, E., & Dulieu, F. 2016, A&A, 585, A146
- Minissale, M., Dulieu, F., Cazaux, S. & Hocuk, S. 2016, A&A, 585, A24
- Möller, T., Endres, C., & Schilke, P. 2017, A&A, 598, A7. doi:10.1051/0004-6361/201527203
- Mousis, O., Ronnet, T., Brugger, B., et al. 2016, ApJ, 823, L41
- Nejad, L. A. M., Williams, D. A., & Charnley, S. B. 1990, ApJ, 246, 183
- Neufeld, D. A., Indriolo, N., DeWitt, C. N., et al. 2015, IAU General Assembly
- Neustock W., Guarnieri A., Demaison J., & Wlodarczak G. 1990, Z. Naturforsch. 45a, 702
- Öberg, K. I., Fuchs, G. W., Awad, Z., et al. 2007, ApJ, 662, L23
- Öberg, K. I., van Dishoeck, E. F., & Linnartz, H. 2009, Astronomy and Astrophysics, 496, 281
- Öberg, K. I., Linnartz, H., Visser, R., et al. 2009, The Astrophysical Journal, 693, 1209
- Öberg K. I., Bottinelli S., Jørgensen J. K., & van Dishoeck E. F. 2010, ApJ, 716, 825
- Öberg, K. I., Boogert, A. C. A., Pontoppidan, K. M., et al. 2011, ApJ, 740, 109. doi:10.1088/0004-637X/740/2/109
- Öberg K. I. 2016, ChRv, 116, 9631

- Ocaña, A. J., Blazquez, S., Ballesteros, B., et al. 2018, *Phys Chem Chem Phys*, 2018;20(8):5865-5873. doi:10.1039/c7cp07868d
- Orozco-Aguilera, M. T., Zapata, L. A., Hirota, T., et al. 2017, *ApJ*, 847, 66. doi:10.3847/1538-4357/aa88cd
- Pagani, L., Favre, C., Goldsmith, P. F., et al. 2017, *A&A*, 604, A32. doi:10.1051/0004-6361/201730466
- Pagani, L., Bergin, E., Goldsmith, P. F., et al. 2019, *A&A*, 624, L5. doi:10.1051/0004-6361/201935267
- Peng, Y., Rivilla, V. M., Zhang, L., et al. 2019, *ApJ*, 871, 251. doi:10.3847/1538-4357/aafad4
- Persi, P., Marenzi, A. R., Gómez, M., et al. 2001, *A&A*, 376, 907. doi:10.1051/0004-6361:20010962
- Penston, M. V. 1969, *MNRAS*, 144, 425. doi:10.1093/mnras/144.4.425
- Plummer G. M., Blake G. A., Herbst E., and De Lucia F. C. 1984, *ApJS*, 55, 633
- Pontoppidan, K. M., van Dishoeck, E. F., & Dartois, E. 2004, *A&A*, 426, 925
- Rachid, M. G., Terwisscha van Scheltinga, J., Koletzki, D., et al. 2020, *A&A*, 639, A4. doi:10.1051/0004-6361/202037497
- Reipurth, B., Nyman, L.-A., & Chini, R. 1996, *A&A*, 314, 258
- Requena-Torres, M. A., Martín-Pintado, J., Martín, S., et al. 2008, *ApJ*, 672, 352.
- Rieke, G. H., Low, F. J., & Kleinmann, D. E. 1973, *ApJ*, 186, L7. doi:10.1086/181346
- Rodgers, S. D. & Charnley, S. B. 2003, *ApJ*, 585, 355.
- Ruaud, M., Loison, J. C., Hickson, K. M., et al. 2015, *MNRAS*, 447, 4004
- Rubin, M., Altwegg, K., van Dishoeck, E. F., et al. 2015, *ApJ*, 815, L11
- Rawlings, J. M. C., Hartquist, T. W., Menten, K. M., et al. 1992, *MNRAS*, 255, 471
- Rawlings, J. M. C., Williams, D. A., Viti, S., Cecchi-Pestellini, C., & Duley, W. W. 2013, *MNRAS*, 430, 264
- Reboussin, L., Wakelam, V., Guilloteau, S., & Hersant, F. 2014, *MNRAS*, 440, 3557
- Sandford, S. A. & Allamandola, L. J. 1990, *Icarus*, 87, 188. doi:10.1016/0019-1035(90)90028-8
- Schlaflly, E. F., Meisner, A. M., Stutz, A. M., et al. 2016, *ApJ*, 821, 78. doi:10.3847/0004-637X/821/2/78
- Schutte, W. A., Boogert, A. C. A., Tielens, A. G. G. M., et al. 1999, *A&A*, 343, 966
- Shuping, R. Y., Morris, M., & Bally, J. 2004, *AJ*, 128, 363. doi:10.1086/421373

- Scibelli, S. & Shirley, Y. 2020, ApJ, 891, 73. doi:10.3847/1538-4357/ab7375
- Senosiain, J. P., Klippenstein, S. J. and Miller, J. A. 2006 J. Phys. Chem. A, 110, 17, 5772–5781
- Shannon, R., Blitz, M., Goddard, A. et al. 2013, Nature Chem 5, 745 doi: 10.1038/nchem.1692
- Senevirathne, B., Andersson, S., Dulieu, F. & Nyman, G. Molecular Astrophysics, 6, 59
- Senosiain, J.P., Klippenstein, S.J., & Miller, J.A. 2016, J. Phys. Chem. A, 110, 5772
- Shannon, R. J., Cossou, C., Loison, J.-C., et al. 2014, arXiv e-prints, arXiv:1406.1363
- Shingledecker, C. N., Le Gal, R., & Herbst, E. 2017, Physical Chemistry Chemical Physics (Incorporating Faraday Transactions), 19, 11043
- Shingledecker, C. N., Tennis, J., Le Gal, R., & Herbst, E. 2018, ApJ, 861, 20
- Slate, E. C. S., Barker, R., Euesden, R. T., et al. 2020, MNRAS, 497, 5413. doi:10.1093/mnras/staa2436
- Spinks, J., & Woods, R. 1990, An introduction to Radiation Chemistry (New York: Wiley)
- Stone, J. M., Tomida, K., White, C. J., et al. 2020, ApJS, 249, 4. doi:10.3847/1538-4365/ab929b
- Takahashi, K., Yamamoto, O., Inomata, T. & Kogoma, M. 2007, Int. J. Chem. Kinet., 39, 97
- Taquet, V., Charnley, S. B., & Sipilä, O. 2014, ApJ, 791, 1
- Taquet, V., Furuya, K., Walsh, C., et al. 2016, MNRAS, 462, S99
- Taquet, V., Wirström, E. S., Charnley, S. B., et al. 2017, A&A, 607, A20
- Tennekes, P. P., Harju, J., Juvela, M., et al. 2006, A&A, 456, 1037. doi:10.1051/0004-6361:20040294
- Tennis, J., Loison, J.-C. & Herbst, E., *in prep.*
- Tercero, B., Cernicharo, J., López, A., et al. 2015, A&A, 582, L1. doi:10.1051/0004-6361/201526255
- Tercero, B., Cuadrado, S., López, A., et al. 2018, A&A, 620, L6. doi:10.1051/0004-6361/201834417
- Terwisscha van Scheltinga, J., Ligterink, N. F. W., Boogert, A. C. A., et al. 2018, A&A, 611, A35. doi:10.1051/0004-6361/201731998
- Terwisscha van Scheltinga, J., Marcandalli, G., McClure, M. K., Hogerheijde, M. R., & Linnartz, H. 2021, <https://arxiv.org/abs/2105.02226>
- Tielens, A. G. G. M., Tokunaga, A. T., Geballe, T. R., & Baas, F. 1991, ApJ, 381, 181

- Tsang, W. 1987, *J. Phys. Chem. Ref. Data*, 16
- Turner, B. E. 1991, *ApJS*, 76, 617. doi:10.1086/191577
- van Dishoeck, E. F., Kristensen, L. E., Mottram, J. C., et al. 2021, *A&A*, 648, A24. doi:10.1051/0004-6361/202039084
- Vastel, C., Ceccarelli, C., Lefloch, B., & Bachiller, R. 2014, *ApJ*, 795, L2
- Vasyunin, A. I., & Herbst, E. 2013, *ApJ*, 769, 34
- Vasyunin, A. I., Caselli, P., Dulieu, F., & Jiménez-Serra, I. 2017, *ApJ*, 842, 33
- Vazart, F., Ceccarelli, C., Balucani, N., et al. 2020, *MNRAS*, 499, 5547. doi:10.1093/mnras/staa3060
- Wakelam, V. & Herbst, E. 2008, *ApJ*, 680, 371
- Wakelam, V., Loison, J.-C., Mereau, R., et al. 2017, *Molecular Astrophysics*, 6, 22. doi:10.1016/j.molap.2017.01.002
- Walsh, C., Loomis, R. A., Öberg, K. I., et al. 2016, *ApJ*, 823, L10
- Warnatz, J. 1984, *Combustion Chemistry*, ed. W. C. Gardiner, Jr., Springer-Verlag, New York, USA
- Westenberg, A.A. & DeHaas, N. 1967, *J. Chem. Phys.*, 46
- Willis, E. R., & Garrod, R. T. 2017, *ApJ*, 840, 61
- Willis, E. R., Garrod, R. T., Belloche, A., et al. 2020, *A&A*, 636, A29
- Wynn-Williams, C. G., Genzel, R., Becklin, E. E., et al. 1984, *ApJ*, 281, 172. doi:10.1086/162086
- Xu L.-H., Fisher J., Lees R.M., Shy H.Y., Hougen J.T., et al. 2008, *J. Mol. Spectrosc.* 251, 305.
- Xue, M., Jiang, B. W., Gao, J., et al. 2016, *ApJS*, 224, 23. doi:10.3847/0067-0049/224/2/23
- Ziurys, L. M. & McGonagle, D. 1993, *ApJS*, 89, 155. doi:10.1086/191842
- Zucconi, A., Walmsley, C. M., & Galli, D. 2001, *A&A*, 376, 650

